Semiflexible Polymers: Fundamental Theory and Applications in DNA Packaging

Thesis by

Andrew James Spakowitz

In Partial Fulfillment of the Requirements

for the Degree of

Doctor of Philosophy

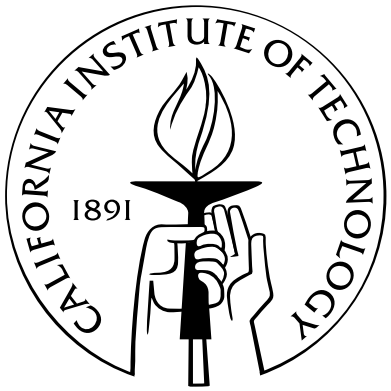

California Institute of Technology

MC 210-41 Caltech

Pasadena, California 91125

2004

(Defended September 28, 2004)

Acknowledgements

Over the last five years, I have benefitted greatly from my interactions with many people in the Caltech community. I am particularly grateful to the members of my thesis committee: John Brady, Rob Phillips, Niles Pierce, and David Tirrell. Their example has served as guidance in my scientific development, and their professional assistance and coaching have proven to be invaluable in my future career plans. Our collaboration has impacted my research in many ways and will continue to be fruitful for years to come.

I am grateful to my research advisor, Zhen-Gang Wang. Throughout my scientific development, Zhen-Gang's ongoing patience and honesty have been instrumental in my scientific growth. As a researcher, his curiosity and fearlessness have been inspirational in developing my approach and philosophy. As an advisor, he serves as a model that I will turn to throughout the rest of my career.

Throughout my life, my family's love, encouragement, and understanding have been of utmost importance in my development, and I thank them for their ongoing devotion. My friends have provided the support and, at times, distraction that are necessary in maintaining my sanity; for this, I am thankful.

Finally, I am thankful to my fiancée, Sarah Heilshorn, for her love, support, encouragement, honesty, critique, devotion, and wisdom. As a scientist who has my utmost respect, she serves as a model of integrity and discipline that has shaped my development. She is my most trusted friend, and I could not have done this without her.

Abstract

Much is understood about the behavior of perfectly flexible and perfectly rigid polymer chains; however, many polymers, for example DNA, are somewhere in between these two limiting cases. Such polymers are termed semiflexible, and their molecular elasticity can play a significant role in single-chain behavior as well as contribute to collective effects. Using analytical theory and numerical methods, we address several problems that focus on the equilibrium and dynamic behavior of semiflexible polymers to gain a deeper understanding of their fundamental physics. We consider the equilibrium statistical behavior of semiflexible polymers under the influence of external fields, confinement, and the collective influence of a nematic liquid-crystal phase. We then turn to the dynamics of a deformed elastic thread, addressing instances of instability and the subsequent nonlinear relaxation. Once we establish an understanding of these physical effects, we discuss the role that they play in DNA packaging, specifically focusing on the role of twist in DNA packaging in chromatin and the formation of an ordered conformation within a viral capsid.

Contents

List of Figures

Chapter 1

Introduction

Polymers are big molecules. Because of their large size, the physical behavior of individual polymer molecules is dramatically different than that of their small-molecule analogues. In many instances, interactions that occur at molecular length scales convey information that persists up to macroscopic length scales, significantly altering material properties and behavior in frequently unexpected and novel ways. As a consequence, polymeric materials play an important role in many technological applications. Furthermore, all biological entities are based on polymeric materials.

Much of our theoretical understanding of the behavior of polymeric materials is based on descriptions of macromolecules as either perfectly rigid bodies or perfectly flexible threads [1, 2]. Certainly a wide range of physical issues are elucidated by such treatments; however, many polymers are somewhere in between these two limiting cases. For example, a polymer molecule with molecular architecture that instills rigidity to the resulting assembly can behave dramatically different than its idealized counterparts in its equilibrium, dynamic, single-molecule, and collective behavior. We utilize analytical theory and computational techniques to explore the physical behavior of macromolecular systems, focusing on the effect of molecular elasticity on single-molecule and collective behavior.

Elasticity has historically played an important role in macroscopic mechanics and ma-

terial physics [3, 4]. For elastic bodies that exist at very small length scales, the energy associated with substantial deformation of the elastic body is comparable to the thermal energy; therefore, the thermal energy acts to deform the malleable elastic object. An elastic chain resists bending deformation; the energetic cost is larger for shorter or tighter bends than for more sweeping deformations. As a result, thermally induced deformation is more dramatic at larger length scales than at smaller length scales. This effect is demonstrated in Fig. 1.1, which shows a typical equilibrium conformation of an elastic thread subject to thermal fluctuations at successively smaller length scales. Figure 1.1 demonstrates the dual behavior that arises from molecular elasticity: at small length scales, the chain behaves as a rigid rod, and at large length scales, the chain appears flexible. This effect is called semiflexibility, which plays a key role in the behavior of such polymers.

This thesis represents research on the behavior of semiflexible polymers. Chapters 2 through 4 present fundamental theory on the equilibrium behavior of semiflexible polymers in several scenarios of physical and biological relevance, focusing on the coupling between thermodynamic behavior and chain conformation. Chapters 5 and 6 address two instances where chain deformation results in dynamic instability, leading to complex relaxation dynamics. After establishing a fundamental understanding of the equilibrium and dynamic behavior of semiflexible polymers in Chaps. 2 through 6, Chaps. 7 and 8 turn to two problems of biological relevance that intrinsically involve these effects.

Much of our theoretical understanding of the equilibrium behavior of polymeric materials is based on field-theoretical techniques, which require as input a method of evaluating the statistical behavior of a single polymer chain in a fluctuating external field [5]. The calculation of the statistical behavior of a flexible polymer frequently yields analytical solutions; however, very few problems involving semiflexible polymers admit solutions for their statis-

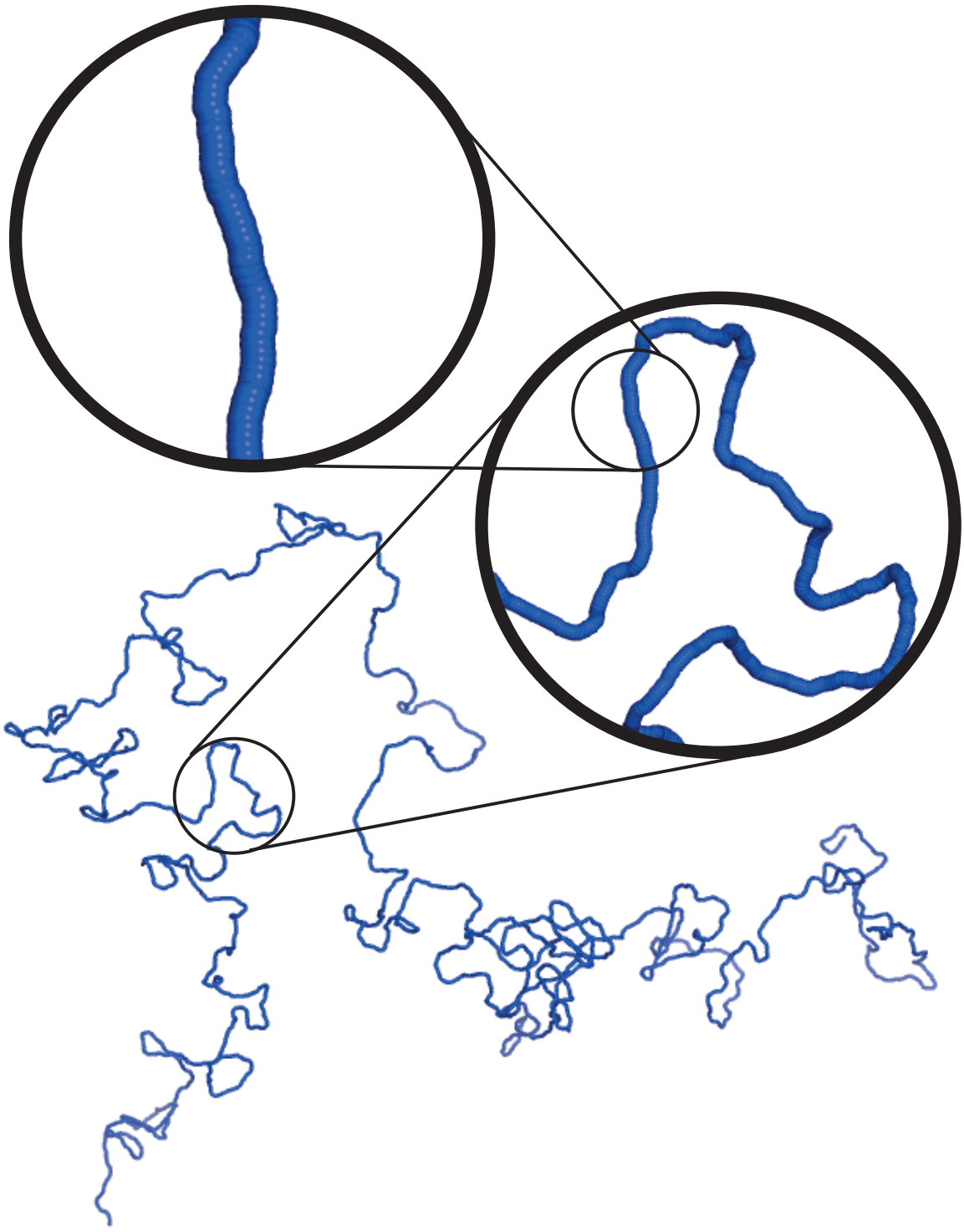

Figure 1.1: Conformation of a semiflexible polymer at successively smaller length scales.

tical behavior. Therefore, there are many unsolved problems that address the fundamental thermodynamic behavior of polymeric materials composed of semiflexible polymers.

The behavior of a semiflexible polymer in a homogeneous external field is important in addressing several important physical problems. The response of DNA to end tension, as in optical and magnetic tweezer experiments [6], is modeled as a semiflexible polymer chain in an external dipole field [7, 8]. Furthermore, a semiflexible polymer in a dipole field is needed to calculate the structure factor, which is required to predict the results of scattering experiments of a dilute solution of semiflexible polymers [9] and to study the thermodynamic behavior of a polymer solution including mean-field fluctuations [10]. The behavior of a semiflexible polymer in a nematic liquid crystal phase is frequently studied using polymer field theory, requiring as input a solution for the statistical behavior of a semiflexible chain in an external quadrupole field [11]. Thus, the statistical behavior of a semiflexible polymer in an external field is necessary to study several important biological and material systems.

In Chap. 2, we provide exact analytical solutions for the statistical behavior of a semiflexible polymer, modeled as a wormlike chain, subject to the influence of a dipole and a quadrupole field in both two and three spatial dimensions [12]. With these solutions, we address all of the problems mentioned in the previous paragraph without approximations whose validity is not generally well understood. Our results adopt a simple and compact analytical structure that make them extremely convenient to use, and our techniques are applicable to a wide range of additional physical problems including a helical wormlike chain [13], a quantum-mechanical rigid rotor, and a rotating Brownian particle.

The physical confinement of a polymer molecule is important in a number of technological applications and biological processes. The packaging of DNA or RNA in viruses

involves confinement of the polymer chain to a region that is much smaller than the unconstrained radius of gyration of the strand [14]. Confinement also occurs in the case of a polymer chain interacting with a strongly attractive particle, which is relevant in a number of instances including colloidal stabilization [15] and DNA condensation in chromatin [16] and gene therapy applications [17].

The thermodynamic effect of confinement on a flexible polymer is entirely entropic, thus the confined flexible chain tends to fill the available volume [1]. Confining a semiflexible polymer involves both energetic and entropic contributions with the balance controlled by the ratio between the persistence length and the length scale of the confinement. A number of analytical results exist that describe the behavior of a flexible polymer in a confinement; however, solutions for the behavior of semiflexible polymer in a confined geometry are nonexistent.

In Chap. 3, we consider the behavior of a semiflexible polymer confined to the surface of a sphere, which acts as a model problem for the confinement of a semiflexible polymer [18]. Our closed-form, analytical solution for the mean-square end-to-end distance, which is valid for arbitrary chain length, persistence length, and sphere radius, provides insight into the balance between energy and entropy that is a common feature in the confinement of a semiflexible polymer chain. Furthermore, this problem is relevant to systems with a polymer strongly adsorbed to a sphere surface, which model DNA/protein complexes and polymer adsorption on colloidal particles [19, 20, 21].

The enhanced alignment associated with the formation of liquid crystal phases influences bulk properties, resulting in novel high-strength and optical materials [22], and processing behavior including flow-induced crystallization [23]. Solutions of rigid molecules tend to form liquid crystal phases at low temperatures and/or high concentrations, resulting in a loss

of rotational freedom [24]. Semiflexible polymer solutions also form ordered liquid crystal phases; this transition is accompanied by a loss of both the rotational degrees of freedom as well as the conformation entropy of the chain segments. The thermodynamic contribution of the conformation entropy dramatically alters the equilibrium behavior of semiflexible polymer solutions from their perfectly rigid analogous. Furthermore, the conformation of a semiflexible chain in a liquid crystal phase is dramatically influenced by its ability to adopt a variety of shapes. For example, the polymer chain can exhibit sharp reversals in direction called hairpin defects, which dramatically alter the volume that the polymer occupies [25].

Chapter 4 turns to the equilibrium behavior of a semiflexible polymer solution using polymer field theory to predict the phase behavior and the conformation statistics of a main-chain polymer liquid-crystal solution [11]. We use the exact solution for the chain statistics of a semiflexible polymer chain in the nematic liquid-crystalline phase, which provides a simple set of equations that govern the phase behavior and the single-chain conformation properties and is a necessary input in addressing concentration and order fluctuations away from the mean-field solution. Conformation fluctuations are shown to significantly suppress molecular ordering and thus dramatically decrease the isotropic-nematic transition temperature. Analysis of the conformation statistics predicts the conditions where hairpin defects are prevalent in the polymer chain and their influence on the polymer volume.

Slender elastic filaments [3, 4] play a role in a wide range of engineering applications from macroscopic beams and cables, to nanoscale devices, to molecular threads. Furthermore, microscopic organisms use the whip-like motion of their flagella to propel themselves through the surrounding viscous environment. The response of an elastic filament to extreme deformation exhibits rich physical behavior that includes instability and subsequent nonlinear relaxation. Predicting the resulting dynamics from deformation provides insight

into the dynamic behavior of elastic filaments in a number of engineering applications and biological phenomena.

Novel materials such as anionic hydrogels respond to changes in pH and salt concentration by reversibly swelling to many times their original volume [26]; filaments composed of such materials have potential application as mechanical levers in nanoscale devices [27]. In Chap. 5, we study the dynamics of an initially straight elastic filament undergoing expansion after a sudden change in the solvent conditions using computer simulation [28]. The expansion proceeds by buckling in the transverse direction with a characteristic wavelength that we predict using linear stability analysis. The wavelike buckles locally adopt helical structures with domains of common handedness; these domains grow in time until the conformation tends to a pure helix in the late stages in the relaxation process. The coarsening dynamics exhibited in the simulations are analyzed using nonlinear scaling arguments that provide insight into the fundamental nature of the relaxation processes.

The dynamics of a twisted elastic filament is applicable to a wide range of engineering applications and biological phenomena including macroscopic cables [29], bacterial propulsion [30, 31, 32], and DNA supercoiling [33, 34, 35]. The supercoiling phenomenon is marked by a competition between purely helical structures and the interwound helices that are generally seen in DNA supercoiling; these interwound helices, or plectonemes, are favored over pure helices, or solenoids, as they are more efficient at alleviating the twist deformation in the chain [36]. Chapter 6 studies the dynamic problem of a clamped, twisted elastic filament undergoing supercoiling dynamics. We perform a linear stability analysis to find the conditions for supercoiling and the structure of the initial instability, which is a pure helix. Analysis of the post-buckling structure shows a localization of the helices into a single loop [29, 35], which eventually becomes the cap of the growing plectonemic supercoil.

Numerical solutions of the equations of motion demonstrate a propensity for loop formation near the chain ends; these loops collapse, and two plectonemes twirl out into the quiescent fluid. The plectonemes grow until they encompass the entire chain or they are arrested by the end tension.

The physical manipulation of DNA is an important goal in the packaging of DNA within a viral capsid or the nucleus of a eukaryotic cell. Precise control is necessary in storing the excessively large DNA strand and in accessing the all-important genetic information that it contains. The exquisite control that Nature has over DNA conformation is desired in a number of technological applications including gene therapy [17] and novel nanomaterials based on DNA self assembly [37]. Understanding the interplay of the underlying physical forces that are at work provides insight into the methods that Nature has designed to conduct the necessary biological processes involving DNA and establishes an understanding of how we can predict and control DNA behavior in technological applications.

DNA is packaged to near-crystalline density inside a virus at the considerable expense of the deformation of the chain, the conformational entropy loss, and the electrostatic self-repulsion. The packaged genome of several species of double-stranded DNA bacteriophage appears to adopt a highly ordered spool conformation within the capsid [38, 39, 40, 41, 42]. The genome of the $\phi 29$ bacteriophage is packaged by a powerful protein motor that literally grabs the DNA and shoves it into the viral capsid. The structure of this packaging motor suggests that the DNA is rotated as it is transferred into the capsid [43], potentially implicating twist as a possible player in the chain ordering. Chapter 7 studies the dynamics of viral packaging using computer simulations of a polymer chain being forced into a spherical cavity with an emphasis on the evolution of a highly ordered conformation within the capsid. When the polymer is rotated during the packaging, the chain adopts a more

ordered conformation than when the polymer is packaged without rotation. Furthermore, ejection dynamics show that the structure resulting from packaging with rotation ejects more polymer than the structure resulting from packaging without rotation.

DNA is packaged in a eukaryotic cell into a structure called chromatin, which is both compact and accessible to the nuclear environment. The fundamental unit of chromatin is a nucleosome core particle consisting of a short stretch of DNA wrapped around a cationic protein complex called the histone octamer [44]. The packaging of DNA in a nucleosome is strongly influenced by the salt concentration [45] and, for plasmid DNA, the linking number of the strand [46], resulting in polymorphism in the stable packaged DNA. The *in vitro* assembly of a chromatin fiber with reproducible physical properties involves a very particular salt history [47]. In Chap. 8, the effect of twist on the formation of a nucleosome core particle is studied by considering a polyelectrolyte ring interacting with an oppositely charged sphere. The interaction between polymer and sphere is modulated by the salt concentration, resulting in wrapping transitions. Our results capture the conformational polymorphism and the salt hysteresis exhibited by the experimental system.

Bibliography

[1] P. G. de Gennes. *Scaling Concepts in Polymer Physics*. Cornell University Press, 1979.

[2] M. Doi and S. F. Edwards. *The Theory of Polymer Dynamics*. Oxford University Press Inc., New York, NY, 1986.

[3] A. E. H. Love. *A Treatise on the Mathematical Theory of Elasticity*. Dover Publications, Inc., New York, NY, 1944.

[4] L. D. Landau and E. M. Lifshitz. *Theory of Elasticity*. Pergamon Press, 1986.

[5] G. H. Fredrickson, V. Ganesan, and F. Drolet. Field-theoretic computer simulation methods for polymers and complex fluids. *Macromolecules*, 35(1):16–39, 2002.

[6] C. Bustamante, Z. Bryant, and S. B. Smith. Ten years of tension: single-molecule DNA mechanics. *Nature*, 421(6921):423–427, 2003.

[7] J. F. Marko and E. D. Siggia. Stretching DNA. *Macromolecules*, 28(26):8759–8770, 1995.

[8] J. D. Moroz and P. Nelson. Torsional directed walks, entropic elasticity, and DNA twist stiffness. *Proceedings of the National Academy of Sciences of the United States of America*, 94(26):14418–14422, 1997.

[9] G. C. Berry. Static and dynamic light-scattering on moderately concentrated-solutions - isotropic solutions of flexible and rodlike chains and nematic solutions of rodlike chains. In *Polymer Analysis and Characterization*, volume 114 of *Advances in Polymer Science*, pages 233–290. Springer-Verlag, New York, 1994.

[10] Z.-G. Wang. Concentration fluctuation in binary polymer blends: χ parameter, spinodal and ginzburg criterion. *J. Chem. Phys.*, 117(1):481–500, 2002.

[11] A. J. Spakowitz and Z.-G. Wang. Semiflexible polymer solutions. I. phase behavior and single- chain statistics. *J. Chem. Phys.*, 119(24):13113–13128, 2003.

[12] A. J. Spakowitz and Z.-G. Wang. Exact results for a semiflexible polymer chain in an aligning field. *Macromolecules*, 37(15):5814–5823, 2004.

[13] H. Yamakawa. *Helical Wormlike Chains in Polymer Solutions*. Springer-Verlag, 1997.

[14] B. Lewin. *Genes VII*. Oxford University Press, 2000.

[15] T. A. Witten and P. A. Pincus. Colloid stabilization by long grafted polymers. *Macromolecules*, 19(10):2509–2513, 1986.

[16] H. Lodish, A. Berk, S. L. Zipursky, D. Baltimore, and J. Darnell. *Molecular Cell Biology*. W. H. Freeman and Company, 2000.

[17] A. K. Pannier and L. D. Shea. Controlled release systems for DNA delivery. *Molecular Therapy*, 10(1):19–26, 2004.

[18] A. J. Spakowitz and Z.-G. Wang. Semiflexible polymer confined to a spherical surface. *Phys. Rev. Lett.*, 91(16):art. no.–166102, 2003.

[19] T. Odijk. Physics of tightly curved semiflexible polymer-chains. *Macromolecules*, 26(25):6897–6902, 1993.

[20] H. Schiessel, J. Widom, R. F. Bruinsma, and W. M. Gelbart. Polymer reptation and nucleosome repositioning. *Phys. Rev. Lett.*, 86(19):4414–4417, 2001.

[21] S. Stoll and P. Chodanowski. Polyelectrolyte adsorption on an oppositely charged spherical particle-chain rigidity effects. *Macromolecules*, 35(25):9556–9562, 2002.

[22] A. A. Collyer. *Liquid Crystal Polymers: From Structures to Applications*. Elsevier Science Publishers Ltd., 1992.

[23] W. J. Zhou, J. A. Kornfield, V. M. Ugaz, W. R. Burghardt, D. R. Link, and N. A. Clark. Dynamics and shear orientation behavior of a main-chain thermotropic liquid crystalline polymer. *Macromolecules*, 32(17):5581–5593, 1999.

[24] P. G. de Gennes and J. Prost. *The Physics of Liquid Crystals*. Clarendon Press, 1993.

[25] P. G. de Gennes. in *Polymer Liquid Crystals*, ed. by A. Ciferri, W. R. Krigbaum, R. B. Meyer. Academic, New York, 1982.

[26] G. M. Eichenbaum, P. F. Kiser, S. A. Simon, and D. Needham. pH and ion-triggered volume response of anionic hydrogel microspheres. *Macromolecules*, 31(15):5084–5093, 1998.

[27] E. Evans, H. Bowman, A. Leung, D. Needham, and D. Tirrell. Biomembrane templates for nanoscale conduits and networks. *Science*, 273(5277):933–935, 1996.

[28] A. J. Spakowitz and Z.-G. Wang. Free expansion of elastic filaments. *Phys. Rev. E*, 6406(6):art. no.–061802, 2001.

[29] J. Coyne. Analysis of the formation and elimination of loops in twisted cable. *IEEE J. Ocean. Eng.*, 15(2):72–83, 1990.

[30] R. E. Goldstein and S. A. Langer. Nonlinear dynamics of stiff polymers. *Phys. Rev. Lett.*, 75(6):1094–1097, 1995.

[31] R. E. Goldstein, T. R. Powers, and C. H. Wiggins. Viscous nonlinear dynamics of twist and writhe. *Phys. Rev. Lett.*, 80(23):5232–5235, 1998.

[32] R. E. Goldstein, A. Goriely, G. Huber, and C. W. Wolgemuth. Bistable helices. *Phys. Rev. Lett.*, 84(7):1631–1634, 2000.

[33] J. Huang, T. Schlick, and A. Vologodskii. Dynamics of site juxtaposition in supercoiled DNA. *Proc. Natl. Acad. Sci. U.S.A.*, 98(3):968–973, 2001.

[34] S. Allison, R. Austin, and M. Hogan. Bending and twisting dynamics of short linear DNAs - analysis of the triplet anisotropy decay of a 209-basepair fragment by Brownian simulation. *J. Chem. Phys.*, 90(7):3843–3854, 1989.

[35] G. H. M. van der Heijden and J. M. T. Thompson. Helical and localised buckling in twisted rods: A unified analysis of the symmetric case. *Nonlinear Dyn.*, 21(1):71–99, 2000.

[36] J. F. Marko and E. D. Siggia. Fluctuations and supercoiling of DNA. *Science*, 265(5171):506–508, 1994.

[37] N. C. Seeman. DNA in a material world. *Nature*, 421(6921):427–431, 2003.

[38] N. H. Olson, M. Gingery, F. A. Eiserling, and T. S. Baker. The structure of isometric capsids of bacteriophage T4. *Virology*, 279(2):385–391, 2001.

[39] L. W. Black, W. W. Newcomb, J. W. Boring, and J. C. Brown. Ion etching of bacteriophage-T4 - support for a spiral-fold model of packaged DNA. *Proc. Natl. Acad. Sci. U.S.A.*, 82(23):7960–7964, 1985.

[40] M. E. Cerritelli, N. Cheng, A. H. Rosenberg, M. N. Simon, and A. C. Steven. Organization of dsDNA in bacteriophage T7 capsids: Support for the coaxial-spool model. *Biophys. J.*, 70(2):WAMC1–WAMC1, 1996.

[41] M. E. Cerritelli, N. Q. Cheng, A. H. Rosenberg, C. E. McPherson, F. P. Booy, and A. C. Steven. Encapsidated conformation of bacteriophage T7 DNA. *Cell*, 91(2):271–280, 1997.

[42] Z. X. Zhang, B. Greene, P. A. Thuman-Commike, J. Jakana, P. E. Prevelige, J. King, and W. Chiu. Visualization of the maturation transition in bacteriophage P22 by electron cryomicroscopy. *J. Mol. Biol.*, 297(3):615–626, 2000.

[43] A. A. Simpson, Y. Z. Tao, P. G. Leiman, M. O. Badasso, Y. N. He, P. J. Jardine, N. H. Olson, M. C. Morais, S. Grimes, D. L. Anderson, T. S. Baker, and M. G. Rossmann. Structure of the bacteriophage ϕ29 DNA packaging motor. *Nature*, 408(6813):745–750, 2000.

[44] K. Luger, A. W. Mader, R. K. Richmond, D. F. Sargent, and T. J. Richmond. Crystal structure of the nucleosome core particle at 2.8 angstrom resolution. *Nature*, 389(6648):251–260, 1997.

[45] T. D. Yager, C. T. McMurray, and K. E. Vanholde. Salt-induced release of DNA from nucleosome core particles. *Biochemistry*, 28(5):2271–2281, 1989.

[46] A. Prunell. A topological approach to nucleosome structure and dynamics: The linking number paradox and other issues. *Biophys. J.*, 74(5):2531–2544, 1998.

[47] K. Hizume, S. H. Yoshimura, H. Maruyama, J. Kim, H. Wada, and K. Takeyasu. Chromatin reconstitution: Development of a salt-dialysis method monitored by nanotechnology. *Arch. Histol. Cytol.*, 65(5):405–413, 2002.

Chapter 2

Exact Results for a Semiflexible Polymer Chain in an Aligning Field

We provide exact results for the Laplace-transformed partition function of a wormlike chain subject to a tensile force and in a nematic field, in both 2 and 3 dimensions. The results are in the form of infinite continued fractions, which are obtained by exploiting the hierarchical structure of a moment-based expansion of the partition function. The case of an imaginary force corresponds to the end-to-end distance distribution in Laplace-Fourier space. We illustrate the utility of these exact results by examining the structure factor of a wormlike chain, the deformation free energy of a chain in a nematic field, and the self-consistent-field solution for the isotropic-nematic transition of wormlike chains.

2.1 Introduction

A number of physical problems involving semiflexible polymers can be mapped to that of a single chain in an external field. The force-extension behavior of a single semiflexible polymer is described as the response of a polymer to a dipole aligning field acting on the end-to-end distance vector [1, 2, 3, 4]. The behavior of a semiflexible chain dissolved in

a nematic liquid crystal corresponds to a polymer in a quadrupole aligning field [5]. The latter problem also naturally arises in the self-consistent-field description of polymer liquid crystals [6, 7, 8, 9]. Perhaps less obvious, finding the end-to-end distance distribution function of a polymer involves solving for the partition function of a chain in an imaginary dipole field [10, 11, 12]. Since these problems share a similar mathematical representation, methods for studying the behavior of a semiflexible chain in an external aligning field have many applications in polymer physics.

In this chapter, we provide exact analytical solutions for the partition function in Laplace space of a wormlike polymer subject to real and imaginary dipole fields and a nematic quadrupole field, in both two and three dimensions, and use these results to examine the structure factor, the deformation free energy of a polymer chain in a nematic liquid crystal, and the self-consistent-field solution for the isotropic-nematic transition of wormlike chains. The methods employed in this chapter rely on the use of the diagrammatic representation of Yamakawa [10] for the moments of the end-to-end distance distribution function. By exploiting the hierarchical structure of the moment expansion of the various partition functions, we are able to re-sum the infinite diagrammatic series into a simple, exact, and concise continued-fraction form. We note that the end-to-end distance distribution for the wormlike chain model was recently obtained by two groups. Samuel and Sinha provided a numerical solution by a direct diagonalization of the truncated scattering matrix [11]. Stepanow and Schütz obtained exact results [12] using algebraic techniques developed by Temperley and Lieb in their study of graph-theoretical problems involving regular planar lattices [13]. However, our results are advantageous by virtue of their simple and compact analytical structure which makes them convenient to use. In addition, our re-summation method is applicable to a single chain in a nematic field, a helical wormlike chain, and

a class of physical problems including a quantum-mechanical rigid rotor and a Brownian particle undergoing rotational diffusion.

The rest of this chapter is organized as follows. In Sec. 2.2, we discuss our analytical solutions in two dimensions with a detailed explanation of the method. In Sec. 2.3, we present the analogous three-dimensional solutions and provide a discussion on the generalization of our techniques. In Sec. 2.4, we use our result for the end-to-end distance distribution function to study the structure factor of a wormlike chain. In Sec. 2.5, we discuss the deformation of a wormlike chain in a nematic liquid crystal and the self-consistent-field free energy of polymer liquid crystals in conjunction with our earlier work on the subject [9]. Finally, we conclude with a summary of our results in Sec. 2.6.

2.2 Two-Dimensional Solutions

The wormlike chain model in d dimensions is described by an inextensible spacecurve $\vec{r}(s)$ parameterized by the path-length coordinate s that runs from zero to the contour length of the chain L. The inextensibility is enforced by constraining the tangent vector $\vec{u} \equiv \partial_s \vec{r}$ such that $|\vec{u}| = 1$ for all s. The bending deformation energy, which is quadratic in the curvature of the spacecurve, is given by [14]

$$\beta\mathcal{H}_0 = \frac{l_p}{2} \int_0^L ds \left(\frac{\partial \vec{u}}{\partial s} \right)^2 , \tag{2.1}$$

where l_p is the persistence length and $\beta = 1/(k_B T)$. The total chain Hamiltonian is given by $\beta\mathcal{H} = \beta\mathcal{H}_0 + \beta\mathcal{H}_{ext}$, where $\beta\mathcal{H}_{ext}$ represents the interaction between the polymer chain and the external field.

In two dimensions, the orientation of the tangent vector is defined by the angle θ between

the tangent and the x-axis of an arbitrarily chosen coordinate system. The orientational statistics of the wormlike chain in the absence of an external field is described by the Green's function $G_0(\theta|\theta_0; L)$ defined to be the conditional probability that a chain of length L with initial orientation angle θ_0 will have the final orientation angle θ. The Green's function is found by summing over the paths between θ_0 and θ, giving each path the amplitude $\exp(-\beta\mathcal{H}_0)$, which is formally stated as

$$G_0(\theta|\theta_0; L) = \int_{\theta(s=0)=\theta_0}^{\theta(s=L)=\theta} \mathcal{D}[\theta(s)] \exp\left(-\beta\mathcal{H}_0[\theta(s)]\right), \tag{2.2}$$

where $\mathcal{D}[\theta(s)]$ indicates path integration over the fluctuating field $\theta(s)$.

The formal statement of $G_0(\theta|\theta_0; L)$ (Eq. 2.2) reflects the correspondence between the Green's function of the wormlike chain model and the quantum-mechanical propagator of a quantum particle confined to a unit circle [15]; our current problem corresponds to finding the propagator of a quantum particle confined to a unit circle with the bending energy playing the role of the kinetic energy and the contour length acting as an imaginary time. Using this quantum-mechanical analogy, the Green's function can be written as an eigenfunction expansion

$$G_0(\theta|\theta_0; L) = \sum_{m=-\infty}^{\infty} \frac{1}{2\pi} e^{im(\theta-\theta_0)} \exp\left(-\frac{m^2 L}{2l_p}\right). \tag{2.3}$$

With this background, we now consider the partition function of a wormlike chain subject to a tensile force $\vec{f}$ acting on the end-to-end distance vector $\vec{R} \equiv \int_0^L ds\vec{u}$. The interaction due to this force is accounted for by $\beta\mathcal{H}_{ext} = -\vec{f} \cdot \int_0^L ds\vec{u}$. Without loss of generality, we assume the force to be aligned along the x-axis. The partition function of the chain $q(f; L)$

relative to that of the free chain is now given by

$$q(f;L) = \langle \exp\left(fR_x\right)\rangle_0 = \sum_{n=0}^{\infty} \frac{f^{2n}}{(2n)!} \left\langle R_x^{2n} \right\rangle_0 , \tag{2.4}$$

where f is the magnitude of $\vec{f}$, and $\langle \ldots \rangle_0$ indicates an average taken with respect to $\beta\mathcal{H}_0$ (Eq. 2.1). We note that the second form of Eq. 2.4 excludes the odd moments of R_x because of the rotational invariance of $\beta\mathcal{H}_0$. The first form of $q(f;L)$ in Eq. 2.4 might suggest that the solution technique would be a cumulant expansion of the argument of the exponential; however, a cumulant expansion is rapidly convergent only for statistics that are close to Gaussian, which is not the case for the wormlike chain model. The second form of $q(f;L)$ in Eq. 2.4 is the so-called moment-based expansion [10], which we proceed to exploit.

Using $R_x = \int_0^L \cos\theta(s)$, we write the moments $\langle R_x^{2n} \rangle_0$ in the following form

$$\left\langle R_x^{2n} \right\rangle_0 = (2n)! \left\langle \prod_{i=1}^{2n} \int_0^{s_{i-1}} ds_i \cos\theta(s_i) \right\rangle_0 , \tag{2.5}$$

where $s_0 = L$, and the factor of $(2n)!$ comes from the "time" ordering of the integrations. Taking advantage of the Markovian nature of the orientation statistics, we evaluate the above average by inserting a propagator (Eq. 2.3) between successive factors in the product on the right-hand side of Eq. 2.5 and integrating over the initial, final, and intermediate orientations. For $\langle R_x^{2n} \rangle_0$, there are $2n+1$ propagators and thus $2n+1$ m-indices to sum over.

The summation over the m-indices after integration over the angular variables is greatly simplified because of the completeness and orthogonality of the eigenfunctions $e^{im\theta}$. The integration over the initial and final orientations results in setting the first and last m-indices to zero. Since $\cos\theta e^{im\theta} = e^{i(m+1)\theta}/2 + e^{i(m-1)\theta}/2$, the intermediate m-indices that

make non-zero contributions to the average are selected by the criteria that they are offset from their neighbors by either 1 or -1. As an example, we consider $\langle R_x^2 \rangle_0$, which contains three m-indices from three propagators. Performing the average, we have

$$\begin{aligned} \left\langle R_x^2 \right\rangle_0 &= \frac{1}{2}\int_0^L ds_1 \int_0^{s_1} ds_2 \sum_{m_1,m_2,m_3} \delta_{0,m_1} C_{m_1}(L-s_1) \\ &\quad \left(\delta_{m_1,m_2+1} + \delta_{m_1,m_2-1}\right) C_{m_2}(s_1-s_2) \\ &\quad \left(\delta_{m_2,m_3+1} + \delta_{m_2,m_3-1}\right) C_{m_3}(s_2)\delta_{m_3,0}, \end{aligned} \tag{2.6}$$

where the summations over the m-indices run from negative infinity to infinity, $\delta_{m,n}$ is the Kronecker delta function, and $C_m(L) = \exp[-m^2 L/(2l_p)]$. Performing the summations over the m-indices leaves only two sets of values that contribute to the average: $(m_1 = 0, m_2 = 1, m_3 = 0)$ and $(m_1 = 0, m_2 = -1, m_3 = 0)$. These two sets of m-indices satisfy the previously mentioned selection criteria; the selected m-indices are offset from their neighbors by either 1 or -1 with starting and ending values of zero.

We now generalize the calculation to $\langle R_x^{2n} \rangle_0$. Using Eq. 2.5 with the solution for the propagator (Eq. 2.3), the value of a given moment is

$$\begin{aligned} \left\langle R_x^{2n} \right\rangle_0 &= \frac{(2n)!}{2^{2n}} \prod_{i=1}^{2n} \sum_{\{m_i\}} \delta_{0,m_1} \int_0^{\tau_{i-1}} d\tau_i C_{m_i}(\tau_{i-1}-\tau_i) \\ &\quad \left(\delta_{m_i,m_{i+1}+1} + \delta_{m_i,m_{i+1}-1}\right) \delta_{m_{2n+1},0} C_{m_{2n+1}}(\tau_{2n}), \end{aligned} \tag{2.7}$$

where $\tau = s/(2l_p)$ $[\tau_0 = N \equiv L/(2l_p)]$, the sum over $\{m_i\}$ indicates summation over all m_i $(i = 1, 2, \ldots, 2n+1)$ from negative infinity to infinity, and we have non-dimensionalized R_x by $2l_p$. Evaluating Eq. 2.7 involves finding the values of the $2n+1$ m-indices that are selected by the Kronecker delta functions upon summing over the m-index values. Essentially, this

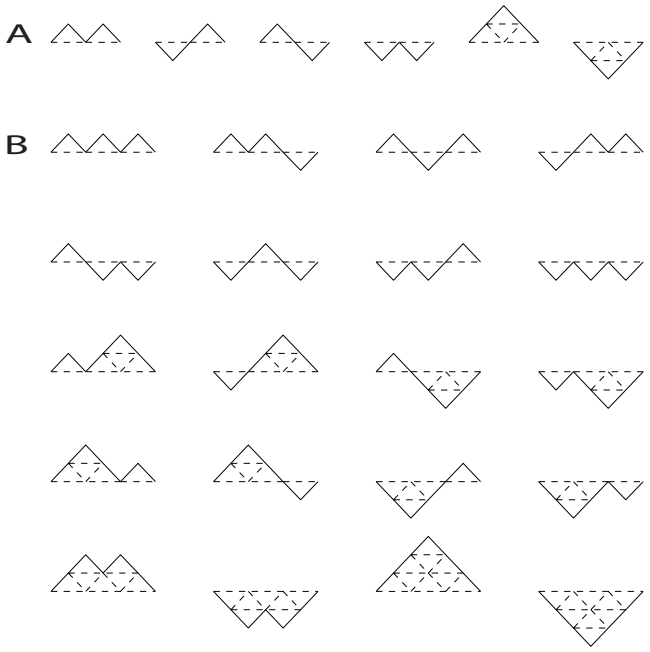

Figure 2.1: The stone-fence diagrams contributing to the calculation of $\langle R_x^4 \rangle$ (A) and $\langle R_x^6 \rangle$ (B) in two dimensions.

task involves finding the m-index values that correspond to paths between zero and zero with $2n$ steps of unit magnitude in between. Performing a Laplace transform of Eq. 2.7 from N to p, we have

$$\begin{aligned} \mathcal{L}\left(\left\langle R_x^{2n} \right\rangle_0\right) &= \frac{(2n)!}{2^{2n}} \prod_{i=1}^{2n} \sum_{\{m_i\}} \delta_{0,m_1} \frac{1}{P_{m_i}} \frac{1}{P_{m_{2n+1}}} \\ &\quad \left(\delta_{m_i,m_{i+1}+1} + \delta_{m_i,m_{i+1}-1}\right) \delta_{m_{2n+1},0}, \end{aligned} \tag{2.8}$$

where $\mathcal{L}$ indicates a Laplace transform from N to p, and $P_m = p + m^2$, which arises from the convolution present in Eq. 2.7. The form of Eq. 2.8 indicates that our current problem involves algebraically summing the terms that contribute to the moment by finding the m-index paths that result in non-zero contributions upon summing over the m-indices.

The selected m-index paths can be expressed diagrammatically using a stone-fence representation proposed by Yamakawa [10]; in Fig. 2.1, we provide the diagrams that contribute

to the calculation of $\langle R_x^4 \rangle_0$ (A) and $\langle R_x^6 \rangle_0$ (B). These diagrams show all the possible m-index combinations that run from zero to zero while following the intermediate selection rules for these two moments. For example, the first diagram in A of Fig. 2.1 corresponds to m-index values of ($m_1 = 0$, $m_2 = 1$, $m_3 = 0$, $m_4 = 1$, $m_5 = 0$), giving an algebraic contribution $P_0^{-3} P_1^{-2}$ to the Laplace transform of $\langle R_x^4 \rangle_0$. Since the moment $\langle R_x^{2n} \rangle_0$ contains $2n + 1$ m-indices and thus $2n$ intermediate steps, contributing diagrams require an equal number (n) of up and down steps to run from zero to zero. As a result, $\langle R_x^{2n} \rangle_0$ contains $(2n)!/(n!)^2$ distinct diagrams, which is the number of ways of distributing n up steps and n down steps in $2n$ total steps.

Using Eq. 2.8, we restate Eq. 2.4 in Laplace space as

$$q(F;p) = \sum_{n=0}^{\infty} \left(\frac{F}{2}\right)^{2n} \sum_{\text{paths } \mu}^{0 \to 0} \prod_{i=1}^{2n+1} \frac{1}{P_{m_i^{(\mu)}}}, \tag{2.9}$$

where $F = 2l_p f$ and the summation over the paths μ implies a summation over all available stone-fence diagrams of $2n$ steps starting and ending at $m = 0$. Equation 2.9 as it stands groups the diagrams according to the number of m-indices they contain, where the nth term in the expansion contains diagrams with $2n + 1$ m-indices. Evaluation of Eq. 2.9 in this manner is a formidable task since all diagrams for each order n must be explicitly calculated, and the number of diagrams increases exponentially with n [as $(2n)!/(n!)^2$].

We now develop a re-summation technique for evaluating Eq. 2.9 by re-grouping the diagrams. To this end, we modify the definition of the stone-fence diagrams by absorbing the factor $(F/2)^{2n}$ into the diagrams. In the modified stone-fence diagrams, each m-index is associated with a factor $P_m^{-1} = (p + m^2)^{-1}$ and each step is associated with a factor $F/2$. Henceforth we will refer to these modified diagrams as F-diagrams. In terms of these

F-diagrams, Eq. 2.9 can be written as

$$\begin{aligned} q(F;p) &= \text{sum of all F-diagrams that begin and} \\ &\quad \text{terminate at } m=0 \end{aligned} \tag{2.10}$$

The full set (infinite number) of F-diagrams can be classified according to the number of intermediate m-indices that are zero; thus

$$\begin{aligned} q(F;p) &= \text{the diagram with a single } m=0 \text{ index} + \\ &\quad \text{sum of all F-diagrams that begin and} \\ &\quad \text{terminate at } m=0 \text{ with no} \\ &\quad \text{intermediate zero-valued } m\text{-indices} + \\ &\quad \text{sum of all F-diagrams that begin and} \\ &\quad \text{terminate at } m=0 \text{ with one} \\ &\quad \text{intermediate zero-valued } m\text{-indices} + \\ &\quad \text{sum of all F-diagrams that begin and} \\ &\quad \text{terminate at } m=0 \text{ with two} \\ &\quad \text{intermediate zero-valued } m\text{-indices} + \ldots \\ &= P_0^{-1} + q^{(1)} + q^{(2)} + q^{(3)} + \ldots, \end{aligned} \tag{2.11}$$

The ellipsis within Eq. 2.11 indicates that $q(F;p)$ is recast as an infinite summation of $q^{(l)}$, where $q^{(l)}$ represents the infinite sum of F-diagrams that begin and terminate at $m=0$ with $l-1$ intermediate zero-valued m-indices.

The diagrams within the first subset of F-diagrams ($q^{(1)}$) fall into two categories: dia-

grams that start and end at $m = 0$ by going through positive values of m and diagrams that start and end at $m = 0$ by going through negative values of m. The diagrams within the first category can be written as

$$\frac{1}{P_0}\frac{F}{2}w_1\frac{F}{2}\frac{1}{P_0} = P_0^{-2}\left(\frac{F^2}{4}\right)w_1, \tag{2.12}$$

where w_1 represents all diagrams beginning and terminating at $m = 1$ with no intermediate m-indices below 1. Similarly, the diagrams within the second category can be written as

$$\frac{1}{P_0}\frac{F}{2}w_{-1}\frac{F}{2}\frac{1}{P_0} = P_0^{-2}\left(\frac{F^2}{4}\right)w_{-1}, \tag{2.13}$$

where w_{-1} represents all diagrams beginning and terminating at $m = -1$ with no intermediate m-indices above -1. Thus,

$$q^{(1)}(F;p) = P_0^{-2}\left(\frac{F^2}{4}\right)(w_1 + w_{-1})\,. \tag{2.14}$$

We can now express the diagrams in each group using the functions w_1 and w_{-1}. Some reflection should convince the reader that the sum of all F-diagrams that begin and terminate at $m = 0$ with one intermediate zero-valued m-index ($q^{(2)}$) can be written as

$$\begin{aligned}
q^{(2)}(F;p) &= P_0^{-1}\frac{F}{2}w_1\frac{F}{2}P_0^{-1}\frac{F}{2}w_1\frac{F}{2}P_0^{-1} \\
&+ P_0^{-1}\frac{F}{2}w_{-1}\frac{F}{2}P_0^{-1}\frac{F}{2}w_{-1}\frac{F}{2}P_0^{-1} \\
&+ P_0^{-1}\frac{F}{2}w_1\frac{F}{2}P_0^{-1}\frac{F}{2}w_{-1}\frac{F}{2}P_0^{-1} \\
&+ P_0^{-1}\frac{F}{2}w_{-1}\frac{F}{2}P_0^{-1}\frac{F}{2}w_1\frac{F}{2}P_0^{-1} \\
&= P_0^{-3}\left(\frac{F^2}{4}\right)^2(w_1 + w_{-1})^2
\end{aligned} \tag{2.15}$$

Generalizing this to $q^{(l)}$, we obtain

$$q^{(l)}(F;p) = P_0^{-l-1}\left(\frac{F^2}{4}\right)^l (w_1 + w_{-1})^l. \tag{2.16}$$

In terms of w_1 and w_{-1}, Eq. 2.9 can now be written as

$$\begin{aligned} q(F;p) &= \sum_{l=0}^{\infty}\left(\frac{F^2}{4}\right)^l \frac{(w_1+w_{-1})^l}{P_0^{l+1}} \\ &= \sum_{l=0}^{\infty}\left(\frac{F^2}{4}\right)^l \frac{(2w_1)^l}{P_0^{l+1}} \\ &= \frac{1}{P_0 - F^2 w_1/2}, \end{aligned} \tag{2.17}$$

where the second form is due to the equivalence between w_1 and w_{-1} (since $P_j = P_{-j}$). Describing Eq. 2.17 in words, we have performed a re-summation of Eq. 2.9 by collecting all diagrams that contain the same number of intermediate zero-valued m-indices and collapsing the sum of diagrams between adjacent zero-valued m-indices into the function w_1 for diagrams that remain above zero and the function w_{-1} for diagrams that remain below zero.

A similar classification scheme to the one we have used to write $q(F;p)$ can be developed for the functions w_1 and w_{-1}. For example,

$$\begin{aligned} w_1 = {} & \text{the diagram with a single } m = 1 \text{ index} + \\ & \text{sum of all F-diagrams that begin and} \\ & \text{terminate at } m = 1 \text{ with all intermediate} \\ & m\text{-indices above } 1 + \\ & \text{sum of all F-diagrams that begin and} \end{aligned}$$

terminate at $m = 1$ with one intermediate

m-index equal 1 and all other intermediate

m-indices above $1 +$

sum of all F-diagrams that begin and

terminate at $m = 1$ with two intermediate

m-indices equal 1 and all other intermediate

m-indices above $1 + \ldots$

$$= P_1^{-1} + w_1^{(1)} + w_1^{(2)} + w_1^{(3)} + \ldots \tag{2.18}$$

The ellipsis within Eq. 2.18 indicates that w_1 is recast as an infinite summation of $w^{(l)}$, where $w^{(l)}$ represents the infinite sum of F-diagrams that begin and terminate at $m = 1$ with $l - 1$ intermediate m-indices equal 1 and all other intermediate m-indices above 1. Introducing w_2 as the infinite sum of all F-diagrams that begin and terminate at $m = 2$ with no intermediate m-indices below 2, w_1 can be written as

$$\begin{aligned} w_1 &= P_1^{-1} + P_1^{-1}\frac{F}{2}w_2\frac{F}{2}P_1^{-1} + P_1^{-1}\frac{F}{2}w_2\frac{F}{2}P_1^{-1}\frac{F}{2}w_2\frac{F}{2}P_1^{-1} + ... \\ &= \sum_{l=0}^{\infty}\left(\frac{F^2}{4}\right)^l \frac{w_2^l}{P_1^{l+1}} \\ &= \frac{1}{P_1 - F^2 w_2/4}. \end{aligned} \tag{2.19}$$

In general, if we define w_j as the infinite sum of all F-diagrams that begin and terminate at $m = j$ with no intermediate m-indices below j (for positive j's), we obtain the following

recursive relation:

$$\begin{aligned} w_j &= \sum_{l=0}^{\infty} \left(\frac{F^2}{4}\right)^l \frac{w_{j+1}^l}{P_j^{l+1}} \\ &= \frac{1}{P_j - F^2 w_{j+1}/4}, \end{aligned} \tag{2.20}$$

where $P_j = p + j^2$. For negative j's, w_{j+1} in the above equation should be replaced by w_{j-1}. The recursive form reflects a hierarchical self-similarity in the relationship between the summation of diagrams at a given level with the summation of diagrams at the next level.

Equation 2.17 can be equivalently written as $q(F;p) = 1/[P_0 - (F^2/2)/J_1]$ with the recursive relation $J_n = P_n - (F^2/4)/J_{n+1}$ $(n \geq 1)$. Repeated use of the recursive relation leads to an infinite continued fraction representation of the partition function of a wormlike chain under tension:

$$q(F;p) = \cfrac{1}{P_0 - \cfrac{F^2/2}{P_1 - \cfrac{F^2/4}{P_2 - \cfrac{F^2/4}{P_3 - \cfrac{F^2/4}{\cdots}}}}}. \tag{2.21}$$

The emergence of the continued fraction form of Eq. 2.21 is a natural manifestation of the self-similarity of the summation of diagrams at different levels. The extra factor of two at the zeroth level of Eq. 2.21 is due to the equivalence between P_m and P_{-m}; the denominator of Eq. 2.21 can be equivalently written as a continued fraction to positive infinity plus a continued fraction to negative infinity.

The partition function $q(F;L)$ can be used to describe the thermodynamic behavior of a wormlike chain under tension. In particular, the derivatives of the partition function with

respect to the force yields moments of the end-to-end distance in the direction of the force:

$$\langle R_x^n \rangle = \frac{1}{q} \frac{d^n q}{dF^n}, \tag{2.22}$$

where R_x is non-dimensionalized by $2l_p$. Of special interest is the first moment, which gives the force-extension behavior of the chain.

When the derivatives in Eq. 2.22 are evaluated at $F = 0$, we obtain the moments of the end-to-end distribution in the absence of the force. Inspection of Eq. 2.4 shows that $q(F; L)$ acts as a moment-generating function, i.e.,

$$\left\langle R_x^{2n} \right\rangle_0 = \left. \frac{d^{2n} q}{dF^{2n}} \right|_{F=0}. \tag{2.23}$$

Using the relationship in two dimensions $\langle R^{2n} \rangle_0 = (n!)^2 4^n \langle R_x^{2n} \rangle_0 / (2n)!$, Eq. 2.21 provides a convenient means for calculating any moments of the end-distribution function without the laborious efforts of enumerating and computing all the stone-fence diagrams that contribute to a moment of a given order. Equation 2.23 also provides an easy way of verifying the validity of Eq. 2.21. We have computed moments up to $\langle R^{10} \rangle_0$ using Eq. 2.23 and find perfect agreement with the known solutions [16].

We now consider the end-to-end distribution function $G(\vec{R}; L)$, which gives the probability that a chain that begins at the origin will have end position $\vec{R}$, independent of the initial and final tangential orientations. $G(\vec{R}; L)$ can be written as

$$G(\vec{R}; L) = \left\langle \delta \left(\vec{R} - \int_0^L ds \vec{u} \right) \right\rangle_0, \tag{2.24}$$

where $\langle \ldots \rangle_0$ indicates an average taken with respect to the unperturbed Hamiltonian $\beta \mathcal{H}_0$.

Upon Fourier transforming from the variable $\vec{R}$ to $\vec{k}$, our problem becomes that of a single wormlike chain in the external dipole field $i\vec{k}$; thus $\beta\mathcal{H}_{ext} = -i\vec{k} \cdot \int_0^L ds\vec{u}$. The form of $\beta\mathcal{H}_{ext}$ is identical to that for the chain under a tensile force $\vec{f}$ with $\vec{f} \to i\vec{k}$. Aligning $\vec{k}$ along the x-axis and defining $K \equiv 2l_p k$, where k is the magnitude of $\vec{k}$, the Laplace-Fourier transformed end-to-end distribution can be trivially obtained from Eq. 2.21 by replacing F^2 with $-K^2$; the result is

$$G(K;p) = \cfrac{1}{P_0 + \cfrac{K^2/2}{P_1 + \cfrac{K^2/4}{P_2 + \cfrac{K^2/4}{P_3 + \cfrac{K^2/4}{\cdots}}}}}. \tag{2.25}$$

The end-to-end distribution function $G(R;L)$ can be obtained by an inverse Laplace-Fourier transform.

Finally, we consider the partition function of a wormlike chain in a nematic quadrupole field, which can either describe a wormlike chain dissolved in a nematic liquid-crystal medium or a wormlike chain in the self-consistent-field potential due to other chains in the nematic state [9]. In two dimensions, the quadrupole field adds $\beta\mathcal{H}_{ext} = -\lambda \int_0^L ds\,(u_x^2 - 1/2)$ to the total chain Hamiltonian, where we have chosen the nematic director to be along the x-axis. Since $u_x^2 - 1/2 = \cos(2\theta)/2$, the diagrammatic representation for this problem has similar rules to those for the previous two problems, with the exception that the step size in the diagrams is of magnitude 2 instead of 1. Following the same derivation as in the previous problems, we find that the partition function q for a single chain in a nematic quadrupole field is given by

$$q(\Lambda;p) = \cfrac{1}{P_0 - \cfrac{\Lambda^2/8}{P_2 - \cfrac{\Lambda^2/16}{P_4 - \cfrac{\Lambda^2/16}{P_6 - \cfrac{\Lambda^2/16}{\cdots}}}}}, \tag{2.26}$$

where $\Lambda = 2l_p\lambda$. This solution permits the evaluation of a number of thermodynamic properties of a wormlike chain in a nematic field including the chain deformation free energy by the field in two dimensions. It also provides the key input in the self-consistent-field theory for the nematic phase of wormlike chains.

All of the solutions given in this section can be verified by generating moments of the external field by taking derivatives of q with respect to the field strength parameters (K, F, and Λ) evaluated at zero field strength. The solutions can be checked by finding the diagrams that represent these moments, a process that further extends the usefulness of the diagrammatic representation. We find agreement between our solutions and the analytical solutions for the moments of the external field for all cases.

2.3 Three-Dimensional Solutions

The analogous solutions in three dimensions are found by using virtually identical techniques as those used to find the two-dimensional solutions. We first review the solution of the chain statistics for a wormlike chain in three dimensions in the absence of an external field. The orientation of the tangent vector is defined by the polar angle θ between the tangent and the z-axis and the azimuthal angle ϕ that defines the rotation of the tangent about the z-axis. The Green's function $G_0(\vec{u}|\vec{u}_0; L)$ gives the conditional probability that a chain of contour length L beginning with an initial tangent orientation $\vec{u}_0$ will end with tangent orientation $\vec{u}$. As in two dimensions, the Green's function is found using the path integral formalism given by

$$G_0(\vec{u}|\vec{u}_0; L) = \int_{\vec{u}(s=0)=\vec{u}_0}^{\vec{u}(s=L)=\vec{u}} \mathcal{D}[\vec{u}(s)] \exp\left(-\beta \mathcal{H}_0[\vec{u}(s)]\right), \tag{2.27}$$

where the path integration includes the spherical angles θ and ϕ. Solving the Schrödinger equation derived from Eq. 2.27, the solution for the Green's function in three dimensions is given by

$$G_0(\vec{u}|\vec{u}_0;L) = \sum_{l=0}^{\infty} \sum_{m=-l}^{l} Y_l^m(\vec{u}) Y_l^{m*}(\vec{u}_0) C_l(N), \tag{2.28}$$

where $C_l(N) = \exp[-l(l+1)N]$ $[N = L/(2l_p)]$, and Y_l^m are the spherical harmonics [17].

We begin with the partition function for a chain under tension described by the interaction $\beta\mathcal{H}_{ext} = -\vec{f} \cdot \int_0^L ds\vec{u}$. We choose our coordinate system so that $\vec{f}$ lies along the z-axis; thus Eq. 2.4 in three dimensions replaces R_x with R_z. As in two dimensions, we make use of the moment-based expansion of Eq. 2.4, with some slight modification of the subsequent steps to account for the statistical behavior in three dimensions.

The moment $\langle R_z^{2n} \rangle_0$ is found by using orientation statistics with the help of Eq. 2.5, where R_x is now replaced with R_z. Because of the "time" ordering in Eq. 2.5, the Markovian nature of the tangent vector statistics permits the evaluation of $\langle R_z^{2n} \rangle_0$ by insertion of a propagator (Eq. 2.28) between each successive factor in the product of Eq. 2.5. Since there are $2n+1$ propagators inserted, there are $2n+1$ l-indices and $2n+1$ m-indices to sum over. The initial, final, and intermediate tangent vector orientations ($2n+1$ total) are then integrated over, which selects for certain values of the l-indices and m-indices. The integration over the initial and final tangent orientation selects $l_1 = l_{2n+1} = 0$ and $m_1 = m_{2n+1} = 0$, and upon integration over the intermediate azimuthal angles ϕ_i, the intermediate m-indices are also set to zero. The intermediate selection rules for the l-indices are found by noting that $\cos\theta Y_l^0 = a_{l+1} Y_{l+1}^0 + a_l Y_{l-1}^0$ where $a_l = l/\sqrt{4l^2-1}$ [17], thus the l-indices selected are off-set from their neighbors by a value of 1 or -1. Since the l-indices cannot take negative values, the chosen l-indices for $\langle R_z^{2n} \rangle_0$ follow paths of $2n$ steps with unit step size that start at zero and end at zero while never wandering below

$l = 0$.

The diagrammatic representation in three dimensions reflects these selection rules. For example, $\langle R_z^2 \rangle_0$ in three dimensions contains only 1 l-index path ($l_1 = 0, l_2 = 1, l_3 = 0$). The three-dimensional version of Fig. 2.1 contains only the first and fifth diagrams in A and the first in lines 1, 3, 4, and 5 and the third in line 5 of B. For the moment $\langle R_z^{2n} \rangle_0$, there are $(2n)!/[n!(n+1)!]$ diagrams that satisfy the selection rules [10]. The value of a given diagram is again most easily stated in Laplace space (with the Laplace variable p): for a diagram corresponding to a particular path $\{l_1, l_2, ..., l_i, ..., l_{2n+1}\}$, the functional value is $P_{l_1}^{-1} \prod_{i=2}^{2n+1} a_{l_i + t_i} P_{l_i}^{-1}$ where $P_l = p + l(l+1)$, and $t_i = 0$ if $l_i = l_{i-1} + 1$ (step up) and $t_i = 1$ if $l_i = l_{i-1} - 1$ (step down). For example, the diagram in three dimensions corresponding to the fifth diagram in A of Fig. 2.1 is given by $P_0^{-1} a_1 P_1^{-1} a_2 P_2^{-1} a_2 P_1^{-1} a_1 P_0^{-1}$.

We now construct the diagrammatic representation of the partition function $q(F; p)$. We assign a factor $P_l^{-1} = [p + l(l+1)]^{-1}$ for each l-index and a factor $F a_{l_i + t_i}$ for a step that connects two adjacent values of the indices l_i and l_{i-1}, where the value of t_i (defined in the previous paragraph) depends on whether the step is up or down. We call these diagrams Fa-diagrams. In terms of these diagrams, the partition function can be written as

$$\begin{aligned} q(F; p) \quad = \quad & \text{sum of all Fa-diagrams that begin and} \\ & \text{terminate at } l = 0 \text{ without ever} \\ & \text{wandering below } l = 0. \end{aligned} \tag{2.29}$$

Following a virtually identical procedure as the two-dimensional analogue for manipulating

the diagrams, we obtain the following recursive form for $q(F;p)$:

$$q(F;p) = 1/J_0 \tag{2.30}$$

where J_n obeys the recursive relation

$$J_n = P_n - a_{n+1}^2 F^2 / J_{n+1} \tag{2.31}$$

with $P_n = p + n(n+1)$ and $a_n = n/\sqrt{4n^2-1}$. Written as an infinite continued fraction, the partition function now reads

$$q(F;p) = \cfrac{1}{P_0 - \cfrac{a_1^2 F^2}{P_1 - \cfrac{a_2^2 F^2}{P_2 - \cfrac{a_3^2 F^2}{\cdots}}}}. \tag{2.32}$$

The validity of Eq. 2.32 can be verified by generating moments of $q(F;p)$ using Eq. 2.23. With the expression $\langle R^{2n} \rangle_0 = (2n+1)! \langle R_z^{2n} \rangle_0 / (2n)!$, our solution provides a convenient method for generating arbitrary moments of the end-to-end distance analytically. As in two dimensions, we have checked our solution by generating moments up to $\langle R^{10} \rangle_0$ and have found exact agreement with the available solutions [10].

As in two dimensions, the end-to-end distance distribution function in Fourier-Laplace space can be obtained trivially from Eq. 2.32 by the substitution $\vec{f} \to i\vec{k}$; the result is

$$G(K;p) = \cfrac{1}{P_0 + \cfrac{a_1^2 K^2}{P_1 + \cfrac{a_2^2 K^2}{P_2 + \cfrac{a_3^2 K^2}{\cdots}}}}, \tag{2.33}$$

where $K = 2l_p k$ and k is the magnitude of $\vec{k}$. We verify that our techniques produce identical

results as those given in a previous study [12] by truncating the infinite continued fraction (Eq. 2.33) at the third level and finding equivalence between the two solution methods.

A semiflexible chain in the nematic quadrupole field in three dimensions is described by the interaction term $\beta\mathcal{H}_{ext} = -\lambda \int_0^L ds\,(u_z^2 - 1/3)$ in the chain Hamiltonian. Noting that $(\cos^2\theta - 1/3)\,Y_l^0 = \alpha_{l+2}Y_{l+2}^0 + \beta_l Y_l^0 + \alpha_l Y_{l-2}^0$ where $\alpha_l = a_{l-1}a_l$ ($a_l = l/\sqrt{4l^2-1}$) and $\beta_l = a_{l+1}^2 + a_l^2 - 1/3$ [17], we see that the selection rules for this external field includes up and down steps of magnitude 2 as well as horizontal steps. However, the diagrammatic resummation technique discussed earlier can be easily extended to account for this additional horizontal step. The result is

$$q(\Lambda;p) = \cfrac{1}{P_0 - \beta_0\Lambda - \cfrac{\alpha_2^2\Lambda^2}{P_2-\beta_2\Lambda-\cfrac{\alpha_4^2\Lambda^2}{P_4-\beta_4\Lambda-\cfrac{\alpha_6^2\Lambda^2}{\cdots}}}}, \tag{2.34}$$

where $P_n = p + n(n+1)$, $\Lambda = 2l_p\lambda$, $\alpha_l = a_{l-1}a_l$ ($a_l = l/\sqrt{4l^2-1}$), and $\beta_l = a_{l+1}^2 + a_l^2 - 1/3$ (note $\beta_0 = 0$). Equation 2.34 is equivalently stated as $q(\Lambda;p) = 1/J_0$ where $J_n = P_n - \beta_n\Lambda - \alpha_{n+2}^2\Lambda^2/J_{n+2}$ for $n \geq 0$.

We conclude this section by providing a discussion of the similarities between the solutions in two and three dimensions and generalization of our solution methods to a wider range of similar problems. One important conclusion that is evident from our results is that the infinite continued fraction is a natural form for these solutions, which is highly advantageous in its simplicity and its convergence behavior. In deriving our solutions, we have described the formation of the continued fraction as adding layers onto the diagrammatic representation; the use of the diagrammatic techniques provides a means of visualizing our algebraic methods.

The end-to-end distribution function in two dimensions (Eq. 2.25) and three dimensions

(Eq. 2.33) are almost identical with only subtle differences. Consulting the selection rules in two and three dimensions, we see that $a_n = 1/2$ for all n in two dimensions; whereas $a_n = n/\sqrt{4n^2-1}$ in three dimensions. Inserting $a_n = 1/2$ (the two-dimensional case) into Eq. 2.33 yields Eq. 2.25 with a factor of two missing in the first layer of the continued fraction. This difference is due to the selection rules for the m-index of the two-dimensional case: m runs from negative infinity to infinity whereas the l-index of the three-dimensional case runs from zero to infinity.

We clarify this distinction by considering an interesting variant of the end-distribution function. We define $G^{(j)}(k;p)$ as the collection of diagrams that run from j to j [thus $G(k;p) = G^{(0)}(k;p)$]. In two dimensions, $G^{(j)}(k;p)$ is given by

$$G^{(j)}(k;p) = \frac{1}{\frac{K^2/4}{J^{(-)}_{j-1}} + P_j + \frac{K^2/4}{J^{(+)}_{j+1}}}, \tag{2.35}$$

where $P_n = p + n^2$, $K = 2l_p k$, and the recursive forms of the continued fractions are given by $J^{(+)}_n = P_n + (K^2/4)/J^{(+)}_{n+1}$ and $J^{(-)}_n = P_n + (K^2/4)/J^{(-)}_{n-1}$ for any value of n. In three dimensions, $G^{(j)}(k;p)$ is given by

$$G^{(j)}(k;p) = \frac{1}{\frac{a_j^2 K^2}{J^{(-)}_{j-1}} + P_j + \frac{a_{j+1}^2 K^2}{J^{(+)}_{j+1}}}, \tag{2.36}$$

where $P_n = p + n(n+1)$, $a_n = n/\sqrt{4n^2-1}$, $K = 2l_p k$, and the recursive forms of the continued fractions are given by $J^{(+)}_n = P_n + (a^2_{n+1}K^2)/J^{(+)}_{n+1}$ $(n \geq 0)$, $J^{(-)}_n = P_n + (a^2_n K^2)/J^{(-)}_{n-1}$ $(n \geq 1)$, and $J^{(-)}_0 = P_0$. The partial continued fractions provide the diagrammatic contributions to $G^{(j)}$ that are above j in the case of $J^{(+)}_{j+1}$ and below j in the case of $J^{(-)}_{j-1}$. We see the three-dimensional solution for $G^{(j)}(k;p)$ differs from the two-dimensional solution since

the continued fractions do not extend past the zeroth layer in three dimensions because the l-index in three dimensions take only non-negative values. The function $G^{(j)}(k;p)$ is necessary in constructing the full end-distribution function including end-tangent orientations, where the diagrams included in the summation have non-zero initial and final m- and l-index values [10]; thus Eq. 2.35 and Eq. 2.36 are important in further extending our current results.

2.4 Structure Factor of a Wormlike Chain

The single-chain structure factor is one of the most important properties of a polymer. It provides a direct connection to scattering experiments and also the essential theoretical input for treating many-chain systems. While the structure factor for a flexible Gaussian chain model is the well-known Debye function, rigorous results for the structure factor of a semiflexible chain that are valid for arbitrary chain length and persistence length have not been explicitly provided [18]. To date, quantitatively the best available theory for the structure factor for a semiflexible polymer is based on a Dirac-equation model proposed by Kholodenko [19, 20]. However, this model is designed to smoothly interpolate between the rigid and flexible limits; the extent of its accuracy for intermediate stiffness is not clear. Furthermore, the model cannot be described by a simple Hamiltonian (such as given by Eq. 2.1); thus the physical interpretation of its parameters is not straightforward. A variant of the wormlike chain model that permits analytical expressions for the chain statistics involves relaxing the local chain length constraint and enforcing a total chain length constraint instead [21, 22]. The accuracy of such a model in predicting the structure factor is questionable due to uncertain contribution of local chain length fluctuations.

In this section, we examine the structure factor of a free wormlike chain for arbitrary

chain stiffness using Eq. 2.33. We define the structure factor as

$$S(\vec{k}) = \frac{1}{L^2}\int_0^L ds_1 \int_0^L ds_2 \left\langle \exp\left[i\vec{k}\cdot(\vec{r}(s_1)-\vec{r}(s_2))\right]\right\rangle, \tag{2.37}$$

where the angular brackets indicate an average with respect to the particular chain statistics (in our case wormlike chain in the absence of external fields). Note that this definition differs from the more conventional one by an extra factor of L in the denominator. We choose this dimensionless form in order to simplify our comparison with previous results by Kholodenko [23, 24].

We first recapitulate the structure factors for a Gaussian chain and for a rigid rod. For a chain obeying Gaussian statistics, the scattering function is given by

$$\begin{aligned} S(\vec{k}) &= \frac{1}{L^2}\int_0^L ds_1 \int_0^L ds_2 \exp\left(-\frac{2l_p\,|s_1 - s_2|\,\vec{k}^2}{6}\right) \\ &= \frac{72}{NK^2}\left(\frac{1}{6} - \frac{1-\exp(-NK^2/6)}{NK^2}\right), \end{aligned} \tag{2.38}$$

where $N = L/(2l_p)$ and $K = 2l_p|\vec{k}|$. We have set the Gaussian step size b to the Kuhn length $2l_p$ to facilitate comparison with the wormlike chain model. For a perfectly rigid chain, the scattering function is given by

$$S(\vec{k}) = \frac{2}{NK}\left(\mathrm{Si}(NK) - \frac{1-\cos(NK)}{NK}\right), \tag{2.39}$$

where $\mathrm{Si}(x)$ is the sine integral, defined as $\mathrm{Si}(x) = \int_0^x dz\,\sin(z)/z$. We express Eq. 2.39 in terms of NK, which is equal to kL, for ease of comparison with the Gaussian-chain behavior and our current results. We note that as $NK \to \infty$, the structure factor behaves as $S(k) \to \pi/(NK)$.

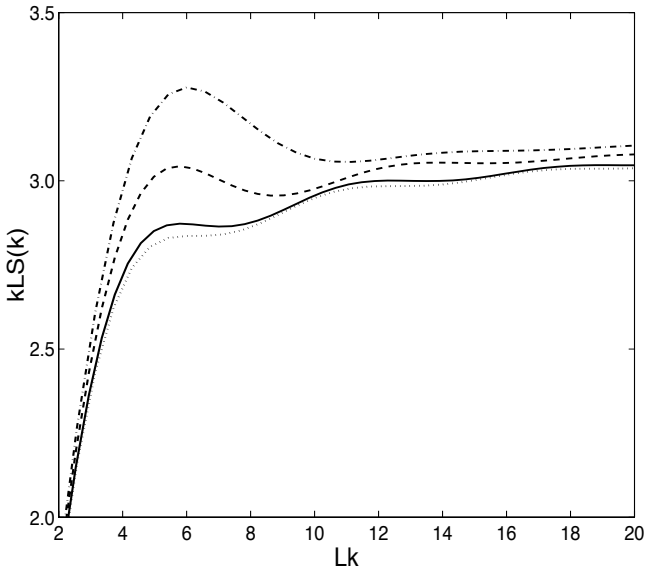

Figure 2.2: The scattering function $kLS(k)$ versus the wavenumber Lk for $N = 0.1$ (solid curve), $N = 0.5$ (dashed curve), and $N = 1$ (dashed-dotted curve). We include the scattering function for a rigid rod (dotted curve), given by Eq. 2.39.

The structure factor is related to the Green's function through

$$\begin{aligned} S(\vec{k}) &= \frac{1}{L^2}\int_0^L ds_1 \int_0^L ds_2 G(\vec{k}; s_1 - s_2) \\ &= \frac{2}{N^2}\mathcal{L}^{-1}\left(\frac{G(K;p)}{p^2}\right), \end{aligned} \tag{2.40}$$

where $\mathcal{L}^{-1}$ indicates Laplace inversion from p to N. In two dimensions, $G(K;p)$ in Eq. 2.40 is given by Eq. 2.25; in three dimensions, it is given by Eq. 2.33. Equation 2.40 is valid for a polymer chain of arbitrary rigidity, provided the Laplace inversion can be accurately performed. All of our numerical results are obtained by truncating the infinite continued fraction at the 20th level and evaluating the inverse Laplace transform by computing residues of the resulting expression numerically. We limit our discussion of the behavior of the structure factor to 3 dimensions.

Figure 2.2 shows the behavior of the structure factor (Eq. 2.40) in three dimensions for relatively rigid chains [$N = 0.1$ (solid curve), $N = 0.5$ (dashed curve), and $N = 1$

(dashed-dotted curve)]. We plot the product $kLS(k)$ in order to clearly show the asymptotic behavior as $Lk \to \infty$ to be $kLS(k) \to \pi$ regardless of the chain rigidity. The rigid rod solution (Eq. 2.39) is also included in Fig. 2.2 (dotted curve) for comparison. We see that as $N \to 0$ the structure factor approaches that for the rigid rod; the two become virtually indistinguishable for $N < 0.02$ (not shown in the Figure). The rigid-rod solution exhibits an oscillation in $kLS(k)$ when the wavelength $1/k$ are multiples of the chain length L. As the stiffness decreases in Fig. 2.2, the frequency of the oscillations in the structure factor decreases due to the presence of thermal wrinkles in the conformation which shorten the effective length of the chain. In addition, the first peak in $kLS(k)$ emerges dominant as the stiffness decreases, and the subsequent peaks are suppressed because of decreased persistence length.

The behavior of the structure factor for intermediate stiffness is presented in Fig. 2.3 for N ranging from 0.1 (relatively rigid) to 10 (essentially flexible). The dominant peak in the scattering function continues to grow as N increases, and the secondary peaks are no longer noticeable for $N > 1$. For comparison we include in Fig. 2.3 the behavior of the structure factor for a semiflexible chain as defined by Dirac statistics [23, 24] (dashed curves). This theory is designed to exactly capture the wormlike chain behavior in the perfectly rigid and flexible limits with an interpolating behavior that captures the wormlike chain behavior in a qualitative manner (see reference [24] for a comparison). Although these two models agree qualitatively, we see in Fig. 2.3 that the wormlike chain model and the Dirac model differ appreciably for semiflexible chains of intermediate stiffness ($N \approx 1$).

As the chain length increases further, the chain becomes more flexible. In Fig. 2.4, we present the scaled structure factor $kLS(k)$ for a chain of length $N = 100$ (solid curve) and compare it with that for a Gaussian chain (dashed curve) given by Eq. 2.38. Here we plot

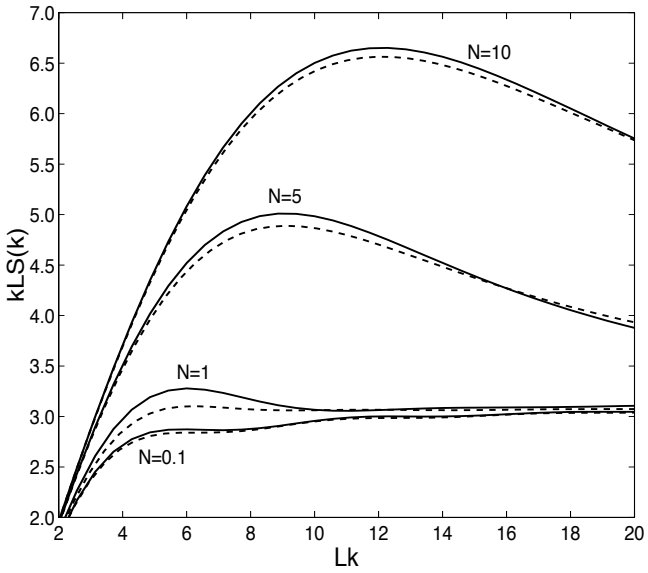

Figure 2.3: The scattering function $kLS(k)$ versus the wavenumber Lk for $N = 0.1$, $N = 1$, $N = 5$, and $N = 10$ calculated using Eq. 2.40 (solid curves) and from solutions found in reference [23] (dashed curves).

$kLS(k)$ against $K = 2l_p k$ since the shortest length scale is now l_p. The dominant peak in Fig. 2.4 occurs when $K \approx 1$, i.e., when the incident wavelength is approximately a Kuhn length $2l_p$. The wormlike chain model closely agrees with the Gaussian chain model for small K; however, as K increases, these two models diverge. Since a wormlike chain is rigid at sufficiently small length scales, the structure factor for the wormlike chain model approaches the rigid rod limit $kLS(k) \to \pi$ as $k \to \infty$ regardless of the stiffness of the chain. This limit occurs when $K \gg 1$ for flexible chains ($N \gg 1$) or $kL \gg 1$ for rigid chains ($N \ll 1$). Such behavior is not captured by the Gaussian chain model since a Gaussian chain has no (bending) stiffness at any length scales.

The features of the structure factor illustrated in Figs. 2.2 through 2.4 demonstrate the behavior of a wormlike chain ranging from perfectly rigid to flexible. On the rigid side of the spectrum (shown in Fig. 2.2), the structure factor of a wormlike chain becomes essentially indistinguishable from that for the perfectly rigid rod when $N < 0.02$ or when the length

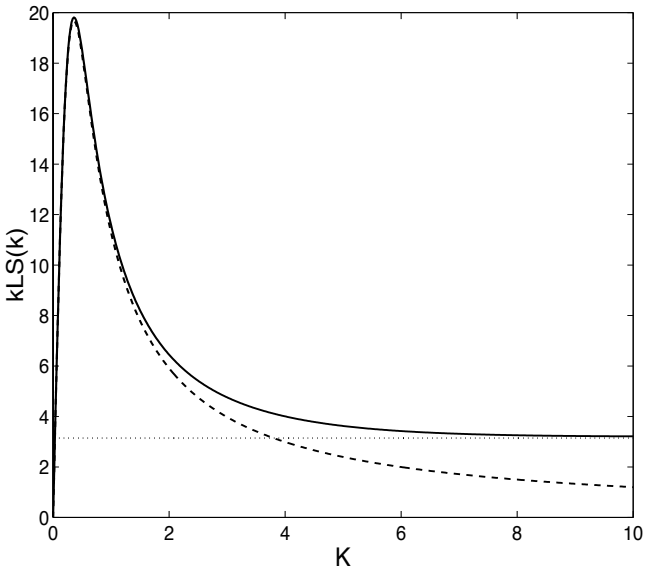

Figure 2.4: The scattering function $kLS(k)$ versus the wavenumber $K = 2l_p k$ for $N = 100$ for the wormlike chain (solid curve) and the Gaussian chain (dashed curve). The dotted line is the asymptotic value for the wormlike chain $kLS(k) \to \pi$ as $K \to \infty$.

of the chain is roughly one twentieth of a Kuhn length. However, the difference can be appreciable even for relatively stiff chains ($N \approx 0.1$). This is consistent with the effect of semiflexibility on the thermodynamic behavior of a polymer liquid-crystal solution [9], where conformation fluctuation substantially alters the nematic-isotropic transition temperature. In the flexible-chain limit (cf. Fig. 2.4), the structure factor for a wormlike chain only coincides with the Gaussian chain result in the small k-limit. The large k-limit of the structure factor, which probes the small length scales of the fluctuating chain, is affected by the bending stiffness of the wormlike chain, which renders the chain rigid at length scales much less than the persistence length.

2.5 Polymer Nematics

The formation of a liquid-crystalline phase can be studied at the mean-field level by considering an isolated molecule interacting with an effective self-consistent field that captures the

local structure of the ordered phase. In the case of a homogeneous nematic liquid-crystal, the mean-field behavior is captured at the lowest order by a quadrupolar interaction between the molecular orientation and the effective field [6, 7]. For semiflexible polymer chains interacting with a Maier-Saupe pseudopotential, the mean-field statistical mechanics of the nematic phase has been solved exactly [8, 9] through an expansion of the tangent-vector orientation Green's function in the spheroidal functions [25]. However, evaluating the spheroidal functions is a nontrivial mathematical/computational task.

The solutions we provide in this chapter for the partition function of a wormlike chain in a quadrupole field provide convenient alternative means for studying a number of important issues involving nematic liquid-crystalline polymers in two and three dimensions. For example, such additional issues include the presence of solvent molecules, both non-mesogenic [9] and mesogenic [5], and the effect of chain self-assembly on the phase-transition behavior [26]. Regardless of the particular situation, an important input is the behavior of a single semiflexible chain interacting with a quadrupole field.

We thus begin the discussion of the use of our results by considering the thermodynamic behavior of a wormlike chain in an external quadrupole field of strength λ. Focusing on the three-dimensional behavior, the partition function q is given by Eq. 2.34, and the Gibbs free energy is given by $\beta g(N;\lambda) = -\log q$. The nematic order parameter, which measures the degree of orientational order is given by

$$m = \frac{1}{L}\int_0^L ds \left\langle \left(\frac{3}{2}u_z^2 - \frac{1}{2}\right)\right\rangle = \frac{3}{2L}\frac{\partial \log q}{\partial \lambda}. \tag{2.41}$$

The Helmholtz free energy $f(N;m)$ is then obtained through a Legendre transform as $\beta f(N;m) = \beta g(N;\lambda) + (3/2)\lambda m$. Since both the Gibbs and Helmholtz free energies are

defined relative to the isotropic (rotationally invariant) state, the free energy f includes a decrease in the bending energy and a loss of conformation entropy due to alignment by the quadrupole field. We plot the free energy versus the field strength $\Lambda = 2l_p\lambda$ in Fig. 2.5 for $N = L/(2l_p) = 3.3333$.

The free energy in Fig. 2.5, exhibits two distinct scaling regimes. The small Λ scaling of Λ^2 arises from the fact that in the isotropic phase there is no quadrupole order; thus the lowest-order contribution to q must be quadratic in the quadrupole order in the limit of weak field strength. Mathematically, this is seen by noting that $\beta_0 = 0$ in Eq. 2.34; thus as $\Lambda \to 0$, the lowest contribution to q is quadratic in Λ. The large Λ scaling can be understood by considering the behavior of the chain conformation in the quadrupole field. In reference [9], we found that the thermodynamic behavior has a distinct cross-over when the chain is essentially aligned in the quadrupole field, dictated by suppression of the conformation fluctuations in the direction perpendicular to the quadrupole field. This cross-over results in the large Λ scaling of $\Lambda^{1/2}$ exhibited in Fig. 2.5. The thermodynamic behavior demonstrated in Fig. 2.5 captures the free energy of confining a single semiflexible chain in a quadrupole field, regardless of the underlying cause of the field.

We now specify to the mean-field (self-consistent field) treatment of nematic liquid-crystalline polymer phase by replacing the external field with a self-consistent field that approximates the many-body interactions within the nematic phase. The derivation of the full set of self-consistent-field equations is given in reference [9]. For simplicity, here we restrict our discussion to the solvent-free thermotropic system. If the strength of the Maier-Saupe interaction is defined to be κ, the self-consistent field is then $\lambda = \kappa m$ and the

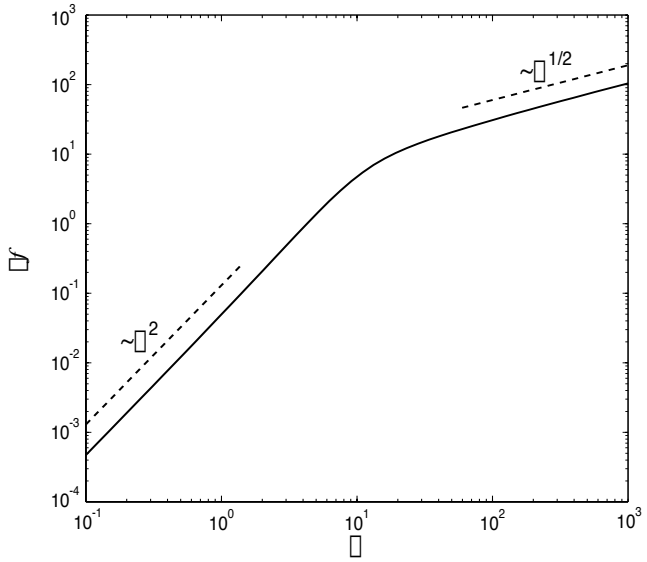

Figure 2.5: The behavior of the free energy βf versus the quadrupole field strength $\Lambda = 2l_p\lambda$ for $N = L/(2l_p) = 3.3333$ with appropriate scaling behavior for large and small Λ.

Helmholtz free energy of the nematic phase relative to the isotropic phase is given by [9]

$$\beta\Delta f = \frac{\kappa L}{3}m^2 - \log q(\kappa m). \tag{2.42}$$

The self-consistent calculation of the order parameter m is performed by evaluating Eq. 2.42, treating m as a variational parameter and finding values of m that minimize $\beta\Delta f$. The stability of the nematic phase is determined by finding the curvature at the thermodynamically determined value of m. In Fig. 2.6, we show the behavior of the Helmholtz free energy $\beta\Delta f$ versus the order parameter m for $N = L/(2l_p) = 3.3333$ and three different values of κ; these three curves represent the conditions corresponding to the spinodal of the nematic phase, coexistence between the isotropic and nematic phases, and the spinodal of the isotropic phase. When $2l_p\kappa = 20.7582$ (dashed curve), $\beta\Delta f$ has an inflection point at $m = 0.2631$ (indicated by the circle); thus a system initially in the nematic phase becomes unstable with respect to order fluctuations and will spontaneously transform to the ther-

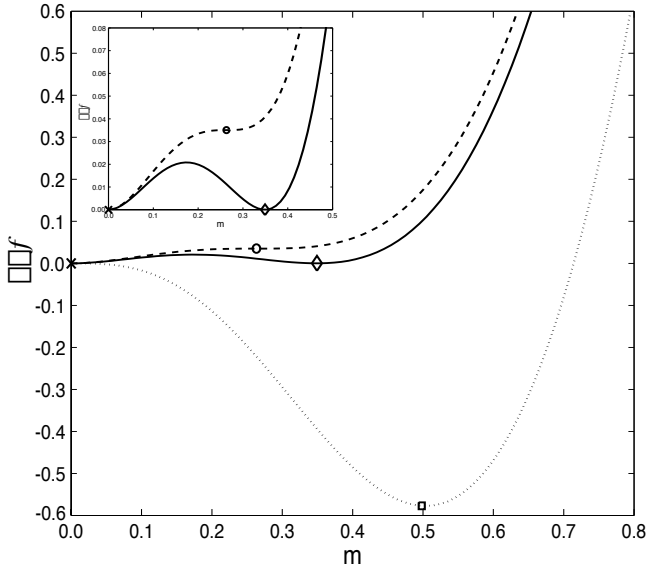

Figure 2.6: The free energy relative to the isotropic state $\beta\Delta f$ versus the order parameter m for a thermotropic liquid-crystalline polymer system with $N = L/(2l_p) = 3.3333$. When the nematic interaction $2l_p\kappa = 20.7582$ (dashed curve), the nematic phase with $m = 0.2631$ ($\circ$) is unstable, thus the system will spontaneously transition to the isotropic phase with $m = 0$ ($\times$). When $2l_p\kappa = 21.0606$ (solid curve), the isotropic phase ($\times$) is in coexistence with the nematic phase with $m = 0.3493$ ($\diamond$). When $2l_p\kappa = 23.6844$ (dotted curve), the isotropic phase ($\times$) spontaneously orders into a nematic phase with $m = 0.4983$ ($\square$). The inset magnifies the behavior near the origin to clarify the coexistence and nematic-spinodal curves.

modynamically favored isotropic phase with $m = 0$ (indicated by the $\times$). By increasing the strength of the nematic interaction to $2l_p\kappa = 21.0606$ (solid curve), we reach coexistence between the isotropic phase with $m = 0$ ($\times$) and nematic phase with $m = 0.3493$ ($\diamond$), where the Helmholtz free energy for the two phases become degenerate. When we increase the nematic interaction further to $2l_p\kappa = 23.6844$, $\beta\Delta f$ exhibits an inflection point at $m = 0$ ($\times$); thus a system initially in the isotropic phase is unstable with respect to order parameter fluctuations and will spontaneously order to a nematic phase with $m = 0.4983$ ($\square$). The inset of Fig. 2.6 provides a close-up of the dashed and solid curves for clarification.

The results shown in Fig. 2.6 are in full agreement with those obtained in reference [9] using spheroidal functions, thus reaffirming the equivalence between these two approaches.

This equivalence implies an interesting mathematical connection between the poles of the continued fraction representation and the eigenvalues of the spheroidal functions, which is worth exploring further.

2.6 Conclusions

In this chapter, we present exact, analytical results for the partition function in Laplace space of a single wormlike chain in an external dipole and quadrupole field in two and three dimensions. The results are in the form of infinite continued fractions, which emerge naturally from the hierarchical structure of the diagrammatic techniques employed. The diagrammatic representation, taken from reference [10], provides a visually intuitive means for re-summing the infinite, moment-based expansion of the various partition functions into successive layers. Thus the rank order of the layers in the continued fraction corresponds to the rank order of layers in the diagrammatic representation.

The greatest appeal of our results is the simplicity and conciseness of the form of the solutions, which makes them easy to use in practical calculations. Because of the rapid convergence of the continued fraction as opposed to simple power series expansions, truncation after a few layers in the infinite continued fraction usually results in sufficient numerical accuracy. For example, the scattering function for a polymer chain in three dimensions with $N = 1$ is accurately captured [less than 1% maximum deviation from the data displayed in Fig. 2.2 ($2 < kL < 20$)] by truncation of the infinite continued fraction at the fourth level [27] We note that truncation at the nth level exactly reproduces all moments of the distribution function up to the $2n$th moment and approximately captures the higher moments.

The solutions given by eqs 2.21, 2.25, 2.26, 2.32, 2.33, and 2.34 provide the governing

equations that are necessary to solve for the end-to-end distance distribution, the structure factor, the response of a chain subject to end tension, and the thermodynamics of nematic liquid-crystalline polymers in two and three dimensions. We have illustrated the use of our results by presenting the exact structure factor of a wormlike chain and the exact mean-field solution for the isotropic-nematic transition in solvent-free semiflexible polymers interacting with a Maier-Saupe type potential. That a number of physical problems involving semiflexible polymers can be addressed by using our results demonstrates their utility.

Bibliography

[1] J. F. Marko and E. D. Siggia. Stretching DNA. *Macromolecules*, 28(26):8759–8770, 1995.

[2] A. Lamura, T. W. Burkhardt, and G. Gompper. Semiflexible polymer in a uniform force field in two dimensions. *Phys. Rev. E*, 6406(6):art. no.–061801, 2001.

[3] J. D. Moroz and P. Nelson. Entropic elasticity of twist-storing polymers. *Macromolecules*, 31(18):6333–6347, 1998.

[4] J. D. Moroz and P. Nelson. Torsional directed walks, entropic elasticity, and DNA twist stiffness. *Proc. Natl. Acad. Sci. U.S.A.*, 94(26):14418–14422, 1997.

[5] T. Odijk. DNA in a liquid-crystalline environment: Tight bends, rings, supercoils. *J. Chem. Phys.*, 105(3):1270–1286, 1996.

[6] W. Maier and A. Saupe. Eine einfache molekulare theorie des nematischen kristallinflussigen zustandes. *Z. Naturforsch. Pt. A*, 13(7):564–566, 1958.

[7] W. Maier and A. Saupe. Eine einfache molekular-statistische theorie der nematischen kristallinflussigen phase .1. *Z. Naturforsch. Pt. A*, 14(10):882–889, 1959.

[8] X. J. Wang and M. Warner. Theory of nematic backbone polymer phases and conformations. *J. Phys. A-Math. Gen.*, 19(11):2215–2227, 1986.

[9] A. J. Spakowitz and Z.-G. Wang. Semiflexible polymer solutions. I. phase behavior and single- chain statistics. *J. Chem. Phys.*, 119(24):13113–13128, 2003.

[10] H. Yamakawa. *Helical Wormlike Chains in Polymer Solutions*. Springer-Verlag, 1997.

[11] J. Samuel and S. Sinha. Elasticity of semiflexible polymers. *Phys. Rev. E*, 66(5):art. no.–050801, 2002.

[12] S. Stepanow and G. M. Schütz. The distribution function of a semiflexible polymer and random walks with constraints. *Europhys. Lett.*, 60(4):546–551, 2002.

[13] H. N. V. Temperley and E. H. Lieb. Relations between percolation and colouring problem and other graph-theoretical problems associated with regular planar lattices - some exact results for percolation problem. *Proceedings of the Royal Society of London Series a- Mathematical and Physical Sciences*, 322(1549):251–&, 1971.

[14] N. Saito, Takahash.K, and Y. Yunoki. Statistical mechanical theory of stiff chains. *J. Phys. Soc. Jpn.*, 22(1):219–&, 1967.

[15] R. P. Feynman and A. R. Hibbs. *Quantum Mechanics and Path Integrals*. McGraw-Hill, 1965.

[16] J. J. Hermans and R. Ullman. The statistics of stiff chains, with applications to light scattering. *Physica*, 18(11):951–971, 1952.

[17] G. B. Arfken and H. J. Weber. *Mathematical Methods for Physicists*. Academic Press, 4 edition, 1995.

[18] The study by Stepanow and Schütz [12] mentions the structure factor calculation but does not provide results or discussion.

[19] A. L. Kholodenko. Fermi-Bose transmutation - from semiflexible polymers to superstrings. *Ann. Phys.*, 202(1):186–225, 1990.

[20] A. L. Kholodenko. Persistence length and related conformational properties of semiflexible polymers from Dirac propagator. *J. Chem. Phys.*, 96(1):700–713, 1992.

[21] M. G. Bawendi and K. F. Freed. A Wiener-integral model for stiff polymer-chains. *J. Chem. Phys.*, 83(5):2491–2496, 1985.

[22] K. Ghosh and M. Muthukumar. Scattering properties of a single semiflexible polyelectrolyte. *J. Polym. Sci. Pt. B-Polym. Phys.*, 39(21):2644–2652, 2001.

[23] A. L. Kholodenko. Analytical calculation of the scattering function for polymers of arbitrary flexibility using the Dirac propagator. *Macromolecules*, 26(16):4179–4183, 1993.

[24] A. L. Kholodenko. Scattering function for semiflexible polymers - Dirac versus Kratky-Porod. *Phys. Lett. A*, 178(1-2):180–185, 1993.

[25] J. Meixner and F. M. Schäfke. *Mathieusche Funktionen und Sphäroidfunktionen*. Springer, 1954.

[26] J. T. Kindt and W. M. Gelbart. Chain self-assembly and phase transitions in semiflexible polymer systems. *J. Chem. Phys.*, 114(3):1432–1439, 2001.

[27] For more rigid chains, accurate calculation of the structure factor requires higher levels of truncation in the continued fraction.

Chapter 3

A Semiflexible Polymer Confined to a Spherical Surface

We develop a formalism for describing the kinematics of a wormlike chain confined to the surface of a sphere that simultaneously satisfies the spherical confinement and the inextensibility of the chain contour. We use this formalism to study the statistical behavior of the wormlike chain on a spherical surface. In particular, we provide an exact, closed-form expression for the mean square end-to-end distance that is valid for any value of chain length L, persistence length l_p, and sphere radius R. We predict two qualitatively different behaviors for a long polymer depending on the ratio R/l_p. For $R/l_p > 4$, the mean square end-to-end distance increases monotonically with the chain length, whereas for $R/l_p < 4$, a damped oscillatory behavior is predicted.

3.1 Introduction

A polymer in a confined geometry is a fundamental problem in polymer physics that underlies some important biological processes and technological applications. For example, polymer confinement is relevant to DNA or RNA packaging in viruses [1] and DNA packaging in eukaryotic cells [2], where, in both cases, the genome is confined within a cavity that is many orders of magnitude smaller than its unconfined radius of gyration.

While the effect of confinement for a flexible polymer is primarily entropic [3], confining a semiflexible polymer involves both energetic and entropic effects, with the balance controlled by the stiffness of the chain and the length scale of confinement [4, 5, 6]. Consider a long, ideal polymer chain confined to a spherical cavity. In the case of a flexible polymer, the chain has the entropic tendency to fill the available space, with the highest concentration of chain segments in the center of the cavity [7]. In the limit of high stiffness, on the other hand, the chain is forced to circle near the surface of the cavity due to its tendency to minimize the bending energy cost. The interplay among the three length scales, namely, the length of the chain, the persistence length, and the characteristic size of the confinement, is thus a fundamental feature in the study of a semiflexible polymer in a confined geometry. Unfortunately, few problems involving semiflexible chains admit exact, closed-form solutions, and we are not aware of such solutions for a semiflexible chain in a confined geometry.

In this chapter, we present an exact, closed-form solution for the conformation of a semiflexible chain confined to the surface of a sphere using the wormlike chain model [8]. This problem is relevant to systems involving strongly adsorbed polymers on spherical surfaces which are often used as simple models for studying DNA/protein complexes and adsorption of a polymer on colloidal particles [5, 9, 10]. By exploiting a novel representation of the differential geometry of an inextensible curve on a spherical surface, we arrive at a simple and concise description of the chain kinematics, which in turn permits the evaluation of the mean square end-to-end distance in a simple, closed-form expression valid for arbitrary chain length, stiffness, and sphere radius.

3.2 Spherical Kinematics

We consider a wormlike chain of contour length L that is confined to the surface of a sphere of radius R. The chain trajectory defines a space curve $\vec{r}(s)$ where the pathlength parameter s has units of length and runs from zero at one end of the polymer chain to L at the other end. The chain contour is assumed inextensible, which requires that the tangent vector $\vec{u} \equiv \partial_s \vec{r}(s)$ satisfies $|\vec{u}(s)| = 1$. The energetics of the wormlike chain model is given by a bending Hamiltonian of the form [11]

$$\beta\mathcal{H} = \frac{l_p}{2} \int_0^L ds \left(\frac{\partial^2 \vec{r}}{\partial s^2} \right)^2 , \tag{3.1}$$

where $\beta = 1/(k_B T)$ and l_p is the persistence length of the free polymer chain. Since we are interested in the equilibrium statistical behavior of an open chain with free ends, the twist degrees of freedom are irrelevant. In problems where the polymer is either closed or torsionally constrained, twist plays a crucial role in the equilibrium and dynamic properties of the polymer; these problems are beyond the scope of this chapter, however.

The constraint that the chain must lie on the surface of the sphere requires that the position vector $\vec{r}(s)$ be a fixed distance R away from the center of the sphere. We now seek a convenient description of the chain kinematics that automatically satisfies this constraint as well as the local inextensibility of the chain contour. Setting the origin of the coordinate system to be the center of the sphere, we define a local orthogonal unit triad $\vec{t}_i$ $(i = 1, 2, 3)$ and choose the position vector to lie in the 3rd direction $[\vec{r}(s) = R\vec{t}_3(s)]$; this guarantees that the chain is confined to the spherical surface. The rotation of the triad system as we progress along the chain contour is given by a rotation vector $\vec{\omega}$ that acts as $\partial_s \vec{t}_i = \vec{\omega} \times \vec{t}_i$; thus the chain position is determined by the rotation of $\vec{t}_3$ over s. The tangent vector is

easily shown to be $\vec{u} = R(\omega_2\vec{t}_1 - \omega_1\vec{t}_2)$, and the chain inextensibility constraint is satisfied by requiring $\omega_1^2 + \omega_2^2 = R^{-2}$. By choosing this coordinate frame, we have effectively altered the complicated constraints on the chain conformation to a simple relationship between ω_1 and ω_2 that can be trivially satisfied.

We now relate the rotation vector $\vec{\omega}$ to the three Euler angles of rotation ϕ, θ, and ψ. Performing an infinitesimal rotation of the triad system, we can express the components of $\vec{\omega}$ in terms of $\partial_s\phi$, $\partial_s\theta$, $\partial_s\psi$ [8]. We complete our description of the spherical chain kinematics by setting $\partial_s\phi$ equal to zero and $\partial_s\theta$ equal to R^{-1}, leaving only the angle ψ to describe the chain conformation that satisfies the constraints. Our mathematical description of the chain kinematics is more clearly understood by considering the chain curvature vector

$$\frac{\partial\vec{u}}{\partial s} = 2\cos\psi\frac{\partial\psi}{\partial s}\vec{t}_1 + 2\sin\psi\frac{\partial\psi}{\partial s}\vec{t}_2 - \frac{1}{R}\vec{t}_3, \tag{3.2}$$

which shows that the choice of ψ as the chain coordinate effectively decouples the curvature due to the spherical confinement from the curvature due to deflection of the chain on the spherical surface.

A physically intuitive description of the conformation is to consider the triad system as a spinning top. For stretches of the chain where the angle ψ is constant, the top rotates about a fixed axis, and the chain lies along an equator of the spherical body. When the angle ψ is altered, the spinning top wobbles and resets its axis of rotation such that the pathlength of the chain is maintained during the deflection. We can consider a reference frame of the spinning top that removes the wobbling motion associated with deflection of the angle ψ [12]. This frame is constructed by removing the accumulated wobble by rotating $\vec{t}_1$ and $\vec{t}_2$ about the vector $\vec{t}_3$ by the total wobble angle $\psi(s) - \psi(0)$. We set $\psi(0)$ to zero

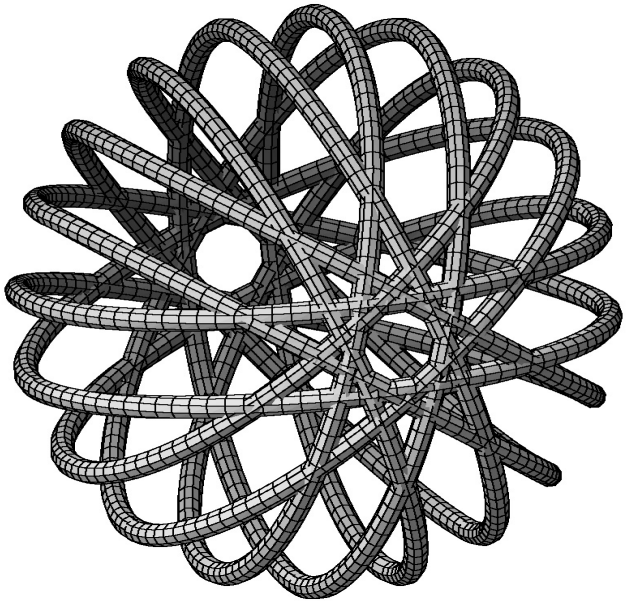

Figure 3.1: The conformation of a polymer chain wrapping around a unit sphere with a constant curvature that orbits after ten revolutions around the sphere.

without loss of generality and define the complex tangent $\vec{\epsilon} \equiv (\vec{t_1} + i\vec{t_2})\exp(i\psi)$ and the complex curvature $\eta \equiv iR^{-1}\exp(i2\psi)$ to give the rate of rotation of this reference frame. Using these definitions, the kinematic equations describing the polymer conformations lying on a spherical surface are given by

$$\frac{\partial \vec{\epsilon}}{\partial s} = \frac{i}{R} e^{i2\psi} \vec{t_3}, \tag{3.3}$$

$$\frac{\partial \vec{t_3}}{\partial s} = -\mathrm{Real}\left(\frac{i}{R} e^{i2\psi} \vec{\epsilon}^{*} \right), \tag{3.4}$$

where the asterisk indicates complex conjugation.

We now give two examples of the solution to Eqs. 3.3 and 3.4 to clarify the use of this coordinate frame. The simplest example is the function $\psi = \nu s$ which describes a circle with radius $R(1 + 4R^2\nu^2)^{-1/2}$ and period $2\pi/\omega$ where $\omega^2 = R^{-2} + 4\nu^2$. As the second example, we consider a function ψ that is a saw-tooth function of s with a slope ν and period $2\pi/\omega$.

This function results in a conformation with a constant curvature similar to wrapping yarn in a spool. Figure 3.1 shows such a conformation that comes to a closed orbit after ten periods around a sphere. Chain conformations like this are of particular importance when dealing with chain self-interaction, which are very difficult to describe in terms of cartesian coordinates.

3.3 Mean Square End-to-End Distance

With our description of the chain kinematics, the bending Hamiltonian becomes

$$\beta\mathcal{H} = 2l_p \int_0^L ds \left(\frac{\partial\psi}{\partial s}\right)^2 + \frac{Ll_p}{2R^2}, \tag{3.5}$$

where the first term is due to chain curvature deformation in the spherical surface and the second term is due to the curvature of the confining surface. The chain statistics are given by the probability that a chain with initial angle $\psi(0) = \psi_0$ will have a final angle $\psi(L) = \psi$ defined as the Green's function $G(\psi|\psi_0, L)$. The Green's function is found by summing all of the statistical contributions of the paths between ψ_0 and ψ of the fluctuating field $\psi(s)$, weighted by the Boltzmann factor $\exp(-\beta\mathcal{H}[\psi(s)])$ [8]. The result can be written as an eigenfunction expansion

$$G(\psi|\psi_0, L) = \sum_{m=-\infty}^{\infty} \frac{1}{2\pi} e^{im(\psi-\psi_0)} \exp\left(-\frac{m^2 L}{8l_p}\right). \tag{3.6}$$

Equation 3.6 is equivalent to the quantum mechanical propagator for a particle confined to a circle, with the bending energy in Eq. 3.5 playing the role of the kinetic energy and the contour length acting as an imaginary time. Use of Eq. 3.6 in finding chain averages

requires expressing the quantity of interest in terms of the function ψ, thus making our compact expressions for the chain kinematics (Eqs. 3.3 and 3.4) extremely useful.

We note that the bending deformation due to the confinement of the sphere is uncoupled from undulations within the surface of the sphere; thus conformation fluctuations within the spherical surface are unaffected by the overall spherical confinement. This is consistent with previous work which demonstrates that, in a tightly bent semiflexible polymer, those fluctuations that do not affect the constraint are not suppressed [6].

We now evaluate the mean square end-to-end distance for the polymer. Using the definition of the end-to-end vector $\vec{R} = \vec{r}(L) - \vec{r}(0)$, we can write $\vec{R}^2$ as

$$\begin{aligned} \vec{R}^2 &= 2R^2\left(1 - \vec{t}_3(0)\cdot\vec{t}_3(L)\right) \\ &= 2R^2\sum_{n=1}^{\infty}\frac{(-1)^{n+1}}{2^n R^{2n}}\left(\prod_{j=1}^{2n}\int_0^{s_{j-1}} ds_j\right)\left\{\prod_{k=1}^{n}\text{Real}\left[e^{i2(\psi_{2k-1}-\psi_{2k})}\right]\right\}, \end{aligned} \tag{3.7}$$

where $s_0 = L$ and $\psi_k = \psi(s_k)$. The second line of Eq. 3.7 is obtained by eliminating the complex tangent $\vec{\epsilon}$ from Eqs. 3.3 and 3.4 iteratively starting from the initial position. The average of Eq. 3.7 is performed by inserting a propagator (Eq. 3.6) between each successive function of ψ in the expansion. The resulting expression is

$$\left\langle \vec{R}^2 \right\rangle = -\sum_{n=1}^{\infty} 2R^2(-1)^n\left(\frac{2l_p}{R}\right)^{2n} A_n(N), \tag{3.8}$$

where we define $N = L/(2l_p)$. The coefficients of the expansion $A_n(N)$ are compactly defined through the recursive relation

$$A_n(N) = \int_0^N d\tau_1 \int_0^{\tau_1} d\tau_2 \exp(-\tau_1 + \tau_2)\, A_{n-1}(\tau_2), \tag{3.9}$$

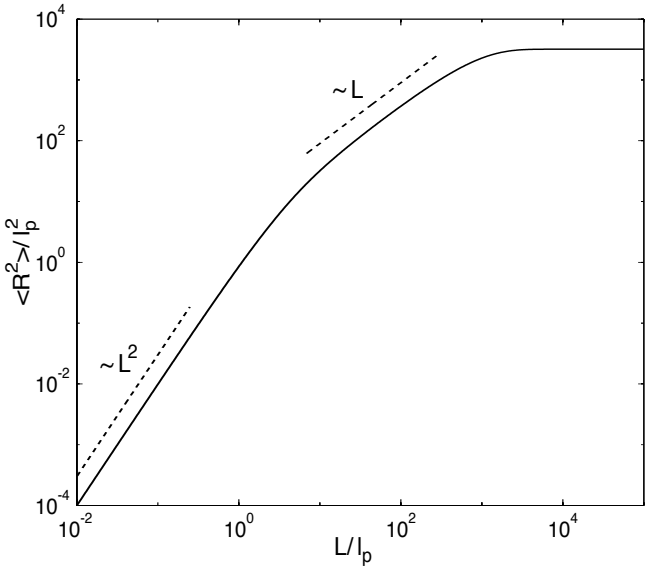

Figure 3.2: The mean square end-to-end distance of a polymer chain confined to a sphere with $R/l_p = 40$.

with $A_0(N) = 1$. The recursive relation is more conveniently written in the differential form $(\partial_N^2 + \partial_N)\, A_n(N) = A_{n-1}(N)$, with the initial conditions $A_n(0) = 0$ and $\partial_N A_n(0) = 0$. This differential recursive equation can be readily solved by a Laplace transform from the variable N to p to give $A_n(p) = p^{-n-1}(p+1)^{-n}$. Inserting this result into Eq. 3.8, performing the straightforward summation, and inverse Laplace transforming the resulting expression lead to our final result for the mean square end-to-end distance of a chain confined to a spherical surface

$$\begin{aligned}\left\langle \vec{R}^2 \right\rangle &= 2R^2 - 2R^2 \exp\left(-\frac{L}{4l_p}\right)\left\{\cosh\left[\frac{L}{4l_p}\left(1-\frac{16l_p^2}{R^2}\right)^{1/2}\right] + \right. \\ &\left. \left(1-\frac{16l_p^2}{R^2}\right)^{-1/2} \sinh\left[\frac{L}{4l_p}\left(1-\frac{16l_p^2}{R^2}\right)^{1/2}\right]\right\}. \end{aligned} \tag{3.10}$$

It can be easily verified that Eq. 3.10 recovers several important limiting results. If the chain length is much less than the radius, we expect that the chain will not feel the

effect of the spherical confinement. As the radius goes to infinity, the leading order term in the l_p/R expansion of Eq. 3.10 yields the 2 dimensional solution for a free wormlike chain $4l_pL + 8l_p^2\{\exp[-L/(2l_p)] - 1\}$ [13]. Similarly, as the chain length goes to zero, Eq. 3.10 approaches L^2 for any finite sphere radius. Finally, for a fixed radius R, we expect that for a sufficiently long chain the end position becomes uncorrelated from the initial position, thus leading to a uniform coverage of the sphere by the chain segments. This results in a mean square end-to-end distance of $2R^2$ as can be seen from Eq. 3.10 in the limit of L approaching infinity for fixed l_p and R.

In Fig. 3.2, we present a plot of Eq. 3.10 as a function of the chain length for a fixed value of R/l_p of 40. The mean square end-to-end distance in Fig. 3.2 exhibits three distinct scaling regimes due to the three relevant length scales. With $R/l_p = 40$, the radius is large enough that short stretches of the chain behave as a chain in two dimensions. Figure 3.2 scales as L^2 for short chains ($L < 2l_p$), which is the rigid-rod behavior. In the intermediate regime [$2l_p < L < R^2/(2l_p)$], the chain behaves with the random walk scaling of L. Essentially, the chain is sufficiently long such that the end orientations are uncorrelated; however, the chain is not long enough to feel the finite area of the confining spherical surface. For a sufficiently long chain [$L > R^2/(2l_p)$], the polymer has diffused over a distance where the curvature of the confining surface restricts the magnitude of the end-to-end vector; thus the final regime approaches a value of $2R^2$. Our results for these latter two regimes agree with those predicted using the flexible Gaussian chain model [14].

A qualitatively different behavior emerges when the radius of the sphere is smaller than the persistence length. Specifically, for $R < 4l_p$, the arguments of the hyperbolic functions in Eq. 3.10 are imaginary, resulting in an oscillatory mean square end-to-end distance. Physically, the chain revolves around the sphere due to the orientation correlation. In

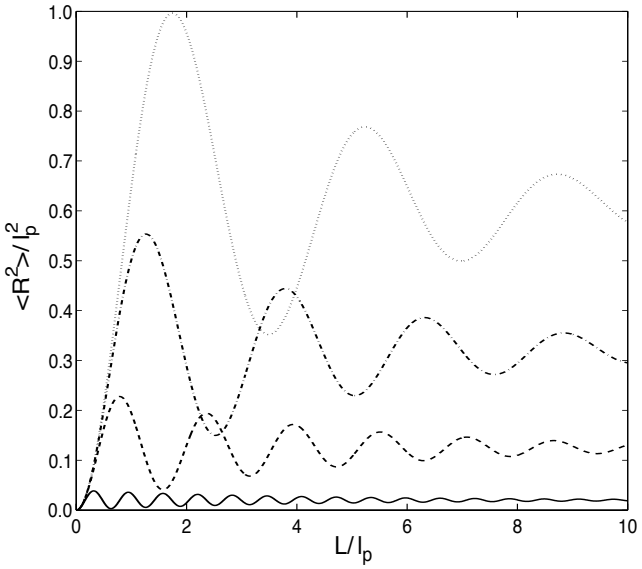

Figure 3.3: The mean square end-to-end distance versus the polymer chain length for $R/l_p = 1/10$ (solid curve), $R/l_p = 1/4$ (dashed curve), $R/l_p = 2/5$ (dashed-dotted curve), and $R/l_p = 11/20$ (dotted curve).

the limit of infinite chain stiffness, the mean square end-to-end distance becomes $2R^2 - 2R^2\cos(L/R)$, which corresponds to a polymer chain confined to the equator of a sphere. For finite chain stiffness, the L dependence of Eq. 3.10 contains an exponentially decaying oscillation with a periodicity in L of $8\pi l_p R(16l_p^2 - R^2)^{-1/2}$. The exponential decay of the oscillations reflects the eventual loss of correlation due to the thermal fluctuations of the semiflexible chain. The periodicity in L is larger than that at infinite chain stiffness ($2\pi R$) because of the wrinkling of the chain due to fluctuation. For $R > 4l_p$, the chain orientation becomes uncorrelated before the polymer completes a single pass over the sphere, manifested in the lack of oscillation in Fig. 3.2. The cross-over at $R = 4l_p$ is analogous to a damped harmonic oscillator where critical damping occurs when the damping coefficient [$1/(4l_p)$ in our case] is equal to the natural frequency of the oscillation ($1/R$) [15].

The oscillatory behavior of Eq. 3.10 for $R < 4l_p$ is shown in Fig. 3.3. As expected, the short chain ($L \ll l_p$) behavior is independent of the radius. The damping of the oscillations

occurs exponentially in L with a correlation length of $4l_p$ (independent of R); however, since the period of the oscillations is shorter for smaller radius, the number of correlated spherical wraps decreases with increasing sphere radius. As the chain length goes to infinity, all of the curves in Fig. 3.3 approach $2R^2$.

The behavior of the mean square end-to-end distance suggests the nature of the surface coverage by the polymer as the length of the polymer increases. In the regime corresponding to Fig. 3.2, the polymer covers the sphere in a diffusive manner from the starting point. The scenario is that of the polymer chain creeping over the sphere starting at one pole towards the opposite pole as the length of the chain increases. For the high chain stiffness shown in Fig. 3.3, the orientation correlation causes the chain to lie on the equator of the sphere, and conformation fluctuations cause the segment density to spread from the equator toward the poles.

Our treatment ignores the interactions between chain segments, which will modify the predicted behavior. However, some salient features predicted by our work will remain. For example, our predicted change in the manner in which the chain wraps the sphere as the stiffness increases is consistent with the Monte Carlo results in ref. [10], which included both excluded volume and electrostatic interactions. Thus our results both provide a concise and unified expression for elucidating the dominant effects due to the interplay among the three length scales in the problem and serve as a useful reference for examining new effects due to additional interactions.

The main advantage of the chain kinematics we have developed is that it provides a convenient way to satisfy the constraints associated with the wormlike chain model and the chain confinement. Physically, strict confinement of the chain to a sphere surface corresponds to infinitely strong adsorption. However, our formalism can be extended to allow

radial fluctuations away from the sphere surface while still conserving the contour length. This will enable us to treat a wormlike chain near an attractive spherical particle or within a spherical cavity.

Bibliography

[1] B. Lewin. *Genes VII*. Oxford University Press, 2000.

[2] H. Lodish, A. Berk, S. L. Zipursky, D. Baltimore, and J. Darnell. *Molecular Cell Biology*. W. H. Freeman and Company, 2000.

[3] P. G. de Gennes. *Scaling Concepts in Polymer Physics*. Cornell University Press, 1979.

[4] T. W. Burkhardt. Free energy of a semiflexible polymer in a tube and statistics of a randomly-accelerated particle. *J. Phys. A-Math. Gen.*, 30(7):L167–L172, 1997.

[5] T. Odijk. Physics of tightly curved semiflexible polymer-chains. *Macromolecules*, 26(25):6897–6902, 1993.

[6] T. Odijk. DNA in a liquid-crystalline environment: Tight bends, rings, supercoils. *J. Chem. Phys.*, 105(3):1270–1286, 1996.

[7] M. Doi and S. F. Edwards. *The Theory of Polymer Dynamics*. Oxford University Press Inc., New York, NY, 1986.

[8] H. Yamakawa. *Helical Wormlike Chains in Polymer Solutions*. Springer-Verlag, 1997.

[9] H. Schiessel, J. Widom, R. F. Bruinsma, and W. M. Gelbart. Polymer reptation and nucleosome repositioning. *Phys. Rev. Lett.*, 86(19):4414–4417, 2001.

[10] S. Stoll and P. Chodanowski. Polyelectrolyte adsorption on an oppositely charged spherical particle-chain rigidity effects. *Macromolecules*, 35(25):9556–9562, 2002.

[11] N. Saito, Takahash.K, and Y. Yunoki. Statistical mechanical theory of stiff chains. *J. Phys. Soc. Jpn.*, 22(1):219–&, 1967.

[12] R. E. Goldstein, T. R. Powers, and C. H. Wiggins. Viscous nonlinear dynamics of twist and writhe. *Phys. Rev. Lett.*, 80(23):5232–5235, 1998.

[13] J. J. Hermans and R. Ullman. The statistics of stiff chains, with applications to light scattering. *Physica*, 18(11):951–971, 1952.

[14] R. P. Mondescu and M. Muthukumar. Brownian motion and polymer statistics on certain curved manifolds. *Phys. Rev. E*, 57(4):4411–4419, 1998.

[15] L. D. Landau and E. M. Lifshitz. *Mechanics*. Pergamon Press, 3 edition, 1976.

Chapter 4

Semiflexible Polymer Solutions: Phase Behavior and Single-Chain Statistics

We study the thermodynamics and single-chain statistics of wormlike polymer solutions with Maier-Saupe type interactions using self-consistent-field (SCF) theory. The SCF equations are derived using a systematic field-theoretical approach which yields the SCF equations as the lowest order approximation, but permits fluctuation corrections to be incorporated. We solve the SCF equations using the spheroidal functions, which provides a non-perturbative description of the thermodynamics and single-chain statistics in the nematic state for arbitrary degrees of nematic order. Several types of phase diagrams are predicted, with an emphasis on the limit of metastability (spinodal) associated with each phase. The shape and location of these spinodals suggest interesting scenarios for the phase transition kinetics. A large but finite persistence length is shown to significantly decrease the isotropic-nematic transition temperature relative to that for rigid rods. In the nematic state, the mean-square end-to-end distance in the parallel and perpendicular directions are governed by two separate correlation lengths. An exact relationship between these correlation lengths and the eigenvalues of the spheroidal functions is provided, which reproduces the analytical expressions predicted from earlier studies in the limit of large nematic strength. The

dominant contribution to the single-chain thermodynamics is shown to arise from small amplitude undulations in the directions perpendicular to the nematic direction; the presence of hairpins, though crucial for determining the dimensions of the polymer, has insignificant consequences on the single-chain thermodynamics.

4.1 Introduction

Polymers with sufficient backbone bending rigidity can form nematic liquid crystalline phases at low temperatures and/or high concentrations. The enhanced alignment of the polymer chains in the nematic state is the basis for several material properties and processes such as high strength fibers [1] and flow induced crystallization [2, 3, 4, 5, 6]. Solutions of DNA form lyotropic liquid crystalline phases under several biologically relevant conditions including molecular crowding [7], large molecular weight [8], polycationic agents (synthetic [9] and natural [10]), and supercoiling in plasmid DNA [11]. Thus the nematic state of main-chain liquid crystalline polymers is a subject of importance in both materials science and biology.

In this chapter, we study the nematic phase of solutions of semiflexible polymers: polymers with a backbone of uniform, finite stiffness. In contrast to the simpler case of rigid rods where nematic ordering is associated with only a loss of the rotational degrees of freedom, the nematic state of semiflexible polymers is accompanied by a loss of both the overall rotational entropy of the chain and the conformation entropy of the chain segments. The conformation degrees of freedom lead to two important effects. At length scales less than the natural persistence length, the undulation of the chain backbone acts to weaken the aligning interactions between neighboring molecules and is thus expected to affect the nematic ordering of the chains. At larger length scales, for sufficiently long chains, the poly-

mer can undergo sharp reversals in direction to form hairpin defects [12]. The presence of hairpins in liquid-crystalline polymers has profound effects on the chain dimensions [13, 14] and the elastic behavior [15] of the nematic state. The finite bending rigidity of the chains has also been suggested as being responsible for the unusual rheological behavior of nematic liquid-crystalline polymers, such as shear-induced banding [16].

We examine the phase behavior and conformation properties of lyotropic polymer liquid crystals using the wormlike chain model [17] with a Maier-Saupe pseudopotential [18, 19]. This model has been employed by a number of authors to study main-chain liquid crystalline polymers. Warner and co-workers studied both the phase behavior and chain conformation properties in solvent-free systems based on the exact solution of the mean-field equations using spheroidal functions [20, 14]. However, the addition of a second component (whether another polymer species or small nonmesogenic solvent) produces new qualitative features in the phase behavior as shown by Liu and Fredrickson [21, 22]. In addition, in the approach by Warner and co-workers, the mean-field approximation is introduced as an *ansatz* instead of being derived as the lowest order approximation in a systematic approach. Furthermore, by restricting the interaction to a spatially independent scalar form using the second Legendre polynomial $P_2(\tau) = 3u_z^2(\tau)/2 - 1/2$, the approach can only treat the homogeneous state.

Liu and Fredrickson [21] derived an analytical free energy functional for semiflexible polymer blends using a gradient and order parameter expansion to the quartic order around the uniform isotropic state. Their approach begins with a field-theoretical formulation of the exact partition function and develops the free energy expansion in a systematic manner. The advantage of the Liu-Fredrickson theory is that it is analytical and convenient for treating inhomogenous systems [23]. However, its accuracy for describing the nematic state is *a priori* not clear, given the strongly first-order nature of the isotropic-nematic transition.

Furthermore, the order parameter expansion uses chain statistics in the isotropic state and thus cannot describe the chain conformation properties in the nematic state.

Other authors used simplified versions of the wormlike chain model which do not conserve the local contour length [24, 25, 26, 27]. While such simplified models may capture the qualitative behavior of certain aggregate properties, the chain statistics described by these models are different from that given by the wormlike chain model. They also fail to capture the dynamic properties of a semiflexible chain [28, 29].

In this article, we adapt the exact mean-field solution method of Warner and co-workers to the study of lyotropic systems. We follow the field-theoretical formulation of Liu and Fredrickson, but instead of performing an expansion around the isotropic state, we derive the exact mean-field equations valid for both the isotropic and nematic states, and solve these equations using the spheroidal functions. Our work thus combines the strengths of both approaches. In particular, it provides a non-perturbative description of the thermodynamics and single-chain conformation properties in the nematic state and is amenable to systematic corrections to account for fluctuation effects.

This chapter is organized as follows. In Sec. 4.2, we present the model and develop the mean-field equations as the lowest-order approximation to a more systematic approach. The solution method using spheroidal functions is discussed in Sec. 4.3 where we also work out the ground-state dominance criteria useful for obtaining a number of analytical results in the long chain limit and explore the asymptotic behavior of some thermodynamic properties in the strong nematic field limit. In Sec. 4.4, we present the bulk (zero wavenumber) fluctuation free energy to quadratic order around the mean-field solution in connection to the calculation of the limit of stability (spinodal) of the various phases. In Sec. 4.5 we present the main results of the calculation. Several phase diagrams are calculated to illustrate different

types of phase behaviors that can result depending on the interplay between the isotropic and anisotropic part of the two-body interaction. By analyzing the shape and location of spinodal curves in these phase diagrams, we propose several interesting scenarios for the phase transition kinetics. The effects of chain stiffness on the nematic order are also briefly discussed in reference to the rigid-rod limit and we find that small fluctuations of the backbone of the polymers can significantly suppress the emergence of nematic order. We then examine a number of single-chain properties in the nematic state, with an emphasis on the anisotropy of the chain conformation and various energetic contributions. For sufficiently long chains, we provide exact expressions for the longitudinal and transverse correlation lengths in terms of the eigenvalues of the spheroidal functions, which reduce to earlier results by Odijk [30, 31, 32] and Tkachenko and Rabin [33] derived in the limit of large nematic field strength. We end this chapter with a brief summary and conclusion in Sec. 4.6.

4.2 Self-Consistent-Field Theory

We consider an incompressible system composed of n_p polymer chains and n_s solvent molecules. The polymer molecules are modeled as wormlike chains [17] with cross-sectional area A and fixed contour length L, and the solvent molecules are spherical, non-mesogenic particles with volume v. We work with an open system (grand canonical ensemble) wherein the polymer solution in volume V and at temperature T is connected to an external reservior; thus the characteristic free energy G of our system is

$$G(V,\mu) = Vg(\mu) = V[f(\phi_p) - \mu\phi_p], \tag{4.1}$$

where f is the Helmholtz free energy density and μ a chemical potential-like variable that is conjugate to the polymer volume fraction ϕ_p.

The configuration of our system is given by the position and conformation of each polymer molecule and the position of each solvent molecule. The position and conformation of the i-th polymer is described by the spacecurve $\vec{r}_i(\tau)$ where the path coordinate τ runs from zero to L. We define the tangent vector $\vec{u}_i(\tau) = \partial_\tau \vec{r}_i(\tau)$ and enforce the fixed polymer length constraint by requiring $|\vec{u}_i(\tau)| = 1$ at all τ. The position of the j-th solvent molecule is denoted by $\vec{r}_j$.

We model the interactions in the system by a local two-body pseudopotential and separate the pseudopotential into isotropic and anisotropic contributions. Thus the Hamiltonian of our system is

$$\beta\mathcal{H} = \sum_{i=1}^{n_p} \frac{\epsilon}{2} \int_0^L \left(\frac{\partial \vec{u}_i}{\partial \tau} \right)^2 d\tau + \chi \int d\vec{r}\, \hat{\phi}_s(\vec{r}) \hat{\phi}_p(\vec{r}) - \frac{a}{2} \int d\vec{r}\, \hat{\mathbf{S}}(\vec{r}) : \hat{\mathbf{S}}(\vec{r}), \tag{4.2}$$

where $\hat{\phi}_s$ and $\hat{\phi}_p$, are respectively the local dimensionless density (volume fraction) of the solvent and polymer molecules, and $\hat{\mathbf{S}}$ is the tensorial nematic order parameter density (again made dimensionless). They are given by

$$\hat{\phi}_s(\vec{r}) = v \sum_{j=1}^{n_s} \delta(\vec{r} - \vec{r}_j), \tag{4.3}$$

$$\hat{\phi}_p(\vec{r}) = A \sum_{i=1}^{n_p} \int_0^L d\tau \delta(\vec{r} - \vec{r}_i(\tau)), \tag{4.4}$$

$$\hat{\mathbf{S}}(\vec{r}) = A \sum_{i=1}^{n_p} \int_0^L d\tau \delta(\vec{r} - \vec{r}_i(\tau)) \left(\vec{u}_i(\tau)\vec{u}_i(\tau) - \frac{1}{3}\mathbf{I} \right). \tag{4.5}$$

The first term in the Hamiltonian (Eq. 4.2) is the bending energy of the n_p polymer chains, assumed to be quadratic in the curvature of the polymer conformations. The bending

modulus ϵ, which has units of length, is equal to the persistence length of the fluctuating chain in the absence of inter-molecular interactions. The second term in Eq. 4.2 is the isotropic part of the two-body interaction between polymer and solvent molecules, taken to be the Flory-Huggins type [34]. The Flory-Huggins parameter χ contains both an athermal entropic contribution as well as an enthalpic component [35], thus we may write χ as $\chi = \chi_S + \chi_H/T$. The last term in Eq. 4.2 is the anisotropic component of the two-body polymer-polymer interaction taken to be of the Maier-Saupe type [18, 19], which prefers to align the polymer chains within the solution. In general, the Maier-Saupe potential contains both hard-core contact interactions and soft attractive interactions; therefore, we anticipate the Maier-Saupe parameter a, which has units of inverse volume, to have the temperature dependence $a = a_S + a_H/T$ [24]. The details of the molecular interactions are simplified by introducing these two phenomenological pseudo-potentials, and the effect of hard-core short-ranged repulsion is accounted for through the incompressibility constraint.

The grand canonical partition function Ξ is found by summing over all system configurations that are consistent with the incompressibility and chain length constraints that we impose on our system; it is given by

$$\begin{aligned}
\Xi &= \exp[-\beta G(T,V,\mu)] \\
&= \sum_{n_s,n_p=0}^{\infty} \frac{1}{n_s! n_p!} \frac{e^{\beta\mu LAn_p}}{v^{n_s}(LA)^{n_p}} \int \prod_{j=1}^{n_s} d\vec{r}_j \int \prod_{i=1}^{n_p} \mathcal{D}[\vec{r}_i] \\
&\quad \times \prod_{\vec{r}} \delta(\hat{\phi}_s + \hat{\phi}_p - 1) \prod_{\tau} \delta(|\partial_\tau \vec{r}_i| - 1) e^{-\beta\mathcal{H}},
\end{aligned} \tag{4.6}$$

where $\prod_{\vec{r}} \delta(\hat{\phi}_s + \hat{\phi}_p - 1)$ accounts for the incompressibility constraint $\hat{\phi}_s + \hat{\phi}_p = 1$ at all locations within the system volume, and $\prod_\tau \delta(|\partial_\tau \vec{r}_i| - 1)$ denotes the fixed chain length constraint $|\partial_\tau \vec{r}_i| = 1$ over the entirety of the path coordinate τ for each polymer chain.

The integration over $\mathcal{D}[\vec{r}_i]$ implies path integration over all conformations of the polymer chain [36]. We use the solvent volume v and polymer volume LA as volume scales instead of the de Broglie wavelengths cubed, which merely shifts the chemical potential by a constant quantity and does not affect the thermodynamic behavior of our system.

The partition function Eq. 4.6 cannot be evaluated exactly due to the many-chain nature of the molecular interactions and the incompressibility constraint. To make progress, we use field-theoretical techniques [37, 38] to transform the many-chain problem into a single-chain problem in fluctuating effective potential fields. This is done by performing a series of identity transformations through functional integration over a number of auxiliary field variables. The resulting expression for the grand canonical partition function is now

$$\begin{aligned}\Xi &= \int \mathcal{D}\phi_p \mathcal{D}W_s \mathcal{D}W_p \mathcal{D}\mathbf{S} \mathcal{D}\mathbf{\Lambda} \exp\left\{ i\int d\vec{r}\, W_s(1-\phi_p) + \right. \\ & \quad i\int d\vec{r}\, [W_p\phi_p + \mathbf{\Lambda}:\mathbf{S}] - \chi\int d\vec{r}\,\phi_p(1-\phi_p) + \\ & \quad \left. \frac{a}{2}\int d\vec{r}\,\mathbf{S}:\mathbf{S} + \frac{1}{v} z_s(W_s) + \frac{e^{\beta\mu LA}}{LA} z_p(W_p, \mathbf{\Lambda}) \right\}, \end{aligned} \tag{4.7}$$

where ϕ_p and $\mathbf{S}$ are respectively the local volume fraction and order parameter density fields, and W_s,W_p, and $\mathbf{\Lambda}$ are effective fluctuating fields conjugate to the solvent volume fraction, the polymer volume fraction, and the order parameter density, respectively. The solvent volume fraction has been eliminated by the use of the incompressibility constraint. In Eq. 4.7, $z_s(W_s)$ and $z_p(W_p, \mathbf{\Lambda})$ are respectively the single-solvent-molecule partition function and single-polymer-chain partition function, given by

$$z_s(W_s) = \int d\vec{r}\, e^{-ivW_s(\vec{r})}, \tag{4.8}$$

and

$$z_p(W_p, \mathbf{\Lambda}) = \int \mathcal{D}[\vec{r}(\tau)] \exp\left\{ -\frac{\epsilon}{2} \int_0^L \left(\frac{\partial \vec{u}}{\partial \tau} \right)^2 d\tau - iA \int_0^L d\tau \left[W_p(\vec{r}(\tau)) + \mathbf{\Lambda}(\vec{r}(\tau)) : \left(\vec{u}\vec{u} - \frac{1}{3}\mathbf{I} \right) \right] \right\}. \tag{4.9}$$

Though equally difficult to evaluate exactly, the partition function written in the form of Eq. 4.7 is more amenable to systematic approximations. In particular, the self-consistent-field, or mean-field approximation (we will use these two terms synonymously in this chapter), is obtained by a saddle-point approximation to the functional integrals, i.e.,by locating the stationary points of the exponent in Eq. 4.7 with respect to the field variables.

Setting the functional derivatives of the exponent in Eq. 4.7 with respect to the field variables to zero, we obtain the self-consistent-field equations:

$$1 - \phi_p = e^{-v w_s}, \tag{4.10}$$

$$\phi_p = -\frac{e^{\beta\mu LA}}{LA} \frac{\delta z_p}{\delta w_p}, \tag{4.11}$$

$$w_p - w_s = \chi(1 - 2\phi_p), \tag{4.12}$$

$$\mathbf{h} = -a\mathbf{S}, \tag{4.13}$$

$$\mathbf{S} = -\frac{e^{\beta\mu LA}}{LA} \frac{\delta z_p}{\delta \mathbf{h}}, \tag{4.14}$$

where we have defined the fields $w_s = iW_s$, $w_p = iW_p$, and $\mathbf{h} = i\mathbf{\Lambda}$ on account of the fact that the saddle-point values of the field variables W_s, W_p and $\mathbf{\Lambda}$ lie on the imaginary axis.

At the mean-field level, the above set of equations fully describe the thermodynamics, and, through the single-chain partition function (Eq. 4.9), the conformation properties of the liquid-crystalline polymer solution modeled by the Hamiltonian (Eq. 4.2). They are

applicable to problems involving spatial inhomogeneity of polymer concentration and order. Here we focus on the equilibrium, bulk behavior with uniaxial order.

We choose the nematic director to be aligned in the z-direction; thus the order parameter is given by

$$\mathbf{S} = S_0 \left(\hat{z}\hat{z} - \frac{1}{3}\mathbf{I} \right). \tag{4.15}$$

The self-consistent-field equations can be solved analytically by first eliminating the variables, w_s, w_p and $\mathbf{h}$ in favor of the bulk volume fraction of the polymers, ϕ_p, and the scalar order parameter S_0. Because $\mathbf{S}$ is defined as the order parameter density, S_0 vanishes in the limit of zero concentration even if all the chains are fully aligned. We thus define a normalized scalar order parameter m by

$$m = \frac{S_0}{\phi_p} = \frac{1}{L} \int_0^L d\tau \left\langle \left(\frac{3}{2} u_z^2(\tau) - \frac{1}{2} \right) \right\rangle, \tag{4.16}$$

where $\langle \ldots \rangle$ indicates an average with respect to the single-chain, self-consistent-field Hamiltonian,

$$\beta \mathcal{H}_0 = \frac{\epsilon}{2} \int_0^L \left(\frac{\partial \vec{u}}{\partial \tau} \right)^2 d\tau - a\phi_p m A \int_0^L d\tau \left(u_z^2(\tau) - \frac{1}{3} \right). \tag{4.17}$$

We note the effective Hamiltonian (Eq. 4.17) only contains orientation terms thus simplifying the calculation of the chain statistics, which we discuss in more detail in the following section.

The grand potential density g is equivalently expressed as the osmotic pressure defined through $p = -[g(\phi_p) - g(0)]$ and given by

$$\beta p = -\frac{1}{v} \log(1 - \phi_p) - \chi \phi_p^2 - \frac{1}{3} a \phi_p^2 m^2 - \frac{\phi_p}{v} + \frac{\phi_p}{LA}. \tag{4.18}$$

The chemical potential μ is given by

$$\beta\mu = \frac{1}{LA}\log\phi_p - \frac{1}{v}\log(1-\phi_p) + \chi(1-2\phi_p) - \frac{1}{LA}\log q, \tag{4.19}$$

where the single-polymer molecule orientation partition function q is calculated from the self-consistent field Hamiltonian, Eq. 4.17. And finally, the Helmholtz free energy density (up to an additive constant) for a single, homogeneous phase is

$$\begin{aligned}\beta f &= -\beta p + \beta\mu\phi_p \\ &= \frac{\phi_p}{LA}\log\phi_p + \frac{(1-\phi_p)}{v}\log(1-\phi_p) + \chi\phi_p(1-\phi_p) \\ &\quad + \frac{a}{3}\phi_p^2 m^2 + \frac{\phi_p}{v} - \frac{\phi_p}{LA} - \frac{\phi_p}{LA}\log q.\end{aligned} \tag{4.20}$$

Phase coexistence can be found by minimizing the total Helmholtz free energy of a composite system of two homogeneous phases or equivalently by the respective equality of the osmotic pressure and the chemical potential of the two coexisting phases. In Sec. 4.5, we demonstrate several scenarios for phase separation that is predicted by our model.

Eqs. 4.10 through 4.14 constitute the exact solution for the saddle point of Eq. 4.7. The solution of the self-consistent Eq. 4.16 and the evaluation of the single-chain partition function q in Eq. 4.19 require the conformation statistics of a single chain in a finite nematic field (cf. Eq. 4.17). We address the single chain statistics in Sec. 4.3 by mapping it to the quantum mechanics of a rigid rotor in a quadrupole field for which spheroidal functions provide the exact eigenfunctions.

In the solvent-free limit, our results reduce to that previously given by Wang and Warner for thermotropic nematic polymers [20]. Transition from an isotropic phase to a nematic

phase occurs when

$$-\log 4\pi = \frac{aLA}{3}m^2 - \log q, \tag{4.21}$$

where m is determined self-consistently from Eq. 4.16.

4.3 Chain Statistics

The self-consistent-field approximation reduces the many-chain problem to a single chain in a (self-consistent) external field. Thus an essential input to the SCF theory is the single-chain statistics. The chain statistics are described by a Green's function $G(\vec{r}, \vec{u}|\vec{r}_0, \vec{u}_0, L)$, which gives the joint probability for a polymer chain to start and end with specified positions and orientations as a function of the chain length. While in general we need to consider both the position and orientation dependence of the Green's function, for the homogeneous phases we consider here, it suffices to focus on the orientation variable. Thus we consider the reduced Green's function $G(\vec{u}|\vec{u}_0, L)$, defined as

$$G(\vec{u}|\vec{u}_0, L) = \int_{\vec{u}_0}^{\vec{u}} \mathcal{D}[\vec{u}(\tau)] e^{-\beta \mathcal{H}_0[\vec{u}(\tau)]}, \tag{4.22}$$

from which the partition function q and the order parameter m can be calculated using

$$q = \int d\vec{u} \int d\vec{u}_0 G(\vec{u}|\vec{u}_0, L), \tag{4.23}$$

$$m = \frac{3}{2L}\left(\frac{\partial \log q}{\partial \kappa}\right)_\epsilon, \tag{4.24}$$

where $\kappa = a\phi_p m A$.

The orientation path integration for the Green's function of a wormlike chain is analogous to the calculation of the probability amplitude for a quantum mechanical rotor, where

the chain length plays the role of an imaginary time variable [36, 39]. Using this analogy, we derive a diffusion equation for the chain statistics that is analogous to the Schrödinger equation. The diffusion equation for the Green's function is

$$\left[\frac{\partial}{\partial L} - \frac{1}{2\epsilon}\nabla_u^2 - a\phi_p mA\left(u_z u_z - \frac{1}{3}\right)\right] G(\vec{u}|\vec{u}_0, L) = \delta(L)\delta(\vec{u} - \vec{u}_0) \tag{4.25}$$

where ∇_u^2 is the angular portion of the Laplace operator. Our statistical problem is essentially a unit vector diffusing over the surface of a sphere, biased by a quadrupole potential favoring the poles.

Equation 4.25 is solved using an eigenfunction expansion by defining the Hamiltonian operator $\mathcal{H} = -\nabla_u^2 - \gamma u_z u_z$, where $\gamma = 2a\phi_p \epsilon mA = 2\epsilon\kappa$. The eigenfunctions of $\mathcal{H}$ are the spheroidal functions [40] Ysp_l^m with eigenvalues $\mathcal{E}_l^m(\gamma)$. Owing to the completeness of the spheroidal functions, the Green's function is written as

$$G(\vec{u}|\vec{u}_0, L) = \sum_{l=0}^{\infty}\sum_{m=-l}^{l} C_l^m(L) Ysp_l^m(\vec{u}) Ysp_l^{m*}(\vec{u}_0), \tag{4.26}$$

accounting for the initial condition $G(\vec{u}|\vec{u}_0, 0) = \delta(\vec{u} - \vec{u}_0)$, where the chain-length dependent coefficients are given by

$$C_l^m = \exp\left[-\left(\mathcal{E}_l^m(\gamma) + \frac{\gamma}{3}\right)\frac{L}{2\epsilon}\right]. \tag{4.27}$$

Since the Green's function only provides orientation statistics, the expectation value of any quantity must be expressed in terms of orientation variables only. Clearly the Green's function including position variables provides an easier formalism for calculating arbitrary averages; however, analytical expressions for the full Green's function do not exist, and approximate techniques have a limited range of validity [39].

Several methods exist for the calculation of the spheroidal functions. Numerical packages [41, 42, 43] have been developed that accurately evaluate the functions and their eigenvalues. The spheroidal functions can also be evaluated by expansion in terms of the more common spherical harmonics (Y_l^m) [40, 20]; we outline this technique in Appendix A. The spheroidal functions asymptotically approach the spherical harmonics in the limit of $\gamma \to 0$, thus in this limit, $\mathcal{E}_l^m$ approaches $l(l+1)$. The opposite limit ($\gamma \to \infty$) yields asymptotic expressions for $\mathcal{E}_l^m$ in terms of γ [40], which we exploit later in this section.

While the eigenfunction expansion Eq. 4.26 is formally exact for any bending rigidity, the limit of a fully rigid chain ($\epsilon \to \infty$) is more conveniently solved directly by setting $\epsilon \to \infty$ in Eq. 4.25, which yields

$$G(\vec{u}|\vec{u}_0, L) = \exp\left[a\phi_p mAL\left(u_z^2 - \frac{1}{3}\right)\right]\delta(\vec{u} - \vec{u}_0). \tag{4.28}$$

The partition function in this limit is

$$\begin{aligned} q &= 4\pi h^{-1}\exp\left(-\frac{h^2}{3}\right)\int_0^h dx\exp(x^2) \\ &= 2\pi^{3/2}h^{-1}\exp\left(-\frac{h^2}{3}\right)\mathrm{erf}(ih), \end{aligned} \tag{4.29}$$

where $h = \sqrt{a\phi_p mAL}$ and erf is the error function. The order parameter is given by

$$m = \frac{3\pi\exp\left(\frac{2}{3}h^2\right)}{h^2 q} - \frac{3}{4h^2} - \frac{1}{2}. \tag{4.30}$$

The expression for the partition function requires evaluation of the parameter h by solving the self-consistent equation for the order parameter. The rigid rod limit provides an important reference for examining the effects of finite chain flexibility, which we discuss in

Sec. 4.5.

Since the rigid rod limit represents the limit where all eigenfunctions are necessary in the Green's function to properly capture the chain statistics, the opposite limit occurs when only a couple of eigenfunctions need to be included in the Green's function, which we define as the limit of ground-state dominance [20, 44]. This typically occurs for long chain length; however, the behavior of the arguments of C_l^m within Eq. 4.26 in the presence of the nematic interaction alters the criteria for ground-state dominance. Furthermore, the number of eigenfunctions required to capture the chain statistics depends on the field strength; for example, the isotropic state requires only the ground state, whereas it is necessary to include both the ground and first excited states to capture the chain statistics in the limit of strong field strength. Therefore for arbitrary field strength γ, we identify the general criteria for ground-state dominance as

$$\frac{L(\mathcal{E}_2^0 - \mathcal{E}_0^0)}{2\epsilon} \gg 1, \tag{4.31}$$

requiring a large separation between the ground and second excited states. We determine the ground-state dominance criteria analytically for the limit of weak and strong field strength.

As previously stated, the eigenvalues $\mathcal{E}_l^m$ approach $l(l+1)$ as γ goes to zero (weak nematic interaction). In this limit, ground-state dominance occurs when $L/\epsilon \gg 1$. The Green's function is dominated by the first term only, which has a trivial behavior since $Ysp_0^0 \to 1/\sqrt{4\pi}$ in this limit (independent of orientation); the effect of the chain rigidity is only significant when the chain length is comparable in size to the persistence length.

The case of strong nematic interaction ($\gamma \gg 1$) presents a very different scenario. In this limit, adjacent eigenvalues of the spheroidal functions asymptotically approach each

other, i.e. $\mathcal{E}^m_{m+2n+1} \to \mathcal{E}^m_{m+2n}$ $(n = 0, 1, 2, \ldots)$ as $\gamma \to \infty$; therefore, the coefficient of the ground and first excited states asymptotically approach each other in Eq. 4.26 ($C^0_0 \to C^0_1$). We must include both the ground and first excited states in this limit in order to properly capture the chain statistics. Criteria for ground-state dominance (Eq. 4.31) requires a large separation between the nearly degenerate ground states and the next excited state. Using the asymptotic behavior of $\mathcal{E}^m_l$ for $\gamma \gg 1$ [40], this occurs when

$$\frac{L}{2\epsilon}\left[4\gamma^{1/2} - 4 - \frac{7}{2\gamma^{1/2}} + \mathcal{O}(\gamma^{-1})\right] \gg 1. \tag{4.32}$$

Ground-state dominance thus occurs for a combination of long polymer chains and/or large interaction strength. Unlike the case of ground-state dominance for weak interaction, the Green's function in this limit demonstrates very rich physical behavior, which we explore in Sec. 4.5.

Here we provide the asymptotic expressions for the single-chain partition function and the normalized nematic order parameter that appear in the SCF equations in the limit of $\gamma \gg 1$. Keeping all available terms,

$$\begin{aligned} \log q &= \frac{L}{2\epsilon}\left(\frac{2}{3}\gamma - 2\gamma^{1/2} + 1 + \frac{1}{4\gamma^{1/2}} + \frac{1}{4\gamma} + \right. \\ &\qquad \left. \frac{23}{64\gamma^{3/2}} + \frac{41}{64\gamma^2} + \frac{681}{512\gamma^{5/2}} + \mathcal{O}(\gamma^{-3})\right), \qquad (4.33) \\ m &= 1 - \frac{3}{2\gamma^{1/2}} - \frac{3}{16\gamma^{3/2}} - \frac{3}{8\gamma^2} - \frac{207}{256\gamma^{5/2}} - \\ &\qquad \frac{123}{64\gamma^3} - \frac{10215}{2048\gamma^{7/2}} - \mathcal{O}(\gamma^{-4}). \qquad (4.34) \end{aligned}$$

As in the rigid limit, Eq. 4.34 provides a self-consistent equation for solving for the order parameter m, or equivalently the interaction strength γ, which is then used in the expres-

sion for q. We define the single-chain quadrupole (i.e., second Legendre polynomial P_2) fluctuation as

$$\begin{aligned}\Delta_m &= \frac{1}{L^2}\int_0^L d\tau \int_0^L d\tau' \left\langle P_2(\tau)P_2(\tau')\right\rangle - \left(\frac{1}{L}\int_0^L d\tau \left\langle P_2(\tau)\right\rangle\right)^2 \\ &= \frac{9}{4L^2}\left(\frac{\partial^2 \log q}{\partial \kappa^2}\right)_\epsilon , \end{aligned} \tag{4.35}$$

which we make use of in Sec. 4.4. The asymptotic behavior of Δ_m is given by

$$\begin{aligned}\Delta_m &= \frac{9\epsilon}{4L}\left(\frac{1}{\gamma^{3/2}} + \frac{3}{8\gamma^{5/2}} + \frac{1}{\gamma^3} + \frac{345}{128\gamma^{7/2}} + \right. \\ &\qquad \left. \frac{123}{16\gamma^4} + \frac{23835}{1024\gamma^{9/2}} + \mathcal{O}(\gamma^{-5})\right). \end{aligned} \tag{4.36}$$

The asymptotic behavior for q, m, and Δ_m permits the evaluation of the binodal and spinodal curves in the limit defined by Eq. 4.31.

In the flexible chain limit ($\epsilon/L \to 0$), the spheroidal functions become the spherical harmonics; therefore, the use of Eq. 4.26 in the flexible limit provides analytical expressions for chain averages. The flexible limit results in a solution with no orientational order ($m = 0$); however, the quadrupole fluctuation Δ_m has a finite value [21], which is given by

$$\Delta_m = \frac{6\epsilon}{45L}\left\{1 - \frac{\epsilon}{3L}\left[1 - \exp\left(-\frac{3L}{\epsilon}\right)\right]\right\}. \tag{4.37}$$

With this expression, the limit of metastability of the isotropic phase can be calculated using the equations provided in Sec. 4.4.

4.4 Gaussian Fluctuations

Our development of the SCF theory provides a natural framework for incorporating fluctuations. This is accomplished by including fluctuations in the field variables from their saddle-point or SCF values. Of particular interest is the free energy cost for arbitrary density and order parameter fluctuations in the nematic state. Such a free energy yields information on the concentration-concentration, order-parameter-order-parameter, and concentration-order-parameter correlations, as well as the thermodynamic stability of the system. When properly projected, the fluctuation free energy in the nematic state can be used to determine the three Frank elastic constants [45] for the long wavelength bending, splay and twist deformation of the nematic director. This idea has been used in the work of Liu and Fredrickson [21]. However, as alluded to in the introduction, their treatment of the nematic state is through an order-parameter expansion around the isotropic state which makes use of chain statistics in the isotropic state. Not only is the description of the nematic state approximate, but the chain conformation change as described in Sec. 4.5 and its influence on the thermodynamics cannot be properly captured in this perturbative approach. In contrast, our theory will treat fluctuations around the exact saddle point; the chain conformation changes and the attended changes in thermodynamics will be automatically incorporated through the single-chain partition function in the self-consistent field.

We defer the presentation of the general fluctuation theory to a future paper. In this chapter, we restrict our consideration to homogeneous, or zero-wavenumber fluctuations in the density and the magnitude of the order-parameter to illustrate the main idea. The spinodal, or limit of metastability, is determined from the vanishing of the determinant of the quadratic coefficients of the fluctuation free energy.

Starting from our expression for Ξ in terms of the functional integral (Eq. 4.7), we write

the field variables as their saddle-point values plus fluctuations, and expand the exponent in the integrand to quadratic order in the fluctuations. The linear terms vanish identically owing to the saddle-point nature of the expansion. The quadratic fluctuations in the auxilliary fields ΔW_s, ΔW_p and $\Delta\Lambda$ can be easily integrated out to yield a resulting fluctuation free energy in terms of the fluctuation in the physical fields: the density $\Delta\phi_p$ and the order-parameter ΔS. The fluctuation free energy is

$$\begin{aligned}\frac{\beta\Delta G}{V} &= \frac{1}{2}\left(\frac{1}{v(1-\phi_p)}+\frac{1}{LA\phi_p}+\frac{m^2}{LA\phi_p\Delta_m}-2\chi\right)\Delta\phi_p\Delta\phi_p - \\ &\quad \frac{m}{LA\phi_p\Delta_m}\Delta\phi_p\Delta S+\frac{1}{2}\left(\frac{1}{LA\phi_p\Delta_m}-\frac{2a}{3}\right)\Delta S\Delta S \\ &\equiv \frac{C_{\phi\phi}}{2}\Delta\phi_p\Delta\phi_p + C_{\phi S}\Delta\phi_p\Delta S+\frac{C_{SS}}{2}\Delta S\Delta S. \qquad (4.38)\end{aligned}$$

We use Eq. 4.38 to determine the limit of metastability, or spinodal, of a homogeneous phase, either isotropic or nematic. Instability occurs when fluctuations reduce the free energy. In the case of an isotropic phase, the order-parameter and concentration fluctuations are uncoupled; thus the spinodal occurs when either C_{SS} or $C_{\phi\phi}$ is equal to zero, the former corresponding to an instability with respect to the nematic state and the latter corresponding to isotropic-isotropic phase separation. For the nematic case, we see that the modes are coupled in the fluctuation free energy; therefore, instability occurs by a mixture of concentration and order-parameter fluctuations, marked by the vanishing of the determinant of C_{ij} (i,$j = \phi_p$,S).

We note that, perhaps to be expected, the spinodals identified from examining the fluctuation around the saddle point coincide with those determined from the matrix of the second derivatives of the Helmholtz free energy. However, the free energy cost for fluctuations around the saddle point can only be correctly calculated by the fluctuation free

energy described here.

4.5 Results and Discussion

With the self-consistent-field theory, we can address both the phase behavior and the chain statistics at the mean-field level. We first define the set of dimensionless parameters that will be used in the calculations presented in this section. Since the volume of the solvent v enters as a natural volume scale, we define a dimensionless volume of the polymer N by $N = LA/v$, which can be considered an effective degree of polymerization. The Maier-Saupe and Flory-Huggins parameters, both having dimensions of inverse volume, can be similarly made dimensionless by defining $\tilde{a} = av$ and $\tilde{\chi} = \chi v$. A dimensionless persistence length (or bending energy) can be defined by $\tilde{\epsilon} = \epsilon A/v$; thus, $N/\tilde{\epsilon} = L/\epsilon$. In the interest of simplifying notation, we will drop the tilde from these dimensionless parameters.

4.5.1 Phase Behavior

We start with a discussion of the phase behavior of a semiflexible polymer solution. In addition to the coexistence curves between thermodynamically stable phases, we are also interested in determining the various spinodals for the limit of metastable states. Both pieces of information can be obtained from examining the behavior of the grand free energy density (the negative of the osmotic pressure p up to a constant) and the chemical potential μ. A typical plot of these two quantities that shows coexistence and spinodal is given in Fig. 4.1 for a fixed set of parameter values ($N = 20$, $\epsilon = a = 3.7875$, and $\chi = 1.0100$). We now discuss its key features.

In Fig. 4.1, we denote the isotropic branch by the solid line and the nematic branch by the dashed line. For low polymer volume fractions, the osmotic pressure is low and the

chemical potential is large and negative; the system is a dilute isotropic solution. On the scale of the figure this dilute solution behavior is represented by the nearly vertical line. This line intersects the line representing the concentrated isotropic solution ($\phi_p = \partial p/\partial \mu$) at the point indicated by the diamond. This is the coexistence between a polymer-lean isotropic phase ($\phi_p = 0.0030$) and a polymer-rich isotropic phase ($\phi_p = 0.6404$). This transition is caused by the positive (repulsive) Flory-Huggins parameter between the solvent and the polymer and is identical to phase separation of flexible polymer solutions at the mean-field level. The segment between the diamond and the asterisk represents a metastable (supersaturated) polymer-lean solution. The asterisk with $\phi_p = 0.0518$ marks the limit of metastability. Similarly, the segment between the diamond and the pentagram corresponds to a metastable (undersaturated) polymer-rich phase, the limit of metastability occuring at the pentagram with $\phi_p = 0.4779$. The segment between the pentagram and the asterisk corresponds to thermodynamically unstable states; a system having an overall composition in this range will spontaneously phase separate into the thermodynamically stable polymer-rich and polymer-lean phases with their equilibrium compositions.

For overall volume fractions above $\phi_p = 0.6404$, the isotropic branch of the polymer-rich phase crosses the nematic branch at the point indicated by the circle. At this point, the isotropic phase, with a volume fraction of $\phi_p = 0.6966$, is in coexistence with a nematic phase, with a volume fraction of $\phi_p = 0.8082$. The transition from isotropic to nematic is associated with a first order jump in the order parameter from zero to $m = 0.4711$ for the chosen set of parameters. To the right of the circle, the thermodynamically stable state is the nematic phase. However, the isotropic phase can remain metastable for volume fractions up to $\phi_p = 0.8371$ indicated by the square in Fig. 4.1, where the isotropic phase reaches its spinodal with respect to the nematic state. An interesting characteristic of this instability

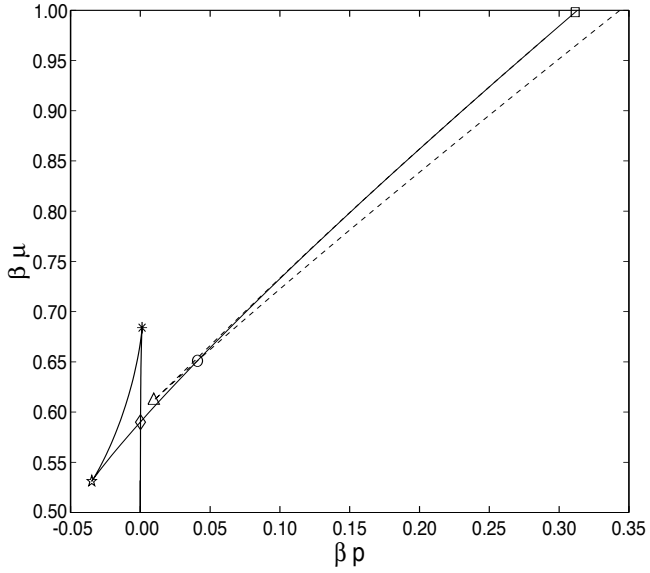

Figure 4.1: The solution for the phase behavior for $N = 20$, $a = \epsilon = 3.7875$, and $\chi = 1.0100$ is indicated in this plot of βp verses $\beta\mu$. The nematic branch (dashed line) approaches the isotropic branch (solid line) as the field strength approaches zero. The point of isotropic-nematic coexistence (circle) occurs when the two branches cross. The points of instability associated with this phase transition occur at the triangle and the square. The point of isotropic-isotropic coexistence (diamond) corresponds to the Flory-Huggins phase transition [34], and the limits of metastability associated with this phase transition are indicated by the asterisk and the pentagram.

is that the volume fraction of the isotropic phase at the spinodal is larger than the volume fraction of the nematic phase at the binodal. Consequently, we expect that the metastable isotropic phase will transition directly into a pure nematic phase rather than phase separate into coexisting isotropic and nematic phases. On the nematic branch, in the direction of decreasing the polymer volume fraction, the nematic state becomes metastable below the coexistence volume fraction, $\phi_p = 0.8082$. The metastable state terminates at the spinodal point of $\phi_p = 0.7589$, indicated by the triangle. As discussed in Sec. IV, the instability of the nematic state is due to a combination of concentration and order-parameter fluctuation.

Performing the analysis discussed above as we vary the parameters of the model allows us to construct the phase diagram in these parameters. The interplay between the isotropic Flory-Huggins interaction and the nematic Maier-Saupe interaction, and the different combinations of the enthalpic and entropic contributions in these parameters, can lead to different types of equilibrium phase diagrams. Phase diagrams of our current system, as well as closely related systems, have been found with similar topology as the diagrams that we present in this section [22, 46, 47]. Assuming a given temperature dependence of the parameters in the model, these phase diagrams can be reproduced more accurately with our current SCF method. However, rather than an exhaustive listing of the types of phase diagrams, we will only discuss three phase diagrams, as examples of the application of our SCF method and to discuss certain issues not emphasized in previous studies.

In the first example, we show a full phase diagram (Fig. 4.2) for a fixed length of polymer chains $N = 20$ over a range of the other parameters ($a = \epsilon = 3.75\chi$). When these parameters are purely energetic in origin, increasing them is equivalent to decreasing the temperature. In general, however, χ and a contain both entropic and enthalpic components; thus varying them with the fixed ratio should be more properly interpreted as specifying

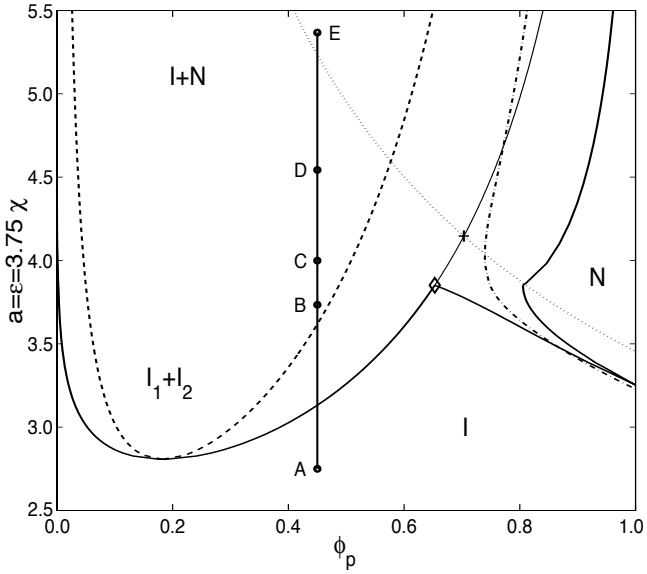

Figure 4.2: A phase diagram for a polymer-solvent system with polymer molecules with degree of polymerization $N = 20$ for parameter values of $a = \epsilon = 3.75\chi$. The solid lines are the binodal coexistence curves. The dashed line is the isotropic spinodal curve due to concentration fluctuations, and the dotted line is the isotropic spinodal curve due to order fluctuations. The dashed-dotted line is the nematic phase spinodal curve, which occurs due to a combination of concentration and order fluctuations. The equilibrium phase behavior is labeled within each region. We label several points of significance that are explained further in the text.

a particular surface in the larger multi-dimensional phase diagram. The features we will discuss are not affected by how these parameters are to be interpreted, but for convenience, we will refer to the increase in these interaction parameters as decreasing the temperature.

The equilibrium coexistence curves for the different phases labeled in Fig. 4.2 are shown by the thick solid lines. As the values of these interaction parameters increase from zero, the first point of significance in Fig. 4.2 is a critical point at $\chi = 0.7486$ and $\phi_p = 0.1829$ indicating the beginning of a two-phase region of the phase diagram where a polymer-lean isotropic phase is in coexistence with a polymer-rich isotropic phase. This point corresponds to the critical point predicted in the Flory-Huggins theory [34], which at the mean-field level is unaffected by the alignment interaction and the bending rigidity. The second point of

interest is the onset of nematic ordering in the solvent-free limit ($\phi_p = 1$), which occurs at $a = \epsilon = 3.2528$ where the order parameter jumps from zero to $m = 0.3488$. When solvent is present, the first-order transition in the order parameter is accompanied by a finite concentration change between the isotropic and nematic phases. The isotropic-isotropic coexistence and the isotropic-nematic coexistence meet at a triple point (indicated by the diamond) for $\chi = 1.0271$ and $a = \epsilon = 3.8515$ where three phases coexist [isotropic 1 ($\phi_p = 0.0024$), isotropic 2 ($\phi_p = 0.6530$), and nematic ($\phi_p = 0.8055$)]. Above the triple point, the thermodynamically preferred phase behavior within the binodal envelope is a polymer-lean isotropic phase in coexistence with a polymer-rich nematic phase.

Of particular interest are the various spinodal lines in the phase diagram. Examination of the location of these spinodals reveals interesting mechanisms for the possible kinetics of the phase changes. Consider, for example, a temperature quench along the vertical bar at $\phi_p = 0.45$ in Fig. 4.2 from the isotropic phase (point A) to a point inside the dashed spinodal. If the quench is to a temperature higher than the triple point (point B), then the system will undergo spinodal decomposition into a polymer-lean isotropic phase and a polymer-rich isotropic phase. However, if the quench is deeper than the triple point, the situation is quite subtle. The reason is that the polymer-rich isotropic branch of the binodal (shown by the thin solid line), though superseded by the nematic branch, never loses its local thermodynamic stability. As long as the concentration of the (isotropic) polymer-rich phase is still below the spinodal with respect to the nematic state shown by the dotted line, it can exist as a metastable state. Thus it is conceivable that for quenches slightly above the triple-point but less than indicated by the cross (point C), the first step in the phase separation is still spinodal decomposition into a polymer-lean isotropic phase and a polymer-rich isotropic phase. The appearance of the nematic phase will take place

inside the polymer-rich phase via nucleation. For quenches beyond the cross (point D), the concentration of the polymer in the polymer-rich phase that results from the spinodal decomposition exceeds the spinodal for appearance of the nematic phase; thus as soon as the system phase separates in concentration, the nematic phase will appear spontaneously in the polymer-rich phase. Finally, for very deep quenches beyond the spinodal with respect to the nematic phase (point E), nematic order will appear directly, driving the phase separation into a polymer-lean isotropic phase and a polymer-rich nematic phase. In practice, the last two phase separation scenarios may not be distinguishable, although the primary driving forces are different.

The spinodals to the right of the triple point similarly have interesting kinetic implications. In particular, part of the spinodal of the isotropic polymer-rich phase with respect to nematic ordering lies within the two-phase coexistence region and part of it lies in the single-phase nematic region. Thus, for example, a quench at say $\phi_p = 0.7$ beyond this spinodal will lead to phase separation into a polymer-lean isotropic phase and a polymer-rich nematic phase, whereas a quench at $\phi_p = 0.9$ will lead to the spontaneous appearance of the nematic order without any phase separation. The kinetic scenario for the latter case is likely the coarsening of nematic domains via non-conserved order parameter dynamics.

The dynamics of spinodal decomposition in a liquid crystal (rodlike)-polymer system [46] is shown to exhibit fibrillar network morphologies in similar scenarios of decomposition as described here. These findings suggest that domain morphology during phase separation is strongly influenced by the quench on the phase diagram as well as the phase separation and ordering kinetics.

As we decrease the Flory-Huggins parameter relative to the Maier-Saupe interaction, the isotropic-isotropic bulge in the phase diagram will shrink, eventually shifting the critical

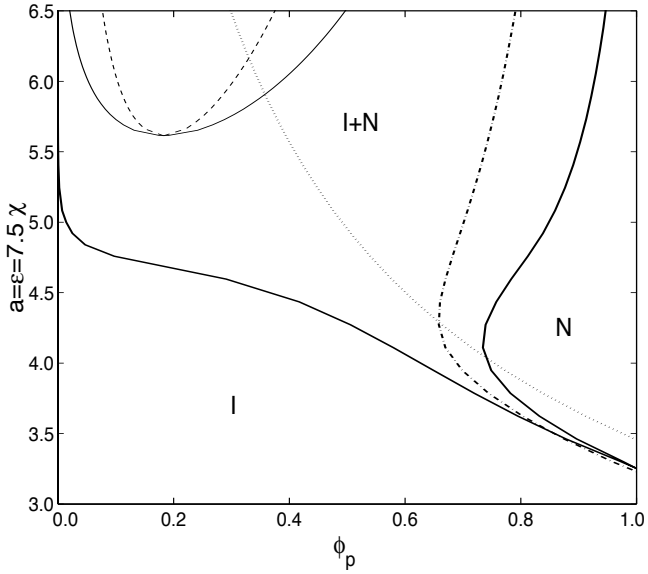

Figure 4.3: A phase diagram for a polymer-solvent system with polymer molecules with degree of polymerization $N = 20$ for parameter values of $a = \epsilon = 7.5\chi$. The solid lines are the binodal coexistence curves. The dashed line is the isotropic spinodal curve due to concentration fluctuations, the dotted line is the isotropic spinodal due to order fluctuations, and the dashed-dotted line is the nematic phase spinodal curve. The equilibrium phase behavior is labeled within each region.

point inside the isotropic-nematic envelope, thus making it a metastable critical point. Fig. 4.3 shows such a phase diagram for a system with $N = 20$ and $a = \epsilon = 7.5\chi$ (similar parameters as for Fig. 4.2 with a reduced χ-parameter). Metastable critical points occur in a number of physical systems. In model colloidal systems, for example, when the coexistence curve between two fluid phases lies within the phase envelope between a dilute fluid phase and a crystalline phase, the presence of the metastable critical point is shown to have a dramatic effect on the nucleation barrier for the formation of the crystalline phase [48, 49]. In the vicinity of the critical point, the free-energy barrier is dramatically decreased, and nucleation rates increase by many orders of magnitude. Critical fluctuation in the colloidal density creates a locally dense fluid pocket which facilitates the formation of the crystalline phase. It has also been suggested that polymer crystallization from the melt can be similarly assisted by the presence of a buried fluid-fluid binodal curve within the fluid-

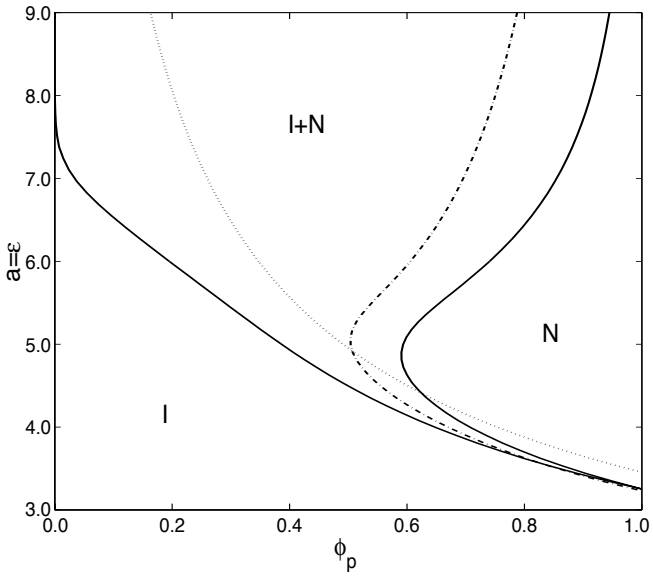

Figure 4.4: A phase diagram for a polymer-solvent system with polymer molecules with degree of polymerization $N = 20$ for parameter values of $a = \epsilon$ and $\chi = 0$. The solid lines are the binodal coexistence curves. The dotted line is the isotropic spinodal curve, and the dashed-dotted line is the nematic phase spinodal curve. The equilibrium phase behavior is labeled within each region.

crystal coexistence envelope, where the nucleation barrier also goes through a minimum at the metastable critical point [50]. The enhancement of crystal nucleation due to the presence of a metastable critical point has important implications in protein and polymer crystallization, where the quality of the final crystalline material is dramatically influenced by the nature of the crystallization process. Because the phase diagram shown in Fig. 4.3 has identical topology to those for the systems just mentioned, we expect phenomenologically similar effects on nucleation of the nematic phase due to the presence of a metastable isotropic-isotropic critical point.

To complete our discussion of the effect of reduced Flory-Huggins parameter on the phase behavior, we show in Fig. 4.4 a phase diagram for the limiting case of $\chi = 0$, keeping other parameters to be the same as in Figs. 4.2 and 4.3. In this case, the isotropic-isotropic coexistence has completely disappeared and the driving force for phase separation is entirely

due to the Maier-Saupe alignment interaction. Nevertheless, the energy gain for chains to locally align with each other creates an effective attraction between the chain segments, leading to a large fractionation in the chain density between the isotropic phase and the nematic phase.

The three phase diagrams presented in this article are essentially snapshots of the full phase diagrams along some particular coordinate in the parameter space. Many other types of phase diagrams are possible. For example, for systems where chain alignment is caused by hard-core repulsion, the isotropic part of the chain-chain interaction is repulsive, leading to a negative χ parameter. The phase diagram that results from this case then resembles that of the Onsager type [51] for the hard rods with a narrow concentration gap between the isotropic and nematic phases.

We end this section on the phase behavior with a brief discussion of the effects of chain rigidity. Depending on the ratio between the persistence length and the contour length, a wormlike chain is broadly categorized into three scaling regimes: flexible when this ratio is small, rigid when this ratio is large, and semiflexible when this ratio is of order unity. An interesting question is to what extent can a wormlike chain with large but finite stiffness be described as an effective rigid rod with regard to the phase behavior. To address this question, we have computed several phase diagrams by varying the chain stiffness while keeping other parameters fixed. Instead of showing more phase diagrams, in this article we focus on the value of the Maier-Saupe parameter a_T at the thermotropic ($\phi_p = 1$) isotropic-nematic transition, which is governed by Eq. 4.21. This information is implicitly included in most theoretical studies on the isotropic-nematic transition in wormlike polymers, but we are not aware of any efforts at explicitly addressing the effect of chain stiffness in reference to the rigid limit.

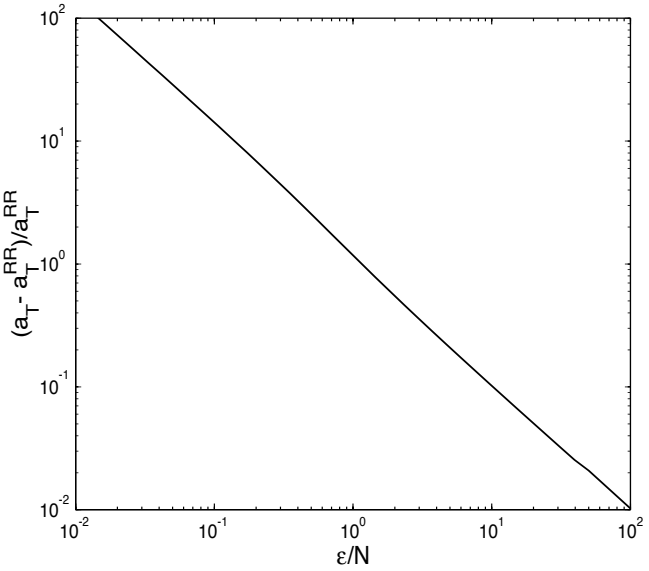

Figure 4.5: The behavior of the Maier-Saupe parameter at the thermotropic transition point a_T relative to the rigid rod value versus the reduced chain rigidity ϵ/N for a chain length of $N = 20$.

Using Eqs. 4.29 and 4.30, we find, for a rigid rod system, the thermotropic isotropic-nematic transition occurs at $a_T^{RR} = 6.8122/N$ (the superscript RR denotes rigid rod) where the order parameter transitions from zero to $m^{RR} = 0.4290$. Since fluctuation from the perfectly straight conformation reduces the degree of orientational order, the onset of nematic order requires a larger Maier-Saupe parameter (or lower temperature) when the bending rigidity is reduced. We plot in Fig. 4.5 the deviation of a_T from a_T^{RR} $[(a_T - a_T^{RR})/a_T^{RR}]$ over a range of bending rigidity for a fixed chain length $N = 20$, found by solving Eq. 4.21. Fig. 4.5 covers the transition behavior over several orders of magnitude of the reduced chain rigidity ϵ/N thus providing data for polymer systems ranging from very flexible to very rigid. Even for relatively rigid polymer chains, the difference from the perfectly rigid rod transition is substantial. For example, when $\epsilon/N \approx 10$, we see the rigid rod prediction for a_T, and thus the isotropic-nematic transition temperature, is inaccurate by approximately 10%. This substantial inaccuracy suggests that the range of validity of the rigid rod approximation is

quite limited, thus demonstrating the need to consider the finite flexibility for predicting the isotropic-nematic transition in experimental systems.

4.5.2 Chain Statistics

In this section, we consider the single-chain conformation and thermodynamic properties in a nematic field. At the self-consistent-field level, the single-chain behavior is described by a wormlike chain in a quadrupole potential field of strength $\kappa = a\phi_p mA$; see Eq. 4.17. Note that since several different combinations of the Maier-Saupe parameter a, the volume fraction of the polymer ϕ_p and the normalized order-parameter m can give the same κ, the single-chain behavior at the SCF level does not correspond to a unique thermodynamic state.

We start with mean-square end-to-end distance tensor given by

$$\langle R_i R_j \rangle = \int_0^L d\tau_1 \int_0^L d\tau_2 \, \langle u_i(\tau_1) u_j(\tau_2) \rangle \,, \tag{4.39}$$

where R_i $(i = 1, 2, 3)$ is the i-th component of the end-to-end vector $\vec{R} \equiv \vec{r}(L) - \vec{r}(0)$ of the polymer and we choose the 3rd direction to be that of the nematic director. Evaluation of Eq. 4.39 is accomplished by calculating the thermal average using the Green's function provided in Sec. 4.3 or, alternatively, using the perturbation partition function method given in Appendix B. Since the perturbation partition function is a generator of arbitrary moments of $\vec{R}$, it can be used to numerically solve for the Green's function that includes the end locations by performing a moment-based expansion [39]; we will not pursue such an effort in this chapter, however.

In the limit of zero field strength κ, the Hamiltonian Eq. 4.17 is invariant under arbitrary rotation of the coordinate frame; therefore, the average end-to-end distance is equivalent

in all three directions, and symmetry dictates that $\langle R_i R_j \rangle = 0$ for $i \neq j$. In this limit, the polymer chain end-to-end behavior is

$$\langle R_i R_j \rangle = \frac{2}{3}\delta_{ij}\left[\epsilon L + \epsilon^2 \exp\left(-\frac{L}{\epsilon}\right) - \epsilon^2\right], \tag{4.40}$$

where δ_{ij} is the Kronecker delta. Eq. 4.40 has the ballistic scaling L^2 for $L/\epsilon \ll 1$ and the diffusive scaling L for $L/\epsilon \gg 1$, signifying the cross-over from a relatively rigid to a relatively flexible polymer chain. The chain statistics identify the persistence length ϵ as an orientation correlation length.

For finite values of the field strength κ, the arbitrary rotational invariance of the Hamiltonian is broken. However, Eq. 4.17 is invariant under rotation about the z axis (3rd direction). The chain statistics for the Hamiltonian results in $\langle R_1^2 \rangle = \langle R_2^2 \rangle \neq \langle R_3^2 \rangle$, and symmetry dictates that $\langle R_i R_j \rangle = 0$ for $i \neq j$. The splitting of the average end-to-end distance in the directions perpendicular (transverse) to the nematic field (1 and 2) from the parallel (longitudinal) direction (3) implies the emergence of two different orientation correlation lengths: the transverse correlation length $\xi_\perp$ and the longitudinal correlation length $\xi_\parallel$. Due to the favorable interaction between the chain tangent vector and the nematic field, we expect $\xi_\parallel > \xi_\perp$.

The average $\langle R_i R_j \rangle$ can be readily evaluated numerically using the eigenfunction expansion of the Green's function. However, ground-state dominance is valid over a wide range of parameter values (criteria discussed in Sec. 4.3) and is useful in predicting the behavior of $\xi_\perp$ and $\xi_\parallel$. Evaluation of $\langle u_i(\tau_1) u_j(\tau_j) \rangle$ is greatly simplified for the case of ground-state

dominance, and we find

$$\xi_{\perp} = \frac{2\epsilon}{\mathcal{E}_1^1 - \mathcal{E}_0^0}, \tag{4.41}$$

$$\xi_{\parallel} = \frac{2\epsilon}{\mathcal{E}_1^0 - \mathcal{E}_0^0}. \tag{4.42}$$

Eqs. 4.41 and 4.42 are valid for arbitrary values of γ (recall $\gamma = 2\epsilon\kappa$) provided that the ground-state dominance conditions are met. It is instructive to consider the asymptotic behaviors for weak and strong nematic interaction. For weak field strength ($\gamma \ll 1$), the correlation lengths in the two directions are $\xi_{\perp} = \xi_{\parallel} = \epsilon$, as expected, since $\mathcal{E}_0^0 = 0$ and $\mathcal{E}_1^1 = \mathcal{E}_1^0 = 2$ at $\gamma = 0$. In the limit of strong nematic interaction ($\gamma \gg 1$), we make use of the asymptotic behavior of $\mathcal{E}_l^m$ [40, 20] and find

$$\xi_{\perp} = \frac{\epsilon}{\gamma^{1/2}\left(1 - \frac{1}{2\gamma^{1/2}} - \mathcal{O}(\gamma^{-1})\right)}, \tag{4.43}$$

$$\xi_{\parallel} = \frac{\epsilon \exp\left(2\gamma^{1/2}\right)}{16\gamma\left(1 - \frac{1}{\gamma^{1/2}} - \mathcal{O}(\gamma^{-1})\right)}. \tag{4.44}$$

The leading-order terms in these asymptotic expressions recover the scaling behavior of these two correlation lengths given in previous studies [30, 31, 32, 33]. Note that the chain deformation in the nematic phase is characterized by an exponential growth of $\xi_{\parallel}$ in the field strength γ and an algebraic decay of $\xi_{\perp}$. The large discrepancy in the chain geometry has been demonstrated experimentally [13], clearly showing the elongation of the chain in the direction of nematic ordering.

In Fig. 4.6, we show the behavior of $\xi_{\perp}$ (solid line) and $\xi_{\parallel}$ (dashed line) versus the field strength γ using the exact solutions given by Eqs. 4.41 and 4.42. In the isotropic phase ($\gamma = 0$), the two correlation lengths are equal, and, as we increase the nematic interaction

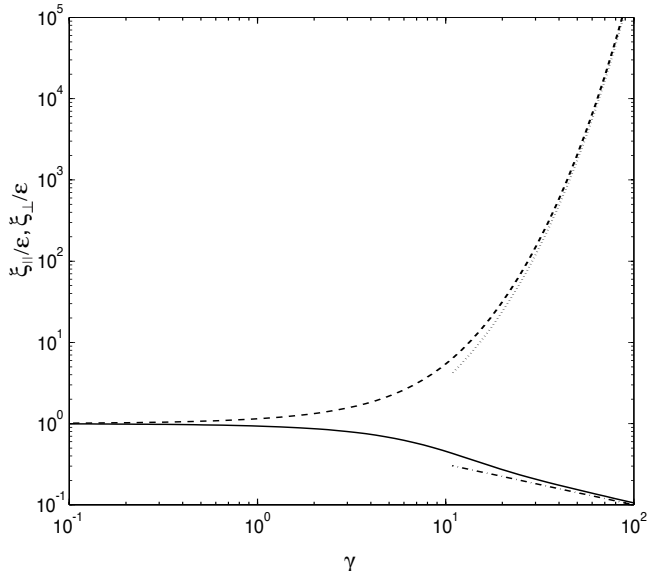

Figure 4.6: The perpendicular correlation length $\xi_\perp/\epsilon$ (solid line) and parallel correlation length $\xi_\parallel/\epsilon$ (dashed line) versus the field strength γ from Eqs. 4.41 and 4.42, respectively. The asymptotic behavior of $\xi_\perp$ (dashed-dotted line) and $\xi_\parallel$ (dotted line), given by the leading-order term in Eqs. 4.43 and 4.44, respectively, are included for large γ.

from zero, the two correlation lengths split. For $\gamma > 10$, we see the correlation lengths rapidly diverge from each other, indicative of the coil-to-stretch transition. The asymptotic behavior given by the leading-order term in Eq. 4.43 (dashed-dotted line) and Eq. 4.44 (dotted line) respectively, are included in Fig. 4.6 for large γ, which converge on our exact solutions near $\gamma = 100$. Fig. 4.6 illustrates the usefulness of our results in capturing the chain statistical behavior in the intermediate-field-strength regime, which is important in describing the chain behavior under experimentally relevant conditions.

Following Ref. [33], we construct a general expression for $\langle u_i(\tau_1)u_j(\tau_2)\rangle$ making use of the correlation lengths $\xi_\perp$ and $\xi_\parallel$ that are consistent with the definition of the order parameter m [33],

$$\begin{aligned}\langle u_i(\tau_1)u_j(\tau_2)\rangle &= \frac{\delta_{ij}-\delta_{i3}\delta_{j3}}{3}(1-m)\exp\left(-\frac{|\tau_1-\tau_2|}{\xi_\perp}\right)+ \\ &\quad \frac{\delta_{i3}\delta_{j3}}{3}(1+2m)\exp\left(-\frac{|\tau_1-\tau_2|}{\xi_\parallel}\right). \qquad (4.45)\end{aligned}$$

We comment that while this expression recovers the exact known result in the isotropic state, it is only valid for sufficiently long chain or large field strength in the nematic state. The reason is that in the nematic state the end portions of the chain behave differently from the mid portion; the difference becomes insignificant only in the long chain or large field strength limit. Mathematically this limit is equivalent to the ground-state dominance condition discussed in Sec. 4.3. Combining the ground-state dominance criterion (Eq. 4.31) with the general expression for the correlation length in the perpendicular direction Eq. 4.43, we find that the condition becomes simply $L \gg \xi_\perp$ [52]. Using Eq. 4.45 in Eq. 4.39 and noting the condition $L \gg \xi_\perp$, we obtain

$$\begin{aligned} \langle R_i R_j \rangle &= \frac{2}{3}(\delta_{ij} - \delta_{i3}\delta_{j3})(1-m)\xi_\perp L + \\ &\quad \frac{1}{3}\delta_{i3}\delta_{j3}(1+2m)\left\{2\xi_\parallel L - 2\xi_\parallel^2\left[1 - \exp\left(-\frac{L}{\xi_\parallel}\right)\right]\right\}, \end{aligned} \tag{4.46}$$

The behavior of $\langle R_3^2 \rangle$ (parallel direction) shows a scaling cross-over from L^2 to L at $L \sim \xi_\parallel$ caused by the emergence of hairpin defects in the chain conformation; thus the correlation length $\xi_\parallel$ can be identified as the average length between hairpin defects for a polymer chain in a uniform nematic phase.

In Fig. 4.7, we show the behavior of the mean square end-to-end distance (Eq. 4.39) for a range of chain lengths at a fixed value of $\epsilon = \kappa = 3$, which is consistent with the order of magnitude of the parameters in Figs. 4.2, 4.3, and 4.4. The plot shows $\langle R_3^2 \rangle$ (solid line) and $\langle R_1^2 \rangle$ (dashed line) together with the isotropic solution (dotted line) (Eq. 4.40) as a function of the non-dimensionalized chain length N (recall $N = LA/v$, where A is the cross-section area of the chain and v is the volume of a solvent molecule). Fig. 4.7 shows three distinct regimes. For very short chains ($L < \xi_\perp$), the mean square end-to-end

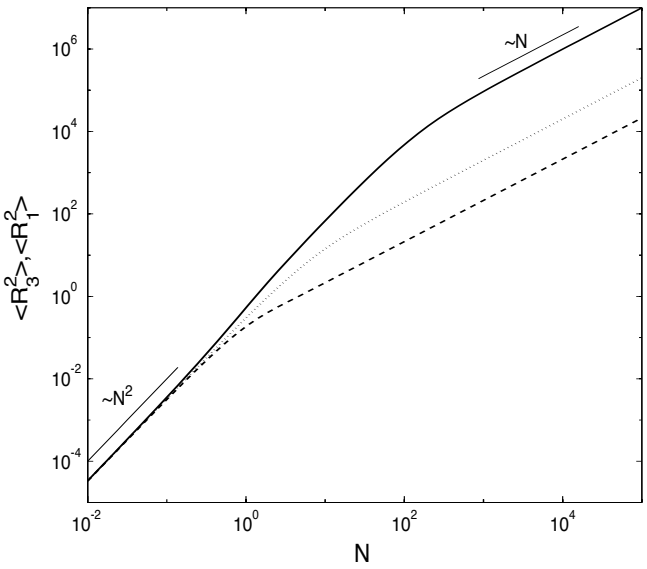

Figure 4.7: The mean square end-to-end distance in the nematic and the perpendicular directions versus the chain length for fixed $\epsilon = \kappa = 3$. The top figure shows $\langle R_3^2 \rangle$ (solid line) and $\langle R_1^2 \rangle$ (dashed line) plotted with the isotropic solution (dotted line) given by Eq. 4.40, with appropriate scalings included.

distances in the transverse (1st) and longitudinal (3rd) directions are equal to the mean-square end-to-end distance in the isotropic phase and exhibit the ballistic N^2 scaling. For longer chains ($\xi_\perp < L < \xi_\parallel$), we see the separation between the end-to-end distances in the transverse and longitudinal directions due to the presence of nematic order. The chain conformation is essentially aligned in the nematic direction with small excursions in the transverse directions thus resulting in the ballistic scaling N^2 in the longitudinal direction and the diffusive scaling N in the transverse direction in this intermediate regime. In the final regime ($N > \xi_\parallel$), the end-to-end distance in the parallel direction now also scales as N due to the introduction of hairpin turns in the conformation that can be located anywhere along the chain with nearly equal probability.

Next we discuss the effect of the nematic interaction on the single-chain energetics. We define the free energy of a single chain $f_{SC} = -\log[q/(4\pi)]$ relative to the isotropic phase in units of $k_B T$. There are two energy contributions to the free energy, the bending energy,

E_{SC}^{bend}, and the energy due to alignment by the nematic field, E_{SC}^{align}, which can be obtained from

$$E_{SC}^{bend} = -\epsilon \left(\frac{\partial \log q}{\partial \epsilon} \right)_{\kappa}, \tag{4.47}$$

$$E_{SC}^{align} = -\kappa \left(\frac{\partial \log q}{\partial \kappa} \right)_{\epsilon}. \tag{4.48}$$

The single chain entropy s_{SC}, in units of k_B, is calculated using the definition of the free energy $f_{SC} = E_{SC}^{bend} + E_{SC}^{align} - s_{SC}$. Since these thermodynamic quantities are relative to the isotropic phase, they all approach zero in the limit of $\kappa \to 0$.

Upon increasing κ from zero, all these thermodynamic quantities decrease: E_{SC}^{align} obviously decreases as can be seen directly from the second term in the effective single-chain Hamiltonian Eq. 4.17. The increased degree of alignment suppresses the thermal wrinkles in the chain conformation, which reduces the bending energy E_{SC}^{bend}. The entropy s_{SC} is similarly reduced because of the reduction in the effective number of degrees of freedom associated with the thermal wrinkles. And finally, thermodynamic stability dictates the free energy f_{SC} must decrease as the alignment field strength increases.

In the limit of weak field strength κ, the partition function can be expanded in powers of κ. This is equivalent to a perturbation expansion around the isotropic state. Because of the rotational symmetry, the linear terms in the field κ vanish identically. Thus, the thermodynamic quantities all scale as κ^2 as the leading correction in the weak field limit.

In the limit of strong field strength κ, we can find the asymptotic behavior of the thermodynamic quantities using ground-state dominance of the partition function q (Eq. 4.33), which is good for parameters satisfying Eq. 4.31. The limiting behavior of the free energy and the alignment energy is $f_{SC} = E_{SC}^{align} = -2L\kappa/3 + \mathcal{O}(\kappa^{1/2})$, and the bending energy

and entropy approach $s_{SC} = 2E_{SC}^{bend} = -L\sqrt{2\kappa/\epsilon} + \mathcal{O}(\kappa^0)$ as $\kappa \to \infty$. Thus the free energy is dominated by the alignment energy and the relationship between the entropy and the bending energy is a manifestation of the equipartition theorem for the small transverse fluctuation of a nearly straight chain. In this strong field limit, it is more instructive to define changes in the thermodynamic quantities relative to the infinite field (perfectly aligned) state. Using the ground-state equations in Sec. 4.3 and the limiting behavior of $\xi_\perp$ (Eq. 4.43), we find

$$\frac{\Delta f_{SC}}{f_{SC}} \sim \frac{\Delta E_{SC}^{align}}{E_{SC}^{align}} \sim \frac{\Delta E_{SC}^{bend}}{E_{SC}^{bend}} \sim \frac{\Delta s_{SC}}{s_{SC}} \sim \frac{\xi_\perp}{\epsilon}, \tag{4.49}$$

where $\Delta f_{SC} = f_{SC} - f_{SC}(\kappa \to \infty)$ (similarly for the other quantities). Thus in the strong field limit, the relative change in the thermodynamic quantities with reference to the perfectly aligned state scales as the ratio of the transverse correlation length to the natural persistence length of the chain. This scaling reflects the importance of the small amplitude fluctuations in the transverse directions for the single-chain thermodynamics in this limit. Since the longitudinal correlation length $\xi_\parallel$ does not appear at the leading order, hairpin defects do not play a significant role in the thermodynamic quantities, even though they play a key role in determining the chain size. The reason is that in the strong field limit, $\xi_\parallel$ is exponentially larger than $\xi_\perp$ (see Eqs. 4.43 and 4.44), and hence the number of active degrees of freedom associated with the hairpin defects is exponentially small compared to the degrees of freedom due to the local transverse fluctuations.

In Fig. 4.8, we show the behavior of the single-chain free energy (solid line), the bending energy (dashed-dotted line), the alignment energy (dashed line), and the entropy (dotted line) over a range of the field strength κ for a fixed chain length $N = 20$ and persistence

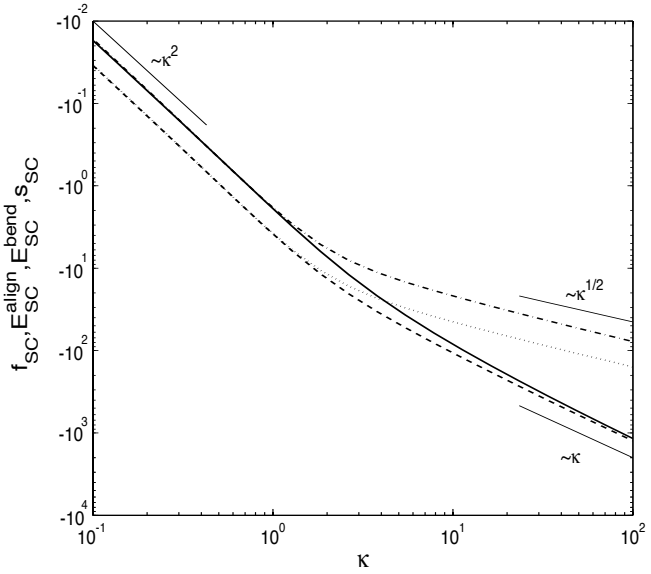

Figure 4.8: The behavior of the Free Energy f_{SC}(solid line), the bending energy E_{SC}^{bend}(dashed-dotted line), the alignment energy E_{SC}^{align}(dashed line), and the entropy (dotted line) of a single chain relative to the isotropic state as a function of the field strength κ for a fixed value of $N = 20$ and $\epsilon = 3$. Appropriate scalings in κ are included.

length $\epsilon = 3$. The indicated scalings for large field strength κ are consistent with the limiting behaviors just described. The scaling cross-over evident in Fig. 4.8 is due to the freezing of the small amplitude conformation fluctuations that occurs as $\xi_\perp/\epsilon \to 0$. The crossover occurs at $\xi_\perp/\epsilon \sim 1$ or equivalently $\gamma \sim 1$.

4.6 Summary and Conclusions

In this chapter, we have studied the liquid crystalline polymer solution behavior by using a systematic self-consistent-field approach that simultaneously describes the solution thermodynamics and the single-chain statistical properties. The set of SCF equations are derived by using a field-theoretical approach and emerge as the lowest order approximation to the exact solution. The SCF theory reduces the many-chain problem to a single-chain in a self-consistent quadrupole field, which is then solved exactly using spheroidal functions.

As applications of the SCF theory, we have examined the phase behavior of the liquid-

crystalline polymer solutions and calculated the single-chain conformation and thermodynamic properties in the nematic state. The interplay between the isotropic Flory-Huggins and anisotropic Maier-Saupe part of the two-body interaction leads to a variety of interesting phase diagrams. Analysis of the various spinodal curves in the phase diagram suggests rich and complex phase transition kinetics. For systems with sufficiently strong Flory-Huggins repulsive interactions between the polymer and the solvent, we point out several interesting situations where phase transition kinetics evolves along a multiple-step path that involves changes in the primary thermodynamic driving forces due to the coupling between concentration and nematic order. For example, for temperature quenches into certain part of the phase diagram we predict spinodal decomposition dynamics leading to isotropic-isotropic phase separation followed by subsequent nucleation of the nematic phase from the polymer-rich isotropic phase. When the polymer-solvent interaction is reduced, the critical point for isotropic-isotropic transition shifts inside the isotropic-nematic coexistence envelope thus becoming a metastable critical point. Just as in previous studies on colloidal systems and polymer crystallization with similar phase diagrams where it has been shown that the metastable critical point dramatically facilitates the formation of the crystalline phase near it, so here too we expect that the nucleation barrier for a liquid crystalline phase near a metastable critical point will be significantly reduced. By a comparison with the rigid-rod system. we find that chain flexibility significantly reduces the degree of nematic order even for quite stiff chains.

The single-chain statistics in the nematic state at the mean-field level is shown to be governed by only the natural persistence length of the polymer ϵ and a dimensionless nematic field strength $\gamma = 2\epsilon a \phi_p m A$ where a is the strength of the Maier-Saupe interaction, ϕ_p the volume fraction of the polymer, m a normalized nematic order parameter, and A the cross-

section area of the chain. Thus a given γ can correspond to multiple thermodynamic states of the polymer solution. The presence of a nematic field leads to the appearance of two length scales, a correlation length parallel to the nematic direction $\xi_{\|}$ and a correlation length perpendicular to the nematic direction $\xi_{\perp}$. Using ground-state dominance valid for sufficiently long chains, we provide exact results for these length scales that are valid for arbitrary field strengths and that reduce to the known results in the large field limit. In the strong field limit, these length scales correspond respectively to the average distance between hairpins and the persistence length for the fluctuation of the director in the transverse directions. Interestingly, we find that whereas hairpins play a critical role in determining the chain dimensions in the nematic state, it is the transverse fluctuations that dominate the single-chain thermodynamic properties in the strong field limit.

A major advantage of our approach is the systematicness with which mean-field theory is derived and the exact treatment of the chain statistics at the mean-field level. Our development of the self-consistent-field theory provides a natural framework for incorporating fluctuations, with the mean-field thermodynamic and single-chain properties calculated here serving as the essential input. In particular, the exact treatment of the chain statistics in the nematic state allows a non-perturbative treatment of the coupling between concentration and nematic order in the nematic phase. We have provided a cursory outline of the structure of the fluctuation theory for zero wave-number or homogeneous concentration and order parameter fluctuations and used this theory to determine the limit of metastability of the various phases. In a future publication, we will present the full fluctuation theory; such a theory will provide a non-perturbative, first-principles approach for computing the Frank elastic constants of a nematic polymer solution.

Appendix A: Spheroidal Functions

We have chosen to calculate the spheroidal functions by expanding them in terms of the more familiar spherical harmonics [53]. Application of recursive relations to the spherical harmonics results in

$$\cos\theta Y_l^m = A_l^{(+)m} Y_{l+1}^m + A_l^{(-)m} Y_{l-1}^m, \tag{A-1}$$

where the coefficients are given by

$$A_l^{(+)m} = \left[\frac{(l-m+1)(l+m+1)}{(2l+1)(2l+3)}\right]^{1/2}, \tag{A-2}$$

$$A_l^{(-)m} = \left[\frac{(l-m)(l+m)}{(2l-1)(2l+1)}\right]^{1/2}. \tag{A-3}$$

The Hamiltonian matrix for our eigenvalue problem is given by

$$\begin{aligned}\left\langle Y_{l'}^{m'} | \mathcal{H} Y_l^m \right\rangle &= l(l+1)\delta_{l,l'}\delta_{m,m'} - \\ &\gamma\left[\left(A_l^{(+)m} A_{l+1}^{(-)m} + A_l^{(-)m} A_{l-1}^{(+)m}\right)\delta_{l,l'} + \right. \\ &\left. A_l^{(+)m} A_{l+1}^{(+)m}\delta_{l+2,l'} + A_l^{(-)m} A_{l-1}^{(-)m}\delta_{l-2,l'}\right]\delta_{m,m'},\end{aligned} \tag{A-4}$$

and the spheroidal functions are found by inversion of the Hamiltonian matrix, which is written in expansion form as

$$Ysp_l^m = \sum_{n=0}^{\infty} a_{l,n}^{|m|} Y_n^m. \tag{A-5}$$

We note within the expansion that evaluation of $\cos^2\theta Y_l^m$ results in spherical harmonics with the l index raised and lowered by 2 and the m index unaffected, thus the expansion of the spheroidal functions into spherical harmonics does not require a summation over an m index. Furthermore, the summation over n in the expansion only requires the same parity

functions to show up, meaning that for odd l, the summation need only include odd n, and for even l, the summation need only include even n.

The spherical harmonics are an orthonormal basis set of the form

$$\int d\vec{u} Y_l^m Y_{l'}^{m'*} = \delta_{l,l'}\delta_{m,m'}; \tag{A-6}$$

furthermore, the complex conjugate of a spherical harmonic satisfies

$$Y_l^{m*} = (-1)^m Y_l^{-m}, \tag{A-7}$$

thus the spheroidal functions and their coefficients satisfy

$$Ysp_l^{m*} = (-1)^m Ysp_l^{-m}, \tag{A-8}$$

$$\sum_{n=0}^{\infty} a_{l,n}^{|m|} a_{l',n}^{|m|*} = \delta_{l,l'}. \tag{A-9}$$

The numerical evaluation of the expansion coefficients requires truncation of the summation to a finite number of functions; however, as the ratio $L/(2\epsilon)$ grows large, only the first couple of eigenfunctions are necessary to accurately calculate the chain statistics. We have found agreement of the eigenvalues of the spheroidal functions given in current literature [41] when we sum the spherical harmonics up to an l-index of 150 for modest values of γ.

Numerical evaluation of the spheroidal functions allows for the evaluation of

$$q = 4\pi \sum_{l=0}^{\infty} C_l^0(L) |a_{l,0}^0|^2, \tag{A-10}$$

$$m = \frac{3}{2L} \left(\frac{\partial \log q}{\partial \kappa} \right)_{\epsilon}, \tag{A-11}$$

where $\kappa = a\phi_p mA$. In addition to the evaluation of the equilibrium potentials, knowledge of the chain statistics allows us to evaluate averages within the nematic phase [20].

Appendix B: Perturbation Partition Function

An average quantity can be evaluated by integrating over all values of the quantity times the probability, which, depending on the complexity of the average, is quite difficult to perform numerically. For example, the average end-to-end distance in the z-direction squared requires the evaluation of $\langle \cos\theta(\tau)\cos\theta(\tau')\rangle$, which contains three Green's functions in the integration: $G(\vec{u}_f|\vec{u}(\tau), L-\tau)$, $G(\vec{u}(\tau)|\vec{u}(\tau'), \tau-\tau')$, and $G(\vec{u}(\tau')|\vec{u}_0, \tau')$. After some simplifications, the quantity $\langle \cos\theta(\tau)\cos\theta(\tau')\rangle$ contains five summations in the numerical summation, which is extremely time consuming to calculate accurately. This is a very simple average in comparison to the averages that are necessary to account for density and order fluctuations in the free energy [21].

Since we have already approximated the partition function by expanding the spheroidal functions in the spherical harmonics, we can calculate the partition function by adding a perturbation term to the Hamiltonian, thus rendering a partition function that acts as a generating function of the averages of interest. Specifically, we calculate the partition function for the Hamiltonian

$$\beta\mathcal{H}_\Delta = \beta\mathcal{H}_0 - \vec{\Delta}\cdot\int_0^L d\tau\vec{u}(\tau), \tag{B-1}$$

which has chain statistics that satisfy

$$\left[\frac{\partial}{\partial L} - \frac{1}{2\epsilon}\nabla_u^2 - a\phi_p mA\left(u_z u_z - \frac{1}{3}\right) - \vec{\Delta}\cdot\vec{u}\right] G(\vec{u}|\vec{u}_0, L) = \delta(L)\delta(\vec{u}-\vec{u}_0). \tag{B-2}$$

Formulating the solution identically to the solution of the spheroidal functions, the eigenfunctions of this equation are expanded in terms of the spherical harmonics. Application of recurrence relations to the spherical harmonics [53] results in

$$e^{i\phi}\sin\theta Y_l^m = -B_l^{(+)m}Y_{l+1}^{m+1} + B_l^{(-)m}Y_{l-1}^{m+1}, \tag{B-3}$$

$$e^{-i\phi}\sin\theta Y_l^m = B_l^{(+)-m}Y_{l+1}^{m-1} - B_l^{(-)-m}Y_{l-1}^{m-1}, \tag{B-4}$$

where the coefficients are given by

$$B_l^{(+)m} = \left[\frac{(l+m+1)(l+m+2)}{(2l+1)(2l+3)}\right]^{1/2}, \tag{B-5}$$

$$B_l^{(-)m} = \left[\frac{(l-m)(l-m-1)}{(2l-1)(2l+1)}\right]^{1/2}. \tag{B-6}$$

The resulting Hamiltonian matrix for our eigenvalue problem is

$$\begin{aligned}
&\left\langle Y_{l'}^{m'}|\mathcal{H}Y_l^m\right\rangle = l(l+1)\delta_{l,l'}\delta_{m,m'} - \\
&\gamma\left[\left(A_l^{(+)m}A_{l+1}^{(-)m} + A_l^{(-)m}A_{l-1}^{(+)m}\right)\delta_{l,l'} + \right. \\
&\left. A_l^{(+)m}A_{l+1}^{(+)m}\delta_{l+2,l'} + A_l^{(-)m}A_{l-1}^{(-)m}\delta_{l-2,l'}\right]\delta_{m,m'} \\
&+\frac{\Delta_x}{2}\left(B_l^{(+)m}\delta_{l+1,l'} - B_l^{(-)m}\delta_{l-1,l'}\right)\delta_{m+1,m'} \\
&-\frac{\Delta_x}{2}\left(B_l^{(+)-m}\delta_{l+1,l'} - B_l^{(-)-m}\delta_{l-1,l'}\right)\delta_{m-1,m'} \\
&+\frac{\Delta_y}{2i}\left(B_l^{(+)m}\delta_{l+1,l'} - B_l^{(-)m}\delta_{l-1,l'}\right)\delta_{m+1,m'} \\
&+\frac{\Delta_y}{2i}\left(B_l^{(+)-m}\delta_{l+1,l'} - B_l^{(-)-m}\delta_{l-1,l'}\right)\delta_{m-1,m'} \\
&-\Delta_z\left(A_l^{(+)m}\delta_{l+1,l'} + A_l^{(-)m}\delta_{l-1,l'}\right)\delta_{m,m'}.
\end{aligned} \tag{B-7}$$

Solving the eigenvalue problem, we expand the Green's function in terms of these new

eigenfunctions, which can be integrated over the end orientations to yield the partition function q_{Δ}. Taking derivatives with respect to the perturbation field strength $\vec{\Delta}$ generates end-to-end averages, which we perform numerically.

Bibliography

[1] A. A. Collyer. *Liquid Crystal Polymers: From Structures to Applications.* Elsevier Science Publishers Ltd., 1992.

[2] W. J. Zhou, J. A. Kornfield, V. M. Ugaz, W. R. Burghardt, D. R. Link, and N. A. Clark. Dynamics and shear orientation behavior of a main-chain thermotropic liquid crystalline polymer. *Macromolecules*, 32(17):5581–5593, 1999.

[3] N. Vaish, D. K. Cinader, W. R. Burghardt, W. Zhou, and J. A. Kornfield. Molecular orientation in quenched channel flow of a flow aligning main chain thermotropic liquid crystalline polymer. *Polymer*, 42(26):10147–10153, 2001.

[4] V. M. Ugaz, W. R. Burghardt, W. J. Zhou, and J. A. Kornfield. Transient molecular orientation and rheology in flow aligning thermotropic liquid crystalline polymers. *J. Rheol.*, 45(5):1029–1063, 2001.

[5] T. A. Ezquerra, E. López-Cabarcos, B. S. Hsiao, and F. J. Baltà-Calleja. Precursors of crystallization via density fluctuations in stiff-chain polymers. *Phys. Rev. E*, 54(1):989–992, 1996.

[6] K. Hongladarom, V. M. Ugaz, D. K. Cinader, W. R. Burghardt, J. P. Quintana, B. S. Hsiao, M. D. Dadmun, W. A. Hamilton, and P. D. Butler. Birefringence, X-ray scattering, and neutron scattering measurements of molecular orientation in sheared liquid crystal polymer solutions. *Macromolecules*, 29(16):5346–5355, 1996.

[7] A. Kagemoto, M. Nakazaki, S. Kimura, Y. Momohara, K. Ueno, and Y. Baba. Calorimetric investigation on liquid crystals of deoxyribonucleic acid in concentrated solutions. *Thermochim. Acta*, 284(2):309–324, 1996.

[8] Y. M. Evdokimov, T. V. Nasedkina, V. I. Salyanov, and N. S. Badaev. Transformation of genomic-size DNA from isotropic into liquid- crystalline state. *Mol. Biol.*, 30(2):219–225, 1996.

[9] S. G. Skuridin, A. T. Dembo, V. S. Efimov, and Y. M. Evdokimov. Liquid-crystal phases of DNA complexes with synthetic polycations. *Dokl. Akad. Nauk*, 365(3):400–402, 1999.

[10] J. L. Sikorav, J. Pelta, and F. Livolant. A liquid-crystalline phase in spermidine-condensed DNA. *Biophys. J.*, 67(4):1387–1392, 1994.

[11] S. S. Zakharova, W. Jesse, C. Backendorf, and J. R. C. van der Maarel. Liquid crystal formation in supercoiled DNA solutions. *Biophys. J.*, 83(2):1119–1129, 2002.

[12] P. G. de Gennes. in *Polymer Liquid Crystals*, ed. by A. Ciferri, W. R. Krigbaum, R. B. Meyer. Academic, New York, 1982.

[13] M. H. Li, A. Brûlet, P. Davidson, P. Keller, and J. P. Cotton. Observation of hairpin defects in a nematic main-chain polyester. *Phys. Rev. Lett.*, 70(15):2297–2300, 1993.

[14] M. Warner, J. M. F. Gunn, and A. B. Baumgartner. Rod to coil transitions in nematic polymers. *J. Phys. A-Math. Gen.*, 18(15):3007–3026, 1985.

[15] J. V. Selinger and R. F. Bruinsma. Statistical-mechanics of defects in polymer liquid-crystals. *J. Phys. II*, 2(5):1215–1236, 1992.

[16] H. Fischer, A. Keller, and A. H. Windle. The origin of banded textures induced by shear - a suggested scheme and a relevant rheological effect. *J. Non-Newton. Fluid*, 67:241–268, 1996.

[17] O. Kratky and G. Porod. Rontgenuntersuchung geloster fadenmolekule. *Recl. Trav. Chim. Pay. B.*, 68(12):1106–1122, 1949.

[18] W. Maier and A. Saupe. Eine einfache molekulare theorie des nematischen kristallinflussigen zustandes. *Z. Naturforsch. Pt. A*, 13(7):564–566, 1958.

[19] W. Maier and A. Saupe. Eine einfache molekular-statistische theorie der nematischen kristallinflussigen phase .1. *Z. Naturforsch. Pt. A*, 14(10):882–889, 1959.

[20] X. J. Wang and M. Warner. Theory of nematic backbone polymer phases and conformations. *J. Phys. A-Math. Gen.*, 19(11):2215–2227, 1986.

[21] A. J. Liu and G. H. Fredrickson. Free-energy functionals for semiflexible polymer-solutions and blends. *Macromolecules*, 26(11):2817–2824, 1993.

[22] S. Lee, A. G. Oertli, M. A. Gannon, A. J. Liu, D. S. Pearson, H. W. Schmidt, and G. H. Fredrickson. Phase-behavior of liquid-crystalline polymer model-compound mixtures - theory and experiment. *Macromolecules*, 27(14):3955–3962, 1994.

[23] B. Y. Drovetsky, A. J. Liu, and C. H. Mak. Nematic-isotropic interfaces in semiflexible polymer blends. *J. Chem. Phys.*, 111(9):4334–4342, 1999.

[24] A. M. Gupta and S. F. Edwards. Mean-field theory of phase-transitions in liquid-crystalline polymers. *J. Chem. Phys.*, 98(2):1588–1596, 1993.

[25] G. A. Carri and M. Muthukumar. Configurations of liquid crystalline polymers in nematic solvents. *J. Chem. Phys.*, 109(24):11117–11128, 1998.

[26] S. R. Zhao, C. P. Sun, and W. X. Zhang. Statistics of wormlike chains .1. properties of a single chain. *J. Chem. Phys.*, 106(6):2520–2529, 1997.

[27] W. X. Zhang, S. R. Zhao, and C. P. Sun. Statistics of wormlike chains .2. phase transition of polymer liquid crystals and its mixture with low molecular weight liquid crystals. *J. Chem. Phys.*, 106(6):2530–2540, 1997.

[28] M. Pasquali, V. Shankar, and D. C. Morse. Viscoelasticity of dilute solutions of semiflexible polymers. *Phys. Rev. E*, 6402(2):020802, 2001.

[29] V. Shankar, M. Pasquali, and D. C. Morse. Theory of linear viscoelasticity of semiflexible rods in dilute solution. *J. Rheol.*, 46(5):1111–1154, 2002.

[30] T. Odijk. Theory of lyotropic polymer liquid-crystals. *Macromolecules*, 19(9):2314–2329, 1986.

[31] G. J. Vroege and T. Odijk. Induced chain rigidity, splay modulus, and other properties of nematic polymer liquid-crystals. *Macromolecules*, 21(9):2848–2858, 1988.

[32] T. Odijk. DNA in a liquid-crystalline environment: Tight bends, rings, supercoils. *J. Chem. Phys.*, 105(3):1270–1286, 1996.

[33] A. Tkachenko and Y. Rabin. Coupling between thermodynamics and conformations in wormlike polymer nematics. *Macromolecules*, 28(25):8646–8656, 1995.

[34] P. J. Flory. *Principles of Polymer Chemistry.* Cornell University Press, Ithaca, 1953.

[35] N. Schuld and B. A. Wolf. Solvent quality as reflected in concentration- and temperature- dependent Flory-Huggins interaction parameters. *J. Polym. Sci. Pol. Phys.*, 39(6):651–662, 2001.

[36] R. P. Feynman and A. R. Hibbs. *Quantum Mechanics and Path Integrals.* McGraw-Hill, 1965.

[37] G. H. Fredrickson, V. Ganesan, and F. Drolet. Field-theoretic computer simulation methods for polymers and complex fluids. *Macromolecules*, 35(1):16–39, 2002.

[38] M. W. Matsen. The standard Gaussian model for block copolymer melts. *J. Phys.-Condens. Mat.*, 14(2):R21–R47, 2002.

[39] H. Yamakawa. *Helical Wormlike Chains in Polymer Solutions.* Springer-Verlag, 1997.

[40] J. Meixner and F. M. Schäfke. *Mathieusche Funktionen und Sphäroidfunktionen.* Springer, 1954.

[41] L.-W. Li, M.-S. Leong, T. S. Yeo, P. S. Kooi, and K. Y. Tan. Computations of spheroidal harmonics with complex arguments: A review with an algorithm. *Phys. Rev. E*, 58(5):6792–6806, 1998.

[42] L.-W. Li, X.-S. Kang, and M.-S. Leong. *Spheroidal Wave Functions in Electromagnetic Theory.* John Wiley & Sons, Inc., New York, 2002.

[43] W. H. Press and B. P. Flannery. *Numerical Recipes.* Cambridge University Press, 1989.

[44] D. C. Morse and G. H. Fredrickson. Semiflexible polymers near interfaces. *Phys. Rev. Lett.*, 73(24):3235–3238, 1994.

[45] P. G. de Gennes and J. Prost. *The Physics of Liquid Crystals.* Clarendon Press, 1993.

[46] A. M. Lapeña, S. C. Glotzer, S. A. Langer, and A. J. Liu. Effect of ordering on spinodal decomposition of liquid- crystal/polymer mixtures. *Phys. Rev. E*, 60(1):R29–R32, 1999.

[47] J. T. Kindt and W. M. Gelbart. Chain self-assembly and phase transitions in semiflexible polymer systems. *J. Chem. Phys.*, 114(3):1432–1439, 2001.

[48] P. R. ten Wolde and D. Frenkel. Enhancement of protein crystal nucleation by critical density fluctuations. *Science*, 277(5334):1975–1978, 1997.

[49] V. Talanquer and D. W. Oxtoby. Crystal nucleation in the presence of a metastable critical point. *J. Chem. Phys.*, 109(1):223–227, 1998.

[50] P. D. Olmsted, W. C. K. Poon, T. C. B. McLeish, N. J. Terrill, and A. J. Ryan. Spinodal-assisted crystallization in polymer melts. *Phys. Rev. Lett.*, 81(2):373–376, 1998.

[51] L. Onsager. The effects of shape on the interaction of colloidal particles. *Ann. N. Y. Acad. Sci.*, 51(4):627–659, 1949.

[52] Inserting Eq. 4.43 into Eq. 4.31, we find an additional factor of $(\mathcal{E}_2^0 - \mathcal{E}_0^0)/(\mathcal{E}_1^1 - \mathcal{E}_0^0)$ in the criteria for ground-state dominance; however, this factor is of order 1 for all values of γ and does not alter the criteria.

[53] G. B. Arfken and H. J. Weber. *Mathematical Methods for Physicists*. Academic Press, 4 edition, 1995.

Chapter 5

Free Expansion of Elastic Filaments

The dynamics of an elastic polymer filament undergoing contour length expansion is studied using computer simulation. The expansion occurs by development of transverse buckling waves which grow through a coarsening process. The growing buckles locally organize into a helical structure with a characteristic persistence length. The helical domain boundaries are eliminated from the relaxing structure by unwinding through the ends of the rod. The growth of the helical domains results in self-propulsive motion of the expanding rod as one large helix spanning the entire chain relaxes during the late stages of the dynamics. Stability analyses and scaling arguments are provided to explain the simulation results.

5.1 Introduction

Many important biological and polymeric systems quickly respond to changes in their surrounding conditions by altering their conformations. These conformational adjustments include volume expansion in response to changes in conditions of the solution (pH, temperature, salinity) and volume compression due to externally applied stress or intramolecular attraction. For example, anionic hydrogel [1] microspheres respond to changes in pH and salt concentration by expanding to a swelling ratio of as much as 12. Microgels, which respond

to these changes much faster than slab gels (0.5 seconds verses hours), are being evaluated as likely candidates for drug delivery systems because of their small size ($\sim 10\ \mu m$) and short response time. Similar gel chemistry is employed in the production of nanoscale conduits [2]. Single nanotubes can be formed from biomembrane vesicles by bonding a substrate to the membrane surface and drawing a stabilized fluid-lipid bilayer. The caliber of the nanometer scale tube can be experimentally controlled in the range 20 to 200 nanometers. The nanotube is stabilized by photochemical polymerization of cross-linking monomers contained within the lipid bilayer, resulting in a cross-linked gel cylinder of nanometer scale radius and near-millimeter length. When anionic hydrogel chemistry is employed, nanotubes with the capability of expanding their equilibrium lengths are produced. Nanoscale devices may use the expansion of these nanotubes for hydrodynamic propulsion or as mechanical levers, where adjustments in the solution conditions trigger the desired response. Understanding the dynamics of this expansion process is important for the design of nanoscale devices. Toward this goal, we simulate and analyze the free expansion of an initially straight elastic rod after a sudden change in the solvent conditions.

A closely related problem of buckling of an elastic filament in a viscous medium under uniaxial compression with fixed ends has been studied by Golubovic et al [3]. It was found that the compression causes a transverse buckling instability with a characteristic wavelength. Through buckling, the compressional strain is reduced by expansion in the transverse direction at the expense of incurring bending deformation. The buckling phenomenon occurs spontaneously through a symmetry breaking, and the buckled configuration evolves as a phase ordering process.

The expansion of an elastic filament with free ends after a sudden change of solvent condition can exhibit a similar buckling instability to the case of applied external stress with

fixed ends. This conclusion, however, is not obvious, because whereas transverse buckling is the only mechanism to relieve the compressional strain in the case of fixed ends, a rod with free ends has the option of increasing its length through longitudinal expansion. We will identify the conditions under which longitudinal relaxation dominates the expansion process. Since free expansion through transverse buckling represents a richer and more interesting phenomenon, it will be the focus of our study. Nevertheless, longitudinal motion will be shown to have a significant effect on the dynamics, particularly on the expansion of the major axis of the rod.

We study the expansion dynamics by computer simulation and by extending previous analyses of the buckling phenomenon of filaments with fixed ends. We focus on the three dimensional structure of the dynamic process of expansion. The initial instability produces wavelike deformations in the two transverse directions. As the wavelike buckles grow, they coalesce to form helical structures in order to assume a growing conformation of constant curvature along the backbone. Domains of helical orientation spontaneously form due to statistical deviation of the buckle wavelength from the most unstable value. The sizes of the helical domains grow as the rod expands, until the rod conformation is dominated by a single helical orientation. The final structure is a pure helix (single handedness); although the system initially lacks any chiral preference. An interesting consequence of the growth of the helical domains is the phenomenon of self-propulsion [4] of the expanding body throughout the expansion process. We present methods for measuring the average persistence length of the helical domains and explain their growth as a dissipative process.

5.2 Elastic Rod Model

We consider a thin rod of initial equilibrium length L_0 and uniform circular cross-sectional area A_0, made of isotropic elastic material. At the order of linear elasticity, the deformation of the rod can be decomposed into compression/expansion, bending, and twist. In this first study, we ignore the twist deformation. In the case of a rod with free ends, twist deformation is dissipated out of the unconstrained body. The resistance to twist dissipation is much smaller than the resistance to drift motion of the entire rod; therefore, we neglect body rotation and focus on the drift motion of the chain. The shape of this thin rod is then described by a space curve $\mathbf{r}(s)$ where s is an internal contour coordinate that runs from 0 to L_0. The linear compression/expansion strain, measured with respect to the initial rest length L_0, is given by

$$e(s) = 1 - \left|\frac{\partial \mathbf{r}}{\partial s}\right|, \tag{5.1}$$

where we have defined the strain to be positive if it corresponds to compression. However, we are interested in the dynamic evolution of the rod after a sudden change in the solvent condition causes a change in the equilibrium length. Under the new condition, the equilibrium length of the rod becomes $L_f > L_0$. The rod at the initial length L_0 will now experience a compressional strain with respect to the new equilibrium length. It is therefore more convenient to define a strain with respect to the new equilibrium length L_f:

$$e(s) = \gamma_0 - \left|\frac{\partial \mathbf{r}}{\partial s}\right|, \tag{5.2}$$

where $\gamma_0 \equiv L_f/L_0$ is the swelling ratio in the longitudinal direction.

The strain energy due to compression is then

$$U_{com} = \frac{\tilde{\kappa}}{2} \int_0^{L_0} e(s)^2 ds, \tag{5.3}$$

where $\tilde{\kappa}$ is the compression modulus and is related to the Young's modulus E of the elastic material by $\tilde{\kappa} = EA_0$. We will ignore the change in the Young's modulus due to the expansion of the rod.

The bending energy is due to curvature distortion of the rod from its equilibrium value, which in our case is taken to be zero. For an unstretchable rod model, such as the Kratky-Porod wormlike chain model [5, 6], the curvature is simply $\frac{\partial^2 \mathbf{r}}{\partial s^2}$. However, in our case the length of the rod is not conserved, and curvature is more properly defined as $\frac{1}{\gamma}\frac{\partial}{\partial s}\frac{1}{\gamma}\frac{\partial \mathbf{r}}{\partial s}$ where $\gamma(s) = \left(\frac{d\mathbf{r}}{ds} \cdot \frac{d\mathbf{r}}{ds}\right)^{1/2}$ relates the true arc length to the backbone internal coordinate. The bending energy is then given by

$$U_{bend} = \frac{\tilde{\epsilon}}{2} \int_0^{L_0} \left(\frac{1}{\gamma}\frac{\partial}{\partial s}\frac{1}{\gamma}\frac{\partial \mathbf{r}}{\partial s}\right)^2 ds, \tag{5.4}$$

where the bending modulus $\tilde{\epsilon}$ is found from the geometry of a gently bent cylinder to be $EA_0^2/(4\pi)$ [7].

To numerically solve the dynamic equation of motion, we discretize the rod into $N+1$ "beads" with an initial bead separation of $l_0 = L_0/N$. In this discretized representation, the compression and bending energies become

$$U_{com} = \frac{\kappa}{2} \sum_{n=1}^{N} e_n^2, \tag{5.5}$$

where $e_n = \gamma_0 - \frac{|\mathbf{R}_{n+1}-\mathbf{R}_n|}{l_0}$ gives the internal strain, and

$$U_{bend} = \frac{\epsilon}{2}\sum_{n=1}^{N-1}(\mathbf{t}_{n+1}-\mathbf{t}_n)^2, \tag{5.6}$$

where $\mathbf{t}_n = \frac{(\mathbf{R}_{n+1}-\mathbf{R}_n)}{|\mathbf{R}_{n+1}-\mathbf{R}_n|}$ is the unit tangent vector. The moduli are now given by $\kappa = l_0\tilde{\kappa} = El_0A_0$ and $\epsilon = \tilde{\epsilon}/l_0 = EA_0^2/(4\pi l_0)$ and have units of energy. We will use the moduli κ and ϵ in the subsequent analysis.

We describe the dynamics of the thin rod by an overdamped Rouse dynamics in a viscous medium [8]. The equation of motion is

$$\xi\frac{\partial\mathbf{R}_n(t)}{\partial t} = -\frac{\partial U}{\partial\mathbf{R}_n} + \mathbf{f}_n(t), \tag{5.7}$$

where ξ is the friction coefficient of the solvent and $\mathbf{f}_n(t)$ represents the random forces due to thermal noise. We will be interested in deformation energies (both bending and compression) that are large compared to the thermal energy; therefore, we will ignore any randomness except that associated with the initial perturbation. In Sec. IV, we further discuss the conditions where thermal fluctuations significantly contribute to the expansion dynamics and justify the neglect of the thermal fluctuations in our study.

Analysis of the equations of motion of the beads yields two fundamental time scales $\tau_{com} = \xi l_0^2/\kappa$ and $\tau_{bend} = \xi l_0^2/\epsilon$, associated with the location compression and bending relaxation, respectively. An additional time scale τ_0 associated with the buckling phenomenon (see Sec. IV) arises from the expansion dynamics. In order to resolve these fundamental time scales (τ_{com}, τ_{bend}, and τ_0), the numerical solution of Eq. 5.7 is conducted using time steps that are small in comparison. For the parameters that we choose, these three time scales are on the same order of magnitude; therefore, we arbitrarily choose to scale time by

the fundamental buckling time τ_0.

5.3 Expansion Dynamics

Our simulations focus on the dynamics of an initially straight rod of length 199.0 l_0 expanding to a final equilibrium length of 298.5 l_0 (50 % expansion). We use a Young's modulus of $10^4\ Nm^{-2}$, representing that of polyethyleneglycol (400) methacrylate hydrogel [9]. Choosing an initial interbead spacing $l_o = 346.38\ nm$ and radius $R = 292.40\ nm$ results in a compression modulus $\kappa = 9.304 \times 10^{-16}\ J$ and bending modulus $\epsilon = 1.657 \times 10^{-16}\ J$.

We seed the initially straight chain with a small random perturbation in the transverse direction of an amplitude of 0.01 l_0. (This initial condition does not reflect the tendency for a chain under thermal fluctuations to favor long wavelength perturbations. We have conducted simulations with perturbations produced by thermal equilibration of a chain with the initial interbead spacing, and observe qualitatively similar results to those with random perturbations.) At time zero, the equilibrium interbead separation is suddenly changed from l_0 to 1.5 l_0, and the subsequent evolution of the structure of the chain is followed by numerically integrating Eq. 5.7.

We analyze the dynamics of the expanding chain using several metrics. The compression and bending energies are calculated from the bead coordinates using Eq. 5.5 and Eq. 5.6. The shape of the chain is characterized by the radius-of-gyration tensor $\mathbf{T}$ [10]. The transverse buckling wavelength is measured by using the slope-slope correlation function $K_{ss}(r,t)$ [3]. And finally, the correlation length of the handedness of the transverse fluctuation is measured by introducing the torsion-torsion correlation function $K_{\tau\tau}(r,t)$.

A typical set of snapshots of the expanding chain is shown in Fig. 5.1. It is clearly seen that an initially straight chain develops buckling waves and that these waves grow

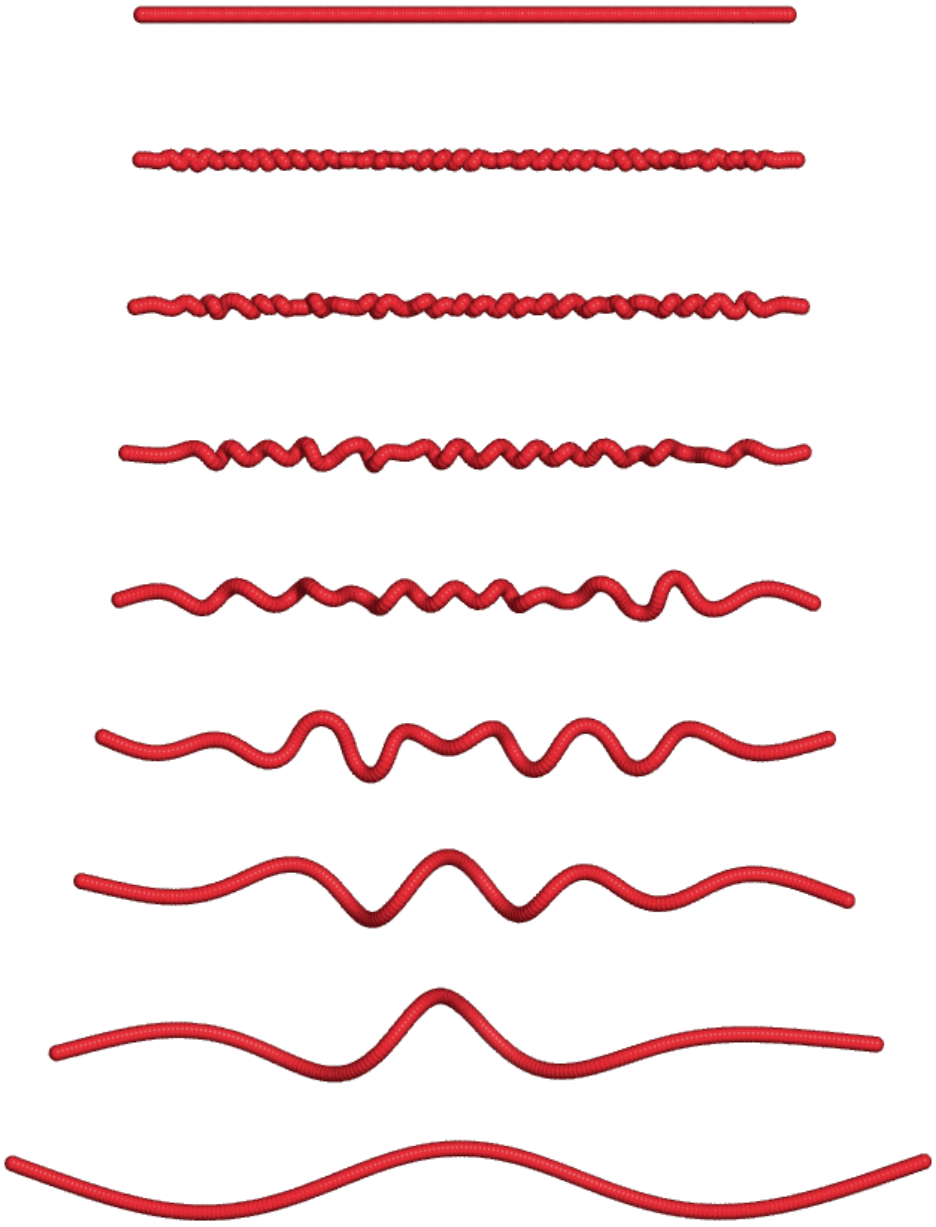

Figure 5.1: Snapshots of the chain conformation during the free expansion process. We show conformations at 2.2051 τ_0, 11.233 τ_0, 57.224 τ_0, 291.51 τ_0, 1485.0 τ_0, 7564.6 τ_0, 38535 τ_0, 196300 τ_0, and 1000000 τ_0, successively.

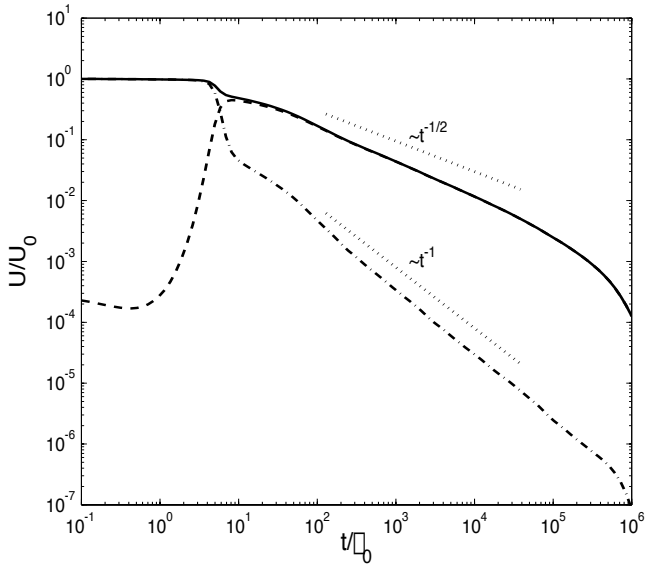

Figure 5.2: Bending energy U_{bend} (dashed curve), compression energy U_{com} (dashed-dotted curve) and total potential energy $U = U_{bend} + U_{com}$ (solid curve) during the expansion process.

through a coarsening process. The organization of the buckling waves into helices can also be observed.

Upon the development of buckling waves, the compression energy due to the altered equilibrium interbead spacing is partially converted into bending energy. This repartitioning of energy continues throughout the entire coarsening process. In Fig. 5.2, we show the evolution of the two energy contributions during the expansion of the chain. The drop in the compression energy and sharp rise in the bending energy corresponds to a time when the buckling waves begin to grow significantly. Once the buckling waves are fully developed, both energy contributions decay due to dissipation. Over a broad intermediate time range, the decay of both contributions follows a power law with exponent $-1/2$ and -1 for the bending and compression energies, respectively. These features are qualitatively similar to those in the buckling dynamics due to compression along a rod with fixed ends, as analyzed by Ref. [3]. The very long time behavior is the relaxation of a bend with a length scale the

size of the entire chain; relaxation of this long wavelength bend should be exponential and will be governed by the longest relaxation time associated with the bending motion. We note that full relaxation cannot be reached in the case of chains with fixed ends, and the simulation time in Ref. [3] was not long enough to reach this terminal regime.

To analyze the shape evolution of the expanding chain, we introduce the radius-of-gyration tensor $\mathbf{T}$, calculated from the bead coordinates $\mathbf{R}_n$ and the center of mass coordinate $\mathbf{R}^c(t) = \frac{1}{N+1}\sum_{n=1}^{N+1}\mathbf{R}_n(t)$:

$$T_{ij}(t) = \frac{1}{N+1}\sum_{n=1}^{N+1}[R_{i,n}(t) - R_i^c(t)][R_{j,n}(t) - R_j^c(t)], \tag{5.8}$$

where i and j denote cartesian components x, y, and z, and n denotes the discrete backbone coordinate. The square roots of the three eigenvalues of the tensor $\mathbf{T}$ (R_1, R_2, and R_3) give a measure of the size of the chain along the major axis $\mathbf{x}_1$ and the two minor axes $\mathbf{x}_2$ and $\mathbf{x}_3$, which are the eigenvectors of $\mathbf{T}$. Fig. 5.3 shows the evolution of the three principal radii of gyration with time. Since the major radius R_1 starts from a large nonzero initial value, we present data for $R_1(t) - R_1(0)$. This difference is seen to increase linearly at first and then turn into a slower square-root power increase around the time the buckling waves develop. The two minor radii start at a small value and then rapidly increase when the buckling waves begin to develop. Afterwards, they follow a $t^{1/4}$ power law growth until eventually dropping back to zero when the chain is fully relaxed. The small differences in R_2 and R_3 are due to statistical errors, as these two axes are equivalent.

Following Ref. [3], we define the slope-slope correlation function K_{ss} to calculate the characteristic wavelength λ of the buckling waves. The transverse slope $\mathbf{V}_n^T$ is the projection

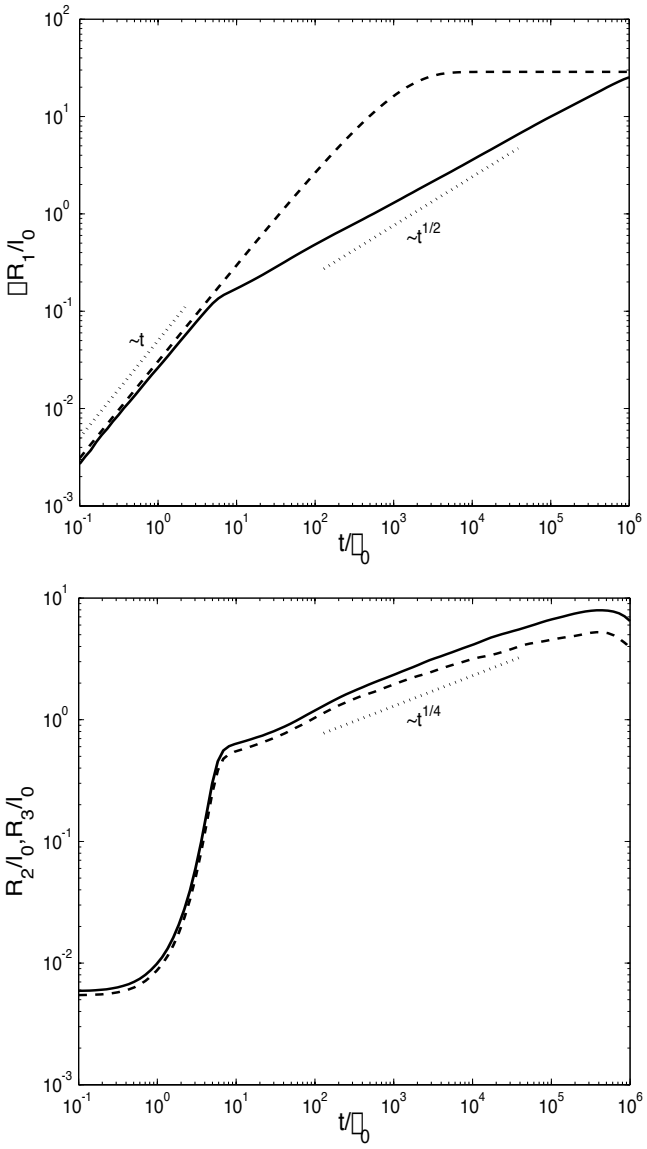

Figure 5.3: (a) Expansion dynamics of the major axis $\Delta R_1 = R_1 - R_1(t = 0)$ (solid curve). The dashed curve corresponds to the analytical solution (Eq. 5.16) for the expansion of a rod in one dimension. (b) Time evolution of the minor axes R_2 (solid curve) and R_3 (dashed curve) during the expansion process.

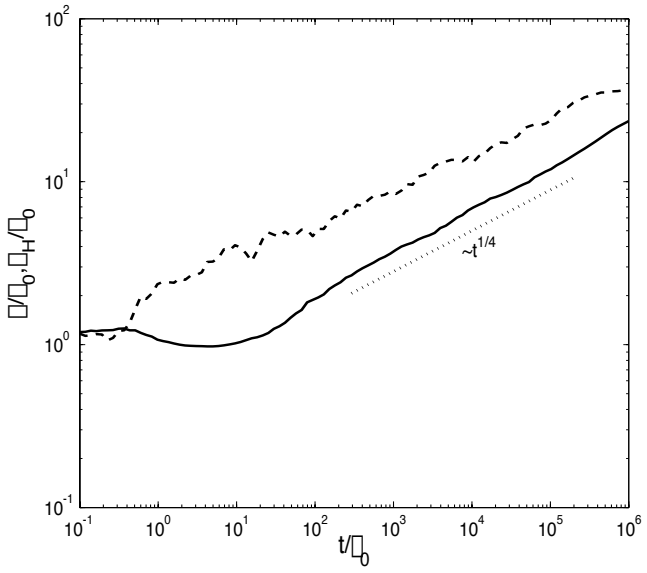

Figure 5.4: The time evolution of the average wavelength of the buckled perturbation λ (solid curve) and the average persistence length of the buckle handedness λ_H (dashed curve).

of the relative bead position $\mathbf{V}_n = \mathbf{R}_{n+1} - \mathbf{R}_n$ onto the tranverse axes $\mathbf{x}_2$ and $\mathbf{x}_3$:

$$\mathbf{V}_n^T(t) = [\mathbf{x}_2(t) \cdot \mathbf{V}_n(t)]\mathbf{x}_2 + [\mathbf{x}_3(t) \cdot \mathbf{V}_n(t)]\mathbf{x}_3, \tag{5.9}$$

and the slope-slope correlation function is defined as

$$K_{ss}(r,t) = < \mathbf{V}_{n+r}^T(t) \cdot \mathbf{V}_n^T(t) >, \tag{5.10}$$

where the angular brackets refer to a statistical averaging of many runs with different realizations of the initial random seeding. For a perfect sinusoidal wave, the function $K_{ss}(r,t)$ changes sign twice during one full period in r, the first zero occurring at one quarter of the wavelength λ. We therefore define the characteristic wavelength as four times the value of r where $K_{ss}(r,t)$ first becomes zero.

In order to measure the persistence of the handedness of the transverse fluctuation λ_H,

we introduce the torsion-torsion correlation function $K_{\tau\tau}$. For a space curve, torsion τ is defined to measure the instantaneous amount that the curve is distorted out of a planar path. Mathematically [11],

$$\tau = -\mathbf{n} \cdot \frac{d\mathbf{b}}{ds}, \tag{5.11}$$

where $\mathbf{n}$ is the unit normal, which is a measure of the normalized rate of change of the tangent vector $\mathbf{t}$ with respect to the arc length s and $\mathbf{b}$ is the unit binormal, defined as the cross product of the tangent vector with the unit normal. The sign of the torsion determines the handedness of the distortion: a right handed distortion generates a positive torsion; a left handed distortion generates a negative torsion. The torsion-torsion correlation function is defined as

$$K_{\tau\tau}(r,t) =< \tau_{n+r}(t)\tau_n(t) > . \tag{5.12}$$

This function switches sign at half the correlation length of the helical orientation λ_H.

In Fig. 5.4, we show the time evolution of the buckling wave length λ and the helical correlation length λ_H. The initial random seeding does not favor any particular wavelength; however, after some initial incubation period, the transverse fluctuation picks up a dominant wavenumber corresponding to a plateau in $\lambda(t)$. Subsequently, the coarsening of the buckles leads to an increase in the average wavelength, manifested as a $t^{1/4}$ power law for a broad range of the intermediate times. The growing wavelike buckles in three dimensions organize into helical domains, which are separated by domain boundaries that may be viewed as imperfections within the helical structure. The energy associated with the boundary imperfections is relaxed by diffusion of the imperfections from the system, thus the helical correlation length increases until the structure is a pure helix.

In order to clearly show the formation of a helical buckled conformation, we have per-

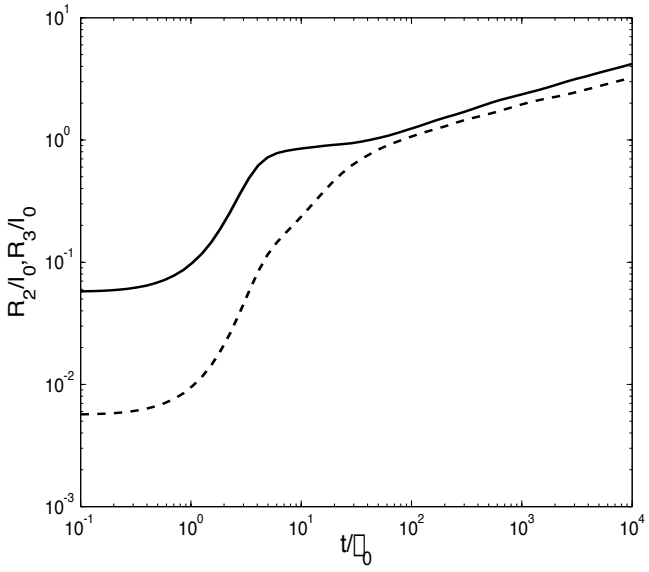

Figure 5.5: Early stage time evolution of the minor axes R_2 (solid curve) and R_3 (dashed curve). This simulation seeds one transverse direction with the unstable wavelength λ_o of amplitude 0.1 l_0 and the other transverse direction with random perturbation of amplitude 0.01 l_0.

formed simulations where the initial condition is seeded with a preferential perturbation along one of the two transverse directions. Specifically, we set the y-component of the initial transverse perturbation to a sinusoidal wave with an amplitude of 0.1 l_0 and with a wavelength λ_o, the fastest growing wavelength determined from the linear stability analysis (see next section). The z-component of the initial perturbation is set to a random fluctuation with an amplitude of 0.01 l_0. The time evolution of the two minor axes is shown in Fig. 5.5. The separation of the two minor axes R_2 and R_3 at the beginning of the expansion process reflects the favoring of the y-component. The two magnitudes increase parallel to each other until R_2 has expanded to a threshold value, at which point R_2 levels off. The smaller minor axis R_3 catches up to the larger minor axis R_2. Thereafter, they continue to increase; however, the two radii become roughly equal. The structure at this point becomes clearly helical, as confirmed by direct visualization of the chain configuration. The helical conformation minimizes the bending energy by distributing a constant curvature over the

length of the elastic chain.

5.4 Linear Stability Analysis and Dynamic Scaling

In this section, we perform a linear stability and scaling analysis with the goal of obtaining a physical understanding of the results presented in the previous section. We first analyze the early stage dynamics which focuses on the initial expansion of the chain in the longitudinal direction and the development of the buckling wave. We then use a simple energy argument to understand the driving force for the formation of helices. Finally, we use scaling analysis to rationalize the observed intermediate and long time scaling behavior of the various quantities.

At the early stage of the expansion, the chain is essentially straight with small transverse perturbations. It is therefore convenient to decompose the chain configuration into longitudinal and transverse components, with the longitudinal axis parallel to the initial orientation of the chain. We define a longitudinal deformation $u(s)$ through $\mathbf{r}_L = [s + u(s,t)]\hat{x}$, where $\mathbf{r}_L$ is the longitudinal position of the chain backbone at internal coordinate s. Note here that the longitudinal deformation is defined with respect to the initial equilibrium position of the chain. The transverse deformation $\mathbf{R}_T(s)$ at s is simply the deviation from the initial chain axis. The equations of motion for these components are obtained in a manner similar to Eq. 5.7 taking special care to maintain the dimensions in the continuous model; they are

$$\xi \frac{\partial u}{\partial t} = -\kappa \frac{\partial e}{\partial s} - \epsilon l_0^2 \frac{\partial}{\partial s}\left\{\frac{1}{\gamma}\frac{\partial}{\partial s}\left[\frac{1}{\gamma^2}\frac{\partial}{\partial s}\left(\frac{1}{\gamma}\frac{\partial (s+u)}{\partial s}\right)\right]\right\}, \tag{5.13}$$

$$\xi \frac{\partial \mathbf{R}_T}{\partial t} = -\kappa \frac{\partial}{\partial s}\left(e\frac{\partial \mathbf{R}_T}{\partial s}\right) - \epsilon l_0^2 \frac{\partial}{\partial s}\left\{\frac{1}{\gamma}\frac{\partial}{\partial s}\left[\frac{1}{\gamma^2}\frac{\partial}{\partial s}\left(\frac{1}{\gamma}\frac{\partial \mathbf{R}_T}{\partial s}\right)\right]\right\}. \tag{5.14}$$

The early stage dynamics is dominated by the compression energy. Since the initial

conformation is essentially straight, the beads move in the longitudinal direction as if they are confined to move in one dimension. Ignoring the transverse components leads to the following simplified equation of motion for the longitudinal deformation:

$$\xi \frac{\partial u}{\partial t} = \kappa \frac{\partial^2 u}{\partial s^2}. \tag{5.15}$$

It is convenient to define the internal coordinate $s \in [-L_0/2, L_0/2]$. This equation is supplemented by the final value $u(s, \infty) = e_0 s$ and the zero strain boundary conditions at the two chain ends. The solution can be readily obtained as an eigenfunction expansion which reads

$$u = e_0 s - \frac{e_0 L_0}{\pi^2} \sum_{p=0}^{\infty} \frac{(-1)^p}{(p+\frac{1}{2})^2} \sin\left[2\pi\left(p+\frac{1}{2}\right)\frac{s}{L_0}\right] \exp\left[-4\pi^2\kappa\left(p+\frac{1}{2}\right)^2 \frac{t}{\xi L_0^2}\right]. \tag{5.16}$$

Eq. 5.16 defines a set of relaxation times for the eigenmodes. In particular, a "Rouse-like" time associated with the slowest longitudinal relaxation mode can be identified as $\tau_{long} = \xi L_0^2/(\pi^2\kappa)$.

Using Eq. 5.16, we obtain the evolution in the radius of gyration for a chain expanding in one dimension. For short times, the change in the radius of gyration is given by

$$\begin{aligned} R_g - R_g(t=0) &= \sqrt{\frac{1}{L_0}\int_{-L_0/2}^{L_0/2}(s+u)^2 ds} - \frac{L_0}{2\sqrt{3}} \\ &\approx \frac{2\sqrt{3}\kappa e_0}{\xi L_0} t \\ &= L_0 e_0 \frac{2\sqrt{3}}{\pi^2}\frac{t}{\tau_{long}}. \end{aligned} \tag{5.17}$$

This predicted linear behavior is in perfect agreement with the simulation result shown in Fig. 5.3.

The one-dimensional configuration of a chain with internal compressional strain is unstable with respect to small transverse perturbation. The initial instability can be understood through a simple linear stability analysis. Representing the transverse perturbation as a sinusoidal wave with wavenumber k, $\mathbf{R}_T \sim \mathbf{A}_k \exp(iks)$, and substituting it into the equation of motion, Eq. 5.14, we find that the amplitude of the perturbation $\mathbf{A}_k$ will grow for k's in the range $|k| < e_0^{1/2}(\kappa/\epsilon)^{1/2}/l_0$. The most unstable (i.e., fastest growing) mode is that with $k_o = \pm e_0^{1/2}(\kappa/\epsilon)^{1/2}/(\sqrt{2}l_0)$, corresponding to a wavelength λ_o of $2\pi l_0[\kappa e_0/(2\epsilon)]^{-1/2}$. The most unstable mode predicted from the linear stability analysis does not favor the y or z directions, nor does it favor the cosine or sine contributions. This suggests that the transverse perturbations in the two unexplored dimensions initially are independent of each other; however, statistically, the amplitude of the most unstable mode is equivalent in these two dimensions.

The linear stability analysis predicts an exponential growth of the most unstable mode at a rate of $\tau_o^{-1} = \kappa^2 e_0^2/(4l_0^2\xi\epsilon)$, thus the transverse displacement becomes significant when $t \sim \tau_o$. This time therefore signals the termination of the one-dimensional growth dominated by the compression energy. This is shown clearly as the end of the plateau in the compression energy in Fig. 5.2, and the deviation from linear growth in the radius of gyration of the major axis (Fig. 5.3). This time also correlates well with the onset of scaling behavior in other properties.

The expanding transverse buckles force the bending energy to overcome the compression energy at times $t > \tau_o$. The growing wavelike structure locally conforms to a path between a planar wave and a helix. The three dimensional buckled structure relaxes by following the steepest descent on the potential energy surface. We now show that the bending energy favors organization of the buckles into helices. To this end, we focus on the bending energy

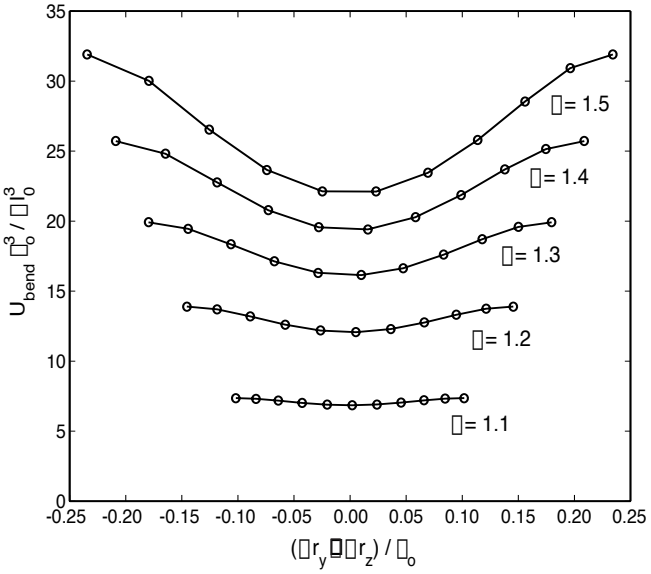

Figure 5.6: Contour plots of the bending energy for a single period wavelike distortion. The amplitudes Δr_y and Δr_z correspond to the relative contribution of the sine component and the cosine component respectively.

contribution in a segment of the chain spanning a single period of wavelength λ_o. Since the longitudinal expansion requires an orchestrated motion of the entire chain, the transverse buckles grow outward without appreciably spreading longitudinally. Thus, for the present purpose we keep the longitudinal distance of this chain segment fixed, so that chain expansion occurs only through the growth of the buckling wave in the transverse directions. We represent the distortion of the chain by assuming

$$\mathbf{r} = X(s)\hat{x} + \Delta r_y \sin(k_o s)\hat{y} + \Delta r_z \cos(k_o s)\hat{z} \tag{5.18}$$

subject to a given swelling ratio $|\frac{d\mathbf{r}}{ds}| = \gamma$, with γ varying between 1 and 1.5 corresponding to the initial and final length of the chain, respectively. Note that either the sine or cosine part in the above equation corresponds to a two-dimensional wave, whereas when both sine and cosine are present with equal coefficients, we obtain a perfect helix. Therefore, we plot the bending energy as a function of $([\Delta r_y - \Delta r_z]/\lambda_0)$; the result is shown in Fig. 5.6. It

is clear that the helical structure is an energy minimum at all values of γ (representing a time progression in the expansion), reflecting the tendency of the wavelike structure to assume a conformation of constant curvature. The energy difference between the helix and a two-dimensional deformation increases with increasing swelling ratio and approaches zero as the swelling ratio approaches one, the latter being consistent with the lack of a transverse directional preference of the buckling predicted by the linear stability analysis. Thus the formation of helices is a nonlinear effect.

As the wavelike deformations grow in the transverse direction, the driving force for coalescing into a helical conformation increases. The handedness of a helix is dictated by the sign of the local torsion τ. The random initial perturbation does not favor one over the other. However, because of the continuity of the space curve, correlation develops as the chain expands so that the local torsion persists over a length λ_H. The result is a helical structure with helical domains of length λ_H, which are separated by kink domain boundaries.

The dynamics for the intermediate times $\tau_f > t > \tau_0$, where τ_f is a terminal relaxation time scale to be obtained later, is characterized by power law dependence in a number of properties. To understand the observed scaling behavior, we perform a scaling analysis, following similar arguments given in Refs. [3, 12] in the study of compressed rods and membranes.

We choose a transverse displacement scale R_T, ignoring for the present purpose the difference between R_2 and R_3. The longitudinal deformation is characterized by the increase of the length along the major axis ΔR_1, which scales similarly to the displacement u introduced at the beginning of this section. The length scale for the bending deformation is the wavelength of the buckles λ and that for the longitudinal displacement is L_0. The

fact that the contour length increases will be accounted for by the leading dependence in longitudinal strain, but otherwise has little effect.

We start with the scaling behavior for the buckling wavelength λ. The driving force for buckling is due to both the compression energy and the bending energy. Assuming that the two driving forces contribute roughly equally, we have, from the transverse equation of motion (Eq. 5.14),

$$\xi \frac{R_T}{t} \sim \kappa \frac{e R_T}{\lambda^2} \sim \epsilon l_0^2 \frac{R_T}{\lambda^4}. \tag{5.19}$$

The above relation can be re-written using the initial strain $e_0 \equiv \gamma_0 - 1$, and the wavelength λ_0 and time scale $\tau_0 = 4 l_0^2 \xi \epsilon / [\kappa^2 e_0^2]$ identified from the linear stability analysis, as

$$\frac{\tau_0 R_T}{t} \sim \frac{e R_T \lambda_0^2}{e_0 \lambda^2} \sim \frac{R_T \lambda_0^4}{\lambda^4}. \tag{5.20}$$

It can be readily seen that the buckling wavelength scales as $\lambda \sim \lambda_0 (t/\tau_0)^{1/4}$. The internal strain is seen to scale as $e \sim e_0 (t/\tau_0)^{-1/2}$. Substituting the internal strain into the compression energy yields $U_{com} \sim \kappa (L_0/l_0) e_0^2 (t/\tau_0)^{-1}$.

To understand the scaling behavior of the increase in the length along the major axis of the rod, we analyze the governing equation for the longitudinal motion (Eq. 5.13). This analysis requires careful consideration of the appropriate length scales. The contribution of the compression energy is relatively unaffected by the presence of transverse buckles; therefore, the proper backbone length scale for the compression energy is L_0, leading to

$$\xi \frac{\Delta R_1}{t} \sim \kappa \frac{e}{L_0}. \tag{5.21}$$

Using the scaling for the internal strain e, we obtain the scaling for the longitudinal dis-

placement u as

$$\Delta R_1 \sim \kappa \frac{e_0 t^{1/2} \tau_0^{1/2}}{\xi L_0} \sim \left(\frac{t}{\tau_{bend}}\right)^{1/2} \frac{l_0^2}{L_0}, \tag{5.22}$$

where the last expression results from using the expressions for τ_0 and $\tau_{bend} = \xi l_0^2/\epsilon$. This accounts for the observed $t^{1/2}$ power law increase in the major axis shown in Fig. 5.3.

The scaling behavior for R_T shown in Fig. 5.3 can be understood by going back to the expression for the internal strain which consists of both longitudinal and transverse contributions:

$$\begin{aligned} e &= e_0 - \frac{\partial u}{\partial n} - \frac{1}{2}\left(\frac{\partial \mathbf{R}_T}{\partial n}\right)^2 \\ &\sim e_0 - \frac{\Delta R_1}{L_0} - \frac{R_T^2}{\lambda^2}. \end{aligned} \tag{5.23}$$

For $t > \tau_0$ the strain becomes negligible compared to each individual term on the right hand side of the equation. Thus, we can obtain the scaling behavior for R_T by balancing the three terms on the right. Assuming for the moment that we can ignore the $(\Delta R_1/L_0)$ term, we have

$$R_T \sim e_0^{1/2}\lambda \sim e_0^{1/2}\lambda_0 \left(\frac{t}{\tau_0}\right)^{1/4}, \tag{5.24}$$

which is in agreement with the power law behavior in Fig. 5.3. Combining the scaling for R_T and λ, we obtain the scaling for the bending energy $U_{bend} \sim \epsilon l_0 L_0 R_T^2/\lambda^4 \sim \kappa e_0^2 (L_0/l_0)(t/\tau_0)^{-1/2}$. The power law behavior of R_T (Eq. 5.24) terminates when the second term in Eq. 5.23 $(\Delta R_1/L_0)$ is no longer negligible, and this happens when

$$\Delta R_1 \sim e_0 L_0 \tag{5.25}$$

or

$$t \sim \tau_f \sim \tau_{bend} e_0^2 \left(\frac{L_0}{l_0}\right)^4. \tag{5.26}$$

τ_f thus defines the terminal relaxation time when the rod has approached its final equilibrium length. This terminal relaxation time can also be obtained as the time required for the wavelength of the buckles to reach the full length of the rod. Setting $\lambda \sim L_0$, we have

$$\tau_f \sim \tau_{bend} \left(\frac{L_0}{l_0}\right)^4, \tag{5.27}$$

which apart from some numerical factor is identical to the scaling expression Eq. 5.26. We note that this relaxation time is nothing but the transverse relaxation time for a semiflexible polymer [13, 14]. Interestingly, the relaxation time associated with the longitudinal relaxation (Eq. 5.16) does not play an explicit role in our study. This is because buckling appears long before this relaxation time is reached since

$$\frac{\tau_0}{\tau_{long}} \sim \frac{4\epsilon l_0^2}{\kappa e_0^2 L_0^2} \ll 1. \tag{5.28}$$

The time scale τ_{long} becomes obliterated once buckling waves dominate the relaxation dynamics. This inequality in fact specifies the condition under which the free expansion problem exhibits similar transverse buckling to that in a compressed rod with fixed ends. This condition reflects the significantly larger resistance associated with longitudinal relaxation than that associated with transverse buckling. If the parameters are altered such that $\tau_{long} \sim \tau_0$, then even though the transverse buckling instability may still exists [15], the buckling waves will not be able to grow to any significant extent since the driving force for buckling will have been dissipated through longitudinal relaxation. For an elastic rod

made of isotropic material, this will be the case if the initial strain is less or comparable to the inverse of the aspect ratio of the rod. (This result can be obtained by substituting the explicit dependence of the bending and compression moduli on the diameter of the rod and on the Young's modulus of the materials.) For long rods with large strain, the scenario we have presented in this study will prevail.

The increase of the helical persistence length λ_H is necessarily slower than that of the wavelength λ. The wavelength λ grows by two modes of relaxation. It grows internally at the helical domain boundaries; two helices meet and eliminate one another by turning the imperfection around the axis of orientation. This process increases the wavelength without effecting the length of the two helical domains. The wavelength also grows at the chain ends by turning the end helices around the axis of orientation. This process increases both the wavelength and the helical domain length. The helical persistence length grows at a slower rate than the wavelength because the helical domains grow only by diffusion of writhe out of the ends, and the wavelength grows by both internal relaxation and unwinding at the ends. The physics of the relaxation of two *pre-existing* competing helical structures has recently been analyzed for a chain of fixed length and bending/twisting degrees of freedom [16]. Two types of imperfection front propagation are identified: "crankshafting", where one helix spins around the axis of the other at the chain end (end dissipation), and "speedometer-cable motion", where each helix revolves around their own axis (internal relaxation). These modes of front propagation are consistent with our description of domain relaxation; however, our problem is complicated by the existence of many domains of helicity, and these two modes occur simultaneously during the free expansion process. Also, the helices studied in Ref. [16] correspond to energy minima in a bistable system, while the helices appearing in our study are transient structures that arise spontaneously during the relaxation process in a system

lacking an obvious propensity for helical formation.

Finally, we discuss the effects of neglecting thermal fluctuation in our study. To this end, we compare the thermal energy with the compression and bending energies. Since the compression energy decays faster than the bending energy, thermal fluctuation is expected to affect the system behavior when $U_{com} \sim Nk_BT$. Since $U_{com} \sim \kappa N e_0^2 (t/\tau_0)^{-1}$, the two energies become comparable when $t = \tau_T \sim (\kappa/k_BT) e_0^2 \tau_0$. For our choice of parameters and assuming room temperature, $\kappa/k_BT \approx 6N^2$; thus we estimate that $\tau_T \sim 10^4 \tau_0$. On the other hand, the bending energy remains much larger than the thermal energy until well past the terminal relaxation time τ_f. Thus the $t^{-1/2}$ decay in the bending energy shown in Fig. 2 will be unaffected by the thermal fluctuation, while the t^{-1} decay in the compression energy will reach a plateau value corresponding to the thermal energy of the rod at $t \sim \tau_T$. However, since the scaling behavior of most the properties studied in this chapter is determined by the bending energy, thermal fluctuation has little effect on these properties. Interestingly, we find from separate calculations that included Brownian forces, that even the $t^{1/2}$ growth in the length of the major axis (which is expected to be affected by the compression energy) persists well past the time when the compression energy reaches a plateau.

We note that there are many situations in which thermal fluctuation plays an essential role in the dynamics of a semiflexible polymer. Stress relaxation in semiflexible polymers is an example that has attracted considerable attention in recent years [13, 14, 17, 18]. Similarly, the propagation of tension upon pulling a semiflexible polymer by one end is shown to depend crucially on the thermal fluctuation spectrum in the initial configuration [19]. While the inclusion of thermal fluctuation in our work would undoubtedly be more realistic and would lead to slight modifications in the behavior of some properties, we have chosen

to focus our attention on situations where relaxation is driven by large mechanical energies and hence the omission of thermal fluctuation is justified.

5.5 Conclusions

The free expansion of an elastic filament progresses along the energetic path of least resistance, notably marked by the emergence of the transverse buckling, which occurs to distribute the energy between compression and bending. The wavelike buckles grow as a coarsening process until the wavelength reaches the full length of the chain, at which point the chain relaxes back to its equilibrium straight conformation. The buckles expand in the transverse direction and prefer to assume a helical orientation due to a nonlinear effect, which is not predicted by linear stability analysis. Although the energetically preferred conformation as the transverse displacement grows is a pure helix (single handedness), the local handedness is determined by the local torsion; therefore, the wavelike buckles coalesce into helical domains separated by kink imperfections, which are eliminated from the expanding body by diffusion from the chain ends. The helical domains grow until the relaxing conformation achieves a pure helical orientation, where the handedness is determined by the orientation of statistical dominance.

The expansion dynamics present an interesting problem of symmetry breaking where the system breaks symmetry in two ways: the straight rod spontaneously buckles in the transverse direction and the wavelike buckles further organize into helical domains of common handedness. The former symmetry breaking occurs to preferentially distribute the energy between bending and compression, rather than dissipating the energy through compression alone. Energy redistribution during the relaxation process is common in problems of stress dissipation. Similar to expanding rods, the expansion of compressed membranes

exhibits transverse buckling in order to alleviate the compression energy [12]. Similarly, when an elastic cube is stressed through inward pointing forces at the cube vertices, the cube buckles along the cube edges [20]. An initially twisted rod may unwind the twist density via "geometric untwisting", where twist is converted to writhe, and stress is dissipated through drift motion of the chain backbone [21]. This process, in which energy is redistributed between twist and bending, is obviously analogous to the free expansion problem we study here. This mode of relaxation, however, is the dominant mechanism only when the moment about the twisted chain generated by the torsional deformation cannot overcome the rotational resistence. Thus there is a further similarity between the relaxation of twist deformation and the free expansion of elastic filaments, as in both systems redistribution of energy through instability occurs only under certain conditions.

A recent theoretical analysis of DNA condensation [22] suggests that the chain collapse occurs via an Euler buckling instability, thus partitioning the total energy into bending and electrostatic energy. Our analysis of the freely expanding rod provides insight into the existence of higher order structure within the buckle phase; therefore, if the chain collapse occurs through a similar instability, it is likely that the condensing DNA strand also contains helical domains. We are interested in analyzing the effect of helicity on the chain collapse dynamics and determining its role in the morphology of the condensed DNA strand.

Bibliography

[1] G. M. Eichenbaum, P. F. Kiser, S. A. Simon, and D. Needham. pH and ion-triggered volume response of anionic hydrogel microspheres. *Macromolecules*, 31(15):5084–5093, 1998.

[2] E. Evans, H. Bowman, A. Leung, D. Needham, and D. Tirrell. Biomembrane templates for nanoscale conduits and networks. *Science*, 273(5277):933–935, 1996.

[3] L. Golubovic, D. Moldovan, and A. Peredera. Flexible polymers and thin rods far from equilibrium: Buckling dynamics. *Phys. Rev. E*, 61(2):1703–1715, 2000.

[4] T. Y. T. Wu, C. J. Brokaw, and C. Brennan. *Swimming and Flying in Nature (Volume 1)*. Plenum, 1975.

[5] O. Kratky and G. Porod. Rontgenuntersuchung geloster fadenmolekule. *Recl. Trav. Chim. Pays-Bas-J. Roy. Neth. Chem. Soc.*, 68(12):1106–1122, 1949.

[6] H. Yamakawa. *Helical Wormlike Chains in Polymer Solutions*. Springer-Verlag, 1997.

[7] L. D. Landau and E. M. Lifshitz. *Theory of Elasticity*. Pergamon Press, 1986.

[8] M. Doi and S. F. Edwards. *The Theory of Polymer Dynamics*. Oxford University Press Inc., New York, NY, 1986.

[9] K. Murphy and N. Ravi. *Polymer Preprints*, 40:630, 1999.

[10] J. Rudnick and G. Gaspari. The shapes of random-walks. *Science*, 237(4813):384–389, 1987.

[11] R. C. Wrede. *Introduction to Vector and Tensor Analysis*. Dover Publications, 1972.

[12] D. Moldovan and L. Golubovic. Buckling dynamics of compressed thin sheets (membranes). *Phys. Rev. Lett.*, 82(14):2884–2887, 1999.

[13] D. C. Morse. Viscoelasticity of tightly entangled solutions of semiflexible polymers. *Phys. Rev. E*, 58(2):R1237–R1240, 1998.

[14] F. Gittes and F. C. MacKintosh. Dynamic shear modulus of a semiflexible polymer network. *Phys. Rev. E*, 58(2):R1241–R1244, 1998.

[15] Note that the critical compressional strain for Euler buckling [7] is $e_c \sim \tilde{\epsilon}\tilde{\kappa}^{-1}L^{-2}$, while the condition in Eq. 5.28 requires $e_0 >> \tilde{\epsilon}^{1/2}\tilde{\kappa}^{-1/2}L^{-1}$.

[16] R. E. Goldstein, A. Goriely, G. Huber, and C. W. Wolgemuth. Bistable helices. *Phys. Rev. Lett.*, 84(7):1631–1634, 2000.

[17] P. Dimitrakopoulos, J. F. Brady, and Z.-G. Wang. Short- and intermediate-time behavior of the linear stress relaxation in semiflexible polymers. *Phys. Rev. E*, 6405(5):art. no.–050803, 2001.

[18] R. Granek. From semi-flexible polymers to membranes: Anomalous diffusion and reptation. *J. Phys. II*, 7(12):1761–1788, 1997.

[19] U. Seifert, W. Wintz, and P. Nelson. Straightening of thermal fluctuations in semiflexible polymers by applied tension. *Phys. Rev. Lett.*, 77(27):5389–5392, 1996.

[20] B. A. DiDonna and T. A. Witten, *arXiv: cond-mat*, http://xxx.lanl.gov/ps/cond-mat/0104119, 2001.

[21] R. E. Goldstein, T. R. Powers, and C. H. Wiggins. Viscous nonlinear dynamics of twist and writhe. *Phys. Rev. Lett.*, 80(23):5232–5235, 1998.

[22] P. L. Hansen, D. Svensek, V. A. Parsegian, and R. Podgornik. Buckling, fluctuations, and collapse in semiflexible polyelectrolytes. *Phys. Rev. E*, 60(2):1956–1966, 1999.

Chapter 6

Dynamics of Supercoiling

We consider the dynamics of a twisted elastic chain held under tension using a combination of analytical theory and numerical simulation. The conditions of stability of a straight conformation are found by performing a linear stability analysis, resulting in a phase diagram that governs the behavior of the twisted chain. The instability is a helical buckle with tighter coils for larger twist deformation, and the chain ends become insignificant as the twist increases. We then analyze the post-buckling behavior by looking at the shape and energy of a localized loop structure that acts as the seed to a plectonemic supercoil. We find the formation of a loop under conditions where the straight conformation is stable is associated with an energetic barrier, thus supercoiling is an activated process that is accessible even under stable conditions. Numerical solution of the equations of motion of a twisted chain shows loop formation and subsequent plectoneme growth, localized near the chain ends.

6.1 Introduction

A rubber band that is clamped at each end and twisted several times maintains a straight conformation by applying sufficient end tension. Upon reducing the tension to some threshold value, helical undulations appear in the conformation. As the helices grow, they tend

to localize, and further growth results in looped structures in one or more locations. These loops flip over, and a plectoneme, composed of two interwound helices, emerges and grows from each loop. The plectonemes continue to grow until either their growth is arrested by the tension or they encompass the entire rubber band. This simple experiment demonstrates the supercoiling phenomenon, which plays a significant role in DNA biomechanics.

The study of the dynamics of twisted elastic threads is rooted in elasticity theory [1, 2], which focuses on the energetics of deformation and the conditions of mechanical stability. The hydrodynamic influence on slender bodies in motion acts to deform elastic objects and is the driving force for the motion of bacteria [3, 4]. The dynamics of slender elastic filaments combines elasticity theory with the effects of hydrodynamics; studies concerning the motion of filaments have recently devoted attention to several biological applications including DNA motion and bacterial propulsion [5, 6, 7]. The further influence of thermal fluctuations introduces additional effects that significantly impact the chain behavior, both at single-molecule and macroscopic length scales [8, 9].

The transition from a straight conformation to a supercoiled conformation marks the point where twist deformation overcomes the elastic resistance to bending deformation. This transition is important in a wide range of applications, including undersea cables [10] and DNA mechanics [11]. The nature of the transition involves a competition between a helical or solenoid state and a supercoiled plectoneme state. Energetic arguments suggest the plectoneme state is preferred over the solenoid state [12]; however, the dynamic transition involves a buckling process similar in nature to buckling due to compression [13, 14]. Such a buckling transition involves a homogeneous wavelike instability; in contrast, the formation of a plectoneme requires the localization of the instability to form a loop. Such helix localization is theoretically observed in a twisted chain [15, 11, 16, 17], and loop formation

is analyzed to predict the conditions of loop growth and elimination [10]. Our focus in this paper is on the transition from a straight conformation and on the energy of the growing looped structure.

In this paper, we analyze the dynamics of a twisted elastic filament held under tension. We focus on the nature of the transition between a straight conformation and a plectonemic supercoil. In Sec. 6.2, we find the conditions that govern the stability of the twisted chain by performing a linear stability analysis. In Sec. 6.3, we analyze the post-buckling behavior of the twisted chain, focusing on the shape and energy of a localized loop structure that seeds the formation of a plectonemic supercoil. Section 6.4 presents numerical solutions of the dynamic equations of motion of a twisted chain for comparison with our analytical results.

6.2 Linear Stability Analysis

We consider the dynamics of a single polymer chain immersed in a quiescent fluid. The polymer centerline coincides with a continuous spacecurve $\vec{r}(s)$ where the arclength parameter s, indicating the location along the chain, runs from $-L/2$ at one end of the chain to $L/2$ at the other end. At each location along the chain, we attach a material orientation triad $\vec{t}_i$ $(i = 1, 2, 3)$ and align the unit vector $\vec{t}_3$ in the direction of the chain tangent vector ($\vec{t}_3 = \partial_s\vec{r}/|\partial_s\vec{r}|$). The rotation of the material triad along the filament centerline, which characterizes the chain deformation, is concisely stated by the kinematic relationship $\partial_s\vec{t}_i = \vec{\omega}\times\vec{t}_i$ where $\vec{\omega}$ is the strain vector. The components of $\vec{\omega}$ decompose into bending and twisting modes of deformation, with ω_1 and ω_2 contributing to the chain bending curvature, and ω_3 identifying the twist rate [1].

The total energy of the polymer chain contains several contributions. The chain de-

formation energy at the lowest order in elasticity theory is expressed as a quadratic-order function in the components of $\vec{\omega}$ [1, 2]. The resistance of a slender elastic filament to compression/extension is much larger than the contributions due to bending and twisting, thus the polymer chain is effectively inextensible, requiring a Lagrange constraint that enforces $g \equiv \sqrt{\partial_s \vec{r} \cdot \partial_s \vec{r}} - 1 = 0$ [5]. The chain tension is included in the dynamics by introducing an energetic term that couples the end-to-end vector $\vec{r}(L/2) - \vec{r}(-L/2)$ to the tension vector $\vec{f} = f\hat{z}$, and the chain self-interaction is given by a potential that is strictly a function of the distance between chain segments $r(s, s') = |\vec{r}(s) - \vec{r}(s')|$. The total energy is given by

$$\begin{aligned} U &= \frac{A}{2}\int_{-L/2}^{L/2} ds \left(\omega_1^2 + \omega_2^2\right) + \frac{B}{2}\int_{-L/2}^{L/2} ds \omega_3^2 - \int_{-L/2}^{L/2} ds \Lambda g \\ &\quad -\vec{f} \cdot \int_{-L/2}^{L/2} ds (\partial_s \vec{r} - \hat{z}) + \frac{1}{2}\int_{-L/2}^{L/2} ds \int_{-L/2}^{L/2} ds' V[r(s, s')], \end{aligned} \tag{6.1}$$

where A and B are the bending and twisting moduli respectively, Λ is a Lagrange tension that enforces the constraint $g = 0$, and $V(r)$ is the functional form of the chain self-interaction.

The equations of motion for the centerline drift and the rotation about the tangent vector are respectively found by a force and moment balance at each point along the chain [18, 6]. Since we consider over-damped viscous dynamics, the inertial forces are neglected. Furthermore, we choose a simple expression for the hydrodynamic resistance to filament motion and rotation that is local and linear in the velocity and angular velocity of the filament. The hydrodynamic drag force per unit length due to filament drift is given by $-\mathbf{\Gamma} \cdot \partial_t \vec{r}$, where generally the resistance tensor is written as $\mathbf{\Gamma} = \Gamma_{\parallel} \vec{t}_3 \vec{t}_3 + \Gamma_{\perp}\left(\mathbf{I} - \vec{t}_3 \vec{t}_3\right)$ to distinguish between chain motion in the tangential and normal directions. The hydrodynamic resistance per unit length due to filament rotation about the centerline is given by $-\Gamma_R \partial_t \alpha$, where α

is the rotation angle about the tangent vector. In this study, we neglect additional forces and moments due to Brownian motion.

As a matter of convenience, we express our final equations of motion in terms of the twist density ω_3 instead of the rotation angle α. The equations of motion for the dynamical variables $\vec{r}$ and ω_3 are found, after some manipulations of the force and moment balance equations, to be

$$\mathbf{\Gamma} \cdot \frac{\partial \vec{r}}{\partial t} = -A\frac{\partial^4 \vec{r}}{\partial s^4} + B\frac{\partial}{\partial s}\left(\omega_3 \frac{\partial \vec{r}}{\partial s} \times \frac{\partial^2 \vec{r}}{\partial s^2}\right) + \frac{\partial}{\partial s}\left(\Lambda \frac{\partial \vec{r}}{\partial s}\right) - \int_{-L/2}^{L/2} ds' \frac{\partial V}{\partial r}\vec{e}(s,s'), \quad (6.2)$$

$$\frac{\partial \omega_3}{\partial t} = \frac{B}{\Gamma_R}\frac{\partial^2 \omega_3}{\partial s^2} + \left(\frac{\partial \vec{r}}{\partial s} \times \frac{\partial^2 \vec{r}}{\partial s^2}\right) \cdot \frac{\partial}{\partial s}\left(\frac{\partial \vec{r}}{\partial t}\right), \quad (6.3)$$

where $\vec{e}(s,s') = (\vec{r}(s) - \vec{r}(s'))/|\vec{r}(s) - \vec{r}(s')|$, and we must solve for $\Lambda(s,t)$ by satisfying $\partial_t g = 0$. We note the absence of the chain tension f in Eqs. 6.2 and 6.3 as it appears in the boundary conditions at the chain ends. The terms on the right-hand side of Eq. 6.3 are identified as the geometric modes of altering the local twist deformation; the first term is the contribution due to inhomogeneous chain rotation, and the second term accounts for writhing motion of the chain.

We consider a chain with clamped ends, thus the chain ends are fixed such that $\hat{x} \cdot \vec{r} = \hat{y} \cdot \vec{r} = 0$ at $s = \pm L/2$, and the tangent vector is aligned along the z axis ($\hat{x} \cdot \partial_s \vec{r} = \hat{y} \cdot \partial_s \vec{r} = 0$ at $s = \pm L/2$). Since the chain ends are free to slide along the z axis, the boundary conditions of the z component of $\vec{r}$ at the chain ends is determined through the force balance; the z component boundary conditions are $\hat{z} \cdot \partial_s^2 \vec{r} = 0$ and, making use of the length constraint, $\hat{z} \cdot \partial_s^3 \vec{r} = -\left|\partial_s^2 \vec{r}\right|^2$. From the force balance, we also find the boundary condition on the Lagrange tension to be $\Lambda = f - A\left|\partial_s^2 \vec{r}\right|^2$. Finally, the clamped ends cannot rotate about the tangent vector ($\partial_t \alpha = 0$ at $s = \pm L/2$), which is equivalent to the condition $\partial_s \omega_3 = 0$.

We consider an initially straight, twisted filament undergoing relaxation dynamics. Defining the Twist as $\int_0^L ds\omega_3/(2\pi)$, we can write the initial conditions for our filament as $\vec{r} = s\hat{z}$, $\omega_3 = 2\pi \mathrm{Tw}_0/L = \omega_0$, and $\Lambda = f$; we define Tw_0 as the initial number of twists within the conformation and ω_0 as the initial twist density. The dynamics of small amplitude deviations from the straight conformation are governed by the linearized representation of Eqs. 6.2 and 6.3. Defining the complex normal as $\vec{\epsilon} \equiv \hat{x} + i\hat{y}$ and the complex normal amplitude as $\psi \equiv X(s) + iY(s)$ [19], the nearly straight conformation is written as $\vec{r}(s) = \mathrm{Re}\left(\psi\vec{\epsilon}^*\right) + \left(s - \delta(s)\right)\hat{z}$ where the compression along the z axis δ is necessary in maintaining the chain length constraint. Inserting this expression for $\vec{r}$ into Eq. 6.2 and defining the dimensionless arclength parameter $\rho = s/L$ and time $\tau = tA/(\Gamma_\perp L^4)$, we have the equation for the normal-direction dynamics

$$\frac{\partial\psi}{\partial\tau} = -\frac{\partial^4\psi}{\partial\rho^4} + i\mathcal{B}\frac{\partial^3\psi}{\partial\rho^3} + \mathcal{F}\frac{\partial^2\psi}{\partial\rho^2}, \tag{6.4}$$

where $\mathcal{B} = 2\pi B\mathrm{Tw}_0/A$ and $\mathcal{F} = fL^2/A$. Similar equations can be derived for the dynamics of δ and ω_3; however, the results are quadratic in ψ at lowest order, thus Eq. 6.4 is decoupled from these dynamics at linear order.

Eq. 6.4 takes the form of a wave equation. Defining the Hermitian operator $\mathcal{H} = -\partial_\rho^4 + i\mathcal{B}\partial_\rho^3 + \mathcal{F}\partial_\rho^2$, the function ψ can be decomposed into eigenfunctions Ψ_n of $\mathcal{H}$ with eigenvalues σ_n, where we adopt the convention of numbering our eigenfunctions in terms of eigenvalue size with $n = 1$ corresponding to the largest eigenvalue. The eigenfunctions of $\mathcal{H}$ represent natural relaxation modes; therefore, these functions are useful in both describing the behavior of dynamic instability [6] as well as the relaxation spectrum of a thermally fluctuating twisted elastic filament under tension [8, 9]. Generally, the eigenfunctions Ψ_n

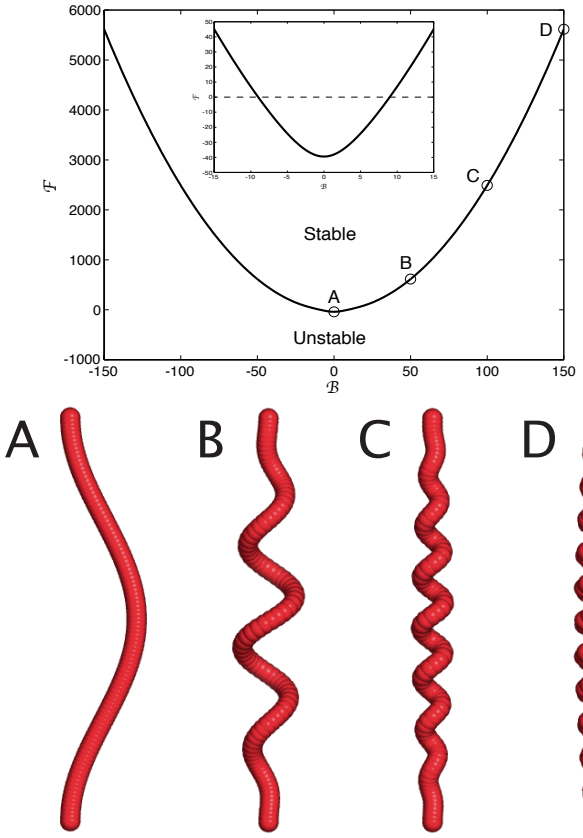

Figure 6.1: The stability diagram of a twisted polymer chain under tension, identifying $\mathcal{B}$ and $\mathcal{F}$ (defined in the text) at the onset of instability. The inset shows the behavior near $\mathcal{B} = 0$, and the conformations for the points A, B, C, and D are shown below the stability diagram.

take the form $\sum_{\mu=1}^{4} C_n^{(\mu)} \exp\left(ik_n^{(\mu)}\rho\right)$ with $k_n^{(\mu)}$ being the four roots of $\sigma_n = -k_n^4 + \mathcal{B}k_n^3 - \mathcal{F}k_n^2$. For fixed values of $\mathcal{B}$ and $\mathcal{F}$, the eigenvalues σ_n are found self-consistently by satisfying the boundary conditions $\psi = \partial_\rho \psi = 0$ at the chain ends ($\rho = \pm 1/2$).

We construct a stability diagram by finding the relationship between $\mathcal{B}$ and $\mathcal{F}$ that results in an eigenvalue of zero, which is equivalent to solving the linearized Euler-Lagrange equation. Such solutions for Ψ_n take the form $\Psi_n = C_n^{(1)} + C_n^{(2)}\rho + C_n^{(3)} \exp\left(ik_n^{(3)}\rho\right) + C_n^{(4)} \exp\left(ik_n^{(4)}\rho\right)$ where $k_n^{(3)} = \left(\mathcal{B} + \sqrt{\mathcal{B}^2 - 4\mathcal{F}}\right)/2$ and $k_n^{(4)} = \left(\mathcal{B} - \sqrt{\mathcal{B}^2 - 4\mathcal{F}}\right)/2$. Satis-

fying the boundary conditions, we find the zero growth eigenfunctions obey the relationship

$$\cos\left(\frac{\mathcal{B}}{2}\right) + \frac{\mathcal{F}}{\sqrt{\mathcal{B}^2 - 4\mathcal{F}}} \sin\left(\frac{\sqrt{\mathcal{B}^2 - 4\mathcal{F}}}{2}\right) = \cos\left(\frac{\sqrt{\mathcal{B}^2 - 4\mathcal{F}}}{2}\right) \tag{6.5}$$

between $\mathcal{B}$ and $\mathcal{F}$. For a fixed value $\mathcal{B}$, there are an infinite number of values of $\mathcal{F}$ that satisfy Eq. 6.5, each value corresponding to the point where one of the eigenfunctions goes from decaying to growing. The solution with the largest value of $\mathcal{F}$ corresponds to the point of initial instability.

In Fig. 6.1, we show a stability diagram for an initially straight, twisted chain subjected to end tension as determined from Eq. 6.5. The inset in Fig. 6.1 shows the behavior near $\mathcal{B} = 0$ where the tension at the instability becomes negative; for $\mathcal{B} = 0$, instability occurs at $\mathcal{F} = -4\pi^2$ [2]. Below the stability diagram, we provide the conformations for the points A, B, C, and D indicated in the stability diagram. Conformation A, with negative tension, corresponds to buckling due to end compression, and the conformations B, C, and D, occur due to the effect of increasing the twist in the initial conformation. Conformations B, C, and D are essentially helical with a deviation near the clamped ends to accommodate the boundary conditions. As the twist increases, the wavelength of the initial instability shortens, and the ends become less significant as $\mathcal{B}$ becomes large. In fact, Fig. 6.1 tends to $\mathcal{F} = \mathcal{B}^2/4$ for $\mathcal{B} \gg 1$, which is equivalent to $f = B^2\omega_0^2/(4A)$ (entirely independent of the chain length L); this result exactly agrees with the stability criterion for an infinite chain [10].

For conditions that lie below the stability diagram, small amplitude transverse fluctuations in the conformation will spontaneously grow with a dominant shape given by Ψ_1, the fastest growing eigenfunction. The initial undulations are essentially helical, which is

analogous to a solenoid conformation in a twisted elastic ring. Under these conditions, it has been shown that although the solenoid conformation is energetically favorable over the straight conformation, plectonemic or supercoiled structures are yet lower in energy [12]. Furthermore, the post-buckling behavior of a twisted elastic filament under tension is shown to exhibit localization and loop formation [11] thus seeding the formation of plectonemes. In the next section, we consider the post-buckling behavior of the twisted strand, focusing on the formation of loops that lead to plectonemic supercoils.

6.3 Post-Buckling Behavior

In the previous section, we found through linear stability analysis that the dominant shape of the instability is helical with a slight deviation near the ends to account for the clamped boundary conditions. However, a twisted elastic thread tends to exhibit localization of the deformation into a loop [15, 11, 17, 16], which seeds the formation of a plectoneme. The plectoneme is energetically favored over the helical solenoid due to its efficiency in alleviating the twist deformation; the interwound helices of a plectoneme eliminate twice the twist per turn as a single helix [12]. In this section, we address the shape and energy of the filament throughout the transition from straight to looped structure in order to understand the idealized formation of a plectoneme and the nature of the transition.

Although the analysis of the previous section is rooted in the dynamic equations of motion, we make use of purely energetic arguments in this section. We assume that for conditions very near the stability curve in Fig. 6.1, the viscous motion of the chain is sufficiently slow such that the conformation proceeds at an energy minimum. Therefore, we perform a quasi-equilibrium analysis in this section of the shape of the filament as it proceeds through the formation of a single loop structure. We specialize our analysis in this section

to conditions where the end effects are negligible or $\mathcal{B} \gg 1$ (previous section). Furthermore, this simple analysis neglects the effect of self-interaction of the chain, which is required to address the formation of the full plectoneme structure. Nonetheless, the initial stage of plectoneme formation is accessible without self-interaction, provided the loop structure is large relative to the diameter of the filament [10]. The looping process studied in Ref. [10] provides the foundation for our analysis of plectoneme formation; in this section, we review and adapt the results of Ref. [10] to our system.

To begin, we define an energy that contains contributions from bending and twisting deformation along with a constraint that fixes the chain ends at a specified distance apart. The constrained energy U_T is given by

$$U_T = \int_{-L/2}^{L/2} ds u_T, \tag{6.6}$$

where

$$u_T = \frac{A}{2}\left(\omega_1^2 + \omega_2^2\right) + \frac{B}{2}\omega_3^2 - T\left(1 - \hat{z}\cdot\vec{d}_3\right). \tag{6.7}$$

The Lagrange multiplier T in Eq. 6.7 enforces the length of the chain retraction along the z-axis, thus it is the conjugate variable to $\Delta = \int_{-L/2}^{L/2} ds \left(1 - \hat{z}\cdot\vec{d}_3\right)$. The energy density defined by Eq. 6.7 is not to be confused with the actual energy density of the filament u, which is extracted from Eq. 6.1 to be

$$u = \frac{A}{2}\left(\omega_1^2 + \omega_2^2\right) + \frac{B}{2}\omega_3^2 + f\left(1 - \hat{z}\cdot\vec{d}_3\right) \tag{6.8}$$

after neglecting the self-interaction energy.

Thus far, we have described the chain conformation using cartesian coordinates; how-

ever, general shapes of elastica are better described using Euler angles (ϕ, θ, ψ) [20], as their use does not require complicated kinematic relationships to constrain the length of the chain. The equations that govern equilibrium shapes for a twisted chain that is clamped and held under tension are given by [1]

$$u_T = \frac{A}{2}\left(\omega_1^2 + \omega_2^2\right) + \frac{B}{2}\omega_3^2 - T\left(1 - \cos\theta\right) = \text{constant}, \tag{6.9}$$

$$m = -A\omega_1 \sin\theta\cos\psi + A\omega_2 \sin\theta\sin\psi + B\omega_3\cos\theta = \text{constant}, \tag{6.10}$$

$$\omega_3 = \frac{\partial\psi}{\partial s} + \frac{\partial\phi}{\partial s}\cos\theta = \text{constant}. \tag{6.11}$$

Eqs. 6.9 through 6.11 are found using the symmetries of the equilibrium conformation, namely invariance with respect to "time" (or path length), rotation about the z-axis, and rotation about the tangent vector. The conformation is found from the Euler angles using the differential relationships: $\hat{x}\cdot\partial_s\vec{r} = \sin\theta\cos\phi$, $\hat{y}\cdot\partial_s\vec{r} = \sin\theta\sin\phi$, and $\hat{z}\cdot\partial_s\vec{r} = \cos\theta$. The other curvature terms are related to the Euler angles through $\omega_1 = \partial_s\theta\sin\psi - \partial_s\phi\sin\theta\cos\psi$ and $\omega_2 = \partial_s\theta\cos\psi + \partial_s\phi\sin\theta\sin\psi$.

Since Eqs. 6.9 through 6.11 are constant for any point along the chain, the constants are evaluated by dictating the values at a single point. Taking into account the end conditions ($\theta = \partial_s\theta = 0$ at $s = \pm L/2$), Eqs. 6.9 and 6.10 can be written as

$$u_T = \frac{B\omega_3^2}{2} \tag{6.12}$$

$$m = B\omega_3. \tag{6.13}$$

From this, we arrive at the governing equations for the chain conformation

$$\left|\frac{\partial\theta}{\partial S}\right| = 2\tan\left(\frac{\theta}{2}\right)\sqrt{\cos^2\left(\frac{\theta}{2}\right) - C^2}, \tag{6.14}$$

$$\frac{\partial\phi}{\partial S} = \frac{C}{\cos^2\left(\frac{\theta}{2}\right)}, \tag{6.15}$$

where $C = B\omega_3/(2\sqrt{AT})$. All lengths are non-dimensionalized by $\sqrt{A/T}$, and $S = s\sqrt{T/A}$. For $L \gg 1$, Eq. 6.14 has the approximate solution

$$\sin\left(\frac{\theta}{2}\right) = \frac{\sqrt{1-C^2}}{\cosh\left(S\sqrt{1-C^2}\right)}, \tag{6.16}$$

and ϕ is found from the solution for θ to be

$$\phi = CS + \arctan\left\{\frac{\sqrt{1-C^2}\tanh\left(S\sqrt{1-C^2}\right)}{C}\right\}. \tag{6.17}$$

These equations give the conformation of a growing loop structure from a straight, twisted chain for sufficiently long chains ($\left|\sqrt{1-C^2}L/2\right| \gg 1$). As the conformation proceeds through the loop formation, the twist density ω_3 changes from the initial twist density ω_0 due to the writhe of the looped structure. The Lagrange tension T also responds to the transition. The straight conformation corresponds to a value of $C = 1$ or $T = B^2\omega_0^2/(4A)$, which agrees with the conditions for instability found in the previous section.

In Fig. 6.2, we show the formation of a loop via a quasi-equilibrium transition using Eqs. 6.16 and 6.17. Each of the conformations in Fig. 6.2 represents a stable structure for the tension T found in C, which marks the progress through the transition. The beginning of the transition occurs through a helical formation, much like the structures analyzed in the previous section. However, further progress shows a localization of the helix into a loop

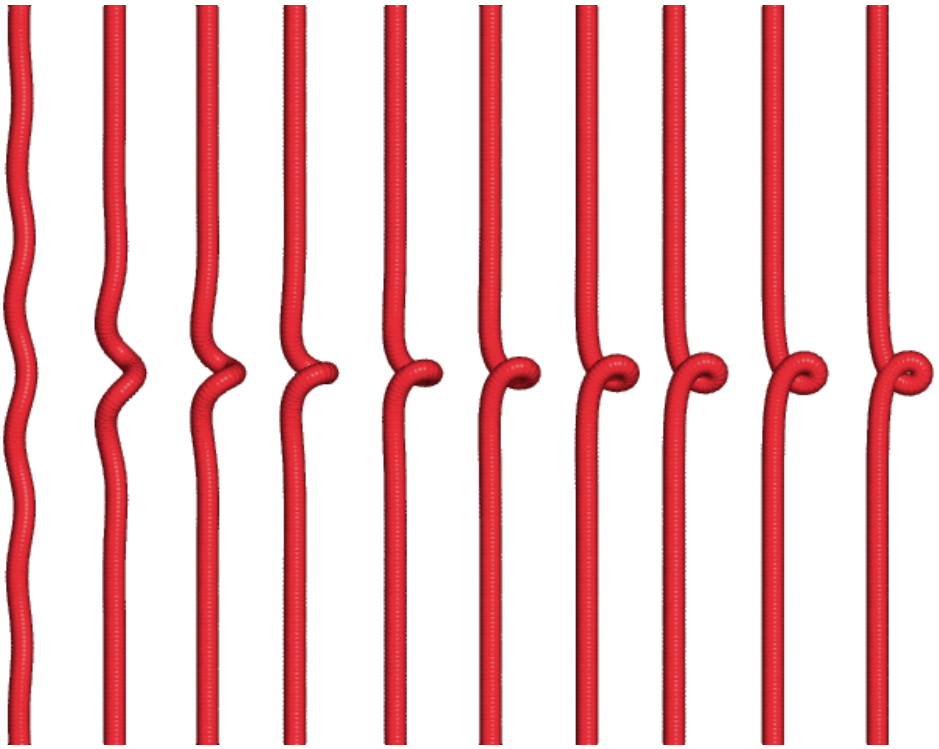

Figure 6.2: Equilibrium conformations for the looping transition determined from Eqs. 6.16 and 6.17. These snapshots represent, from left to right, the stable conformations for $C =$ 0.99, 0.89, 0.79, 0.69, 0.59, 0.49, 0.39, 0.29, 0.19, and 0.09. The length scale in this figure is scaled by $\sqrt{A/T}$.

structure similar to that found in Ref. [11]. This loop formation marks the initial stage of plectoneme formation.

We now turn to the energy of the growing loop. The energetic contributions are found using Eqs. 6.16 and 6.17 along with the total energy (Eq. 6.1). This calculation makes use of the relationship between the retraction distance Δ and the tension T found in Ref. [10], which is given by

$$T = \frac{B^2}{4A} \frac{\left[\omega_0 - \frac{4}{L} \arcsin\left(\frac{\Delta}{4}\sqrt{\frac{T}{A}}\right)\right]^2}{1 - \left(\frac{\Delta}{4}\sqrt{\frac{T}{A}}\right)^2}, \tag{6.18}$$

which is a transcendental equation for T in terms of Δ and the material parameters of the chain. Equation 6.18 exhibits a double value for T at a given retraction distance Δ; this double value is the source of an instability associated with looping and popping-out [10].

The total energy of the looped chain is given by an integral of the energy density, which is found from Eqs. 6.7 and 6.8 to be

$$u = T\left(1 - \cos\theta\right) + \frac{B}{2}\omega_3^2 + f\left(1 - \cos\theta\right). \tag{6.19}$$

The first term in Eq. 6.19 is the bending deformation energy, the second term is the twisting deformation energy, and the third term is the work against the external load f. The total energy is given by

$$U = \frac{BL}{2}\left[\omega_0 - \frac{4}{L}\arcsin\left(\frac{\Delta}{4}\sqrt{\frac{T}{A}}\right)\right]^2 + (f+T)\Delta, \tag{6.20}$$

where the Lagrange tension T is found using Eq. 6.18. The total energy represents a non-equilibrium energy function relating the energy to the distance of retraction Δ, and the equilibrium value of Δ is determined by the minimization of Eq. 6.20.

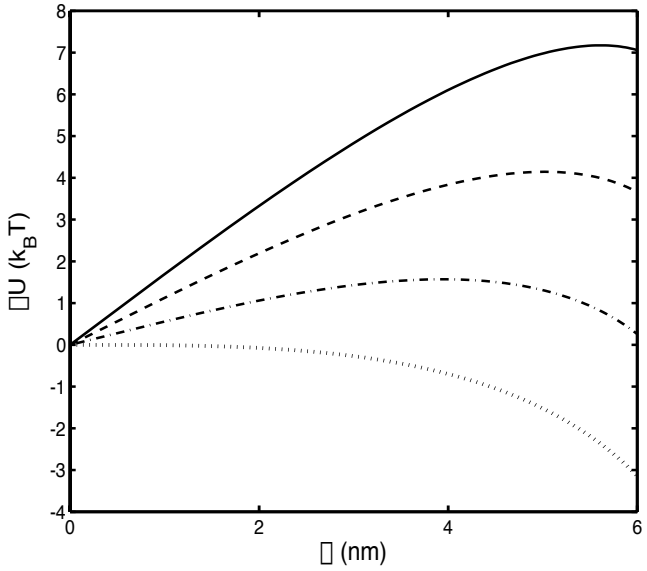

Figure 6.3: The total energy $\Delta U = U - U(\Delta = 0)$ (in k_BT) versus the end retraction Δ (in nm) for a chain with $A = B = 50\,k_BT\,\text{nm}$, $L = 1000\,\text{nm}$, and 100 turns of twist ($\omega_0 = 0.6283\,\text{nm}^{-1}$) subjected to end tension $f = 20.2327\,\text{pN}$ (dotted curve), $f = 22.5561\,\text{pN}$ (dashed-dotted curve), $f = 24.8796\,\text{pN}$ (dashed curve), and $f = 27.2031\,\text{pN}$ (solid curve).

In Fig. 6.3, we plot the total energy $\Delta U = U - U(\Delta = 0)$ (Eq. 6.20) measured in units of the thermal energy k_BT versus the end retraction Δ (in nm) for a chain forming a looped structure from a straight conformation. The properties of the chain in Fig. 6.3 are $A = B = 50\,k_BT\,\text{nm}$, $L = 1000\,\text{nm}$, and 100 turns of twist ($\omega_0 = 0.6283\,\text{nm}^{-1}$), and the end tension f is $f = 20.2327\,\text{pN}$ (dotted curve), $f = 22.5561\,\text{pN}$ (dashed-dotted curve), $f = 24.8796\,\text{pN}$ (dashed curve), and $f = 27.2031\,\text{pN}$ (solid curve). We note that for $f = 20.2327\,\text{pN}$ (dotted curve) the conditions are at the point of instability governed by the stability diagram (Fig. 6.1), thus the other curves with larger tension f show the non-equilibrium looping energy for conditions in the stable region of Fig. 6.1. These curves exhibit an initial increase in the energy with the end retraction; however, these energy plots eventually turn and decrease with further end retraction. The chain properties in Fig. 6.3 correspond to the material properties of a 3000 basepair strand of DNA subjected to end tension. The predictions of Fig. 6.3 demonstrate an energy barrier to the formation of a

loop for tensions above the stability curve; although the straight conformation is stable, loop growth eventually leads to an energy decrease and the subsequent growth of a plectoneme.

In this analysis, we neglect thermal fluctuations. The non-equilibrium energy displayed in Fig. 6.3 suggests that loop formation requires an energetic nudge in order to overcome a barrier for sufficient end tension (conditions above the stability diagram in Fig. 6.1). A molecular strand is subject to thermal fluctuations with characteristic energy k_BT, thus energies comparable to k_BT are attainable by a fluctuating strand. For the conditions in Fig. 6.3, thermal energy can easily overcome the boundary to loop formation, thus an AFM or tweezer experiment conducted under these conditions is predicted to exhibit transient loop formations leading to plectonemic supercoils, even under stable conditions.

In the following section, we numerically solve the equations of motion found in Sec. 6.2 in order to show the progression from straight, twisted chain through the instability and the subsequent nonlinear dynamics. In particular, we compare and contrast the predictions of this section to assess the validity of the pseudo-equilibrium approximation.

6.4 Nonlinear Dynamics

In this section, we numerically solve Eqs. 6.2 and 6.3 in order to see the full relaxation behavior of a twisted elastic chain held under tension. Our mathematical analyses in the previous two sections provide insight into the nature of the instability; however, the contribution of chain self contact is neglected in our treatment. The dynamics in this section include the self contact, which becomes important after the initial instability.

For a value of $\mathcal{B} = 150$ (see Sec. 6.2), the initial instability occurs for a force $\mathcal{F} \approx 5615.12$, indicated by point D in Fig. 6.1. If the force is reduced to $\mathcal{F} = 4700$, the straight conformation becomes unstable with a dominant growth rate $\sigma_1 \approx 5.86 \times 10^6$. We evaluate

the post-buckling, nonlinear dynamics using a discrete representation of the polymer-chain model. We solve the discrete analogues of Eqs. 6.2 and 6.3 for an initially straight polymer chain, with a small random transverse perturbation, with twist $\mathcal{B} = 150$ and tension $\mathcal{F} = 4700$ including a contact term in the energy (Eq. 6.1) such that the chain cannot cross itself.

In Fig. 6.4, we show snapshots from the relaxation dynamics at several points in time, which is nondimensionalized by the time-scale of instability growth $\tau_{inst} = \Gamma_\perp L^4/(A\sigma_1)$. The first snapshot, occurring at $t/\tau_{inst} = 7.30$, shows the conformation just beyond the initial instability, which looks similar to conformation D in Fig. 6.1. Further growth of the instability shows the localization of the helical undulations into loops near the ends of the chain. Since the chain is of fixed length, the chain ends must retract during the transverse growth, which is responsible for the helical localization near the chain ends. The loop formation leads to the growth of plectonemes, which twirl out into the quiescent fluid as the ends retract. From the fourth snapshot ($t/\tau_{inst} = 29.27$) to the final snapshot ($t/\tau_{inst} = 747.34$), the two plectonemes grow as they are fed by the connecting chain segment, thus the chain is reptating within each plectoneme as they grow. We note the plectonemes trail off the ends due to the viscous drag as the chain ends are pulled towards each other. The final snapshot in Fig. 6.4 shows the plectonemes in the final conformation eventually cease to grow as they encompass the entire chain. Further relaxation shows the two plectoneme straighten perpendicular to the tension direction; however, this process is extremely slow in comparison to the dynamics shown here.

We find an interesting phenomenon occurs if we decrease the tension further than the quench in Fig. 6.4; the retraction of the chain ends occur faster than the loop collapses on itself. This has different ramifications depending on the method that the chain ends are clamped. If the ends are clamped between two bars, the chain will loop around the bars

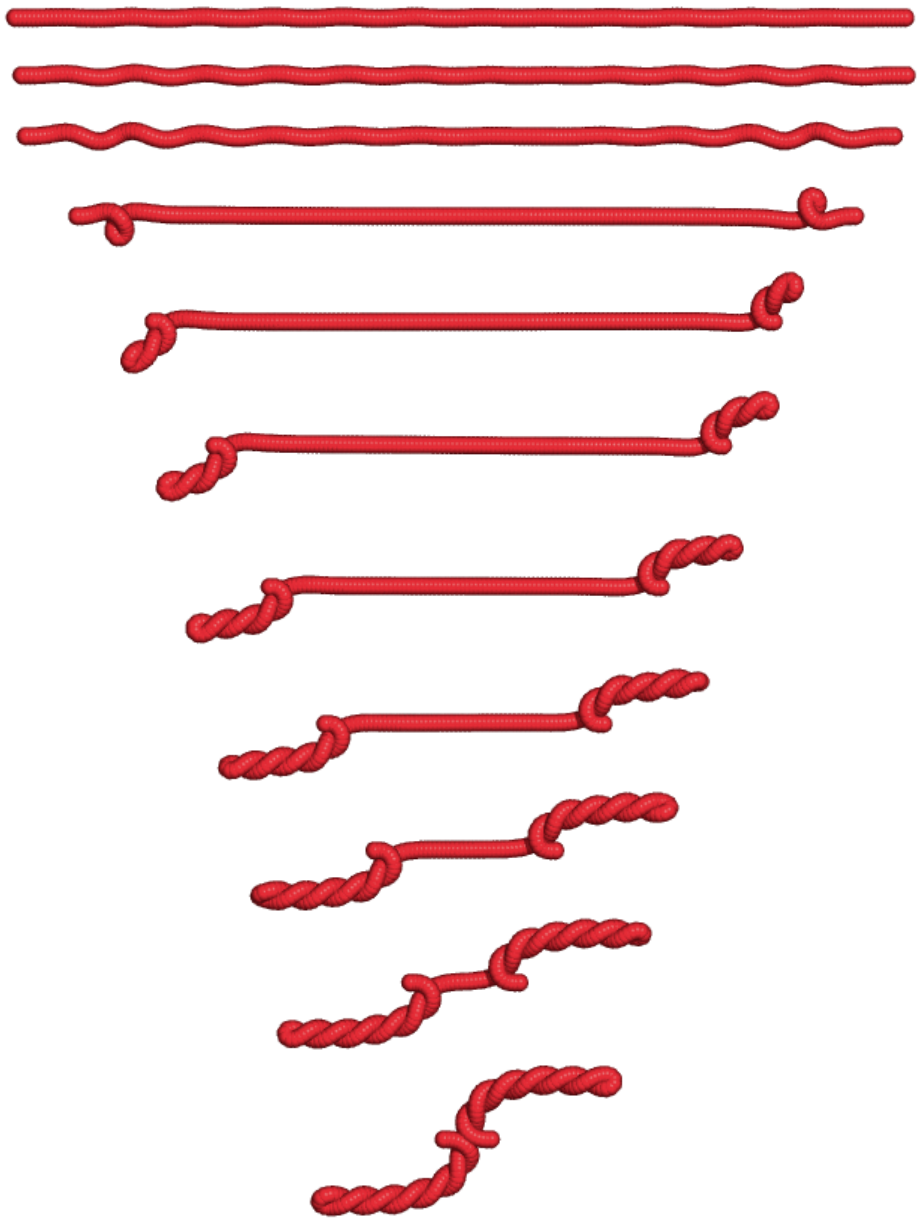

Figure 6.4: Snapshots from the relaxation dynamics for $\mathcal{B} = 150$ and $\mathcal{F} = 4700$. The snapshots are for $t/\tau_{inst} = 7.30, 11.60, 18.43, 29.27, 46.50, 73.87, 117.35, 186.42, 296.15, 470.45, 747.34$, respectively.

at each end and climb them as they are pulled towards each other. If the chain ends are fixed in space, as in an optical tweezers experiment, the chain is looped around the ends several times, and then the chain is extended due to the elimination of the twist during this process.

The dynamics presented in Fig. 6.4 suggest the chain ends play the role of nucleation sites for plectoneme growth; however, in the case of DNA, several other factors may seed the growth of supercoils. For example, sequence-specific elasticity has a dramatic effect on the coiling of DNA around nucleosome particles [21]; therefore, we expect sequence-dependent weak spots to serve as nucleation sights for supercoiling as well. Also, if the chain conformation is not initially straight, as is certainly the case in DNA, the formation of plectonemes is more likely to occur at locations of high curvature, since they form the plectoneme end and also serve as a tension gradient to feed the growing plectoneme. In this analysis, we neglect the role of thermal fluctuations; however, their effect would change the dynamic behavior. For example, the stable region in the stability diagram (Fig. 6.1) results in a stable straight chain; however, thermal fluctuations would allow the formation of the loop structures shown in Fig. 6.2, leading to plectonemic supercoiling.

Bibliography

[1] A. E. H. Love. *A Treatise on the Mathematical Theory of Elasticity.* Dover Publications, Inc., New York, NY, 1944.

[2] L. D. Landau and E. M. Lifshitz. *Theory of Elasticity.* Pergamon Press, 1986.

[3] J. J. L. Higdon. Hydrodynamics of flagellar propulsion - helical waves. *J. Fluid Mech.*, 94(SEP):331–351, 1979.

[4] R. E. Johnson. An improved slender-body theory for Stokes-flow. *J. Fluid Mech.*, 99(JUL):411–431, 1980.

[5] R. E. Goldstein and S. A. Langer. Nonlinear dynamics of stiff polymers. *Phys. Rev. Lett.*, 75(6):1094–1097, 1995.

[6] R. E. Goldstein, T. R. Powers, and C. H. Wiggins. Viscous nonlinear dynamics of twist and writhe. *Phys. Rev. Lett.*, 80(23):5232–5235, 1998.

[7] R. E. Goldstein, A. Goriely, G. Huber, and C. W. Wolgemuth. Bistable helices. *Phys. Rev. Lett.*, 84(7):1631–1634, 2000.

[8] F. Gittes and F. C. MacKintosh. Dynamic shear modulus of a semiflexible polymer network. *Phys. Rev. E*, 58(2):R1241–R1244, 1998.

[9] V. Shankar, M. Pasquali, and D. C. Morse. Theory of linear viscoelasticity of semiflexible rods in dilute solution. *J. Rheol.*, 46(5):1111–1154, 2002.

[10] J. Coyne. Analysis of the formation and elimination of loops in twisted cable. *IEEE J. Ocean. Eng.*, 15(2):72–83, 1990.

[11] G. H. M. van der Heijden and J. M. T. Thompson. Helical and localised buckling in twisted rods: A unified analysis of the symmetric case. *Nonlinear Dyn.*, 21(1):71–99, 2000.

[12] J. F. Marko and E. D. Siggia. Fluctuations and supercoiling of DNA. *Science*, 265(5171):506–508, 1994.

[13] L. Golubovic, D. Moldovan, and A. Peredera. Flexible polymers and thin rods far from equilibrium: Buckling dynamics. *Phys. Rev. E*, 61(2):1703–1715, 2000.

[14] A. J. Spakowitz and Z.-G. Wang. Free expansion of elastic filaments. *Phys. Rev. E*, 6406(6):art. no.–061802, 2001.

[15] A. R. Champneys and J. M. T. Thompson. A multiplicity of localized buckling modes for twisted rod equations. *Proceedings of the Royal Society of London Series a-Mathematical Physical and Engineering Sciences*, 452(1954):2467–2491, 1996.

[16] G. H. M. van der Heijden, S. Neukirch, V. G. A. Goss, and J. M. T. Thompson. Instability and self-contact phenomena in the writhing of clamped rods. *Int. J. Mech. Sci.*, 45(1):161–196, 2003.

[17] G. H. M. Van Der Heijden, A. R. Champneys, and J. M. T. Thompson. The spatial complexity of localized buckling in rods with noncircular cross section. *Siam Journal on Applied Mathematics*, 59(1):198–221, 1998.

[18] I. Klapper and M. Tabor. A new twist in the kinematics and elastic dynamics of thin-filaments and ribbons. *J. Phys. A-Math. Gen.*, 27(14):4919–4924, 1994.

[19] C. W. Wolgemuth, T. R. Powers, and R. E. Goldstein. Twirling and whirling: Viscous dynamics of rotating elastic filaments. *Phys. Rev. Lett.*, 84(7):1623–1626, 2000.

[20] M. E. Rose. *Elementary Theory of Angular Momentum*. Wiley, New York, NY, 1957.

[21] J. Widom. Role of DNA sequence in nucleosome stability and dynamics. *Q. Rev. Biophys.*, 34(3):269–324, 2001.

Chapter 7

DNA Packaging in Bacteriophage: Is Twist Important?

We study the packaging of DNA into a bacteriophage capsid using computer simulation, specifically focusing on the potential impact of twist on the final packaged conformation. We perform two dynamic simulations of packaging a polymer chain into a spherical confinement: one where the chain end is rotated as it is fed, and one where the chain is fed without end rotation. The final packaged conformation exhibits distinct differences in these two cases: the packaged conformation from feeding with rotation exhibits a spool-like character that is consistent with experimental and previous theoretical work, whereas feeding without rotation results in a folded conformation inconsistent with a spool conformation. The chain segment density shows a layered structure, which is more pronounced for packaging with rotation. However in both cases, the conformation is marked by frequent jumps of the polymer chain from layer to layer, potentially influencing the ability to disentangle during subsequent ejection. Ejection simulations with and without Brownian forces show that Brownian forces are necessary to achieve complete ejection of the polymer chain in the absence of external forces.

7.1 Introduction

The ability of bacteriophage to package, transport, and deliver its genome to a host bacterium involves the precise manipulation of DNA throughout the life cycle of the virus. Despite the apparent simplicity of most species of bacteriophage, their ability to control the conformation of DNA through physical manipulation is quite remarkable, a feat that is desirable in many different biological and technological settings. Therefore, developing a fundamental understanding of the physical mechanisms responsible for the exquisite control that bacteriophage has over its DNA is important for understanding the principles of DNA manipulation. In this chapter, we focus on the processes involved in the packaging of DNA into an empty viral capsid. Specifically, we address whether the twist rigidity of the DNA molecule plays an important role in affecting its conformation during the packaging process.

Although different species of bacteriophage can vary in many ways (host species, specific structural geometry, size of virus, size of genome/number of genes, as well as many important biochemical distinctions), they also share several important similarities that are relevant to our current discussion. A bacteriophage assembles its capsid particle before the genome is packaged; then the genome is inserted into the empty capsid by an ATP-driven packaging motor. As the capsid is filled with DNA, the packaging motor works against the increasing resistance associated with compacting the long polymer chain to near-crystalline density into the relatively small cavity. Once the new bacteriophage are packaged, the now-virulent viruses lyse the host cell and escape into the surrounding medium to infect other hosts, producing further progeny. The viruses no longer have access to the energy source ATP once outside their host; therefore, any work performed during infection must be stored within the virus particles before they leave the cell that produced them. Because of these similarities, experimental observations of specific bacteriophage species can be incorporated

into the general framework of DNA packaging.

The force generated by the bacteriophage ϕ29 packaging motor has been directly measured using optical tweezers [1], which showed a continuous build-up of the internal pressure as packaging proceeds. The measured stall force of 57 pN makes the ϕ29 packaging motor one of the most powerful protein motors known to date. Similarly, the pressurization of packaged phage λ has been confirmed by using osmotic pressure as a resistive force against DNA ejection, causing the ejection to cease and leaving partially filled capsid particles [2]. The internal pressure within these packaged viruses is directly related to the free energy cost of forcing the DNA into a small cavity and provides the energy for conversion to work in the injection of the DNA into the host cell.

A number of studies have addressed the DNA conformation within the capsid interior using various experimental techniques for several different viral species [3, 4, 5, 6, 7, 8, 9, 10, 11, 12, 13]. The experimental evidences have inspired potential models for DNA arrangement within the packaged capsid, including liquid crystal [8], folded toroid [14], coaxial spool [15, 4], folded coaxial spool [16], and concentric spool [17, 18]. By electron microscopy with image reconstruction, the conformation of the packaged genome of phage T7 [11, 12], T4 [9], and P22 [13] appears to adopt a spool-like conformation with several layers of order, consistent with the coaxial spool model, where the spools are ordered parallel to each other and perpendicular to the axis of the tail. However, flow linear dichroism studies of phage T4 suggest that the mean square value of the cosine of the angle between the tail axis and the DNA strand is inconsistent with the coaxial spool model, lending credit to the concentric spool model, where the spools are arranged at angles to each other [17, 18]. Recent theoretical work shows that the energetically preferred conformation of a polymer in a spherical confinement is consistent with the concentric spool model [19]. The packaged

conformation within a viral capsid remains an intriguing subject of debate.

Details of the packaging motor of $\phi 29$ suggest the potential for twist to play a role in the packaging process. From the crystal structure of the $\phi 29$ packaging motor, a mechanism for DNA translocation has been proposed whereby either the motor or the DNA itself is rotated during the process [20]. The proposed mechanism involves a 12^o rotation for every 2 basepairs that enter the capsid or a rate of rotation of roughly 1/6 the periodicity of the DNA double helix. By existing experimental evidence, it is not clear whether the DNA rotates during translocation; however, some results suggest that the final packaged conformation is twisted or supercoiled. For example, the conformation of the genomes of phage λ [21] and P22 [22] exhibit supercoiling when treated with cross-linker and released from their capsids, indicative of a certain degree of twist deformation trapped within the internalized conformation. Furthermore, bacteriophage $\phi 29$ genome with the covalently bound terminal protein gp3 exhibits supercoiling; the supercoiling is believed to be a prerequisite for efficient packaging [23].

If the DNA rotates as it enters the capsid, then either the DNA relaxes the twist deformation by axial rotation of the strand, or the conformation of the strand responds to the twist deformation in some way. Inspired by this possible mechanism, we address the problem of what qualitative features are altered in the packaged conformation if the DNA is rotated while it is fed into the capsid.

Twist plays an essential role in the biophysical behavior of DNA, particularly manifest in torsionally constrained DNA elements commonly present in plasmids of prokaryotes and transiently-closed loops in gene regulation in eukaryotes. For example, binding of the *lac* repressor of *Escherichia coli* is modulated by the length of DNA between binding sites, resulting in oscillations in the repression level as the length passes through integer numbers of

helical turns [24]. Twist affects the conformation of DNA through a well-known topological constraint on torsionally constrained paths, which states that the linking number is a sum of the twist and the writhe of the curve [25]. The underlying mathematical expressions for these topological entities dictate the allowable states of a closed chain; however, the thermodynamically preferred distribution between twist and writhe is determined by the energetics of the chain conformation. The importance of chain topology on DNA biomechanics is evidenced by the existence of topoisomerases, a class of enzymes that control the topology of DNA [26].

Provided the packaging motor of a bacteriophage rotates the DNA as it enters the capsid, the conformation of the DNA within the capsid interior would be impacted by the twist deformation. Specifically, we propose that twist deformation could provide the driving force for adopting an ordered, spool-like conformation, as is observed in T7 [11, 12], T4 [9], and P22 [13]. The concept of local action influencing global behavior is a common theme in the biological function of DNA, and twist is an important mechanism for such "action at a distance" [27]. Previous theoretical treatments of the packaging process have neglected the role of twist on the packaged conformation [28, 29, 30, 31, 32, 33, 19, 34, 35, 36], based on the assumption that either the motor does not introduce twist into the conformation or that this twist is relaxed by axial rotation on timescales shorter than the the timescale for the packaging process [37, 38]. While we do not suggest that neglecting twist is without justification, it is not currently known whether the end of the DNA is completely free to relax. Alternatively, twist may be locked in the conformation by a number of possible mechanisms, including DNA interaction with proteins, either unattached to the DNA (capsid proteins, for example) or covalently bound to the DNA (the ϕ29 terminal protein gp3, for example), or anomalous twist relaxation rates owing to the crowded electrolyte environment within

the capsid interior. Therefore, a reasonable question is how the conformation of DNA is altered by twist deformation if the DNA is torsionally constrained.

In this chapter, we address this question using computer simulation. Since the end condition of the DNA inside the capsid is unknown at present, we adopt the simplest model of torsional constraint by taking the end to be clamped and fixed on the capsid wall opposite to the portal of entry. We then perform two dynamic simulations of a polymer chain fed into a spherical confinement: one where the chain is rotated at the portal as it is fed, and one where the chain is fed without rotation. We compare the packaged conformation of the chain in these two cases, and examine the consequences for ejection from these different conformation structures. In order to focus on the most important aspects of the problem, we move on directly to the description of the results and relegate the details of the model and simulation method to the appendix.

7.2 Results

In order to simulate genome-length DNA at biologically relevant timescales, it is necessary to adopt a simplified model of the DNA/capsid system. We model the DNA using a discrete wormlike chain that includes the twist degrees of freedom [39, 40]; each discrete segment of chain represents $\sim$8 basepairs of DNA. The elastic properties of the chain are chosen to match the persistence length and torsional persistence length of DNA, with a large stretching modulus that essentially renders the chain inextensible. The chain self-interaction includes a screened electrostatic potential to approximate the influence of physiological salt concentration ($\sim 140\,\mathrm{mM}$ monovalent salt) and a hard-core repulsive potential that addresses the short-range repulsive behavior of DNA (modeled using the repulsive part of a Leonnard-Jones potential). The capsid is modeled as a spherical confinement through a

simple repulsive potential that scales as the radius to the fourth power outside the capsid radius [28]. With this model, we perform dynamic simulations, both with and without the effect of Brownian forces and torques, to track the temporal evolution of the chain conformation as it is fed into the spherical confinement. Further details of our model are found in the appendix of this chapter.

We perform two sets of packaging simulations. The first simulation involves the simultaneous rotation of the chain segment at the portal of entry as the chain is fed into the spherical confinement; thus the linking number increases linearly with the number of beads fed. As mentioned in the introduction, the proposed mechanism for DNA translocation by the $\phi 29$ motor involves approximately 60^o of rotation of the chain per helical-turn fed. Since it is not clear whether this mechanism involves rotation of the DNA or the motor, and the packaging of $\phi 29$ is marked by frequent pauses and slips of the chain [1], we choose to reduce the rate of rotation by a factor of 1/3 from the proposed mechanism of DNA translocation [20]. The second simulation is performed without rotation of the chain as it enters; thus the linking number remains at zero. In both sets of simulations, the feeding is performed by alternating between feed intervals and relaxation intervals until the desired volume fraction Φ_{P} is achieved. One feed interval involves feeding 10 beads into the spherical cavity at a feed rate of 1 per time step (t_B, defined in the appendix), and one relaxation interval involves an equal amount of time (10 time steps) to relax the conformation to a local minimum energy. In the feeding simulations, we neglect the role of Brownian forces and torques in order to focus on the mechanical aspects of the packaging process and to develop a basis for comparison with the case when Brownian fluctuations are included.

In Fig. 7.1, we show snapshots from the packaging dynamics for packaged volume fraction ranging from $\Phi_{\mathrm{P}} = 0.063$ to $\Phi_{\mathrm{P}} = 0.463$ in even increments of 0.050. The snapshots in A of

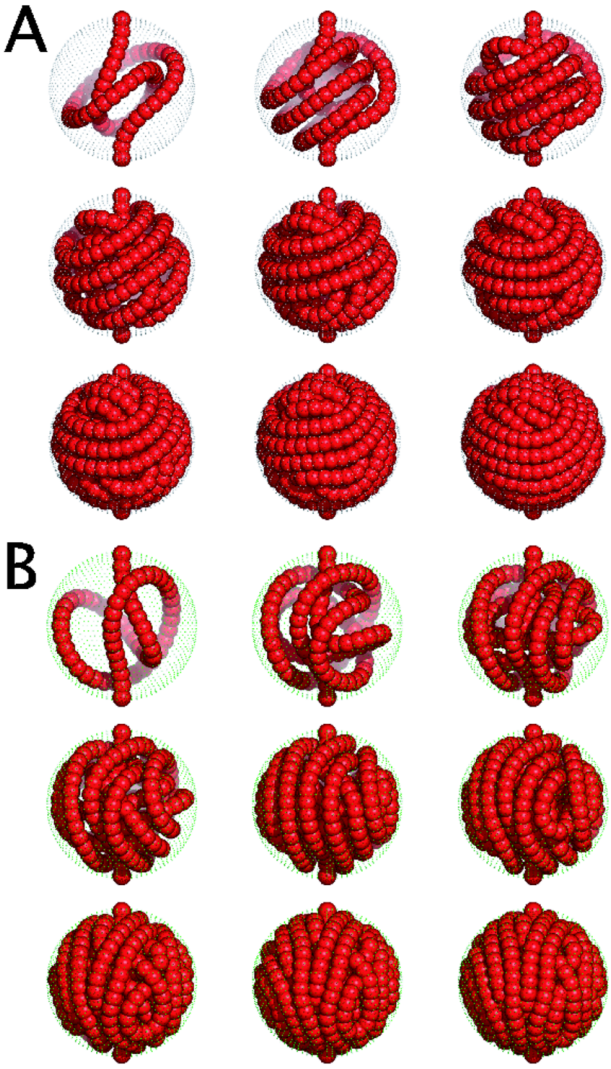

Figure 7.1: Snapshots during the process of feeding a single polyelectrolyte into a spherical confinement. The snapshots in A track the progress for feeding with rotation (as described in the text) for polymer volume fraction ranging in even increments from 0.063 to 0.463. The snapshots in B are for feeding without rotation for the same polymer volume fractions as A.

Fig. 7.1 show the progress of packaging for coupled translocation and rotation during the packaging process, while the snapshots in B of Fig. 7.1 are for packaging without rotation. The most clear distinction between the two sets of snapshots is the qualitative manner in which the packaged conformation evolves. The conformations in A (with rotation) appear to evolve in a spool-like manner, whereas the process of packaging without rotation in B occurs via a folding-type mechanism. Notably, the final conformations in A and B appear to have distinctly different chain orientations. The final conformation in A is wrapped in a spool that is on average perpendicular to the direction of entry, whereas in B the chain segments tend to locally align along the longitudes.

The snapshots presented in Fig. 7.1 display the structure of the outermost layers of the packaged polymer chain; however, it is desirable to look at the polymer density in the interior of the spherical confinement. Taking the final conformation from the two simulations, we perform Brownian dynamics simulations (thus including Brownian forces and torques) in order to evaluate a thermally averaged density of beads as a function of position within the capsid interior (averages are performed over 100 time steps). In Fig. 7.2A, we show the angle-averaged radial density ρ versus the radial distance R for the final packaged conformation for the case of feeding with rotation (solid line) and feeding without rotation (dashed line). In the case of feeding with rotation, four peaks are clearly visible in the density plot, indicative of four layers of order, with the outermost peak dominating; this layer ordering is quite reminiscent of the experimentally observed ordering in T7 [11, 12], T4 [9], and P22 [13]. For feeding without rotation, the peaks are not as easily discernible after the first two layers, indicative of the reduced degrees of layer order after the outermost layers.

The density plot gives the positional order of the chain segments within the spherical

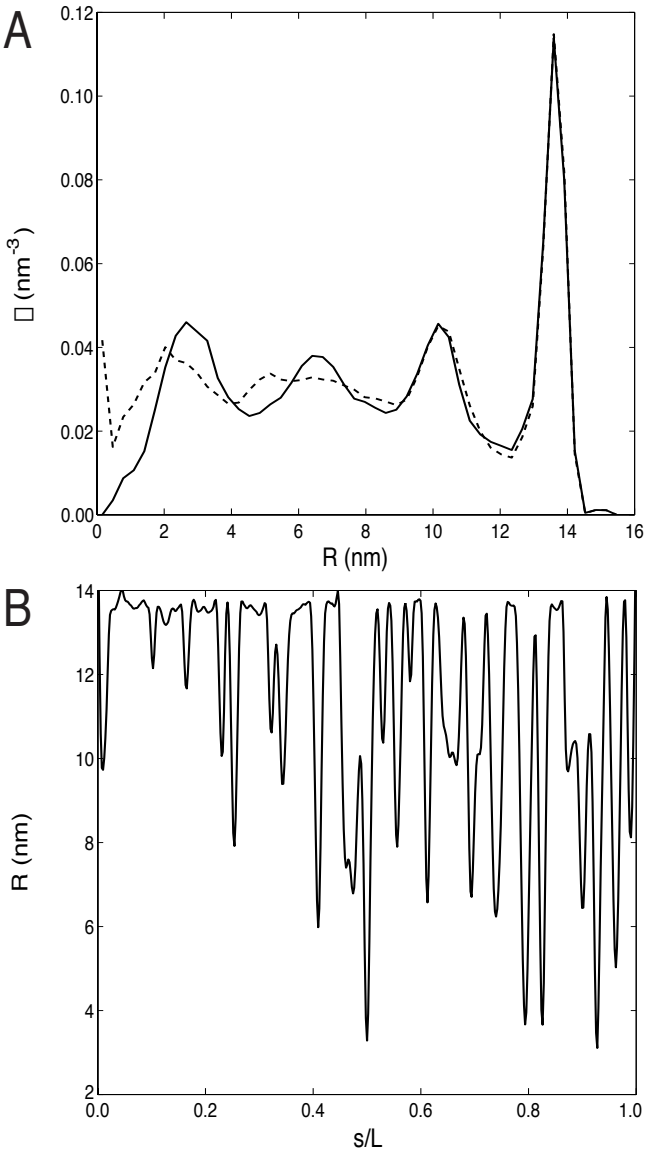

Figure 7.2: Figure A shows the density of polymer ρ versus the radial distance from the sphere center R for feeding with rotation (solid line) and without rotation (dashed line). Figure B gives the average radial distance of polymer segments versus the chain contour distance s/L for feeding with rotation. We note that $s/L = 0$ corresponds to the first segment inserted into the spherical confinement.

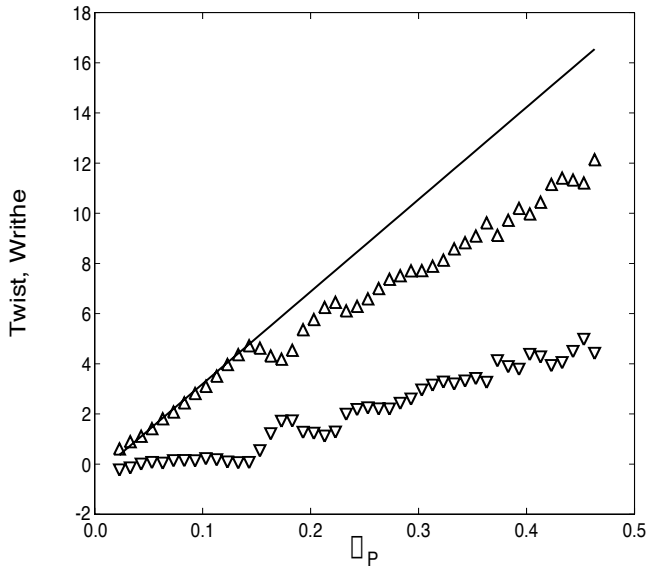

Figure 7.3: The topological quantities twist Tw ($\bigtriangledown$), writhe Wr ($\bigtriangleup$), and linking number Lk (solid line) of the packaged conformation for feeding with rotation versus the volume fraction of polymer added Φ_{P}.

confinement; however, the density does not resolve the sections along the chain that contribute to the layer ordering. Therefore in Fig. 7.2B, we plot the average radial distance versus the rank order along the polymer chain s/L ($s = 0$ at the chain end attached to the capsid wall, and $s = L$ at the chain end that is fed through the portal) for the final packaged conformation for feeding with rotation. The average for each data point in this figure is performed over time (100 time steps) for each point along the chain. The layering of the polymer within the sphere displays a preference for the beads first fed into the sphere to be located near the sphere surface, and later beads fed tend to be localized closer to the sphere center. However, the later fed beads frequently penetrate out to the sphere surface; thus the plot exhibits frequent spikes associated with these "out of rank" penetrations. A similar trend is displayed in the case of feeding without rotation (not shown).

Topological quantities including the linking number Lk (solid line), twist Tw ($\bigtriangledown$), and writhe Wr ($\bigtriangleup$) for packaging with rotation are plotted in Fig. 7.3 against the volume fraction

of packaged polymer Φ_{P}. All three topological quantities are calculated independently. We find that the topological constraint $Lk = Tw + Wr$ is satisfied throughout the simulation (to within machine precision), which is confirmation that the chain does not cross itself during the simulation. For small volume fractions ($\Phi_{\mathrm{P}} < 0.163$), the linking number is almost entirely in the form of writhe, as the spooling process efficiently converts the twist into the writhed spools. However, for larger volume fractions ($\Phi_{\mathrm{P}} \geq 0.163$), twist increases essentially linearly with the added polymer. The twist remains much smaller than the writhe as the chain is fed into the sphere, presumably due to the propensity for the chain to adopt the spool-like conformation, which converts most of the twist from the loading into writhe. As the twist and writhe increase linearly with the volume fraction, they maintain essentially a constant ratio between them. Similarly, the process of DNA supercoiling generally involves a distribution between twist and writhe, strongly influenced by salt concentration [41]. We do not include the analogous plot as Fig. 7.3 for packaging without rotation since the linking number Lk is zero throughout, and the twist and writhe remain near zero for most of the packaging process (maximum value of $|Tw| = |Wr| = 2.14$ and final value at fully packaged of $Tw = -Wr = 0.39$).

In Fig. 7.4A, the total energy E [$\circ$, measured in $k_BT(\sim 4.1\,\mathrm{pN\,nm} = 0.6\,\mathrm{kcal/mol})$], compression energy E_{com} ($+$), bending energy E_{bend} ($\triangle$), twisting energy E_{twist} ($\square$), self-interaction energy E_{int} ($\triangledown$), and capsid-interaction energy E_{capsid} ($\times$) are plotted against the packaged volume fraction Φ_{P} for packaging with rotation. The solid line is a polynomial fit (fourth order) to the total energy E, which we make use of later to determine the force opposing the packaging process. Early in the packaging process, the total energy E is dominated by the bending deformation energy E_{bend}; however, at approximately $\Phi_{\mathrm{P}} = 0.32$, the bending energy E_{bend} is overcome by the self-interaction energy E_{int}. The capsid-interaction

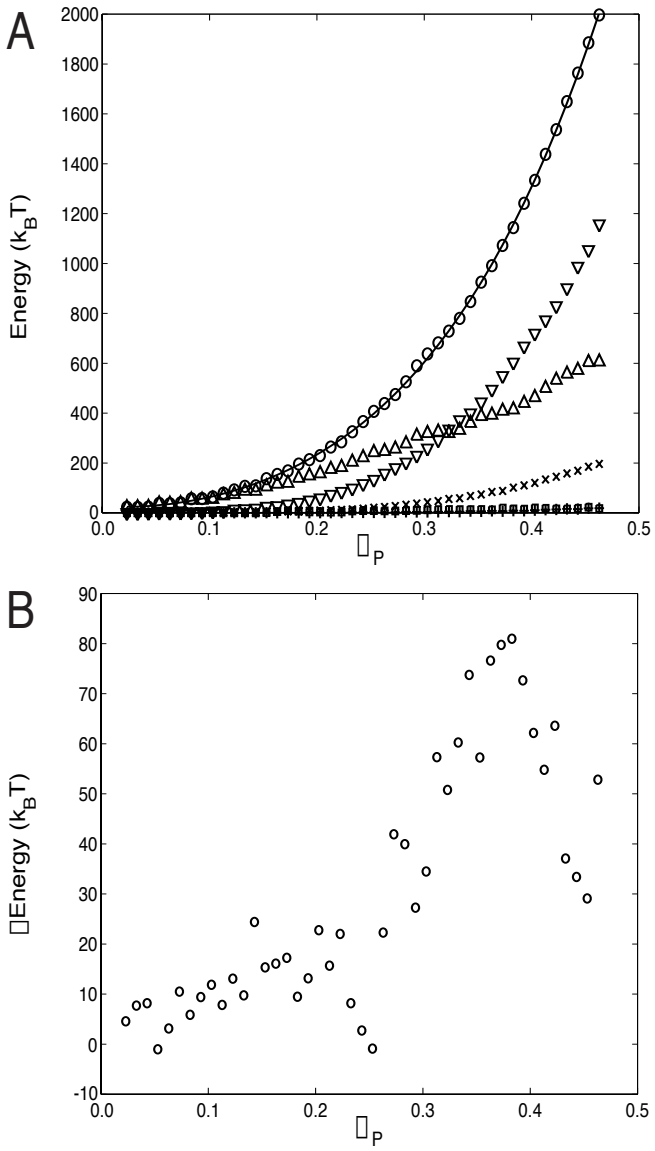

Figure 7.4: Figure A shows the total energy E ($\circ$), compression energy E_{com} ($+$), bending energy E_{bend} ($\triangle$), twisting energy E_{twist} ($\square$), self-interaction energy E_{int} ($\bigtriangledown$), and capsid-interaction energy E_{capsid} ($\times$) versus the packed volume fraction $\Phi_{\rm P}$ for packaging with rotation. The solid line is a polynomial fit (fourth order) to the total energy E. Figure B is the difference between the total energy for packaging without rotation and packaging with rotation ΔE versus the packaged volume fraction $\Phi_{\rm P}$. Note, packaging without rotation leads to a larger total energy ($\Delta E > 0$ in our simulations).

energy E_{capsid} remains small for small volume fraction polymer ($\Phi_P < 0.3$) but rises noticeably at large volume fractions as the packing presses the polymer against the confining wall. The compression energy E_{com} and twisting energy E_{twist} are insignificant contributions throughout the packaging process. Although packaging involves chain rotation, the twist is efficiently converted to writhe, thus the twisting energy E_{twist} remains quite small. Specifically, the final value of the twisting energy E_{twist} is $17.3k_BT$ for packaging with chain rotation, and if all of the linking number remained in the form of twist, the final twisting energy E_{twist} would be $234.8k_BT$.

Since the range in the figure is so large, the complimentary plot for packaging without rotation is virtually indistinguishable from the one shown. Therefore to facilitate comparison, we plot in Fig. 7.4B the difference between the total energy of the packaged conformation without rotation and the total energy for packaging with rotation ΔE against the polymer volume fraction Φ_P. The energy for packaging without rotation is larger than the energy for packaging with rotation, thus $\Delta E > 0$ (with two exceptions at $\Phi_P = 0.053$ and $\Phi_P = 0.263$), with a maximum value of $81.0\,k_BT$. We note that, in the case of feeding with rotation, the added twist deformation represents an additional energetic contribution that presumably is not present in the case of feeding without rotation. In the case of feeding without rotation, we restrict both ends from rotating, thus any writhe produced results in an equal and opposite amount of twist to maintain the linking number. This local twist results in twist deformation energy; however, this is small in comparison to the twist present in the case of feeding with rotation. Therefore, it is quite remarkable that the energy of the conformation resulting from packaging with rotation is less than that without rotation; this is due to the reduced bending energy of the spooled conformation in the former versus the folded conformation in the latter.

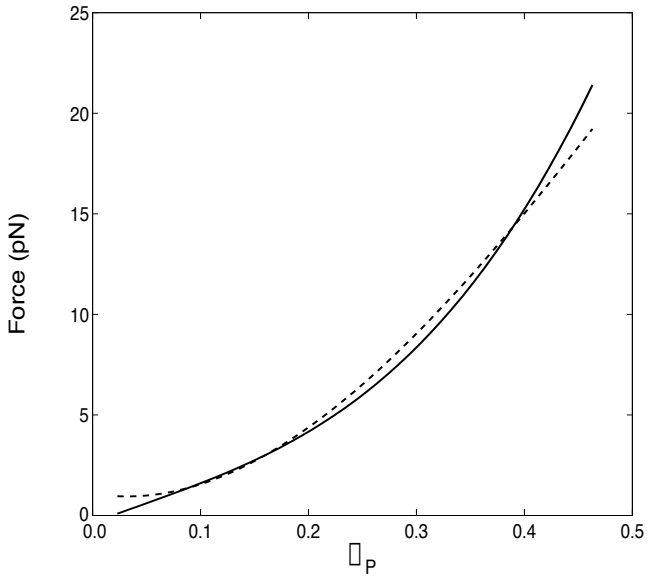

Figure 7.5: The force opposing packaging (expressed in pN) versus volume fraction $\Phi_{\rm P}$ for packaging with rotation (solid line) and without rotation (dashed line) determined using a fourth-order polynomial fit to the total energy E (see text and Fig. 7.4).

The polynomial fit to the total energy E in Fig. 7.4A is used to calculate the force opposing packaging F, from $F = \partial_L E$. This assumes that the conformation within the confinement remains at equilibrium throughout the packaging process, requiring that the packaging is sufficiently slow to maintain equilibrium. In Fig. 7.5, we show the predicted force opposing packaging (units of pN) using a fourth-order polynomial fit to the total energy data (as in Fig. 7.4A) for packaging with rotation (solid line) and without rotation (dashed line) against the packaged volume fraction $\Phi_{\rm P}$. In both cases, the force opposing packaging increases with the packaged length to a final value of approximately 20 pN. This value is about three times smaller than the stall force of $\phi 29$ (57 pN) [1]. Because we have neglected the thermal contributions to the osmotic pressure of the chain segments by ignoring the Brownian forces and have used a crude interaction potential between the segments, a factor of three discrepancy is not unreasonable. From the final twist value in Fig. 7.3, we estimate the value of the torque $\tau_{END} = 2\pi CTw/(N-2)$ necessary to disallow the attached end from

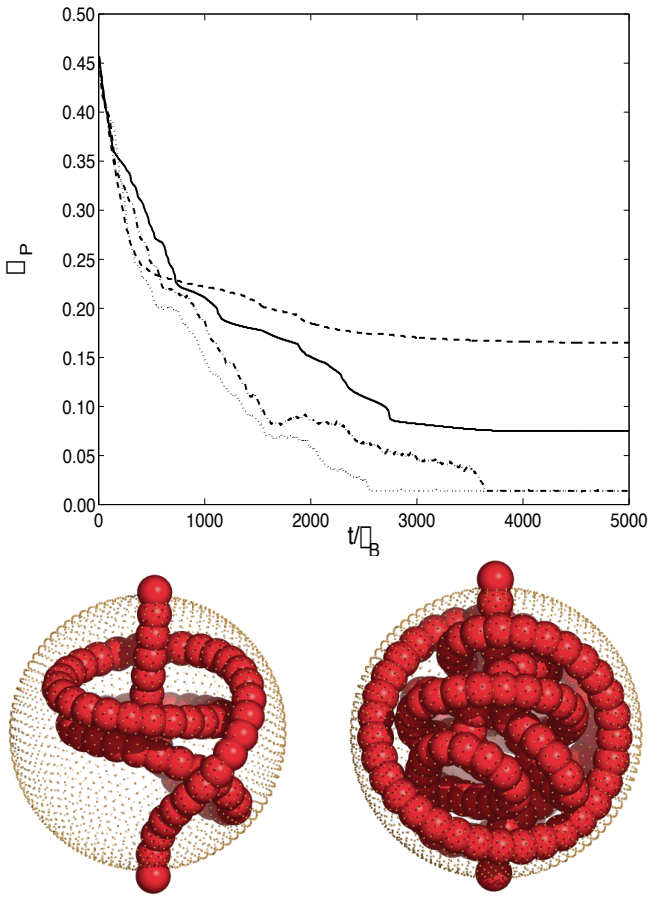

Figure 7.6: The volume fraction Φ_P versus time for ejection from the sphere beginning with the final conformation from packaging with chain rotation [ejection with Brownian forces (dashed-dotted line) and without Brownian forces (solid line)] and from packaging without chain rotation [ejection with Brownian forces (dotted line) and without Brownian forces (dashed line)]. Beneath the figure, we show the final conformations from eject without Brownian forces beginning from packaging with chain rotation (left) and without chain rotation (right).

rotating to be $1.2k_BT$. If all of the linking number remained as twist, the predicted end torque τ_{END} would be $4.5k_BT$. We note that these values of torque are within a reasonable range where typical molecular forces (for example, hydrogen bonding and van der Waals forces) could stabilize the end.

Beginning with the conformations predicted from the packaging simulations, we simulate the ejection of the chain from the spherical confinement by eliminating the feeding force/torque and allowing the chain to exit through the portal of entry. In Fig. 7.6, we show

the results of the ejection simulations by plotting the volume fraction Φ_P left within the sphere versus time (reduced by t_B). For each starting conformation obtained from packaging with and without rotation, we have performed two ejection simulations, one that included the Brownian forces and one that did not. We find that Brownian forces dramatically influence the ability of the packaged sphere to eliminate the polymer within. Specifically, in the absence of Brownian forces, ejection is unable to reach full completion for both conformations obtained from packaging with (solid line) and without rotation (dashed line), indicated by the internal volume fraction tending to a non-zero value at long times. (We note that full ejection occurs at $\Phi_P = 0.017$ because of the chain end attachment to the sphere wall). When Brownian forces are included, ejection is marked by frequent fluctuations in the length of chain within the sphere. Such length fluctuations are most likely related to interior conformation fluctuations that may help to alleviate self entanglement, thus allowing the chain to fully eject.

For ejection without Brownian forces, the ejection halts at a larger value of the volume fraction when the initial conformation is from packaging without rotation, presumably because of a higher degree of entanglement in the folded conformation from packaging without rotation than the spool-like conformation from packaging with rotation. However when Brownian forces are included, the ejection proceeds to completion in both cases, and the conformation from packaging without rotation (dotted line) ejects faster than the conformation from packaging with rotation (dashed-dotted line). Further studies are needed to explain this latter observation.

7.3 Discussion

This preliminary study on the packaging of DNA within a bacteriophage capsid focuses on the potential impact of twist on the packaged conformation, specifically if the packaging motor rotates the DNA as it feeds. Towards this end, we perform two computer simulations of a single polyelectrolyte actively inserted into a spherical confinement: one where the polymer chain is rotated as it is fed, and one where the polymer chain is not rotated during the feeding process. We choose to fix the non-feeding end to the capsid wall directly across from the portal. This does not necessarily imply a proposed biological phenomenon; rather, it is a convenient way to elucidate the effects of twist by imposing the topological constraint.

Our results show distinct differences between the conformation of the packaged polymer in packaging with rotation and without rotation. Most notably, the final conformation in packaging with rotation exhibits a spool-like character, perhaps more consistent with a concentric spool [17, 18] than a coaxial spool [15, 4], whereas the final conformation for packaging without rotation is folded with chain segments generally oriented parallel to the axis of feeding. We note that the preference for the concentric spool is consistent with energy-minimized conformations found in Ref. [19] for feeding without rotation and with a free polymer end in the sphere interior. However, our approach is not to seek global energy minima as in Ref. [19]; but rather to track the process of packaging as it proceeds along a dynamically accessible trajectory.

Rotating the polymer chain while feeding acts to break chiral symmetry of the packaged conformation, whereas feeding without rotation favors neither chirality. Packaging a torsionally constrained polymer without rotation begins by coiling the chain in one direction at random; this writhing gives rise to twist which eventually forces the chain to coil in the opposite direction to alleviate the developing twist. This scenario is reminiscent of coiling

a garden hose without rotation: coiling may proceed in one direction for several wraps but must eventually coil in the opposite direction or suffer other twist-reducing instabilities (formation of plectonemes, for example). On the other hand, orderly coiling a garden hose is accomplished by twisting the hose as it lies down [42]. The energetically preferred conformations found in Ref. [19] are invariant to reflection since they have no twist deformation, which is assumed to be alleviated by axial rotation of the free end. Thus, presumably an average over many packaged conformations predicted by a model that neglects twist deformation would not exhibit chiral preference. Packaging with rotation would provide the driving force for spool-like packaging with a definitive chiral preference.

However, the adopted spool-like conformation from packaging with rotation is not a perfect, idealized spool; rather it contains many defects of chain segments jumping from interior layers to exterior layers. Although the density plot (Fig. 7.2A) exhibits layer ordering (notably more pronounced for packaging with rotation than without rotation), the rank ordering plot (Fig. 7.2B) shows that the conformation does not proceed by filling the outmost layer first before filling the interior shells but by placing the chain in available spaces, preferring the outmost shell throughout the packaging process. The physical argument of the curvature stress off-setting the self-repulsion is certainly at work, as argued by continuum modeling of the packaging process [35]; however, the curvature stress also drives inner loops toward the outer layers when transient gaps or defects present themselves near the sphere surface. Continuum models of the packaging process assume sequential spooling [35, 31] without these layer-jumping instances, since the continuum treatment does not account for local inhomogeneities. However, it is worth noting that such a continuum treatment [31] achieves quantitative agreement with the experimentally measured force opposing packaging in $\phi 29$ [1]. Nonetheless, the instances of defects may lead to entanglements as the polymer

chain is ejected from the confinement. Our ejection results (presented in Fig. 7.6) demonstrate that Brownian forces are necessary to achieve complete ejection of the chain from the spherical cavity. We propose that this is due to the entanglements arising from interior defects, which are not predicted from continuum treatments of the packaging process.

Packaging with chain rotation suggests that the increasing linking number of the strand is introduced in the form of twist as the straight section of chain entering the spherical confinement rotates, and conversion from twist to writhe occurs once the entering bead is released into the capsid interior. During the initial stage of packaging ($\Phi_P < 0.163$ in Fig. 7.3), our simulation shows that all of the twist is converted into writhe, and further packaging results in most of the twist being converted into writhe, as they both increase linearly but with different slopes. This suggests that during the initial stage, the driving force for coiling is dominated by non-twist related forces (self-interaction and bending, mainly), whereas further ordered packaging in coils occurs due to self-interaction, bending, and stresses arising from twist deformation energy. Notably, the manner in which the polymer chain alleviates the twist deformation is to form coils or solenoid-like structures, which is completely dissimilar from the more prevalent plectonemic structures formed in a twisted polymer chain in the absence of confinement. The preference for the plectonemic form in free space is due to the fact that plectonemes more efficiently convert twist into writhe than solenoid structures [43]. Although not shown in the previous section, we find that performing packaging simulations with a larger rotation rate (larger linking number) results in plectonemic structures in the sphere confinement rather than coils or solenoids.

The energy of the packaged conformation shows a steep increase as packaging proceeds, indicative of the escalating resistance opposing packaging, as is evident in ϕ29 [1]. In the early stage of packaging ($\Phi_P < 0.32$ in Fig. 7.4A), the bending energy dominates the

total energy, and the conformation is driven to the outside wall. As packaging proceeds, the self-interaction energy overcomes the bending energy, and the conformation tends to explore more of the interior of the sphere (noting the tendency for layer jumping previously discussed). All other energetic contributions are rather small in comparison to the bending and self-interaction energies throughout the packaging process. This does not imply their influence is insignificant, as demonstrated by the qualitative difference between the final conformation from packaging with rotation and without rotation displayed in Fig. 7.1.

Throughout this chapter, we have deliberately avoided an explicit definition of the Brownian timescale in actual units. This is because of the uncertainty in the drag coefficient for DNA in a crowded, highly charged environment. It is tempting to assume that the drag is the same as in free solution [44, 37, 38] or alternatively to consider a more detailed model that includes hydrodynamic interactions [45] (both polymer/polymer and polymer/capsid wall). However, it is very likely that the drag is not easily interpreted once we reach packaging densities where the chains are separated by only a couple hydration layers, as is the case here. Beyond the equilibrium hydration forces that occur [46], confined water exhibits slow relaxation behaviors that may dramatically alter the effective drag coefficient on the DNA strand [47].

We neglect Brownian forces in the packaging simulations in this chapter, and certainly several features are not captured without their effect. For example, thermally induced reorganization may act to disentangle the polymer chain as packaging proceeds, thus eliminating some of the defects prevalent in our simulation results. However, we note that our thermal averaging of the final conformation does not exhibit large-scale reorganization in the timescale of the average (100 time steps) due to the extremely sluggish processes associated with disentanglement at this volume fraction ($\Phi_P = 0.463$). Although we do not explore

this in our current work, the disentanglement process for a single chain in a confinement has several similarities to and non-trivial distinctions from the relaxation processes prevalent in entanglement of a polymer chain in a melt [48, 49]. Brownian forces also acts as a source of transient inhomogeneities in the local ordering, thus the instances of layer jumping described earlier may be enhanced under the influence of thermal fluctuations. Thermal fluctuations influence the tendency to order; for example, molecular crowding in semiflexible polymer solutions results in ordered liquid-crystal phases [50]. One distinct effect of semiflexibility on the liquid crystal phase is the presence of hairpin defects or instances of sharp reversal of the chain orientation to form a loop [51, 50]. These effects may play a role in the formation of ordered conformations within a packaged bacteriophage capsid, which we plan to explore further in future studies. Overall, the influence of thermal fluctuations on the packaged conformation remains an important issue that requires further investigation.

This study acts as preliminary evidence that twist may play a role in the packaged DNA conformation in a bacteriophage capsid. Further work is needed to elucidate the connection between the packaged conformation and the end goal of the viral packaging, the ability for the virus to eject its genome from the capsid into the host cell. Future work will focus more on the ejection process to make the connection between the manner of packaging and the resulting ejection behavior.

Appendix A: Model of DNA/Capsid

Modeling the process of DNA packaging within a viral capsid is challenging because of the large number of degrees of freedom of the DNA strand and the long timescale for the packaging process. Therefore, it is necessary to adopt a simplified view of the DNA/capsid system. Since our interest is in the behavior of the overall DNA conformation in the capsid,

we neglect the individual atomic coordinates and reduce the description to a coarse-grained model. A suitable model for our purposes is the wormlike chain model that includes the twist degrees of freedom [52, 53], which is used to study a wide range of DNA-related phenomena. The wormlike chain model is approximated as a beaded chain to make it amenable to computer simulation [39, 40].

The DNA conformation is described as a string of beads with positions $\vec{R}_i$ $(i = 1, 2, \ldots, N)$, thus there are $N-1$ bond vectors $\vec{u}_i = (\vec{R}_{i+1} - \vec{R}_i)/b_i$, where $b_i = |\vec{R}_{i+1} - \vec{R}_i|$. To account for the material twisting, two normal vectors $\vec{f}_i$ and $\vec{v}_i$ are attached to each bond vector $\vec{u}_i$ such that $\vec{v}_i = \vec{u}_i \times \vec{f}_i$ and $\vec{f}_i \cdot \vec{u}_i = 0$. This leaves the polymer chain with a total of $4N-1$ degrees of freedom [40].

The behavior of the polymer chain is dictated by the total chain energy, which includes elastic deformation energy, self-interaction energy, and capsid-interaction energy, all expressible in terms of our degrees of freedom. The chain deformation energy takes the simplest form possible: the compression, bending, and twisting deformation energies are quadratic in the displacement away from a straight, untwisted conformation [54]. These energy terms are given by

$$E_{com} = \frac{A}{2} \sum_{i=1}^{N-1} \left(b_i/l_0 - 1\right)^2, \tag{A-1}$$

$$E_{bend} = \frac{B}{2} \sum_{i=1}^{N-2} \left(\vec{u}_{i+1} - \vec{u}_i\right)^2, \tag{A-2}$$

$$E_{twist} = \frac{C}{2} \sum_{i=1}^{N-2} \omega_i^2, \tag{A-3}$$

where A, B, and C are respectively the compression, bending, and twisting moduli (units of energy), l_0 is the equilibrium bond length, and ω_i is the twist angle, which satisfies

$(1 + \vec{u}_i \cdot \vec{u}_{i+1}) \sin\omega_i = \vec{v}_i \cdot \vec{f}_{i+1} - \vec{f}_i \cdot \vec{v}_{i+1}$ [40]. The self-interaction energy takes the form

$$E_{int} = \frac{1}{2} \sum_{i=1}^{N} \sum_{j \neq i} v_{int}(R_{ij}), \tag{A-4}$$

where $R_{ij} = |\vec{R}_i - \vec{R}_j|$, and $v_{int}(R)$ is the two-body interaction potential. In our model, $v_{int}(R)$ is given by

$$v_{int}(R) = \begin{cases} \frac{v_{HC}}{12}\Big[\big(\frac{\sigma}{R}\big)^{12} - 2\,\big(\frac{\sigma}{R}\big)^{6} + 1\Big] + \\ v_e \frac{\exp(-R/l_D)}{R} & \text{if } R < \sigma \\ v_e \frac{\exp(-R/l_D)}{R} & \text{if } R \geq \sigma, \end{cases} \tag{A-5}$$

which incorporates both a screened electrostatic potential (Debye-Hückel form) at all values of interbead distance R and a hard-core potential (repulsive Leonnard-Jones form) for interbead distance R less than the hydrodynamic radius of DNA σ ($\sim 2.5\,\text{nm}$). The electrostatic interaction strength v_e in Eq. A-5 is given by $q^2 k_B T l_B$, where q is the charge per bead (in units of the electron charge), $k_B T$ is the thermal energy, and l_B is the Bjerrum length ($\sim$0.7 nm for water at room temperature); the Debye length l_D scales the length of electrostatic screening. Although typical bacteriophage have icosahedral capsids, we model the confining capsid as a sphere. The interaction between a chain segment and the capsid wall is modeled as

$$E_{capsid} = \sum_{i=1}^{N} v_{capsid}(|\vec{R}_i|); \tag{A-6}$$

as in Ref. [28], we adopt a simple form for the capsid-interaction potential $v_{capsid}(R)$, given by

$$v_{capsid}(R) = \begin{cases} v_c\Big(\frac{R - R_c}{l_0}\Big)^4 & \text{if } R > R_c \\ 0 & \text{if } R \leq R_c, \end{cases} \tag{A-7}$$

where v_c is the capsid-interaction strength, and R_c is the radius of the capsid.

The forces and torques are found from the total energy $E = E_{com} + E_{bend} + E_{twist} + E_{int} + E_{capsid}$ using the method of variations. Specifically, the force $\vec{f}_i^E$ on the ith bead and the torque τ_i^E on the ith bond vector are found using the expression $\delta E = -\sum_{i=1}^{N} \vec{f}_i^E \cdot \delta\vec{R}_i - \sum_{i=1}^{N-1} \tau_i^E \delta\psi_i$, where ψ_i is the Euler angle of pure rotation [55], which is orthogonal to the drift motion of the beads $\delta\vec{R}_i$. The dynamic equations of motion of the chain are found by performing a force balance on the beads and a torque balance on the bonds, which incorporates the forces and torques from the total energy E as well as terms accounting for inertia, hydrodynamic drag, and Brownian fluctuations. As we consider highly viscous dynamics, we neglect inertial forces and torques. The hydrodynamic drag for this preliminary study takes the simplest possible form: the drag force and torque is local and linear in the velocity of the bead and the angular velocity of the bond, respectively. Thus the equations of motion are given by

$$\xi \frac{d\vec{R}_i}{dt} = \vec{f}_i^E + \vec{f}_i^B \tag{A-8}$$

$$\xi_R \frac{d\psi_i}{dt} = \tau_i^E + \tau_i^B, \tag{A-9}$$

where ξ is the drag coefficient for drift, and ξ_R is the drag coefficient for rotation. The Brownian force $\vec{f}_i^B$ and torque τ_i^B satisfy the fluctuation dissipation theorem such that $\left\langle \vec{f}_i^B(t)\vec{f}_j^B(t') \right\rangle = 2k_BT\xi\delta_{ij}\delta(t-t')\mathbf{I}$ and $\left\langle \tau_i^B(t)\tau_j^B(t') \right\rangle = 2k_BT\xi_R\delta_{ij}\delta(t-t')$ [49].

In our simulations, we non-dimensionalize energy by k_BT, length by l_0, and time by $t_B = \xi l_0^2/(k_BT)$. Choosing the equilibrium bond length to be $l_0 = 2.5\,\text{nm}$, the beads in the chain just touch their neighbors, which essentially ensures the noncrossibility of the chain, thus preserving the chain topology. Our non-dimensionalized simulation parameters are

chosen as follows: $A = 500$, $B = C = 20$, $l_B = 0.284$, $l_D = 0.328$, $q = -16.675$, $\sigma = 1$, $v_{HC} = 20$, $R_{cap} = 5$, $v_{cap} = 20$, $\xi = 1$, and $\xi_R = 0.213$. We note that our capsid radius $R_{cap} = 5$ (12.5 nm) is substantially smaller than the typical bacteriophage capsid [32]. As in Ref. [28], the reduced capsid size makes it possible to achieve a packaged volume fraction Φ_{P} of the typical bacteriophage ($\Phi_{\mathrm{P}} \sim 0.45$ [32]) while performing the computationally taxing simulations in a reasonable time. For our choice of parameters, the volume fraction is given by $\Phi_{\mathrm{P}} = 0.001N$.

We perform packaging dynamics in a similar manner as in Ref. [28]; beads are fed into the spherical confinement one at a time while tracking the interior bead motion by numerically solving their equations of motion (Eqs. A-8 and A-9). However, we have two important differences from Ref. [28]. First, the entering bond vector $\vec{u}_{N-1}$ is clamped such that the direction of insertion is held fixed in the negative z-direction. Second, the opposite end of the chain is clamped and held fixed opposite the portal of entry, thus $\vec{u}_1 = \vec{u}_{N-1} = \hat{z}$, and $\vec{R}_1 = -(R_{cap} + l_0)\hat{z}$. We test the effect of twist on the packaged conformation by performing simulations where the feeding chain end is rotated as the chain enters and comparing with simulations where the feeding chain enters without rotation.

The chain topology is characterized by the linking number Lk, the twist Tw, and the writhe Wr of the curve [25]. Typically these quantities are defined only for closed-circular curves; however, we extend the chain ends out to infinity to render a topologically-fixed conformation. The linking number satisfies $Lk = Tw + Wr$, where these two contributions are determined from the chain conformation and twist angles. For our discrete representation, the twist Tw is given by

$$Tw = \frac{1}{2\pi} \sum_{i=1}^{N-2} \omega_i. \tag{A-10}$$

The writhe Wr of the conformation is given by a Gauss integral over the curve; the calcu-

lation of Wr for our discrete chain representation makes use of techniques in Ref. [56] with only slight alterations upon extending the chain ends to infinity. Performing the calculation of Tw and Wr separately provides both a method of characterizing the topology of the chain as well as a test of whether the chain has crossed itself due to the invariance of the linking number Lk.

Bibliography

[1] D. E. Smith, S. J. Tans, S. B. Smith, S. Grimes, D. L. Anderson, and C. Bustamante. The bacteriophage ϕ29 portal motor can package DNA against a large internal force. *Nature*, 413(6857):748–752, 2001.

[2] A. Evilevitch, L. Lavelle, C. M. Knobler, E. Raspaud, and W. M. Gelbart. Osmotic pressure inhibition of DNA ejection from phage. *Proc. Natl. Acad. Sci. U.S.A.*, 100(16):9292–9295, 2003.

[3] A. C. North and A. Rich. X-ray diffraction studies of bacterial viruses. *Nature*, 191(479):1242–&, 1961.

[4] W. C. Earnshaw and S. C. Harrison. DNA arrangement in isometric phage heads. *Nature*, 268(5621):598–602, 1977.

[5] J. Widom and R. L. Baldwin. Tests of spool models for DNA packaging in phage lambda. *J. Mol. Biol.*, 171(4):419–437, 1983.

[6] K. L. Aubrey, S. R. Casjens, and G. J. Thomas. Studies of virus structure by laser raman-spectroscopy .38. secondary structure and interactions of the packaged dsDNA genome of bacteriophage-P22 investigated by raman difference spectroscopy. *Biochemistry*, 31(47):11835–11842, 1992.

[7] P. Serwer, S. J. Hayes, and R. H. Watson. Conformation of DNA packaged in bacteriophage-T7 - analysis by use of ultraviolet light-induced DNA-capsid cross-linking. *J. Mol. Biol.*, 223(4):999–1011, 1992.

[8] J. Lepault, J. Dubochet, W. Baschong, and E. Kellenberger. Organization of double-stranded DNA in bacteriophages - a study by cryoelectron microscopy of vitrified samples. *Embo J.*, 6(5):1507–1512, 1987.

[9] N. H. Olson, M. Gingery, F. A. Eiserling, and T. S. Baker. The structure of isometric capsids of bacteriophage T4. *Virology*, 279(2):385–391, 2001.

[10] L. W. Black, W. W. Newcomb, J. W. Boring, and J. C. Brown. Ion etching of bacteriophage-T4 - support for a spiral-fold model of packaged DNA. *Proc. Natl. Acad. Sci. U.S.A.*, 82(23):7960–7964, 1985.

[11] M. E. Cerritelli, N. Cheng, A. H. Rosenberg, M. N. Simon, and A. C. Steven. Organization of dsDNA in bacteriophage T7 capsids: Support for the coaxial-spool model. *Biophys. J.*, 70(2):WAMC1–WAMC1, 1996.

[12] M. E. Cerritelli, N. Q. Cheng, A. H. Rosenberg, C. E. McPherson, F. P. Booy, and A. C. Steven. Encapsidated conformation of bacteriophage T7 DNA. *Cell*, 91(2):271–280, 1997.

[13] Z. X. Zhang, B. Greene, P. A. Thuman-Commike, J. Jakana, P. E. Prevelige, J. King, and W. Chiu. Visualization of the maturation transition in bacteriophage P22 by electron cryomicroscopy. *J. Mol. Biol.*, 297(3):615–626, 2000.

[14] N. V. Hud. Double-stranded DNA organization in bacteriophage heads - an alternative toroid-based model. *Biophys. J.*, 69(4):1355–1362, 1995.

[15] K. E. Richards, R. C. Williams, and R. Calendar. Mode of DNA packing within bacteriophage heads. *J. Mol. Biol.*, 78(2):255–&, 1973.

[16] P. Serwer. Arrangement of double-stranded DNA packaged in bacteriophage capsids - an alternative model. *J. Mol. Biol.*, 190(3):509–512, 1986.

[17] S. B. Hall and J. A. Schellman. Flow dichroism of capsid DNA phages .1. fast and slow T4b. *Biopolymers*, 21(10):1991–2010, 1982.

[18] S. B. Hall and J. A. Schellman. Flow dichroism of capsid DNA phages .2. effect of DNA deletions and intercalating dyes. *Biopolymers*, 21(10):2011–2031, 1982.

[19] J. C. LaMarque, T. V. L. Le, and S. C. Harvey. Packaging double-helical DNA into viral capsids. *Biopolymers*, 73(3):348–355, 2004.

[20] A. A. Simpson, Y. Z. Tao, P. G. Leiman, M. O. Badasso, Y. N. He, P. J. Jardine, N. H. Olson, M. C. Morais, S. Grimes, D. L. Anderson, T. S. Baker, and M. G. Rossmann. Structure of the bacteriophage ϕ29 DNA packaging motor. *Nature*, 408(6813):745–750, 2000.

[21] V. Virrankoski-Castrodeza, M. J. Fraser, and J. H. Parish. Condensed DNA structures derived from bacteriophage heads. *J. Gen. Virol.*, 58(JAN):181–190, 1982.

[22] S. Casjens. in *Chromosomes: Eucaryotic, Procaryotic and Viral. Vol. III*, ed. by K. Adolph. CRC Press, 1989.

[23] S. Grimes and D. Anderson. The bacteriophage ϕ29 packaging proteins supercoil the DNA ends. *J. Mol. Biol.*, 266(5):901–914, 1997.

[24] J. Muller, S. Oehler, and B. MullerHill. Repression of lac promoter as a function of distance, phase and quality of an auxiliary lac operator. *J. Mol. Biol.*, 257(1):21–29, 1996.

[25] J. H. White. Self-linking and Gauss-integral in higher dimensions. *Am. J. Math.*, 91(3):693–&, 1969.

[26] J. Wang and N. R. Cozzarelli. *Meeting on Biological Effects of DNA Topology.* Cold Spring Harbor Laboratory, N. Y., 1986.

[27] J. C. Wang and G. N. Giaever. Action at a distance along a DNA. *Science*, 240(4850):300–304, 1988.

[28] J. Kindt, S. Tzlil, A. Ben-Shaul, and W. M. Gelbart. DNA packaging and ejection forces in bacteriophage. *Proc. Natl. Acad. Sci. U.S.A.*, 98(24):13671–13674, 2001.

[29] S. Tzlil, J. T. Kindt, W. M. Gelbart, and A. Ben-Shaul. Forces and pressures in DNA packaging and release from viral capsids. *Biophys. J.*, 84(3):1616–1627, 2003.

[30] P. K. Purohit, J. Kondev, and R. Phillips. Force steps during viral DNA packaging? *J. Mech. Phys. Solids*, 51(11-12):2239–2257, 2003.

[31] P. K. Purohit, J. Kondev, and R. Phillips. Mechanics of DNA packaging in viruses. *Proc. Natl. Acad. Sci. U.S.A.*, 100(6):3173–3178, 2003.

[32] P. K. Purohit, M. Inamdar, P. Grayson, T. Squires, J. Kondev, and R. Phillips. Forces during bacteriophage DNA packaging and ejection. *Biophys. J.*, Submitted, 2004.

[33] J. Arsuaga, R. K. Z. Tan, M. Vazquez, D. W. Sumners, and S. C. Harvey. Investigation of viral DNA packaging using molecular mechanics models. *Biophys. Chem.*, 101:475–484, 2002.

[34] D. Marenduzzo and C. Micheletti. Thermodynamics of DNA packaging inside a viral capsid: The role of DNA intrinsic thickness. *J. Mol. Biol.*, 330(3):485–492, 2003.

[35] T. Odijk. Hexagonally packed DNA within bacteriophage T7 stabilized by curvature stress. *Biophys. J.*, 75(3):1223–1227, 1998.

[36] T. Odijk and F. Slok. Nonuniform Donnan equilibrium within bacteriophages packed with DNA. *J. Phys. Chem. B*, 107(32):8074–8077, 2003.

[37] A. S. Krasilnikov, A. Podtelezhnikov, A. Vologodskii, and S. M. Mirkin. Large-scale effects of transcriptional DNA supercoiling in vivo. *J. Mol. Biol.*, 292(5):1149–1160, 1999.

[38] P. Thomen, U. Bockelmann, and F. Heslot. Rotational drag on DNA: A single molecule experiment. *Phys. Rev. Lett.*, 88(24):248102, 2002.

[39] S. Allison, R. Austin, and M. Hogan. Bending and twisting dynamics of short linear DNAs - analysis of the triplet anisotropy decay of a 209-basepair fragment by Brownian simulation. *J. Chem. Phys.*, 90(7):3843–3854, 1989.

[40] G. Chirico and J. Langowski. Kinetics of DNA supercoiling studied by Brownian dynamics simulation. *Biopolymers*, 34(3):415–433, 1994.

[41] J. Bednar, P. Furrer, A. Stasiak, J. Dubochet, E. H. Egelman, and A. D. Bates. The twist, writhe and overall shape of supercoiled DNA change during counterion-induced transition from a loosely to a tightly interwound superhelix - possible implications for DNA- structure in-vivo. *J. Mol. Biol.*, 235(3):825–847, 1994.

[42] L. Mahadevan and J. B. Keller. Coiling of flexible ropes. *Proc. R. Soc. London Ser. A-Math. Phys. Eng. Sci.*, 452(1950):1679–1694, 1996.

[43] J. F. Marko and E. D. Siggia. Fluctuations and supercoiling of DNA. *Science*, 265(5171):506–508, 1994.

[44] J. C. Meiners and S. R. Quake. Femtonewton force spectroscopy of single extended DNA molecules. *Phys. Rev. Lett.*, 84(21):5014–5017, 2000.

[45] R. M. Jendrejack, E. T. Dimalanta, D. C. Schwartz, M. D. Graham, and J. J. de Pablo. DNA dynamics in a microchannel. *Phys. Rev. Lett.*, 91(3):038102, 2003.

[46] S. Leikin, D. C. Rau, and V. A. Parsegian. Measured entropy and enthalpy of hydration as a function of distance between DNA double helices. *Phys. Rev. A*, 44(8):5272–5278, 1991.

[47] Y. X. Zhu and S. Granick. Viscosity of interfacial water. *Phys. Rev. Lett.*, 87(9):096104, 2001.

[48] P. G. de Gennes. Reptation of a polymer chain in presence of fixed obstacles. *J. Chem. Phys.*, 55(2):572–&, 1971.

[49] M. Doi and S. F. Edwards. *The Theory of Polymer Dynamics*. Oxford University Press Inc., New York, NY, 1986.

[50] A. J. Spakowitz and Z.-G. Wang. Semiflexible polymer solutions. I. phase behavior and single- chain statistics. *J. Chem. Phys.*, 119(24):13113–13128, 2003.

[51] P. G. de Gennes. in *Polymer Liquid Crystals*, ed. by A. Ciferri, W. R. Krigbaum, R. B. Meyer. Academic, New York, 1982.

[52] O. Kratky and G. Porod. Rontgenuntersuchung geloster fadenmolekule. *Recl. Trav. Chim. Pay. B.*, 68(12):1106–1122, 1949.

[53] H. Yamakawa. *Helical Wormlike Chains in Polymer Solutions*. Springer-Verlag, 1997.

[54] A. E. H. Love. *A Treatise on the Mathematical Theory of Elasticity*. Dover Publications, Inc., New York, NY, 1944.

[55] M. E. Rose. *Elementary Theory of Angular Momentum*. Wiley, New York, NY, 1957.

[56] K. Klenin and J. Langowski. Computation of writhe in modeling of supercoiled DNA. *Biopolymers*, 54(5):307–317, 2000.

Chapter 8

Wrapping Transitions of Plasmid DNA in a Nucleosome

We study the formation of a nucleosome core particle on a minicircle of DNA by considering a simple polyelectrolyte/macroion model. With this model, we find the equilibrium conformations of a polyelectrolyte ring with fixed linking number interacting with an oppositely charged sphere via a salt-mediated electrostatic potential. Equilibrium conformations show a polymorphism in the stable equilibrium states with a salt-dependent hysteresis controlling the conformational states, which are easily categorized according the number of wraps made by the chain around the attractive particle. These wrapped states represent distinctly different writhed forms, thus the preferred state is strongly dependent on the linking number of the ring. Our results are consistent with experimentally observed polymorphism of DNA minicircles in a nucleosome, which is not observed for short stretches of open nucleosomal DNA.

8.1 Introduction

All of the processes necessary for the survival of a eukaryotic cell hinge on the cell's ability to store and read the genetic information encoded in its DNA. The daunting task of packaging 1 meter of DNA into a 1-micron diameter nucleus is complicated by the necessity

of maintaining the accessibility of the DNA to the cell's enzymatic machinery. The fundamental unit of packaged DNA, the nucleosome core particle, contains 146 base pairs of DNA wrapped 1.7 times around a cationic protein complex called the histone octamer [1]. A string of nucleosomes is organized into higher order structures to form chromatin, a remarkable complex that is compact yet maintains accessibility for genetic expression.

Although *in vivo* processes involving chromatin are aided by ATP-dependent nucleosome remodeling proteins [2, 3], *in vitro* experiments show that RNA polymerase is capable of transcibing through the nucleosome particle in the absence of such proteins [4, 5]. The dual existence of nucleosomal DNA as both bound to the histone octamer and accessible to the nuclear environment alters our picture of the nucleosome core particle from a static entity to a more dynamic, malleable complex. Several conjectures concerning the accessibility of nucleosomal DNA hinge on thermally driven conformation transitions [6, 7, 8], implying that the biological function of packaged DNA hinges on its access to a variety of stable conformations.

Nucleosomal DNA wraps the histone octamer due to favorable interactions between the negative charges along the phosphate backbone of the DNA and positively charged lysine and arginine residues decorating the histone-octamer surface at the expense of the bending deformation energy of the highly curved DNA, the loss of entropy upon adopting a fixed conformation, and the unfavorable interaction of the DNA strand with itself. As electrostatic interaction acts both to wrap the chain and to resist the corresponding collapse, altering the nature of the electrostatic interaction, for example with salt-induced screening, dramatically influences the ability to package DNA. For short strands of DNA (144 ± 2 base pairs) interacting with core histones, the formation of a stable native nucleosome core particle occurs within a range of intermediate salt concentrations (ionic strength $= 2 - 750\,\mathrm{mM}$), and

destabilization occurs at both low ($< 1\,\mathrm{mM}$) and high ($> 1,500\,\mathrm{mM}$) salt concentrations [9]. A simple model of the nucleosome that captures these experimentally observed features is a semiflexible polyelectrolyte interacting with an oppositely charged sphere [10], demonstrating that nucleosome destabilization occurs at low salt concentration due to dominant electrostatic self-interaction and at high salt concentration due to chain deformation. Direct observation of a nucleosome over the intermediate range of ionic strength shows the shape of the particle varies from a prolate ellipsoid to an oblate ellipsoid back to a prolate ellipsoid as the DNA transitions through the salt-induced stability region [11], further demonstrating the importance of salt-mediated electrostatics and the malleability of the nucleosome core particle.

The double-helix structure of DNA results in a molecular strand that resists bending and stretching deformation as well as positive twisting that tightens the double helix and negative twisting that loosens the double helix. Twist plays an important role in the biophysical behavior of DNA in torsionally constrained plasmids of prokaryotes and transiently closed loops that occur during gene regulation in eukaryotes. This is due to an underlying topological invariant of torsionally constrained paths called the linking number, which is given by a sum of the twist and the writhe for such closed elements [12]. The importance of twist and topology on DNA behavior is demonstrated by the existence of topoisomerases, a class of enzymes that control the DNA topology [13].

The crystal structure of the nucleosome core particle contains DNA wrapped in a left-handed helix 1.7 times, thus contributing -1.7 of writhe to the linking number per nucleosome [1]. However, nucleosomal DNA adopts different conformational variants in solution, particularly in the case of closed, circular DNA. Upon injected of its plasmid DNA, a eukaryotic virus such as SV40 hijacks the histone proteins of the host cell to form a minichro-

mosome, and the packaged plasmid DNA undergoes topological relaxation using the host's topoisomerases. The genome of SV40, extracted from the minichromosome, exhibits a topological contribution of ~ -1 per nucleosome relative to a reference population of plasmids relaxed by topoisomerase I [14, 15, 16], contrasting the change in the linking number of ~ -2 per nucleosome predicted by its crystal structure. Similar results are found for *in vitro* packaging of plasmid DNA with only the four core histone proteins present [17, 18, 19]. The discrepancy between the linking number contribution per nucleosome in plasmid DNA versus open DNA is called the "linking number paradox" [20].

Various experimental studies aim to elucidate the underlying mechanism responsible for this apparent discrepancy. Studies of mononucleosomes on DNA minicircles demonstrate the existence of a polymorphism in the states of packaged DNA that is strongly influenced by linking number, salt concentration, and histone acetylation [20, 21]. For example, mononucleosomes of 359 base pair plasmid DNA with linking number -2 in 10 mM monovalent salt exhibit two alternative states, one where the loop extending off the nucleosome crosses itself and one where the loop does not cross itself; whereas in 100 mM salt, only the crossed state exists [20]. This salt-dependent polymorphism in packaged structure may underlie the formation of a chromatin fiber *in vitro*, which requires a particular salt history to form a stable fiber with reproducible physical properties [22]. Furthermore, the existence of a variety of folded chromatin structures impacts the dynamic behavior of the packaged structure *in vivo*, where the DNA conformation and the location of associated proteins affects accessibility and susceptibility to manipulation [23].

Closing DNA into a plasmid introduces several important effects that alter its behavior both with and without interaction with associating proteins such as histones. Since unstressed DNA is straight and untwisted relative to the equilibrium twist of approximately

10 base pairs per helical turn, closing the strand into a ring makes the straight, unstressed state inaccessible, and the topology defined by the linking number identifies the accessible distribution between twist and writhe. For short strands of open DNA interacting with histone core proteins, the wrapped state is marked by a propensity for the nucleosome to be located near the chain ends, predicted both theoretically and experimentally [10, 24]; this of course cannot occur for a DNA minicircle in a nucleosome. Theoretical prediction of the preferred conformation of open DNA in a nucleosome shows a gradual writhed wrapping from the chain end as the salt concentration increases [10]. Closing the chain ends, the writhed wraps incur twist deformation in order to maintain the linking number, and the looped chain extending from the particle applies stresses that act to peel the wraps off the particle surface, strongly enhanced by electrostatic self-interaction.

Polymorphism in the stable states of a mononucleosome exists in the case of plasmid DNA minicircles but apparently does not exist for open DNA strands; therefore, closing the strand into a loop introduces physical effects that qualitatively alter the behavior of the packaged DNA. In this chapter, we show that polymorphism and salt-concentration hysteresis emerges naturally in a simple model of the DNA/protein system, a single polyelectrolyte ring interacting with an oppositely charged sphere. Such a model lacks the molecular detail and the inherent complexity that exists in the biological system [25]; however, several experimentally observed features that exist in the nucleosome system are captured using similar approaches, as demonstrated in studies of open [10, 24] and closed, circular [26, 27, 28, 29] strands of DNA in a nucleosome. Furthermore, this approach provides a fundamental understanding of the dominant features of DNA packaging, acting as a basis for comparison as more complexity is built into the model. This model is also applicable to colloid condensation of DNA used in gene therapy applications.

8.2 Results

Turning to our simple model, we address the minimum energy conformations of a ring polyelectrolyte interacting with an oppositely charged sphere over a wide range of salt concentration. We treat the electrostatic interaction using Debye-Hückel, mean-field theory, characterized by the Debye screening length l_D given by $l_D = 1/\sqrt{8\pi l_B C}$, where C is the monovalent salt concentration, and l_B is the Bjerrum length characterizing the length scale where the unscreened electrostatic potential equals the thermal energy $k_B T$ (approximately 0.7 nm for water at room temperature). The elastic properties of the ring are such that the bare persistence length without charge interaction is 30 nm [30], the twist persistence length is 50 nm, and the stretching modulus is 1000 nm^{-1}. The length of the ring is 100 nm (∼294 base pairs or ∼28 helical turns). The linear charge density along the ring is $2\,e^-/(0.34\,\mathrm{nm})$, and the charge on the spherical macroion is 40. In addition to the electrostatic interaction, we include hard-core interaction between chain segments at 2.5 nm and between chain segments and the attractive particle at 5 nm.

We explore the accessible states over a range of salt concentrations (0 mM to 1 M) by performing elevated-temperature Monte Carlo simulations (10× room temperature) with transient quenches to zero temperature (energy minimization); these transient quenches are recorded, and several distinct conformational variants emerge from the results. Each variant is then subjected to energy minimizations over a range of salt concentrations in order to determine their limit of stability and the transition characteristics at the point of instability.

Figure 8.1 shows a progression of energy minimized structures for our model with the linking number $Lk = 0$ beginning at low salt concentration and leading to high salt concentration. For low salt concentration, the favored conformation is an unwrapped, planar

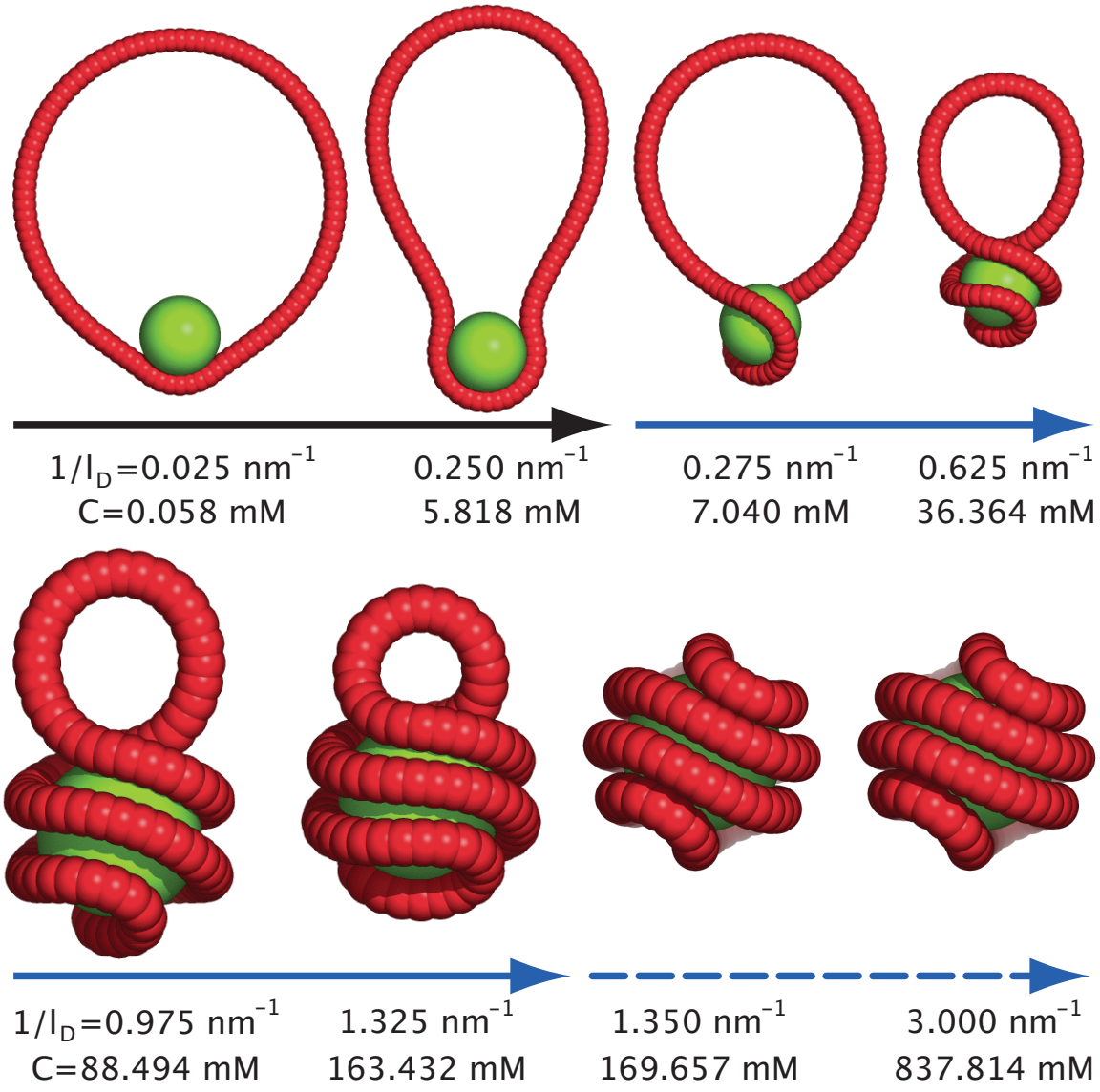

Figure 8.1: Minimum energy conformations of a polyelectrolyte ring ($Lk = 0$) interacting with a charged particle beginning with the low-salt unwrapped conformation and proceeding to the high-salt, tightly wrapped conformation. The colored lines beneath the conformations identify the wrapping state of the conformers (see text), thus first-order transitions occur between the second/third and sixth/seventh conformations. The inverse Debye length $1/l_D$ (units nm^{-1}) and the monovalent salt concentration C (units mM) are identified beneath each conformation. The last two conformations are rotated ninety degrees for clarity.

conformation that glances off the sphere surface with minimal deflection from a circular form, consistent with the short-length predictions of Ref. [29]. As the salt concentration increases, the self-interaction is screened, and the attractive sphere draws in the ring. From the first conformation to the second, the section of the ring in close contact with the sphere increases, and the conformation adopts a peanut shape when viewed from above.

The neck of the peanut narrows with salt concentration, and self repulsion causes one side to buckle out of the plane and the other to buckle into the plane, similar to the out-of-plane buckling for an open strand, though at higher salt concentration [10]. This first-order transition implies a hysteresis when traversing in the opposite direction in salt concentration. For $Lk = 0$, neither buckle direction is preferred; although Fig. 8.1 shows the positive-writhed form (third conformation), its mirror image is energetically identical. Non-zero linking number prefers the buckle with writhe of the same sign as the linking number in order to reduce twist deformation energy, and consequently, the first-order transition occurring between the second and third conformations of Fig. 8.1 would not occur.

Further increase in salt concentration leads to sphere wrapping through rotation of the chain about the south pole of the sphere (as viewed in Fig. 8.1), resulting in an increase in the writhe and negative twisting to maintain zero linking number. The spherical wrapping is comparable to a squat plectonemic structure, thus left-handed coiling about the sphere surface in Fig. 8.1 corresponds to positive writhing. Eventually the loop shrinks until it feels the presence of the attractive sphere at the north pole, which is void of chain segments due to the nature of the wrapping process. At this point the loop collapses on the sphere surface, and the polyelectrolyte ring adopts an essentially spherical conformation. This corresponds to a sudden change in the writhe to zero, since all non-self-crossing closed curves that lie on a sphere surface have zero writhe. For clarity, the last two conformations in Fig. 8.1 are

rotated by 90 degrees about the north/south pole axis.

The conformations in Fig. 8.1 show the kinetically accessible progression as salt concentration increases; the exhibited first-order transitions result in transformations that naturally emerge from the existing conformation. The ring in the first conformation of Fig. 8.1 has the appearance of an orbit that glances off the sphere surface without being caught in its attractive pull, and all subsequent conformations result from smooth deformations from the first. As a result, we categorize these conformations within a common family called the 0-loop state, named for the orbital appearance of the first conformation whose bound segment fails to complete a pass over the sphere surface. A distinguishing feature of the 0-loop state is the void of chain segments at the north pole of the sphere (as viewed in Fig. 8.1), which facilitates the formation of the tightly-bound 0-loop state in the last two conformations of Fig. 8.1. The colored arrows beneath the conformations in Fig. 8.1 identify the conformational state. Conformations above the black arrow exist in a planar 0-loop state. The blue arrow identifies conformers that are in a wrapped 0-loop state, and the dashed blue arrow distinguishes the conformers that are in a tightly wrapped 0-loop state, essentially bound to the particle surface. Although these conformers exist in distinctly different states separated by first-order transitions, they all belong in the 0-loop family.

The conformations in Fig. 8.2 show the opposite salt progression as Fig. 8.1, from high salt to low salt, beginning with a stable looped conformation and proceeding to the unwrapped 0-loop conformation (same as first conformation of Fig. 8.1). We first categorize the conformations in Fig. 8.2 according to the number of loops in the bound segment of the ring. The third conformation of Fig. 8.2 is essentially divided into an unbound loop (essentially planar) and a bound segment that is caught in the attractive pull of the sphere, making two complete passes over the sphere surface. Therefore, we categorize the first three

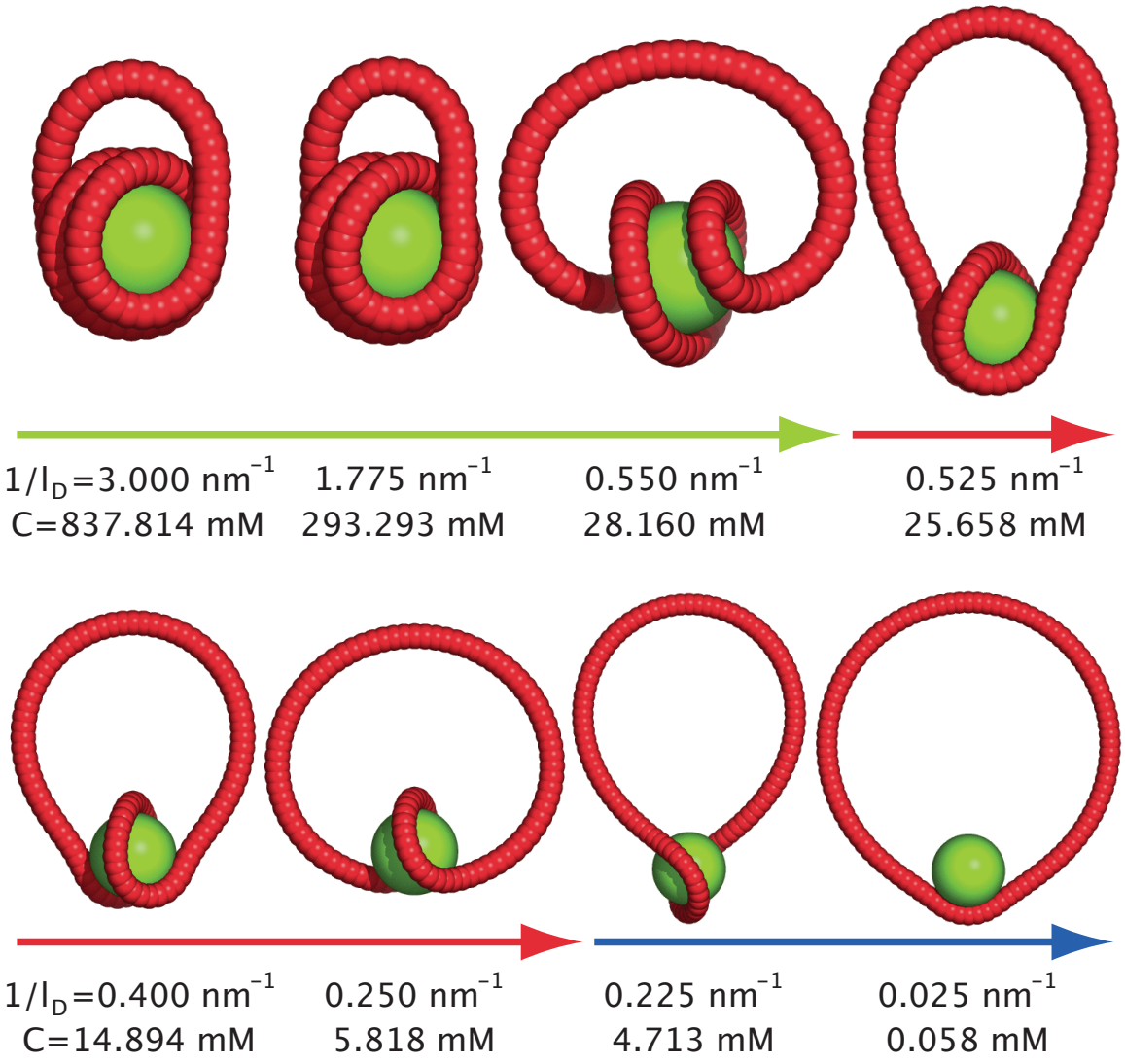

Figure 8.2: Minimum energy conformations of a polyelectrolyte ring ($Lk = 0$) interacting with a charged particle beginning with the stable 2-loop state at high salt concentration and proceeding to the unwrapped 0-loop conformer at low salt concentration. First-order transitions occur between the third/fourth and sixth/seventh conformations.

conformations of Fig. 8.2 in the 2-loop state and identify them by the green arrow. The sixth conformation of Fig. 8.2 has a similar structure as the third conformation; however, the bound segment completes only a single pass over the sphere surface. The fourth through sixth conformations in Fig. 8.2 belong to the same conformer family called the 1-loop state, identified by the red arrow. As in Fig. 8.1, the solid blue arrow denotes the 0-loop state in Fig. 8.2.

Beginning with the stable 2-loop conformation at high salt (first conformation in Fig. 8.2), the highly screened environment permits chain segments to come in close proximity leaving a large portion of the sphere uncovered. The 2-loop wrapping results in two loops passing over the north pole, thus restricting the exterior loop from collapsing on the sphere surface as in Fig. 8.1. As the salt concentration decreases, the self-repulsion and exterior-loop stresses cause the bound segments to separate toward the uncovered sphere region. The third conformation of Fig. 8.2 shows the limit of stability of the 2-loop state; further removal of salt causes a single loop to slip off the sphere surface, either toward the left or right (viewed as in Fig. 8.2), resulting in a 1-loop conformation. Progression of the conformation through the 1-loop region (conformations four to six in Fig. 8.2) occurs in a similar manner as the 2-loop region. The sixth conformation marks the limit of stability of the 1-loop state; further decrease in salt concentration causes the loop to slip off the sphere to the right or left with equal probability, leading to the wrapped 0-loop state.

We show the conformer states that emerge from monotonically increasing and decreasing salt concentration in Figs. 8.1 and 8.2 respectively; however, more complicated salt histories permit access to each state over a wide range of salt concentration. For example, the 1-loop state, accessed as in Fig. 8.2, remains stable upon increasing salt, leading to a highly wrapped 1-loop state. Additionally, a variant of the 1-loop state exists that wraps in the

opposite direction as the conformations of Fig. 8.2. Thus, we identify those conformations in Fig. 8.2 as existing in the 1-loop state A, and the variant is called the 1-loop state B (not shown in Figs. 8.1 and 8.2).

The conformations shown in Figs. 8.1 and 8.2 are for zero linking number; however, qualitatively similar conformers exist for non-zero linking numbers. Despite the apparent similarity in appearance, the energy and writhe of the resulting conformers are dramatically influenced by the linking number. We define the binding energy ΔE as the difference between the energy of the ring bound to the particle and an isolated ring, essentially giving the energy change upon introducing the ring to the attractive particle. In Fig. 8.3, the minimized binding energy ΔE and writhe Wr are plotted versus the inverse Debye length $1/l_D$ for $Lk = 0$ (left plots) and $Lk = 2$ (right plots). The energy plots in Fig. 8.3 show the underlying thermodynamic justification for the polymorphism exhibited in Figs. 8.1 and 8.2. The conformational states exhibit an energetic change with salt concentration that begins at a maximum at the point of instability, and the minimum energy conformer depends on the salt concentration. In comparison to the energy plot for $Lk = 0$, the energy plot for $Lk = 2$ exhibits a dramatic energetic shift favoring the higher loop states owing to the larger writhe of such states reducing the twist contribution to the linking number, thus reducing the twist deformation energy contribution.

The writhe of the conformational states tends to increase with the number of loops. Comparing the two writhe plots in Fig. 8.3, the linking number tends to alter the writhe of each individual state towards the linking number value due to the reduction in the twist deformation energy. The dominant conformer is chosen by a combination of factors. The twist deformation energy is minimized for the conformer with number of loops closest to the linking number of the ring; however, the salt mediated interaction between the ring

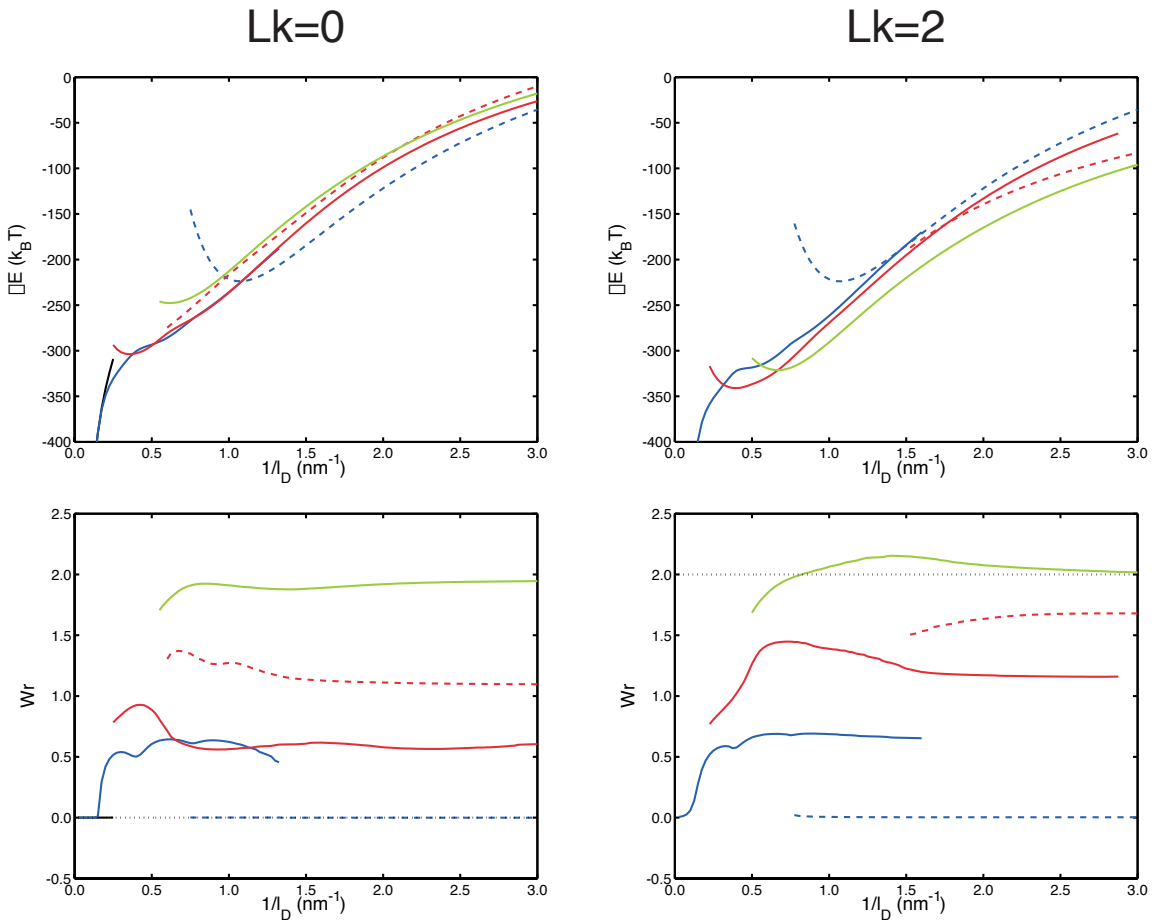

Figure 8.3: Minimized energy of binding ΔE (units $k_B T$) and writhe Wr of a polyelectrolyte ring (left plots are $Lk = 0$ and right plots are $Lk = 2$) interacting with a charged particle against the inverse Debye length $1/l_D$ (units nm^{-1}). Curves within each plot correspond to the 0-loop state (solid blue), the tight-wrapped 0-loop state (dashed blue), the 1-loop state A (solid red), the 1-loop state B (dashed red), and the 2-loop state (solid green) as defined in the text; the $Lk = 0$ plots contain additional curves for an unwrapped 0-loop state (solid black). The dotted black lines in the writhe plots identify the linking number Lk; we note that the twist is given by $Tw = Lk - Wr$.

and particle prefers the tightly bound state (conformations seven and eight in Fig. 8.1), particularly at high salt concentration with short-range attractive pull. As the strength of attraction decays with the salt concentration, the bending deformation stresses become increasingly important, eventually leading to unbinding.

8.3 Discussion

Our simple model of plasmid DNA in a nucleosome captures a number of important effects that are exhibited in the experimental system. The salt-induced wrapping transition exhibited by nucleosomal DNA [9] is clearly reflected in our results. Plasmid DNA in a mononucleosome exhibits a polymorphism in the stable states that is strongly influenced by salt concentration, histone acetylation, and linking number of the plasmid [20, 21]. Certainly our model lacks the molecular detail necessary to address histone acetylation; however, the polymorphism demonstrated by our results is strongly influenced by the salt concentration and the topological state of the closed strand. Salt history is an important factor in the *in vitro* assembly of a chromatin fiber [22]; similarly, the conformational state that is prevalent in our model system is controlled by the particular salt history used in the calculation.

The diversity of the resulting structures that are prevalent in mononucleosomes on plasmid DNA [20, 21] is also exhibited in the results presented in the previous section. This polymorphism is not exhibited for mononucleosomes with open DNA [9, 11]; theoretical predictions from the same model employed in this study but with an open strand does not exhibit salt-induced polymorphism [10]. In our current study and Ref. [10], the histone octamer is modeled as a structureless particle that carries a uniform charge on its surface; clearly this simple model lacks the inherent complexity of the histone octamer [1]. Nonetheless, the diversity of equilibrium structures is an intrinsic manifestation from closing

a chain into a ring, even when the packaging particle is completely structureless, as in our current study. Although the polymorphism may be altered upon adding molecular detail into the model, this structural diversity is inherent in a system as simple as a ring polymer interacting with an attractive sphere, as demonstrated in this chapter.

When a chain interacts with an attractive particle, the adopted conformation is composed of a wrapped section in close proximity of the sphere and an unwrapped section that is less influenced by the attractive pull of the particle. Since the chain is closed, the unwrapped section is looped in a sweeping curve that attempts to minimize the deformation energy while avoiding itself due to self-repulsion. This looped structure applies stresses that act to peel the wrapped section off the sphere surface, clearly exhibited by the third and sixth conformations of Fig. 8.2. The reason for the diversity in the wrapped states lies in the loop stress that peels the chain off the surface of the sphere. The limit of stability of the 2-loop state (third conformation of Fig. 8.2) and the 1-loop state (sixth conformation of Fig. 8.2) show that this peeling stress results in wrapped sections that wind over the sphere surface an integer number of orbital passes. The discrete number of orbital passes at the limit of stability results in distinctly different wrapping structures thus a diversity in the wrapped states.

The salt-dependent hysteresis prevalent in the formation of a chromatin fiber *in vitro* is reflected in the results presented in the previous section. The particular protocol for the *in vitro* assembly of a chromatin fiber involves a salt history beginning at high salt concentration and then performing a slow salt dialysis to physiological conditions [22]; this protocol is similar in nature to the progression given in Fig. 8.2. The resulting structure predicted by our results for this salt history is more closely related to the crystal structure of the nucleosome core particle [1] where the DNA is wrapped 1.7 times around the histone

octamer in a helical manner. We propose that this particular salt history (high salt to low salt) favors the native wrapping of the DNA thus avoiding misfolded structures, as in the conformers prevalent in Fig. 8.1. This favoring of the native wrapped state for this salt history may explain the particular protocol necessary to assemble a chromatin fiber with reproducible physical properties *in vitro* [22].

The topological state of the closed strand, given by the linking number, favors those wrapped states with more wraps. An increase in the linking number is associated with adding twist into the conformation, the resulting twist deformation is energetically costly to the polymer ring. However, the twist is alleviated when the ring adopts a writhed conformation due to the geometric coupling between twist and writhe implied by the linking number conservation in closed, circular threads ($Lk = Tw + Wr$) [12]. Comparing the energy plots in Fig. 8.3 for $Lk = 0$ and $Lk = 2$, we see a dramatic shift in the favored conformers from the small-writhe states for $Lk = 0$ (0-loop state is favored throughout) to the large-writhe states for $Lk = 2$ (1-loop and 2-loop states favored for $1/l_D > 0.316\,\mathrm{nm}^{-1}$).

Although the energetically favored states are thermodynamically preferred, non-energetically favored states are at least mechanically stable. Our current work does not address the energetic barriers between wrapped states at a given salt concentration. Such barriers govern the dynamic behavior in the presence of thermal fluctuations, which certainly play a role in the behavior and function of nucleosomal DNA. In this study, we address the mechanical aspects of the wrapping of a ring polymer around an attractive sphere; in future treatments, we will include the effect of thermal fluctuations to address the dynamics of activated transitions between stable conformational states.

Appendix A: Model of DNA/Core Particle

We study the behavior of a DNA minicircle in a nucleosome using a simple model, namely a polyelectrolyte ring interacting with an oppositely charged sphere through a screened electrostatic potential. This simplified approach neglects the details of the underlying molecular architecture; however, a number of qualitative features of DNA packaging are captured with this simple description. The polyelectrolyte ring is represented by a closed ring that carries a homogeneous charge along its centerline. The ring responds to deformation through an elastic energy that is consistent with the lowest-order contribution in elasticity theory [31]. As the chain is closed in a ring, deformation does not change the topological state provided the ring does not pass through itself; the electrostatic potential of self-interaction is bolstered by a hard-core potential to model the short-range repulsive interaction of DNA. In order to facilitate numerical modeling, we cast the model into a discrete form that is consistent with the continuous description at sufficiently small length scales of discretization.

The DNA conformation is described as a string of beads at spatial locations $\vec{R}_i$ where i runs from 1 to N. The beads are connected by N bond vectors $u_i = (\vec{R}_{i+1} - \vec{R}_i)/|\vec{R}_{i+1} - \vec{R}_i|$ for $i = 1, \ldots, N-1$ and $u_N = (\vec{R}_1 - \vec{R}_N)/|\vec{R}_1 - \vec{R}_N|$, thus closing the ring. The material twisting is accounted for by tracking the two normal vectors $\vec{v}_i$ and $\vec{f}_i$, which form an orthonormal triad with u_i since $\vec{v}_i = \vec{u}_i \times \vec{f}_i$ and $\vec{f}_i \cdot \vec{u}_i = 0$ [32]. Altogether, our model has $4N$ degrees of freedom including the positions of the N beads and N twist angles to determine the material normal orientations.

The total energy of the chain includes terms that account for the elastic deformation energy, the self-interaction energy, and the interaction between the ring and the charged sphere. The deformation energy, including compression, bending, and twisting terms, are quadratic in the displacement away from the straight equilibrium state [31]. These terms

are given by

$$E_{com} = \frac{A}{2}\sum_{i=1}^{N}\left(b_i/l_0 - 1\right)^2, \tag{A-1}$$

$$E_{bend} = \frac{B}{2}\left(\vec{u}_1 - \vec{u}_N\right)^2 + \frac{B}{2}\sum_{i=1}^{N-1}\left(\vec{u}_{i+1} - \vec{u}_i\right)^2, \tag{A-2}$$

$$E_{twist} = \frac{C}{2}\sum_{i=1}^{N}\omega_i^2, \tag{A-3}$$

where A, B, and C are the compression, bending, and twisting moduli, respectively. The bond length b_i is given by $b_i = |\vec{R}_{i+1} - \vec{R}_i|$ for $i = 1, \ldots, N-1$ and $b_N = |\vec{R}_1 - \vec{R}_N|$, and l_0 is the equilibrium bond length. The twist angle ω_i satisfies $(1 + \vec{u}_i \cdot \vec{u}_{i+1}) \sin\omega_i = \vec{v}_i \cdot \vec{f}_{i+1} - \vec{f}_i \cdot \vec{v}_{i+1}$ [32]. The self-interaction energy takes the form

$$E_{int} = \frac{1}{2}\sum_{i=1}^{N}\sum_{j\neq i} v_{int}(R_{ij}), \tag{A-4}$$

where $R_{ij} = |\vec{R}_i - \vec{R}_j|$, and $v_{int}(R)$ is the two-body interaction potential. In our model, $v_{int}(R)$ is given by

$$v_{int}(R) = \frac{k_B T l_B q^2 \exp\left(-R/l_D\right)}{R} + v_{HC}\exp\left[-(R-\sigma)/l_{HC}\right], \tag{A-5}$$

where the first term is the screened electrostatic self-repulsion, and the second term is the hard-core repulsion at short length scales. In the first term, $k_B T$ is the thermal energy, l_B is the Bjerrum length (approximately 0.7 nm at room temperature), q is the charge per bead given by $-2l_0/(0.34\,\text{nm})$, and l_D is the Debye length given by $l_D = 1/\sqrt{8\pi l_B C}$ where C is the monovalent salt concentration. In the second term, v_{HC} gives the strength of the hard-core potential, l_{HC} is the length scale of the potential, and σ is the hydrated diameter of

DNA (approximately 2.5 nm). The purpose of the hard-core potential is to strictly enforce the non-cross-ability of the chain, thus in principle the hard-core length scale should go to zero. However, numerical studies requires a finite value of these terms, which are given by $v_{HC} = k_B T$ and $l_{HC} = 0.05\,\text{nm}$ in our present study. The interaction between the ring and the charged sphere is model as

$$E_{his} = \sum_{i=1}^{N} v_{his}(|R_i|) \tag{A-6}$$

where

$$v_{his} = \frac{k_B T l_B Z q}{1 + R_{his}/l_D} \frac{\exp\left(-R/l_D\right)}{R} + v_{HC} \exp\left[-(R - R_{his})/l_{HC}\right], \tag{A-7}$$

where Z is the sphere charge (40 in our study), and R_{his} is the histone core particle radius (approximately 5 nm). We note that since q and Z have opposite signs, the interaction between ring and sphere is attractive.

With this energetic model in place, we conduct several different types of simulations in order to analyze the behavior of our system. Energy minimization is performed using both dynamic simulations [32] and conjugate gradient minimization of our model. To efficiently search the conformational space, we also perform high-temperature Monte Carlo simulations. The topology of the ring is characterized by the linking number is a constant provided the chain cannot pass through itself. We calculate the twist and writhe separately as a check on the non-cross-ability of the chain. The twist is calculated using the twist angle ω_i along the chain, and we make use of techniques in Ref. [33] to determine the writhe of the ring.

Bibliography

[1] K. Luger, A. W. Mader, R. K. Richmond, D. F. Sargent, and T. J. Richmond. Crystal structure of the nucleosome core particle at 2.8 angstrom resolution. *Nature*, 389(6648):251–260, 1997.

[2] P. B. Becker. Nucleosome sliding: facts and fiction. *Embo J.*, 21(18):4749–4753, 2002.

[3] H. Y. Fan, X. He, R. E. Kingston, and G. J. Narlikar. Distinct strategies to make nucleosomal DNA accessible. *Mol. Cell.*, 11(5):1311–1322, 2003.

[4] V. M. Studitsky, G. A. Kassavetis, E. P. Geiduschek, and G. Felsenfeld. Mechanism of transcription through the nucleosome by eukaryotic RNA polymerase. *Science*, 278(5345):1960–1963, 1997.

[5] J. Widom. Transcription - getting around the nucleosomes. *Science*, 278(5345):1899–1901, 1997.

[6] H. Schiessel, J. Widom, R. F. Bruinsma, and W. M. Gelbart. Polymer reptation and nucleosome repositioning. *Phys. Rev. Lett.*, 86(19):4414–4417, 2001.

[7] I. M. Kulic and H. Schiessel. Nucleosome repositioning via loop formation. *Biophys. J.*, 84(5):3197–3211, 2003.

[8] I. M. Kulic and H. Schiessel. Chromatin dynamics: Nucleosomes go mobile through twist defects. *Phys. Rev. Lett.*, 91(14):art. no.–148103, 2003.

[9] T. D. Yager, C. T. McMurray, and K. E. Vanholde. Salt-induced release of DNA from nucleosome core particles. *Biochemistry*, 28(5):2271–2281, 1989.

[10] K. K. Kunze and R. R. Netz. Salt-induced DNA-histone complexation. *Phys. Rev. Lett.*, 85(20):4389–4392, 2000.

[11] G. J. Czarnota and F. P. Ottensmeyer. Structural states of the nucleosomes. *J. Biol. Chem.*, 271(7):3677–3683, 1996.

[12] J. H. White. Self-linking and Gauss-integral in higher dimensions. *Am. J. Math.*, 91(3):693–&, 1969.

[13] J. Wang and N. R. Cozzarelli. *Meeting on Biological Effects of DNA Topology.* Cold Spring Harbor Laboratory, N. Y., 1986.

[14] M. Shure and J. Vinograd. Number of superhelical turns in native virion SV40 DNA and minicol DNA determined by band counting method. *Cell*, 8(2):215–226, 1976.

[15] S. Saragosti, G. Moyne, and M. Yaniv. Absence of nucleosomes in a fraction of SV40 chromatin between the origin of replication and the region coding for the late leader rna. *Cell*, 20(1):65–73, 1980.

[16] J. M. Sogo, H. Stahl, T. Koller, and R. Knippers. Structure of replicating simian virus-40 minichromosomes - the replication fork, core histone segregation and terminal structures. *J. Mol. Biol.*, 189(1):189–204, 1986.

[17] J. E. Germond, B. Hirt, P. Oudet, M. Grossbellard, and P. Chambon. Folding of DNA double helix in chromatin-like structures from simian virus 40. *Proc. Natl. Acad. Sci. U.S.A.*, 72(5):1843–1847, 1975.

[18] R. T. Simpson, F. Thoma, and J. M. Brubaker. Chromatin reconstituted from tandemly repeated cloned DNA fragments and core histones - a model system for study of higher-order structure. *Cell*, 42(3):799–808, 1985.

[19] V. G. Norton, B. S. Imai, P. Yau, and E. M. Bradbury. Histone acetylation reduces nucleosome core particle linking number change. *Cell*, 57(3):449–457, 1989.

[20] A. Prunell. A topological approach to nucleosome structure and dynamics: The linking number paradox and other issues. *Biophys. J.*, 74(5):2531–2544, 1998.

[21] F. De Lucia, M. Alilat, A. Sivolob, and A. Prunell. Nucleosome dynamics. III. histone tail-dependent fluctuation of nucleosomes between open and closed DNA conformations. implications for chromatin dynamics and the linking number paradox. a relaxation study of mononucleosomes on DNA minicircles. *J. Mol. Biol.*, 285(3):1101–1119, 1999.

[22] K. Hizume, S. H. Yoshimura, H. Maruyama, J. Kim, H. Wada, and K. Takeyasu. Chromatin reconstitution: Development of a salt-dialysis method monitored by nanotechnology. *Arch. Histol. Cytol.*, 65(5):405–413, 2002.

[23] G. Li and J. Widom. Nucleosomes facilitate their own invasion. *Nat. Struct. Mol. Biol.*, 11(8):763–769, 2004.

[24] T. Sakaue, K. Yoshikawa, S. H. Yoshimura, and K. Takeyasu. Histone core slips along DNA and prefers positioning at the chain end. *Phys. Rev. Lett.*, 8707(7):art. no.–078105, 2001.

[25] D. A. Beard and T. Schlick. Modeling salt-mediated electrostatics of macromolecules: The discrete surface charge optimization algorithm and its application to the nucleosome. *Biopolymers*, 58(1):106–115, 2001.

[26] M. Lebret. Computation of the helical twist of nucleosomal DNA. *J. Mol. Biol.*, 200(2):285–290, 1988.

[27] J. A. Martino and W. K. Olson. Modeling protein-induced configurational changes in DNA minicircles. *Biopolymers*, 41(4):419–430, 1997.

[28] D. Swigon, B. D. Coleman, and I. Tobias. The elastic rod model for DNA and its application to the tertiary structure of DNA minicircles in mononucleosomes. *Biophys. J.*, 74(5):2515–2530, 1998.

[29] H. Schiessel, J. Rudnick, R. Bruinsma, and W. M. Gelbart. Organized condensation of worm-like chains. *Europhys. Lett.*, 51(2):237–243, 2000.

[30] E. S. Sobel and J. A. Harpst. Effects of Na^+ on the persistence length and excluded volume of T7-bacteriophage DNA. *Biopolymers*, 31(13):1559–1564, 1991.

[31] A. E. H. Love. *A Treatise on the Mathematical Theory of Elasticity*. Dover Publications, Inc., New York, NY, 1944.

[32] G. Chirico and J. Langowski. Kinetics of DNA supercoiling studied by Brownian dynamics simulation. *Biopolymers*, 34(3):415–433, 1994.

[33] K. Klenin and J. Langowski. Computation of writhe in modeling of supercoiled DNA. *Biopolymers*, 54(5):307–317, 2000.